



Developing Capture Mechanisms and High-Fidelity Dynamic Models for the MXER Tether System

*Stephen Canfield, Principal Investigator
Department of Mechanical Engineering
Tennessee Technological University
Cookeville, Tennessee*

Prepared for Marshall Space Flight Center
under Contract NNM04AB13C

September 2007

The NASA STI Program...in Profile

Since its founding, NASA has been dedicated to the advancement of aeronautics and space science. The NASA Scientific and Technical Information (STI) Program Office plays a key part in helping NASA maintain this important role.

The NASA STI program operates under the auspices of the Agency Chief Information Officer. It collects, organizes, provides for archiving, and disseminates NASA's STI. The NASA STI program provides access to the NASA Aeronautics and Space Database and its public interface, the NASA Technical Report Server, thus providing one of the largest collections of aeronautical and space science STI in the world. Results are published in both non-NASA channels and by NASA in the NASA STI Report Series, which includes the following report types:

- **TECHNICAL PUBLICATION.** Reports of completed research or a major significant phase of research that present the results of NASA programs and include extensive data or theoretical analysis. Includes compilations of significant scientific and technical data and information deemed to be of continuing reference value. NASA's counterpart of peer-reviewed formal professional papers but has less stringent limitations on manuscript length and extent of graphic presentations.
- **TECHNICAL MEMORANDUM.** Scientific and technical findings that are preliminary or of specialized interest, e.g., quick release reports, working papers, and bibliographies that contain minimal annotation. Does not contain extensive analysis.
- **CONTRACTOR REPORT.** Scientific and technical findings by NASA-sponsored contractors and grantees.

- **CONFERENCE PUBLICATION.** Collected papers from scientific and technical conferences, symposia, seminars, or other meetings sponsored or cosponsored by NASA.
- **SPECIAL PUBLICATION.** Scientific, technical, or historical information from NASA programs, projects, and missions, often concerned with subjects having substantial public interest.
- **TECHNICAL TRANSLATION.** English-language translations of foreign scientific and technical material pertinent to NASA's mission.

Specialized services also include creating custom thesauri, building customized databases, and organizing and publishing research results.

For more information about the NASA STI program, see the following:

- Access the NASA STI program home page at [<http://www.sti.nasa.gov>](http://www.sti.nasa.gov)
- E-mail your question via the Internet to [<help@sti.nasa.gov>](mailto:help@sti.nasa.gov)
- Fax your question to the NASA STI Help Desk at 301-621-0134
- Phone the NASA STI Help Desk at 301-621-0390
- Write to:
NASA STI Help Desk
NASA Center for Aerospace Information
7115 Standard Drive
Hanover, MD 21076-1320



Developing Capture Mechanisms and High-Fidelity Dynamic Models for the MXER Tether System

*Stephen Canfield, Principal Investigator
Department of Mechanical Engineering
Tennessee Technological University
Cookeville, Tennessee*

Prepared for Marshall Space Flight Center
under Contract NNM04AB13C

National Aeronautics and
Space Administration

Marshall Space Flight Center • MSFC, Alabama 35812

September 2007

Acknowledgments

This work was performed under contract NNM04AB13C, funded by the Emerging Propulsion Technology Area of the In-Space Propulsion Technology Program, which is managed by SMD and was implemented by the In-Space Propulsion Technology Project at MSFC during the period of performance.

Much appreciation is extended to Kirk Sorensen and Joseph Bonometti, of NASA Marshall Space Flight Center, for their vision, advocacy, and technical expertise in guiding the development of the MXER tether capture mechanism and dynamics work.

Much appreciation goes to the co-investigators of this work, John Peddieson and Joseph Richardson of Tennessee Tech, John Glaese of B.D. Systems, and Sunil Agrawal of University of Delaware. A special thanks to the graduate students and engineering support team without whom this work would not have been possible, Seth Knight, Marshall Norris, Daniel Chlarson, Neil White, Jamie Beard and Mike Renfro.

Available from:

NASA Center for AeroSpace Information
7115 Standard Drive
Hanover, MD 21076-1320
301-621-0390

This report is also available in electronic form at
<<https://www2.sti.nasa.gov>>

TABLE OF CONTENTS

1. EXECUTIVE SUMMARY	1
2. OVERVIEW OF MXER SYSTEM	2
3. PROJECT STATUS	2
4. TTU TEAM AND PRIMARY PARTNER CONTRIBUTIONS	6
5. REPORT SUMMARY	7
SECTION A—DEVELOPMENTS TOWARD CAPTURE MECHANISM.....	8
SECTION B—DYNAMIC MODELS FOR MXER TETHER SYSTEMS	77
SECTION C—ERROR SPACE PREDICTION.....	125
SECTION D—QUAD TRAP CAPTURE MECHANISM PROTOTYPE CAD MODEL.....	136

1. EXECUTIVE SUMMARY

A team consisting of collaborators from Tennessee Technological University, MSFC, BD Systems and the University of Delaware (herein called the TTU team) conducted specific research and development activities in MXER tether systems during the base period of 5-15-04 through 3-24-06 under contract (numbers NNM04AB13C). The team addressed two primary topics related to the MXER tether system; development of validated, high-fidelity dynamic models of an elastic rotating tether and development of feasible mechanisms to enable reliable rendezvous and capture. The following report will describe in detail the activities that were performed during the base period of this cycle 2 MXER tether activity, and will summarize the results of this funded activity. A brief summary of the significant outcomes of this phase I activity are provided here.

MXER Tether Capture Mechanisms:

- Delivery of Quad-Trap, a robust capture mechanism proposed, developed, tested and demonstrated with high degree of feasibility
- High-fidelity dynamic model of the capture mechanism created and validated through comparisons with hardware
- Autonomous capture demonstrated using the Quad-trap mechanism
- Significant number (40+) of unique capture concepts proposed and evaluated
- Trade study tool established for evaluating proposed capture concepts
- Hierarchal (based on technical aspects) categorization tool developing for organizing capture concepts
- A series of other feasible capture mechanisms developed and described
- Passive operation (Gravity-gradient actuation) demonstrated in capture mechanism
- Test facility developed to enable kinematically & dynamically-similar testing of capture systems

MXER Tether Dynamic Modeling

- Detailed development of high-fidelity elastic tether dynamic models provided through multiple formulations
- Detailed development of specific algorithms for efficient implementation of tether dynamic models
- Analysis of error window at capture performed based on Monte Carlo simulation with tether dynamic model used to guide subsequent capture mechanism synthesis
- Validation procedure implemented and conducted based on cross-model of verification
- Observed several, potentially significant, non-linear effects in tether dynamics not currently reported in the literature or in assumed-modes methods:
 - Coupling between axial and transverse modes resulting in resonance or beating
 - System response dependent on initial conditions in a non-linear fashion
 - Resonant conditions possible in all tether configurations
- Developed a series of system response results that can be used to validate other tether algorithms.
- One (1) paper ready to submit to ISPT export control in July, 2004 for publication, additional papers to be submitted in August 2005 to ISPT export control for publication.

MXER Tether System Components

- Spatial 3 dof mechanism proposed, developed and demonstrated mechanism to achieve efficient sun-tracking by tether-node-based solar arrays
- Three prototype models with real-time tracking developed and delivered
- Dynamic models and detailed design presented for practical implementation
- One prototype model developed and tested for possible attitude control system

2. OVERVIEW OF MXER SYSTEM

Momentum-exchange/electrodynamic reboost (MXER) tether systems may enable high-energy missions to the Moon, Mars and beyond by serving as an “upper stage in space”. Existing rockets that use a MXER tether station could double their capability to launch communications satellites and help improve US competitiveness. A MXER tether station would boost spacecraft from low Earth orbit to a high-energy orbit quickly, like a high-thrust rocket. Then, using the same principles that make an electric motor work, it would slowly rebuild its orbital momentum by pushing against the Earth's magnetic field--without using any propellant. While many significant challenges exist in designing a feasible MXER tether system, the proposal of a passive capture mechanism [3] provided the impetus necessary to consider MXER tethers for future in-space transportation. With this approach, the significant challenges in developing a momentum-exchange/electrodynamic reboost tether system are in the ability to predict the behavior of the system in a manner to control tether flight and coordinate a successful rendezvous between tether and payload. Accurate tether propagation, combined with a successful capture mechanism will provide two of the keys in making the technology feasible for future application.

3. PROJECT STATUS

According to task statement and deliverables
TTU performing organization

Task #	Description	Status	Date Completed	Source Materials
Tether Dynamic Modeling and Algorithm Activity				
1.1	Develop the MXER tether system dynamic models and algorithms to be used within the complete tether system model	Four analytical models developed to consider tether dynamics <ol style="list-style-type: none">1. Continuum model using inertial-frame-based coordinates and finite difference (FD) solver2. Continuum model using relative-orbit-based coordinates and finite difference (FD) solver3. Continuum model applicable to multi-noded tether system, inertial-based coordinates, finite difference solver Models to include axial and bending stiffness, various damping types. Three classes of computational ODE algorithms are implemented: <ol style="list-style-type: none">1. Runge Kutta (single-point explicit)	12-1-05	Model development described in section B 1, results of these models can be seen in section B 2, B 3 and Appendix B.

Task #	Description	Status	Date Completed	Source Materials
		2. Adams-Bashforth Moulton (multi-point explicit) 3. Gear Methods (multi-Point implicit) For the implicit techniques, the ODE system gradient is evaluated for use in a Newton-type search		
1.2	Validation of tether system models, with extended implementation	Multi-stage process of model validation defined through the “Model Validation Matrix”. This includes: 1) compare with closed-form solution (Wave equation) 2) Spatial/Temporal convergence trials 3) Limiting MXER configs with CFS 4) Compare with in-Lab experiments 5) Comparison of reference MXER applications This validation will spans TTU team model development activities and is available for other participants.	2-15-06 (Validation material contributed by all team members)	Validation activity described in detail in section B 2 with results included.
1.3	Basic implementation and demonstration in selected software platform.	Analytical Models 1 and 4 implemented and demonstrated in Matlab using three classes of ODE solvers.	11-15-05	Implementation given in section B 3
1.4	Basic application of the dynamic model as a simulation, analysis and design tool.	Initial used of tether model as a simulation, analysis and design tool performed in evaluation of tether capture window, evaluated as a stochastic predictor process using Monte-Carlo simulation.	12-15-05	Demonstration as use as a design tool given in section A 1 and Appendix B.
1.5	Develop initial condition and boundary condition models	Models for initial conditions developed, providing closed-form solution for initial rotational state. Results delivered in algorithmic format along with PDE and its solution.	2-25-05	Material presented in Section B 5
1.6	Participate in integration of tether dynamic model and development of the MXER tether system design and analysis tool.	Integration activities ongoing throughout Base period extension.	3-15-06	
1.7	Final reporting and presentation of year one results shall be prepared in accordance with	Mid-term report delivered 10-13-04 Base-year Final Report deliver 7-15-05 Project final report, delivery date of 5-15-06 (draft 3-31-06)	5-15-06	

Task #	Description	Status	Date Completed	Source Materials
	DRD 1040MA-001.			
Capture Mechanism Development Activity:				
2.1	Enumerate objective functions, figures of merit and associated tether behavior that will drive the design and development of capture system concepts.	Task statement and design objectives prepared to guide capture system design and development process. These are demonstrated in part as evaluation points in the capture-concept trade study. One significant capture objective was definition of a probabilistic capture window based on tether flight dynamics, as well as clear definition of the kinematic and dynamic nature of the tether capture process.	10-15-05	Section A 1
2.2	Define an array of capture system concepts.	Initial set of capture concepts developed and proposed. The final set includes 40 + concepts. Each concept or class of concepts in the set is defined using the quad-chart format. Organization of all capture concepts is provided through the development of the capture concept genealogy and naming system. The genealogy and the capture concept description library are hyperlinked for easy review.	6-15-05	Section A 2
2.3	Conduct a capture system trade study.	A complete trade study on the capture concepts proposed was performed. From this, four concepts were selected for additional analysis.	1-15-05	Section A 3
2.4	Select and develop basic designs for most promising capture concepts selected from Task 2.3.	Four basic designs were selected from the first stage capture concept trade study; 1. Modified IRIS (Quad-Trap) (CCM.T074b.P03x.A) 2. A modified Turkey Trap (CCM.T03.P05b.A) 3. Modified V-Gripper (CCM.T03d.P04.P) 4. Tethered Goal-post flier (CCM.T03.P02b.P) An engineering analysis and simple design of each concept was performed. These results were used to down select to the top capture concept candidate. Advanced models and further trade study analysis performed based on this work.	2-15-05	Section A 4.1 through section A 4.6
2.4.1	Evaluation of 3 dof spatial joint mechanism for	1. Two demonstration prototype mechanisms fabricated and delivered, one capable of real-time control by	2-15-06	Section A 4.7 Simulations delivered:

Task #	Description	Status	Date Completed	Source Materials
	MXER and other in-space propulsion concepts	operator through joystick input. 2. Kinematic models of mechanism constructed and made available 3. Issues in design for as an in-space mechanism considered 4. Alternative applications related to in-space activities considered and addressed: Kinematic analysis and simulation of various in-space uses with supporting data provided (mod. 4). Develop and demonstrated prototype system based on new design with internal, pressurized fluid passageways, tested as a mounting system for attitude control thrusters		2 simulations for Bigelow architecture, 2 general mechanism simulations (thruster applications), n simulations for multiple arrays. 3 prototypes delivered, one integrated with thruster for testing.
2.5	Perform testing and demonstration on proof-of-concept prototypes of capture system concepts developed in task 2.4.	Testing and demonstration initiated through the following activities: 1. Design, construction and testing of the payload launch system (PLS) and test facilities – 11-15-04 2. Design and construction of the payload – 12-13-04 3. Design, construction, testing and demonstration of the capture mechanism. 4-15-05 4. Testing of LM mechanisms (8-05) 5. Advanced dynamic testing of the Quad-Trap (2-06)	2-15-06	Section A 5
2.5.1	Redesign of capture concepts from year one with advanced testing and demonstration of capture system prototype	Advanced developments of the capture mechanism were addressed in the following activities: 1. Detailed dynamic testing and analysis of the capture mechanism, leading to advanced model and system understanding (2-15-06) 2. Continued work in autonomous operation of the capture mechanism with two alternative autonomous capture systems demonstrated, 3-24-06 3. Testing of alternative capture mechanisms 8-15-05	3-24-06	Section A 5.8
2.5.2	Investigate issues resulting from capture concepts developments in year one	The issue associated with slender booms was identified as one of the primary areas for advanced investigation on year-one capture mechanism development. Slender booms were addressed through activities in modeling, analysis, characterizing behavior and issues of practical implementation as associated with the Quad-trap mechanism.	3-29-06	Section A 4.1, 4.2

Task #	Description	Status	Date Completed	Source Materials
2.6	Final reporting and presentation of year one results shall be prepared in accordance with DRD 1040MA-001.	Mid-term report delivered 10-13-04 Final report delivered 11-9-06.		

4. TTU TEAM AND PRIMARY PARTNER CONTRIBUTIONS

Name	PI/Co-I	Org	Work Commitments
Stephen Canfield	PI	TTU	<ul style="list-style-type: none"> Overall project manager, organize activities to meet technical objectives and deliverables Lead effort in capture system trade study Participate in developing specific capture concepts Participate in capture model development
Jamie Beard		TTU	<ul style="list-style-type: none">
John Peddieson	Co-I	TTU	<ul style="list-style-type: none"> Participate in tether dynamic model development and validation
Joe Richardson	Co-I	TTU	<ul style="list-style-type: none"> Participate in capture system trade study Participate in tether model development
Jamie Beard	Research	TTU	<ul style="list-style-type: none"> Computational implementation, capture model development and testing
Mike Renfro	Research	TTU	<ul style="list-style-type: none"> http://mxer.tntech.edu maintenance
Seth Knight	G.S.	TTU	<ul style="list-style-type: none"> Capture system development, prototype testing
Marshall Norris	G.S.	TTU	<ul style="list-style-type: none"> Capture system development, quad trap model (ADAMS)
Daniel Chlarson	G.S.	TTU	<ul style="list-style-type: none"> Prep Facilities, testing, report editing
Neil White	G.S. (hourly)	TTU	<ul style="list-style-type: none"> Developed PLS, fabrication
Sunil Agrawal	Co-I	UD	<ul style="list-style-type: none"> Participate in developing specific capture concepts Participate in dynamic model validation work
John Glaese	Co-I	BDSys	<ul style="list-style-type: none"> Participate in developing specific capture concepts Participate in capture model development

5. REPORT SUMMARY

The remainder of this report describes in detail the activities that were performed during the base year to develop capture mechanisms and dynamic models for the MXER tether system. The report is divided into two sections; Section A covers development of the capture mechanism while Section B covers the dynamic model development and validation activities. Each section proceeds in a sequential order according to the tasks statement, i.e., section A 1.0, Derive Capture System Objectives describes the work conducted to complete task statement 1 on the capture mechanism, and so-forth. Two additional sections are included at the end of the report providing an acronym list, a derivation of the Error Space prediction for capture, and CAD model drawing of the Quad Trap Mechanism prototype. A results and conclusions section is found near the end of the report.

SECTION A—DEVELOPMENTS TOWARD CAPTURE MECHANISM FOR MXER TETHER SYSTEM

Table of Contents

1.0 DERIVE OBJECTIVES.....	12
1.1 EVALUATION CRITERIA FOR THE CAPTURE MECHANISM.....	12
1.2 KINEMATIC DESCRIPTION OF THE CAPTURE EVENT.....	12
2.0 DERIVE AN ARRAY OF POTENTIAL CAPTURE SYSTEM CONCEPTS	15
3.0 CAPTURE SYSTEM TRADE STUDY	17
3.1 BRIEF DESCRIPTION OF AHP	17
3.2 OVERVIEW OF TRADE STUDY CRITERIA	17
3.3 RESULTS FROM THE TRADE STUDY	19
4.0 BASIC DESIGN SELECTION AND DEVELOPMENT	23
4.1 MODIFIED IRIS(QUAD TRAP): FIRST ROUND DESIGN ANALYSIS	23
4.1.1 Overview	23
4.1.2 Brief Description.....	23
4.1.3 Summary of Analysis Performed.....	23
4.1.4 Summary of Key Conclusions	24
4.1.5 Other Elements for the Iris Mechanism under Consideration.....	29
4.2 TURKEY TRAP: FIRST ROUND DESIGN ANALYSIS.....	30
4.2.3 Summary of Analysis Performed.....	32
4.2.4 Summary of Key Conclusions	32
4.3 GOALPOST FLIER: FIRST-ROUND DESIGN ANALYSIS.....	34
4.3.1 Overview	34
4.3.2 Brief Description.....	34
4.3.3 Summary of Design Points.....	34
4.3.4 Summary of Analysis Performed.....	35
4.3.5 Summary of Key Conclusions	35
4.4 MODIFIED V-GRIPPER: FIRST-ROUND DESIGN ANALYSIS.....	38
4.4.1 Overview	38
4.4.2 Brief Description.....	38
4.4.3 Summary of Design Points.....	38
4.4.4 Summary of Analysis Performed.....	38
4.4.5 Summary of Key Conclusions	39
4.4.6 Finite Element Analysis of Concept Name: V-GRIPPER.....	39
4.5 TRADE STUDY ON SECOND ROUND SELECTED DESIGNS.....	46
4.6 DEVELOP ADVANCED MODELS OF SELECTED MECHANISM (QUAD TRAP)	46
4.7 EVALUATION OF 3 DOF SPATIAL JOINT MECHANISM.....	52
4.7.1 Summary of the 3D Solar-Array Tracking Joint Design for Solar-Array Tracking.....	52
4.7.2 Summary of 3-5R Spatial Parallel Architecture and Kinematics	56
5.0 DEVELOP TEST FACILITIES.....	60
5.1 GENERAL DYNAMICS OF TEST AND SIMULATED MOTION OF TETHER	60
5.2 DESCRIPTION OF TEST FACILITIES	60

5.3	FALL-ARREST PAD AND SAFETY MEASURES	61
5.4	PAYLOAD LAUNCHER BUILDING AND DEVELOPMENT	61
5.5	PAYLOAD FABRICATION AND DEVELOPMENT	62
5.6	DATA ACQUISITION METHODS	64
5.7	DESIGN AND FABRICATION OF THE PROTOTYPE CAPTURE MECHANISM	64
5.7.1	<i>General Description of the Quad-Trap Operation</i>	<i>65</i>
5.7.2	<i>Detail Drawings of Scale Model</i>	<i>67</i>
5.7.3	<i>Autonomous Capture Functions: The Automated Capture Control System</i>	<i>67</i>
5.8	PERFORM TESTING AND DEMONSTRATION	68
5.8.1	<i>Testing Procedure</i>	<i>69</i>
5.8.2	<i>Brief Summary of Testing Activity</i>	<i>69</i>
5.8.3	<i>Test Results for the Quad Trap</i>	<i>70</i>
5.8.3.1	<i>Results from Case 1</i>	<i>71</i>
5.8.3.2	<i>Results from Case 2</i>	<i>73</i>
5.8.3.3	<i>Discussion of these Results</i>	<i>74</i>
5.8.4	<i>Test Results for the Harpoon and Net (LM)</i>	<i>76</i>
5.8.5	<i>Test Results for the PatTrap (LM)</i>	<i>76</i>

List of Figures

Figure 1.2-1: Relative Position between the Payload and Tether Tip Around Capture.....	13
Figure 1.2-2: Displacement Limits over 10 Seconds Surrounding Capture	13
Figure 1.2-3: Relative Velocity between the Payload and Tether Tip Around Capture	14
Figure 1.2-4: Schematic of the Capture Event	14
Figure 3.3-1: Summary of the AHP Analysis and Final Scores.....	19
Figure 4.1.4-1: Schematic of the Iris (Quad Trap) Mechanism Concept.....	25
Figure 4.1.4-2: Open Configuration of the Iris and Cross Section of the Spreader Bar	26
Figure 4.1.4-3: FEA of Results for Maximum Loads on the Capture Plate.....	27
Figure 4.1.4-4: Concept of the Gyro-Stabilized Payload Lanyard.....	28
Figure 4.1.5-1: Schematic of the Claw-Hammer Concept	29
Figure 4.2.3-1: Schematic of the Turkey Trap Concept	30
Figure 4.2.3-2: Schematic of the Hamburger Bun Grapple Concept.....	31
Figure 4.2.3-3: Modified Versions of the Turkey Trap.....	31
Figure 4.2.4-1: Moose-Type Turkey Trap with Inflatables	34
Figure 4.3.2-1: Goal-Post Filter Schematic.....	34
Figure 4.3.5-1: Simulation Results of Contact between Tethered Flier and Goal Posts, $t=0.0$	36
Figure 4.3.5-2: Simulation Results of Contact between Tethered Flier and Goal Posts, $t=0.93$	36
Figure 4.3.5-3: Simulation Results of Contact between Tethered Flier and Goal Posts, $t=1.4$	37
Figure 4.3.5-4: Simulation Results of Contact between Tethered Flier and Goal Posts, $t=3.7$	37
Figure 4.4.2-1: V-Gripper Schematic.....	38
Figure 4.4.6-1: Sketch of $\frac{1}{2}$ of the Ugly Stick V-Gripper.....	40
Figure 4.4.6-2: Displacement of Half of V-Gripper.....	40
Figure 4.4.6-3: Displacement Profile	41
Figure 4.4.6-4: Strain Distribution for Half of V-Gripper	41
Figure 4.4.6-5: Stress Distribution for Half of V-Gripper	42
Figure 4.4.6-6: Displacement Plot.....	42
Figure 4.4.6-7: Strain Distribution	43
Figure 4.4.6-8: Stress Distribution	43
Figure 4.4.6-9: Displacement with 1 N load	44
Figure 4.4.6-10: Stress Distribution	44
Figure 4.4.6-11: Deflection with 1 N Load.....	45
Figure 4.4.6-12: Stress Distribution	45
Figure 4.4.6-13: Deflection for Case of 1 N Load in Center	46
Figure 4.6-1: View of Catch Plate.....	46
Figure 4.6-2: Capture Hooks to Replace Plate.....	47
Figure 4.6-3: Initial Plate Response to Typical Loads.....	47
Figure 4.6-4: Intermediate Designs of Capture Plate	48
Figure 4.6-5: Final Second-Order Design of the Modified Iris	48
Figure 4.6-6: Schematic of Lanyard Launch Mechanism	49
Figure 4.6-7: Simplified Version of Deployable Boom.....	49
Figure 4.6-8: Schematic of ADAMS Model of Quad Trap.....	50
Figure 4.7.1-1: Prototype of 3 DOF Mechanism in Two Positions	52
Figure 4.7.1-2: CAD Rendering of Solar Array Tracking Joint	53
Figure 4.7.1-3: Solar Array Tracking Joint.....	53
Figure 4.7.1-4: Wire Frame Solar Array Tracking Joint.....	55
Figure 4.7.1-5: Motor and Bearing Loads.....	56
Figure 4.7.2-1: Prototype 3 DOF Mechanism.....	57

Figure 4.7.2-2: Robotic End-Effector	57
Figure 4.7.2-3: 3 DOF mechanism design for gimbaling a rocket thruster	58
Figure 4.7.2-4: 3 DOF Mechanism with Fuel Passage Integrated into Legs	58
Figure 4.7.2-5: 3 DOF Mechanism as CAD Models, Assembly.....	59
Figure 5.2-1: Overview of Capture Mechanism Test Facility	61
Figure 5.4-1: Payload Launching Mechanism as Built.....	62
Figure 5.5-1: Base Payload	63
Figure 5.5-2: Payload with Gryroscope Flywheel	64
Figure 5.7.1-1: CAD Model of the Quad Trap Mechanism	65
Figure 5.7.1-2: Quad Trap Actuation System	66
Figure 5.7.1-3: CAD Model of the Quad Trap Mechanism Prototype Attached to the Tether Tip	66
Figure 5.7.1-4: Internal Springs to Assist Closing in Quad Trap Prototype	67
Figure 5.7.1-5: Cable Management System in Quad Trap Prototype	67
Figure 5.7.3-1: Schematic Representation of the Automated Capture Control System.....	68
Figure 5.8.3-1: Schematic of the Quad Trap for Instrumentation.....	71
Figure 5.8.3.1-1: Image Record of the Case One Test.....	71
Figure 5.8.3.1-2: (left): X,Y,Z Accelerations for Node 3	72
Figure 5.8.3.1-3: (right) X,Y,Z Accelerations for Node 1	72
Figure 5.8.3.1-4 (left): X (above), Y (below) Accelerations for Node 3	72
Figure 5.8.3.1-5 (right) X (above), Y (below) Accelerations for Node 1	72
Figure 5.8.3.2-1: Image Record of the Error in the Case 2 Test	73
Figure 5.8.3.2-2 (left): X,Y,Z Accelerations for Node 3	73
Figure 5.8.3.2-3 (right) X,Y,Z Accelerations for Node 1	73
Figure 5.8.3.2-4 (left): X (above), Y (below) Accelerations for Node 3	74
Figure 5.8.3.2-5 (right) X (above), Y (below) Accelerations for Node 1	74

List of Tables

Table 1: Capture Mechanism Evaluation Criteria.....	12
Table 2: Naming Scheme for the Capture Mechanism Genealogy	15
Table 3: Trade Study Criteria.....	18
Table 4: Input Rankings for the AHP Analysis for Capture Mechanisms	21
Table 5: Weightings and Scores for the AHP Analysis for Capture Mechanisms.....	22
Table 6: Displacement of Quad Trap during Capture	50
Table 7: Velocity of Quad Trap During Capture	51
Table 8: Sum of System Energy in Quad trap.....	51
Table 9: Acceleration of Quad Trap During Capture.....	52
Table 10: Summary of 3D Solar-Array Tracking Mechanism.....	55
Table 11: Summary of Capture Mechanism Testing Activity	70

1.0 DERIVE OBJECTIVES

The first task derives the objectives that will drive the design and development of capture system concepts.

1.1 Evaluation Criteria for the Capture Mechanism

The capture mechanism design and development process is guided by a task statement and design objectives. These were prepared from a combination of system requirements, kinematic and dynamic description of the capture event, and an evaluation of the expected error window in capture. The specific outcomes of these considerations are demonstrated in part as evaluation points in the capture-concept trade study. The evaluation criteria defined for conducting the trade study are given in Table 1.

Table 1: Capture Mechanism Evaluation Criteria

Criterion	Definition
Low Mass Tether	Physical mass of the portion of the capture device which rides on the tether alone
Low Mass Payload	Physical Mass of the portion of the capture device which rides on the payload
Spatial Expanse	Volume over which the capture mechanism can effect a successful capture.
DoF	Out of plane
Simplicity	Overall simplicity of the design including number of parts, complexity of mechanism, active/ passive and complexity of programming
Attempts Per Payload	The number of attempts at a successful capture expected from a single payload launch
Number of Uses	The number of times a capture mechanism can be expected to boost a payload over the lifetime of the capture mechanism
Current TRL	Technical readiness of the proposed design at the current time
Accuracy of Release	Ability to effect the release of the payload at the time and in the direction desired
Positive Grasp	Ability of the mechanism to firmly latch the payload and tether masses.
Dynamic Effects of Capture	Any extraneous or unpredicted movement of the tether craft caused by the capture operation
Dynamic Effects of Release	Any extraneous or unpredicted movement of the tether craft caused by the release operation
Reliability	Probability of catch within the capture volume of the device
Minimal Tether Considerations	Any additional hardware that may need to be added to the tether craft in order to mate to the capture mechanism
Minimal Payload Considerations	Any additional hardware that may need to be added to the payload in order to mate to the capture mechanism

1.2 Kinematic Description of the Capture Event

The kinematic description of the capture event is described in the series of following figures, which are based on relative motions of the tether tip and payload prior to capture. The following three figures indicate the relative position of the tether with respect to the payload prior to capture (x is local horizontal while y is local vertical) as well as the velocities near point of capture. Note that these are based on models that assume ideal, rigid-body motion of the tether-tip only.

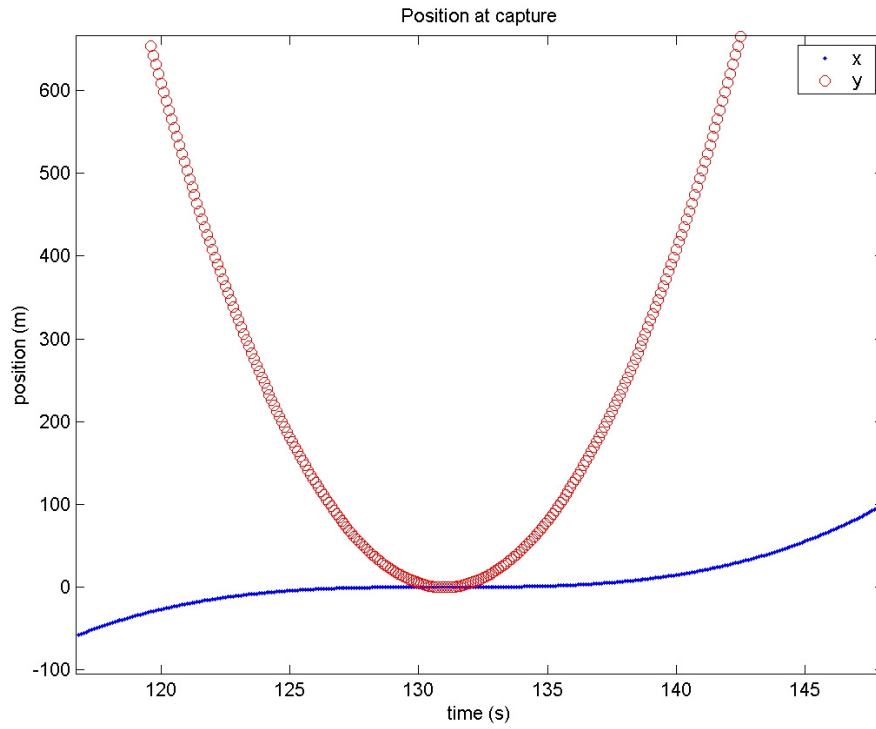


Figure 1.2-1: Relative Position between the Payload and Tether Tip Around Capture

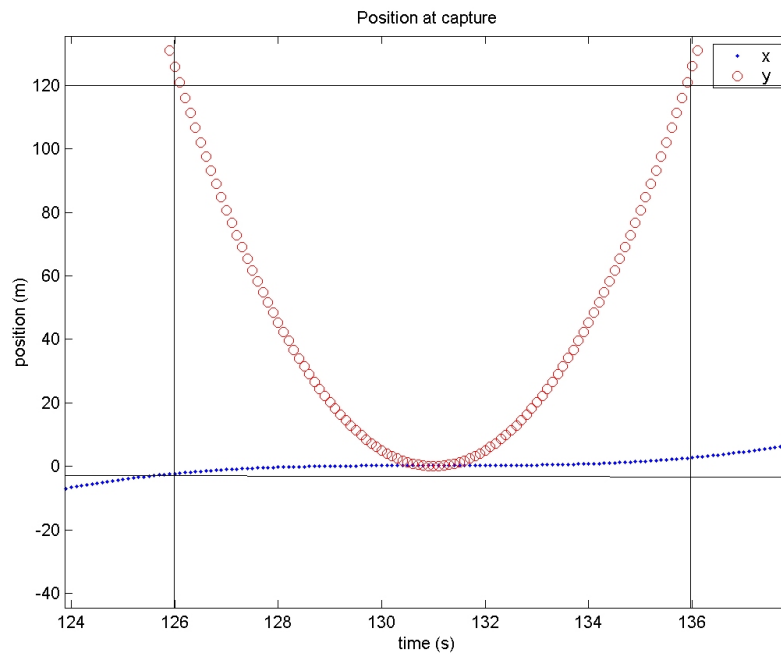


Figure 1.2-2: Displacement Limits over 10 Seconds Surrounding Capture

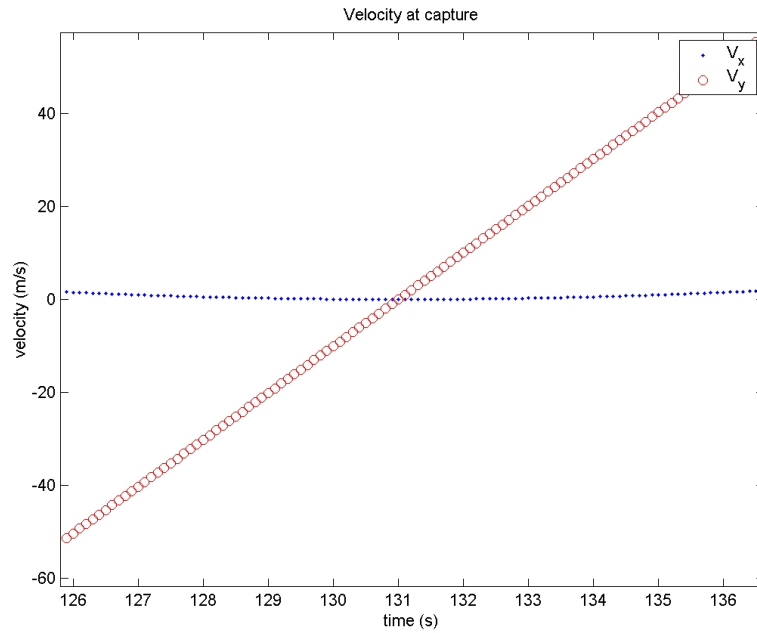


Figure 1.2-3: Relative Velocity between the Payload and Tether Tip Around Capture

Finally, the tether tip motion relative to the payload (observer located on the payload) is described in a single graph (x vs. y) as shown in the figure below. This figure includes an estimate of the expected error in tether position, which will result from the analysis of the following section.

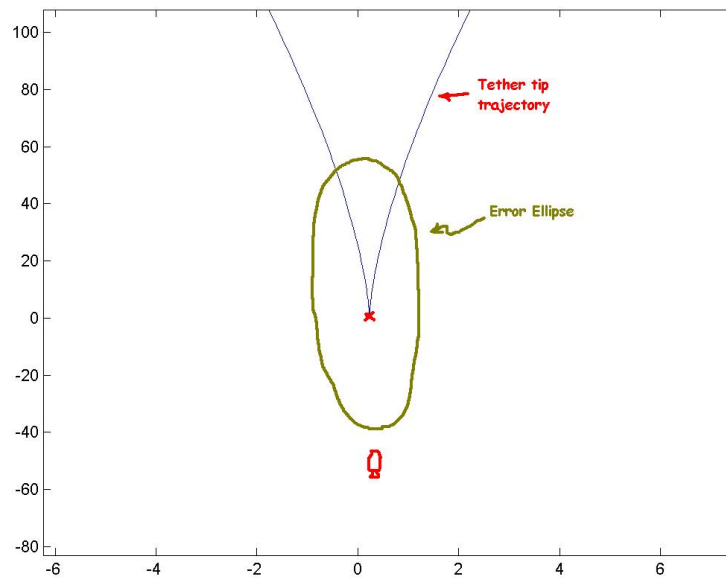


Figure 1.2-4: Schematic of the Capture Event

(Motion relative to payload)

One significant capture objective was definition of a probabilistic capture window based on tether flight dynamics, as well as clear definition of the kinematic and dynamic nature of the tether capture process. The derivation of this error window is explained in Appendix A. Appendix A contains a formal paper prepared for submission to AIAA journal transactions titled “Error Space Prediction and Dynamic Response of Passive Capture Mechanisms in Tether Momentum Exchange”.

2.0 DERIVE AN ARRAY OF POTENTIAL CAPTURE SYSTEM CONCEPTS

A large number of capture system concepts were developed by the extended TTU contract team to form a basis for the eventual capture mechanism. This section will present an overview of the capture concept mechanism development cycle as an iterative process through multiple generations. General areas of consideration are grouped and termed concept families, which in turn generate new members of ideas. In addition, concepts perform cross over functions with other families to form new concepts. This process will be viewed in total through a genealogy chart. This chart is a living document and is updated to keep up with concept development. The genealogy is shown on page 17. A few notes on this figure are made;

- 1) This genealogy attempts to include concepts that originate with TTU, LM and MSFC. A very general means of indicating the originator is given with a color scheme, black, grey and red for the concept specifier. Note that in many cases, the concepts originated from multiple points, at the moment this chart indicates such concepts also with black (TTU color)
- 2) A naming scheme is generated for the concepts that consist of multiple parts. This naming scheme has been designed with the following requirements;
 - a. Name indicates the general form and implementation of the concept
 - b. Name indicates if the concept is passive or active
 - c. Name indicates the general mechanism family
 - d. Names allow room for expansion or insertion of new concepts.

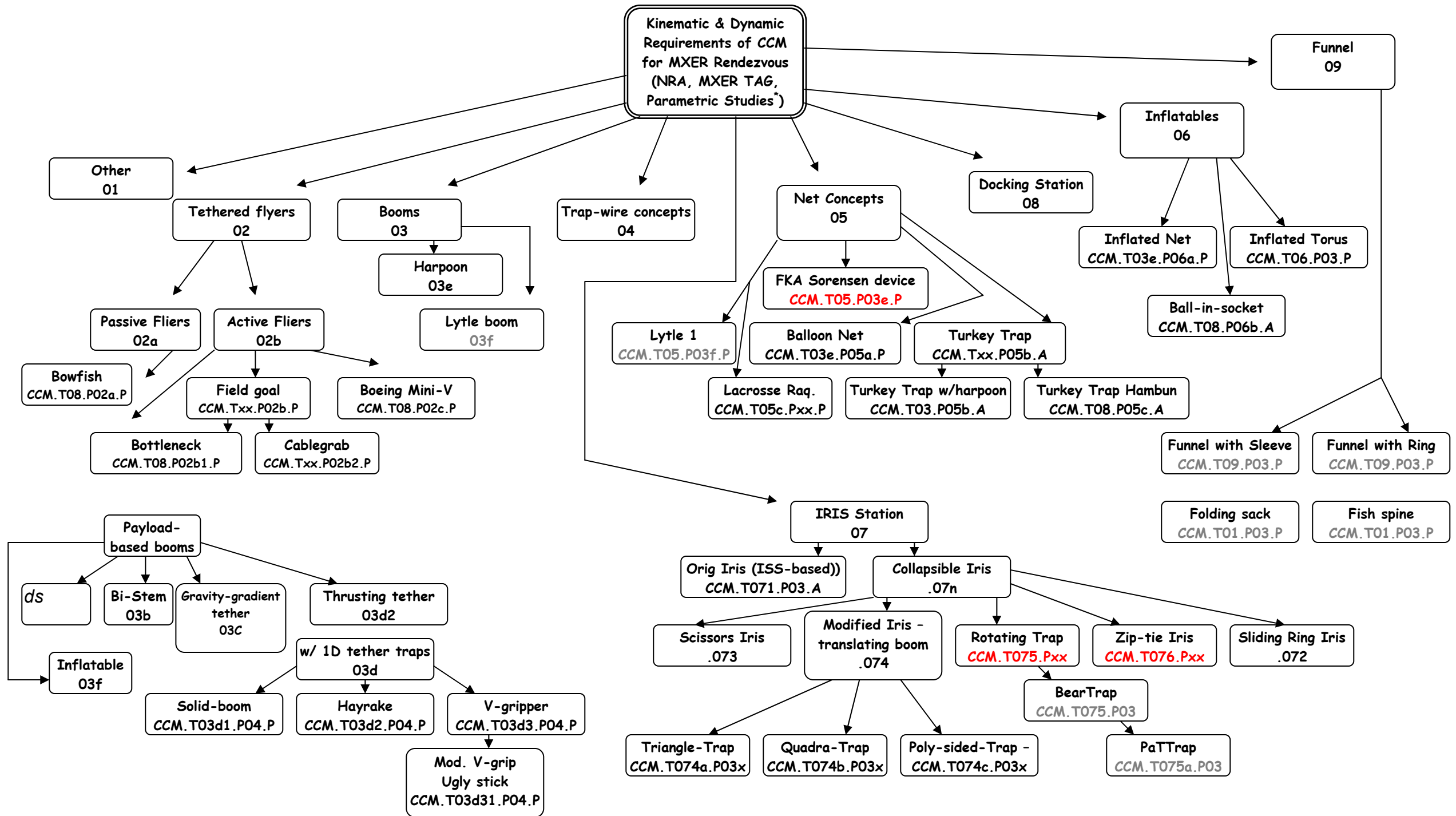
The name consists of the following components as shown in table 2:

Table 2: Naming Scheme for the Capture Mechanism Genealogy

CCM	.Txyz	.Pxyz	.P/A
Capture concept mechanism	Mechanism group on Tether	Mechanism group on payload	Passive or Active
	xx- numeric digits indicating family y-alphanumeric digits indicating subgroup z –alphanumeric digits indication sub-subgroup		

The proposed capture system concepts were then categorized in the form of a genealogy chart (family tree) as shown on page 18. This method of categorization has the following attributes:

- A number/naming scheme is developed that clearly identifies each concept and relates it to other concepts
- All concepts are shown to be derived from a specific number of basic strategies of physical principles
- The categorization scheme also differentiates components required on the tether and/or payload
- Concepts developed by other groups (MSFC ISPT, LM) are included in this scheme
- The genealogy chart is used to spawn new ideas.



3.0 CAPTURE SYSTEM TRADE STUDY

This section will describe the approach used to perform a trade study on all capture system concepts. The trade study was used to identify the capture concepts that would most likely be successful at an early stage in the design process. In this way the trade study would prevent wasting limited resources on capture concepts which were not likely to succeed. The AHP (Analytical Hierarchy Process) was chosen to conduct this study in part because of its history in application to similar type engineering problems and because it can be applied to a large number of concepts quickly while these concepts are still at a very early stage of design. AHP also provided a graduated score for the trade study which would identify second and third place candidates to be tested.

3.1 Brief Description of AHP

AHP or Analytical Hierarchy Process is a means of objectively determining which option from a group of options is the most preferred for a particular set of criteria. This process is frequently used in business environments to make decisions where inputs are unclear or abstract. It is this ability to make an abstract decision objective which makes the AHP tool ideal for selecting a capture concept to build and test early in the design process.

The tool is used as follows. First a set of design criteria are agreed upon. These criteria are specifications or a “wish list” for the resulting design. Each criterion is then pair wise compared to all other criteria to determine a weighting for each. A set of choices or designs is then identified. Each choice is then pair wise compared to all other choices on the basis of the aforementioned criteria to weigh each choice on the basis of each individual criteria. A mathematical algorithm is then applied which outputs a final score for each design telling the user which design is most preferred.

3.2 Overview of Trade Study Criteria

Table 3 below provides an overview and brief explanation of the trade study criterion chosen.

Table 3: Trade Study Criteria

Criterion	Definition
Low Mass Tether	Physical mass of the portion of the capture device which rides on the tether alone
Low Mass Payload	Physical Mass of the portion of the capture device which rides on the payload
Spatial Expanse	Volume over which the capture mechanism can effect a successful capture.
Simplicity	Overall simplicity of the design including number of parts, complexity of mechanism, active/ passive and complexity of programming
Attempts Per Payload	The number of attempts at a successful capture expected from a single payload launch
Number of Uses	The number of times a capture mechanism can be expected to boost a payload over the lifetime of the capture mechanism
Current TRL	Technical readiness of the proposed design at the current time
Release mechanism	Ability of mechanism to cleanly release the payload.
Positive Grasp	Ability of the mechanism to firmly latch the payload and tether masses.
Dynamic Effects of Capture	Any exteraneous or unpredicted movement of the tether craft caused by the capture operation
Dynamic Effects of Release	Any exteraneous or unpredicted movement of the tether craft caused by the release operation
Reliability	Probability of device working as desired (measured as number of independent steps that need to occur)
Minimal Tether Considerations	Any additional hardware that may need to be added to the tether craft in order to mate to the capture mechanism
Minimal Payload Considerations	Any additional hardware that may need to be added to the payload in order to mate to the capture mechanism
cost	
Economic impact	Economic impact for satellite provider
Ground operations	Level of control/monitor needed on ground to make capture work
Sensors	Number and type of sensors needed

3.3 Results from the Trade Study

The inputs into the AHP algorithm and the resulting scores are shown on Tables 4 and 5 below. However, for the convenience of the reader the following graph and tables are provided to illustrate the results of the AHP analysis.

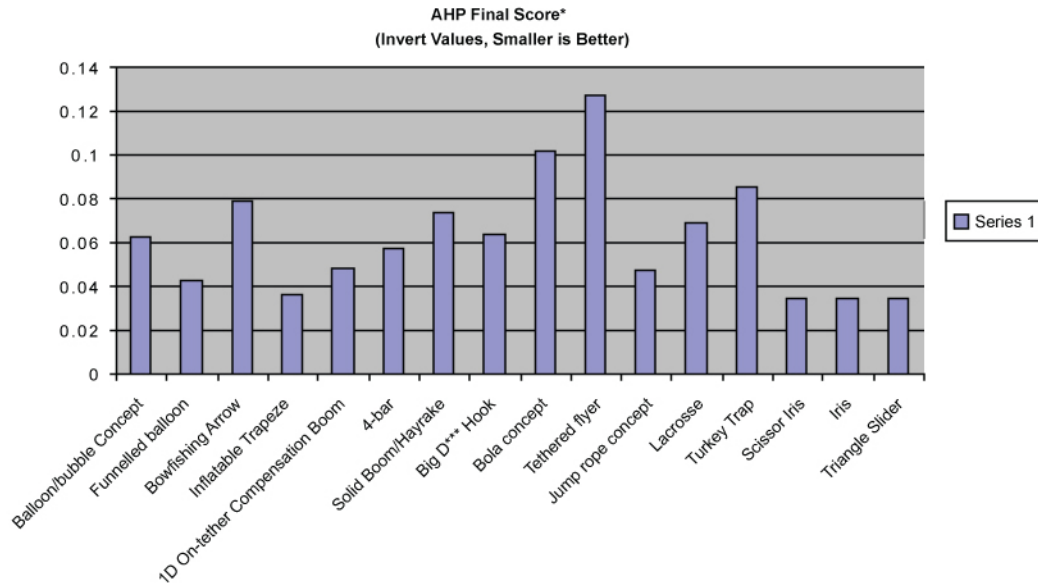


Figure 3.3-1: Summary of the AHP Analysis and Final Scores

	Mass	Current TRL	Probability of Capture	Reliability	Dynamic effects of capture and release	Minimal tether/payload considerations	Const. Cost
Mass	1	0.3333333	0.1111111	0.2	0.3333333	0.3333333	7
Current TRL	3	1	0.1428571	0.2	0.3333333	0.3333333	5
Probability of Capture	9	7	1	5	5	3	9
Reliability	5	5	0.2	1	3	3	9
Dynamic effects of capture and release	3	3	0.2	0.3333333	1	0.3333333	9
Minimal tether/payload considerations	3	3	0.3333333	0.3333333	3	1	9
Const. Cost	0.1428571	0.2	0.1111111	0.1111111	0.1111111	0.1111111	1

Sum24.1419.532.107.1812.788.1149.00

Mass	Current TRL	Probability of Capture	Reliability	Dynamic effects of capture and release	Minimal tether/payload considerations	Const. Cost
0.0414201	0.0170648	0.0529501	0.0278638	0.026087	0.0410959	0.1428571
0.1242604	0.0511945	0.0680787	0.0278638	0.026087	0.0410959	0.1020408
0.3727811	0.3583618	0.4765507	0.6965944	0.3913043	0.369863	0.1836735
0.2071006	0.2559727	0.0953101	0.1393189	0.2347826	0.369863	0.1836735
0.1242604	0.1535836	0.0953101	0.0464396	0.0782609	0.0410959	0.1836735
0.1242604	0.1535836	0.1588502	0.0464396	0.2347826	0.1232877	0.1836735
0.0059172	0.0102389	0.0529501	0.0154799	0.0086957	0.0136986	0.0204082

Sum1.001.001.001.001.001.001.00

Ranking	
0.05	Mass
0.06	Current TRL
0.41	Probability of Capture
0.21	Reliability
0.10	Dynamic effects of capture and release
0.15	Minimal tether/payload considerations
0.02	Const. Cost

		Code name	bowfish		bottleneck		cablegrab		boeing mini-v		solid boom		hayrake		V-gripper	
		Mechanism	.T08.P02a		.T08.P02b2		.T08.P02b1		.T08.P02c		T03d1.P04		T03d2.P04.P		T03d3.P04	
Criteria	Weighting	Score	Raw Score	Wtd Score	Raw Score	Wtd Score	Raw Score	Wtd Score	Raw Score	Wtd Score	Raw Score	Wtd Score	Raw Score	Wtd Score	Raw Score	Wtd Score
Mass	0.05		8	0.3992444	8	0.3992444	8	0.3992444	7	0.3493388	3	0.1497166	2	0.0998111	4	0.1996222
Current TRL	0.06		3	0.1888376	4	0.2517834	5	0.3147293	4	0.2517834	4	0.2517834	3	0.1888376	5	0.3147293
Probability of Capture	0.41		3	0.1888376	5	0.3147293	6	0.3776751	5	0.3147293	4	0.2517834	4	0.2517834	5	0.3147293
Reliability	0.21		4	0.2517834	3	0.1888376	4	0.2517834	2	0.1258917	3	0.1888376	1	0.0629459	4	0.2517834
Dynamic effects of capture and release	0.10		5	0.3147293	5	0.3147293	7	0.440621	5	0.3147293	2	0.1258917	2	0.1258917	6	0.3776751
Minimal tether/payload considerations	0.15		5	0.3147293	5	0.3147293	5	0.3147293	4	0.2517834	2	0.1258917	2	0.1258917	4	0.2517834
Const. Cost	0.02		5	0.3147293	5	0.3147293	5	0.3147293	3	0.1888376	3	0.1888376	2	0.1258917	4	0.2517834

Total score (out of 10)1.97289082.09878252.41351181.79709351.28274210.98105311.9621062Table

Table 4: Input Rankings for the AHP Analysis for Capture Mechanisms

		Code name	ugly stick		Triangle Trap		quad trap		polysidedtrap		scissor Iris		bear trap and family		zip tie		original Iris	
		Mechanism:	T03d31.P04		T074a.P03x		T074b.P03x		T074c.P03x		T073		T075		T076		T072	
Criteria	Weighting	Score	Raw Score	Wtd Score	Raw Score	Wtd Score	Raw Score	Wtd Score	Raw Score	Wtd Score	Raw Score	Wtd Score	Raw Score	Wtd Score	Raw Score	Wtd Score	Raw Score	Wtd Score
Mass	0.05		5	0.249528	3	0.149717	3	0.149717	2	0.099811	2	0.099811	2	0.099811	4	0.199622	2	0.099811
Current TRL	0.06		5	0.314729	7	0.440621	7	0.440621	7	0.440621	6	0.377675	7	0.440621	4	0.251783	8	0.503567
Probability of Cap	0.41		5	0.314729	7	0.440621	8	0.503567	8	0.503567	7	0.440621	6	0.377675	7	0.440621	8	0.503567
Reliability	0.21		6	0.377675	4	0.251783	4	0.251783	3	0.188838	4	0.251783	4	0.251783	2	0.125892	4	0.251783
Dynamic effects	0.10		6	0.377675	6	0.377675	6	0.377675	6	0.377675	6	0.377675	5	0.314729	3	0.188838	5	0.314729
Minimal tether/pa	0.15		7	0.440621	5	0.314729	5	0.314729	5	0.314729	5	0.314729	4	0.251783	5	0.314729	4	0.251783
Const. Cost	0.02		5	0.314729	3	0.188838	4	0.251783	3.5	0.220311	2	0.125892	4	0.251783	4	0.251783	2	0.125892
Total score (out of 10)			2.389687		2.163984		2.289876		2.145551		1.988187		1.988187		1.773269		2.051133	

		Code name	Balloon net		turkey trap w/ harpoon		Hamburger bun		lacrosse		Inflated net		inflated torus		Ball in Socket	
		Mechanism:	T03e.P05a		T03.P05b		T08.P05b		T05c.Pxx		T03e.P06a		T06.P03		T08.P06b	
Criteria	Weighting	Score	Raw Score	Wtd Score	Raw Score	Wtd Score	Raw Score	Wtd Score	Raw Score	Wtd Score	Raw Score	Wtd Score	Raw Score	Wtd Score	Raw Score	Wtd Score
Mass	0.05		4	0.199622	6	0.299433	7	0.349339	3	0.149717	4	0.199622	8	0.399244	2	0.099811
Current TRL	0.06		7	0.440621	6	0.377675	6	0.377675	4	0.251783	7	0.440621	2	0.125892	2	0.125892
Probability of Cap	0.41		4	0.251783	3	0.188838	4	0.251783	4	0.251783	4	0.251783	2	0.125892	2	0.125892
Reliability	0.21		7	0.440621	4	0.251783	4	0.251783	3	0.188838	7	0.440621	2	0.125892	3	0.188838
Dynamic effects	0.10		6	0.377675	6	0.377675	6	0.377675	2	0.125892	6	0.377675	3	0.188838	3	0.188838
Minimal tether/pa	0.15		4	0.251783	4	0.251783	4	0.251783	4	0.251783	4	0.251783	4	0.251783	3	0.188838
Const. Cost	0.02		4	0.251783	7	0.440621	7	0.440621	4	0.251783	4	0.251783	4	0.251783	3	0.188838
Total score (out of 10)			2.21389		2.187809		2.30066		1.47158		2.21389		1.469324		1.106945	

Table 5: Weightings and Scores for the AHP Analysis for Capture Mechanisms

4.0 BASIC DESIGN SELECTION AND DEVELOPMENT

(For Ideal Capture Device)

Capture Mechanism Design

The brainstorming sessions gave birth to a particularly large number of capture mechanisms deemed worthy to perform a more in depth study of. A first order trade study was performed on these mechanisms and the four most promising designs were chosen to endure a brief two week engineering evaluation. These four capture mechanisms were to be presented to the evaluation team of Lockheed Martin/NASA. Of these four, the top mechanism was to be thoroughly designed and a prototype assembled, tested, and evaluated. This process was completed with the prime candidates for further development being:

1. Modified Iris (quad trap)
2. Turkey Trap (Seth noose)
3. Tethered Flyer
4. V-Gripper

This section will provide a first order engineering analysis of each of these four designs (contained in Section A 4.1 through 4.4). These sections immediately follow. The results and conclusions of a study of these first order analyses are contained in Section A 4.5. Based on the conclusions from Section A 4.5, a more detailed analysis of the Quad trap mechanism is conducted in Section A 4.6. Finally, an analysis of an additional mechanism for MXER tether systems, a 3 dof mechanism for pointing solar arrays is provided in Section A 4.7.

4.1 Modified Iris(Quad Trap): First Round Design Analysis

4.1.1 Overview

This section will summarize the results of a first-round of design and analysis of the modified iris capture concept. The primary elements of the design are described, as well as the analysis procedures. The key results are summarized and conclusions are made regarding suitability and future development of this capture concept.

4.1.2 Brief Description

The quad trap is designed to accept an extension from the payload and direct it to the corner plate. For this analysis, that extension is a single cable with a gyroscope at one end for stabilization of the trajectory. This lanyard can be reeled in and reloaded to use as many times as needed, using only mechanical energy for propulsion. The quad trap has smart sensors on it to detect the presence of the lanyard and, upon entry of the lanyard into the capture area of the quad trap, the trap actuates and the lanyard is forced into a plate located at one of its four corners. This plate is designed to hold the full force of the payload as it is accelerated by the tether.

4.1.3 Summary of Analysis Performed

Several key analyses were performed to characterize system behavior and analyze results. These were:

1. Time closure for the iris upon entry of the lanyard into capture area were calculated to be around three and a half seconds for gravity assisted closing.
2. Stress calculations on spreader bars determined.
3. Sizing of the spreader bars(0.67 slugs) and corner plates(1.86 slugs) was performed.
4. Vibration calculations to determine natural frequency of spreader bars were performed to

ensure the tether was not driving the capture system.($f_n=662$ kHz)

5. Design for reset performed and suggested ratchet designed.
6. Mass for lanyard gyroscope determined.

4.1.4 Summary of Key Conclusions

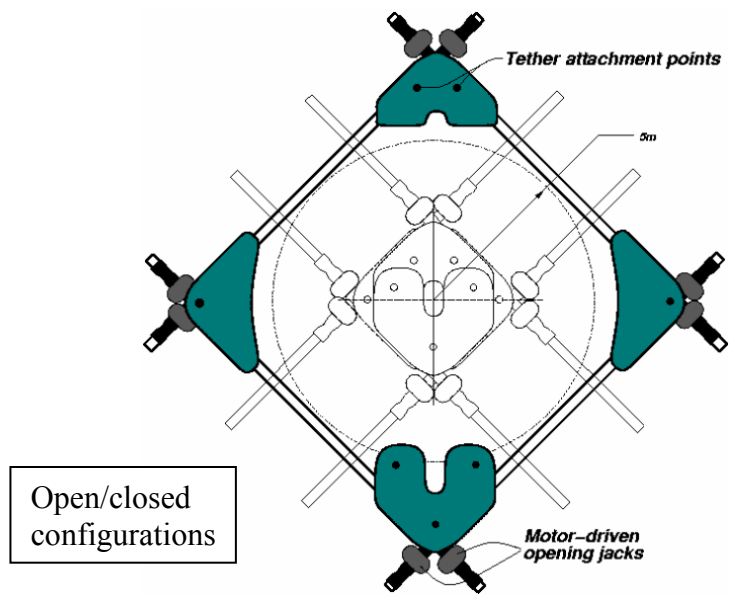
1. The closure of the system can be performed entirely by inertia keeping the system simple.
2. The parameters of the system suggest high probability of capture and part reliability.
3. A tethered lanyard was chosen to connect the payload to the iris mechanism due to its simplicity and feasibility. This lanyard could be light and easily packaged on the payload.
4. The capture plate has been designed to receive the full load of the payload co-aligning the stresses with the cables making the configuration attractive.
5. The design of this capture device should be pursued based on simplicity of design and reliability of mechanism both in capture and in performance.

As noted, this mechanism is capable of closing within the allotted closure time frame entirely from inertial effects, making the closing process entirely passive. This can be demonstrated by assuming a simple pendulum model. Neglecting frictional effects, the period for a pendulum is given by the following relation,

$$\tau = 4 \sqrt{\frac{L}{g}} \int_0^{\pi/2} \frac{d\phi}{\sqrt{1 - \sin^2\left(\frac{\theta}{2}\right) \sin^2(\phi)}} = \frac{2K}{\pi} (2\pi \sqrt{\frac{1}{g}})$$

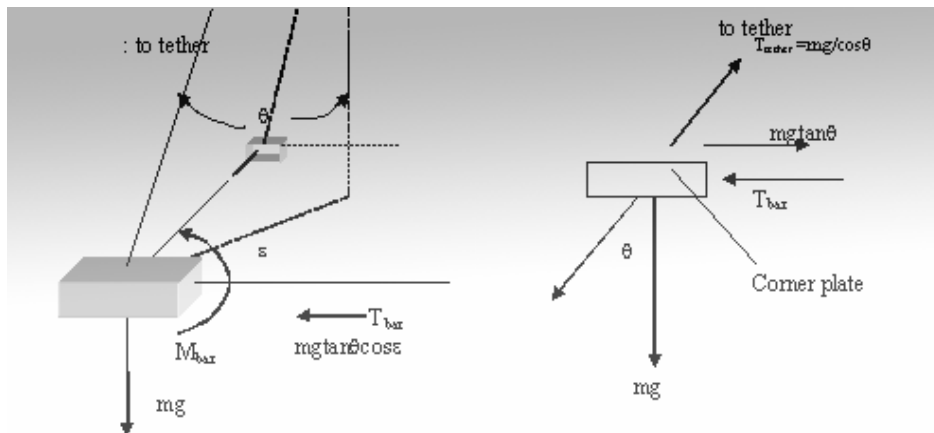
where K denotes the elliptic integral and the factor $2K/\pi \leq 1.002$ for $\theta \leq 10^\circ$. Tabulated values for elliptic integrals are available in standard references, for example. With a value of L of 100 meters to the end of the tether and g replaced by the local acceleration of 19.8 m/s^2 , the period τ is found to be 14.12 seconds. One-quarter of this period is the iris closure time, about 3.53 seconds. Preliminary simulations suggest that the time interval during which the payload is within the capture window is about six seconds so that the inertially-driven closure rate would suggest full closure perhaps one-half second after CAP.

For the release stage, the payload will jettison its lanyard severing the connection between payload and tether. The remaining lanyard will then be shed from the Marshall plate using the lanyard shed mechanism which will push the payload lanyard away from the groove in the Marshall plate. Once shed, the payload lanyard will fall away from the tether due to centripetal acceleration. In this way, the trajectory of the spent payload lanyard can be controlled. Figure 4.1.4-1 below is a conceptual drawing of the quad trap.



Corner plate	Spreader bars
Mass=1.86 slugs	Mass=0.67 slugs
Material: titanium-alloy	Material: titanium-alloy
Inertial acceleration (g): 2x32.2	

Figure 4.1.4-1: Schematic of the Iris (Quad Trap) Mechanism Concept



$$\Sigma M = \frac{d}{dt}[I]\omega$$

$$\Sigma F = \frac{d}{dt}mv = ma$$

Sum of forces and moments with simplified calculations for scaling magnitude

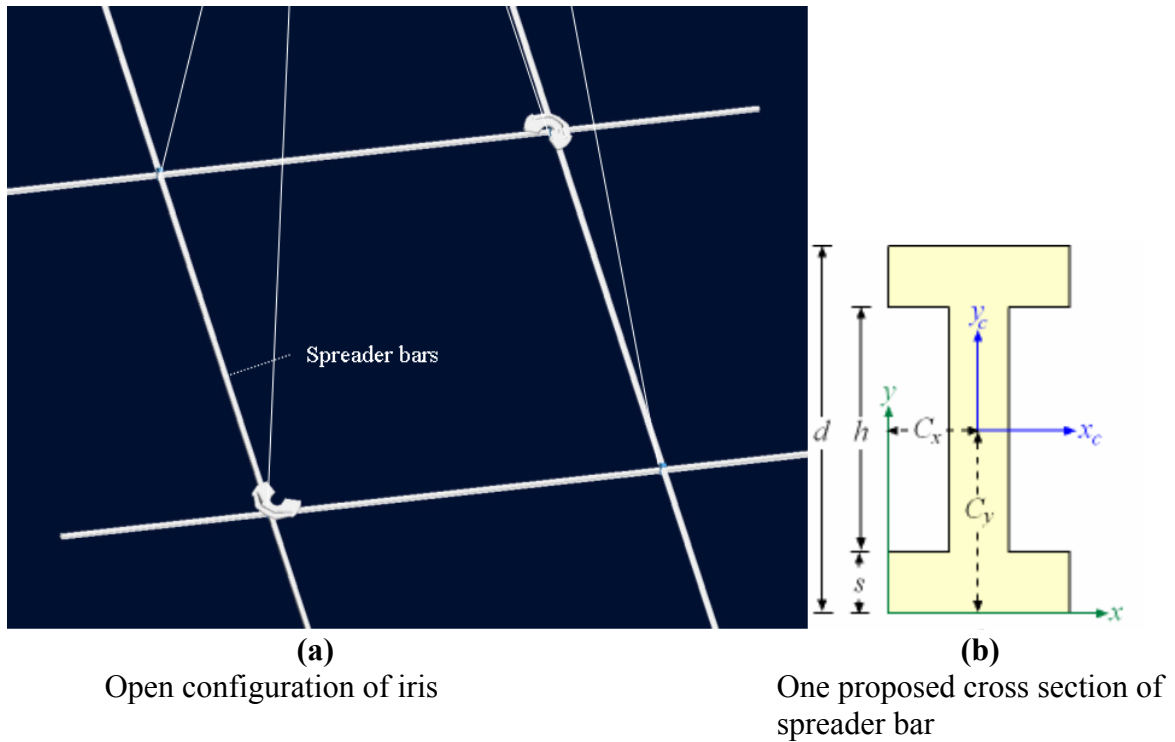


Figure 4.1.4-2: Open Configuration of the Iris and Cross Section of the Spreader Bar

As T_{bar} is the reaction needed to maintain the “open” configuration, it is calculated by a summation of forces on the block and is found to be $mg \tan(\theta)$. Assuming the corner blocks each have an earth weight of 60 lbs and the “spreader bars” have an earth weight of 80 lbs each, the maximum load T_{bar} would be 4.8 lbs, which is the axial load carried by the “spreader bars.” Based on Euler buckling theory, a critical buckling load for pinned ends is given by,

$$F_{\text{cr}} = \frac{EI\pi^2}{L^2},$$

where F_{cr} is the stress that will cause the member to buckle, E is modulus of elasticity, I is the moment of inertia, and L is the length of the beam. Assuming that this member has the cross section shown and that the length is fixed, one can see that F_{cr} is driven by E and I . The material would likely be an I-beam cross section of some titanium alloy.

$$I = \{bd^3 - h^3(b-t)\}/12$$

Using material properties for titanium (E approximately 15 times 10^6 psi), an area moment of inertia of $I=17\text{in}^4$ and a length L of 394 in, the critical buckling load is approximately 16 kips, giving a safety factor of more than 3000. Additionally, the spread bars should not be expected to exhibit low frequency vibrations. For pinned ends, frequencies of vibration are given by,

$$\omega = n\pi \sqrt{\frac{EI}{\rho A}},$$

so that the fundamental frequency is 662 kHz.

The capture plate Figure 4.1.4-3 rests on a corner of the quad trap and takes the full load once the satellite and the tether connect. The maximum loads to be carried should be approximately 10,000lbs. When this static load was applied to the plate in an FEM

model, the maximum stresses in the plate were found to be approximately 10 ksi, well under the yield stress for some forms of titanium-alloy (130-140 ksi). The large stress margin provides significant reliability even though the actual loading will be dynamic.

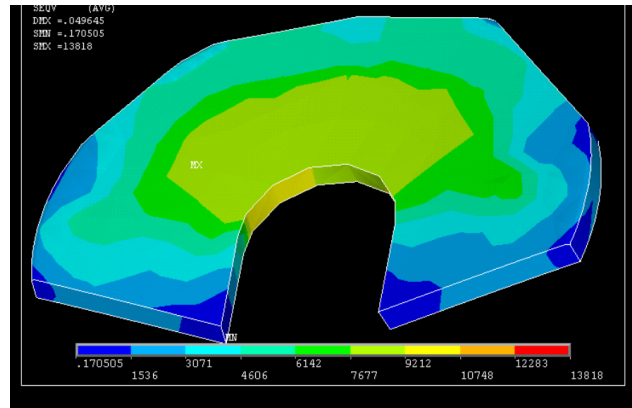


Figure 4.1.4-3: FEA of Results for Maximum Loads on the Capture Plate

After the quad trap closes due to inertial forces, it resets itself to the open configuration using a type of ratchet system. Within the ratchet are two arms, one for resetting the spreader bar to the open configuration and one for holding it in place. Small bearings are mounted inside the casing for this ratchet system to aid in closing. Upon arrival of the payload lanyard within the designated capture area, a small servo behind the holding ratchet pushes it forward releasing the bar to slide through. The reset ratchet is run by a small motor which only needs to provide about .4 ft-lbs of torque. The Payload Lanyard will consist of a small tethered gyroscope cast out from the payload satellite using a preloaded spring.

Prior to the time for deployment a small gyroscope attached to the end of a ~120m satellite mounted tether will be spun up. At time for deployment this gyroscope will be launched from the satellite toward the tether via a pre-loaded spring. As the gyroscope flies it will pull the lanyard from its spool. This is demonstrated conceptually in Figure 4.1.4-4 below.

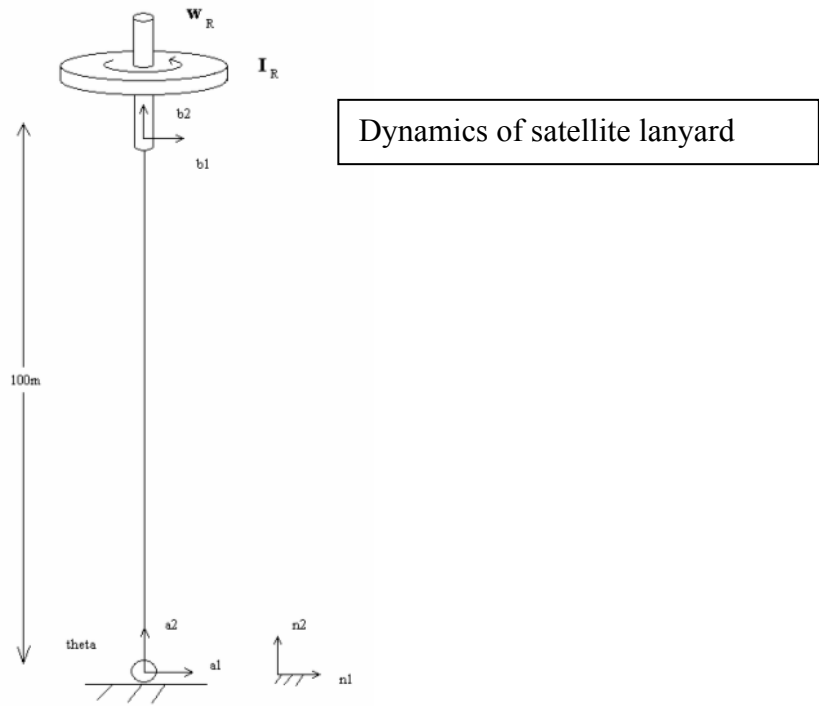


Figure 4.1.4-4: Concept of the Gyro-Stabilized Payload Lanyard

The gyroscopic effects of the spinning gyroscope will help to stabilize the trajectory of the lanyard as it deploys. Some number of stops will be woven into the top portion of the lanyard to allow it to engage the Marshall Plate. These stops will be wound onto the spool along with the rest of the lanyard and will deploy in the same fashion. When the lanyard reaches the limit of its deployment, the storage spool will provide braking torque to slow the gyroscope and prevent “bounce back” effects.

At full deployment the gyroscopic affects of the end-mounted gyroscope will resist moments imposed on the lanyard by outside forces. For the payload lanyard assume:

$$M_{out} = 1n_3$$

$$\varpi_R = 1100RPM \quad a_2 = 4146912 \text{ rad/s}$$

$$M = 25\text{g/m} = 0.025\text{kg/m}$$

$$\alpha_{\max} = 0.01\text{rad/s}^2 \quad n_3$$

(Lanyard approximates thin bar inertial properties) So the formulation for the inertia of the gyroscope I_r proceeds as:

$$I_r = \frac{ML^3}{3} = 8333.3 \text{ kg/m}^2$$

$$I_{Gb2} = 1/2mR^2 = 1/2m(.1016/2)^2 = 0.00129\text{m}$$

$$I_{b1} = I_{b3} = 1/4mR^2 + 1/12mL^2 + md^2 = 1/4m\left(\frac{.1016}{2}\right)^2 + 1/12m(100)^2 = 10,000\text{m}$$

$$R_n^a = \begin{bmatrix} \cos(\theta) & \sin(\theta) & 0 \\ -\sin(\theta) & \cos(\theta) & 0 \\ 0 & 0 & 1 \end{bmatrix} \quad \text{and} \quad R_n^a = \begin{bmatrix} \cos(\phi) & 0 & \sin(\phi) \\ 0 & 1 & 0 \\ -\sin(\phi) & 0 & \cos(\phi) \end{bmatrix}$$

$$\text{then } OP=100a_2=R_n^a 100a_2 = \begin{bmatrix} -100 \sin(\theta)n1 \\ 100 \cos(\theta)n2 \\ 0 \end{bmatrix} \text{ and } \omega_R = R_n^a 4146912 \frac{rad}{s} a_2 = \begin{bmatrix} -4146912 \sin(\theta)n1 \\ 4146912 \cos(\theta)n2 \\ 0 \end{bmatrix}$$

then the lanyard inertia $I_z=R_c^a 8333a_3 = 8333 n_3$

$$\Sigma M = I\alpha + [s\varpi][I][\varpi]$$

and can readily be shown that

$$M = \frac{-82.33 + 1.43E17 \sin(\theta) \cos(\theta)}{10 + 1.7E17 \sin(\theta) \cos(\theta)}$$

These gyroscopic effects in combination with the tension provided by the braking reel will help to preserve the orientation of the lanyard for as long a period as possible. However the tension in the lanyard that aids with its orientation also causes the lanyard to move back toward the payload. Therefore as the lanyard slowly retracts back toward the payload the braking reel will be used to re-spool the excess slack. Once they lanyard is fully retracted back onto the spool the spool torque will be used to reload the launcher spring for another sequence.

4.1.5 Other Elements for the Iris Mechanism under Consideration

Shape Memory Alloy

A strand of shape memory alloy is woven into the payload lanyard in such a way that when the lanyard is un-spooled the shape memory alloy is activated causing the lanyard to straighten and stiffen. This concept was pushed aside due to a general ignorance of the specifics of shape memory alloys. In the first case it is believed that the extreme temperature fluctuations may prevent the SMA from stiffening properly. It is also believed that a structure of sufficient stiffness would likely be quite heavy.

Claw-Hammer Hinge

The claw hammer hinge is a concept that would potentially replace the Marshall Plate as a means of making the terminal connection to the payload boom (Figure 4.1.5-1). In the capture configuration the claw hammer hinge would be folded out ward in such a way that the stops in the payload boom would slide into the “claw hammer” shaped groove cut in the device. At the time for payload release the claw hammer hinge would then pitch backward allowing the payload boom to slide all the way through the claw hammer groove and release from the tether.

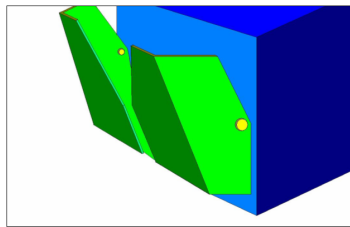


Figure 4.1.5-1: Schematic of the Claw-Hammer Concept

4.2 Turkey Trap: First Round Design Analysis

4.2.1 Overview

This section will summarize the results of a first-round of design and analysis of the Turkey Trap capture concept. The primary elements of the design are described, as well as the analysis procedures. The key results are summarized and conclusions are made regarding suitability and future development of this capture concept.

4.2.2 Brief Description

The Turkey trap is a cable system, enclosing an area of 10m radius by 100m length (Figure 4.2.3-1), which attaches to the payload and extends out to meet a specially designed grapple on the end of the tether. The grapple for this concept is called the “Hamburger Bun” (Figure 4.2.3-2), an oblong spherical mechanism with retracting fingers attached to the end of the tether. Weights on the cables of the Turkey trap are ejected from the payload to the capture area and the mouth of the Turkey trap is expanded by inflatable pillars. After the Hamburger Bun passes thru the mouth of the trap, capture fingers within it are extended perpendicularly outward to meet the Turkey trap. Once this has occurred the inflatable’s are deflated and the noose constricts while being reeled toward the payload where it attaches to the Hamburger Bun.

The concept behind Turkey trap is simple in that it contains a net and a type of hook which, when in contact, simply hook the net with a special type of prong. Upon closer inspection, it became apparent that solving the dynamics for the system was no trivial task. Although nets have been used for thousands of years, no governing equations exist, nor are likely to exist, for a body with such a large number of degrees of freedom. Eventually the design and tests moved from derivable to experimental. The evolution of the net was an area where some design could be applied, beginning with the standard criss-crossing of strands of cable as in Figure 4.2.3-1 and the grappling device in Figure 4.2.3-2 below.

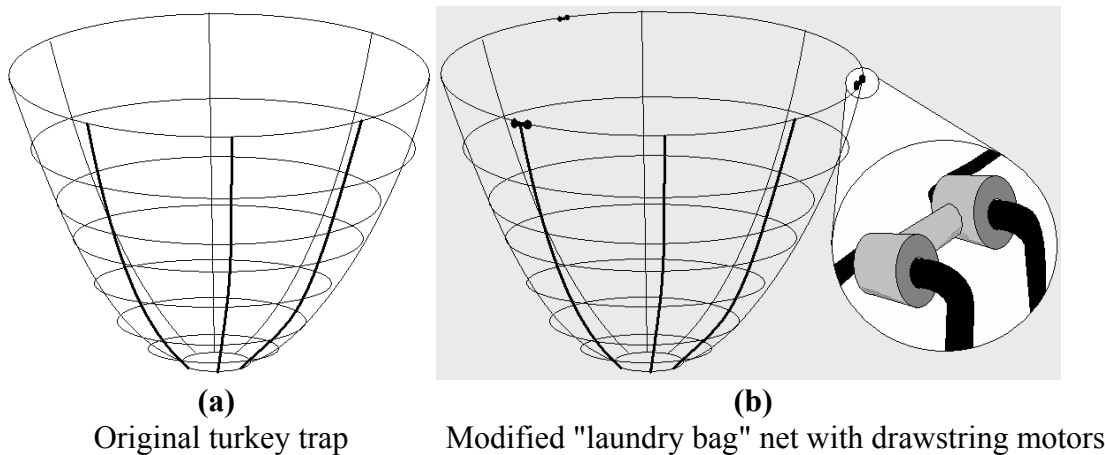


Figure 4.2.3-1: Schematic of the Turkey Trap Concept

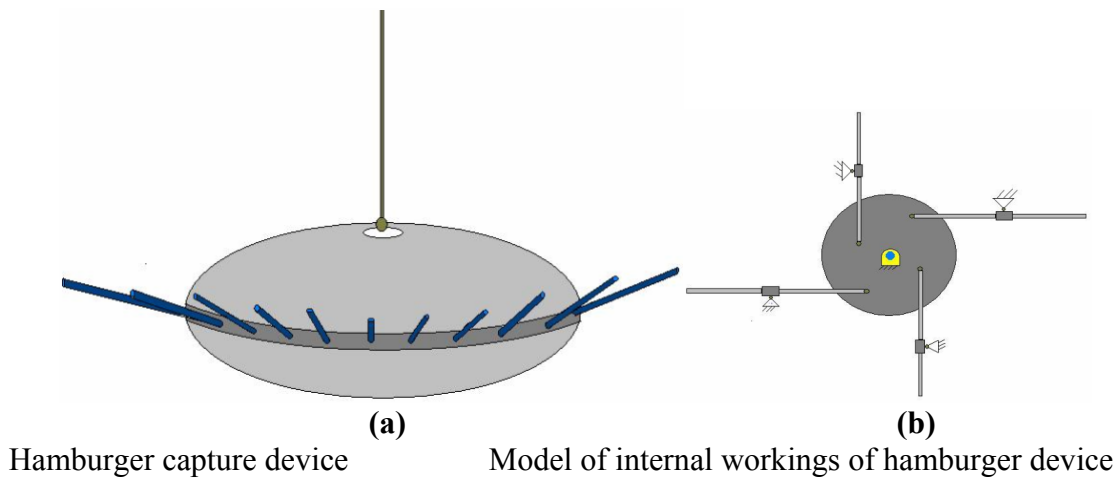


Figure 4.2.3-2: Schematic of the Hamburger Bun Grapple Concept

Upon inspection of this original concept, it was noted that the probability of capture was highly chaotic in that not all hooks might catch a portion of the net. If such a scenario occurred, the worst case scenario would provide one prong hooking on one strand. This would dictate that every strand would need to be robust enough to carry the entire weight of the accelerated load. This design was unacceptable as the total weight of the net would be too much, and the transportation of it too difficult. To correct for this inefficiency, a drawstring system of sorts could be implemented to heighten the probability of capture. Some number of nodes were arranged around the periphery of the mouth of the net (Figure 4.2.3-3). Upon entry of the capture device into the net, the drawstrings would close rapidly ensuring that all prongs on the capture device would interact with the netting. Originally, the net was assumed to be the full volume of the error window, making it 10 meters by 100 meters. To decrease the weight of the net, the size of the net was diminished to simply the mouth and a small extension as in Figure 4.2.3-3 below.

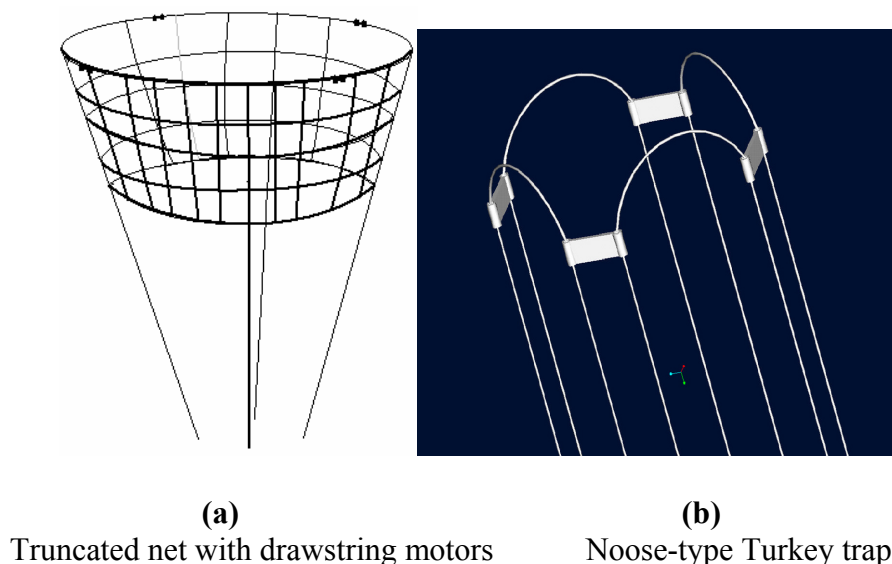


Figure 4.2.3-3: Modified Versions of the Turkey Trap

This net would also have the drawstrings on the mouth, but would also have some type of reel at the base. When the capture concept entered into the mouth, the drawstrings would close upon the device. Any overshoot on part of the tether tip would be countered by the reel at the base of the satellite. The next generation of concepts was radically different in that the net was broken down into its basics; it needed to be lightweight and it needed to catch at a known number of points. To achieve this, the

Noose-type Turkey trap was suggested. Originally it would consist of simple sliders on a number of stings. The net system would begin deployment by spinning the net. The sliders, having some mass would be ejected in the direction of the capture location still spinning, causing them to move away from each other widening the mouth of the Noose-type Turkey trap. The cables would go from the base of the payload out to one slider, loop around to another slider, and back to the payload. When the capture device went thru the mouth of the noose, the cables would be retracted suddenly. Momentum would keep the sliders from speeding up as fast as the cables, and consequently, the sliders would follow the path around the top of the cable arc traveling toward each other. A model of this was built and tested, and found to be somewhat difficult to predict.

4.2.3 Summary of Analysis Performed

After briefly engaging in modeling the net, it was concluded that the system could not be modeled practically due to the large number of degrees of freedom associated with the net. Based on the nature of the system, the suggestion was made to move to an experimental simulation approach. An experimental model was built with the intent to discover any correlations between geometric parameters and system behavior. Further details on the experimental analysis are provided in Section 4.2.5 below.

4.2.4 Summary of Key Conclusions

- 1) The Turkey trap was found to be an attractive net as it minimizes weight while increasing the probability of capture.
- 2) Several inflatables would form a perimeter of the Noose-type Turkey trap for entry of the Hamburger Bun. A minimum compressive force would be needed to hold an open configuration.
- 3) Limited capture attempts exist in the current configuration due to inflation requirements.
- 4) This concept has great potential but also significant modeling costs due to its reliance on nets and inflatables.

During the assigned two week design study phase the generalized turkey trap concept evolved thru three different configurations. The first such configuration has been referred to as the “laundry bag” the second configuration “the Noose” and the third configuration “the Sethnoose”. All of these configurations are intended to mate to some variation of the “hamburger Bun” mace concept.

4.2.5 Experimental Analysis

Due to the non-linear nature of the equations of motion as applied to the Noose-type Turkey trap, any model must be quite complex before it can be considered to be representative of the system. In order to achieve some representative results in the required time span an experimental approach was adopted. This experimental approach would investigate the stability and controllability of the proposed system.

The experiments were conducted as follows. First, a model was constructed. This model consisted of 7 sections of aluminum rod which were drilled with holes so that they were somewhat representative of the pulley masses proposed in the Noose-type Turkey trap system. These pulley masses were then strung together using lightweight fishing line in a manner similar to that proposed by this system. The experimental model was then set spinning using a variety of different techniques to test its stability and controllability. First the model was spun using a simple cordless drill attached to the point where the lines all converge. This particular setup produced mixed results. Initially the pulley masses would align into a circular configuration although they did not extend radially as far as was hoped. After a period of about 15 seconds the circular configuration would then deteriorate into a second stable, but

non geometric configuration where it would remain until stopped. These results were remarkably repeatable from test to test and showed a repeatable time-to-decay.

Several hypotheses were proposed to explain the mixed results of this first experiment. Most importantly the experiment occurred in a gravitational system. In a gravitational system the pulley masses would need a much higher velocity to extend into a large radius circle because the centrifugal force has to overcome gravity. A second hypothesis centered on the irregularity in friction between the fishing lines and the pulley masses. Given that each pulley mass is only a drilled hole the friction thru that hole is assumed to be quite irregular from part to part. Once the system gains enough speed for the pulley masses to begin sliding apart from one another any unbalance in friction between one pulley mass and the next could cause instability. Pulley masses were initially not spread apart from one another and it was proposed that the initial condition of no radius resulted in an instability. There were also concerns that the means of driving the system caused a substantial amount of twist in the lines which may have caused the instability due to a difference in line length.

The next experiment of note involved rotating the system from a turntable. This experiment was intended to address the concerns of line twisting and zero initial circle radius. Pulley masses were arranged on a turntable in a circular configuration some distance from one another. The turntable was then rotated to impart a spinning speed to the system and the pulley masses were lifted off of the turntable. This experiment was somewhat more successful. If the speed of the turntable was well controlled the system would fall into a stable circular configuration and remain in that circular configuration for some time. However, abrupt changes in rotation speed would disturb the system and cause it to decay into a random configuration. The same hypotheses on failure listed above also apply here.

The final experiment used drinking straws to test the hypothesis that some residual stiffness in the lines would dampen instabilities in the system and provide an initial radius. Drinking straws were applied to the lines of the Noose-type Turkey trap so that they divided the pulley masses by a distance of ~3". The model was then spun up using the same cordless drill arrangement as described in the first test. Results were much better in this final test. Although the pulley masses did not spread apart much farther than the straw sections had forced them to the configuration was much more stable and could be sustained for quite some time.

It was then suggested that, instead of a rotation to keep the weights in place, an inflatable was used as shown in Figure 4.2.4-1. This would ensure that the sliders were in an appropriate configuration when the capture device entered. Upon entry of the capture device, the inflatables would deflate, the cables tugged back toward the satellite, and the sliders move to the center to meet the capture device.

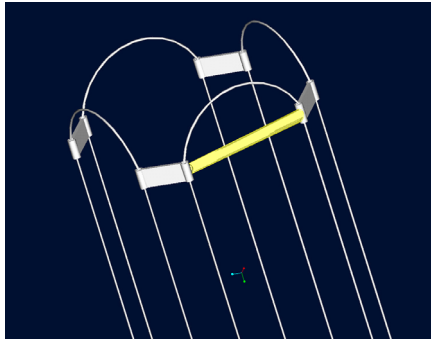


Figure 4.2.4-1: Noose-Type Turkey Trap with Inflatables

4.3 Goalpost Flier: First-Round Design Analysis

4.3.1 Overview

This document will summarize the results of a first-round of design and analysis of the goalpost flier capture concept. The primary elements of the design are described, as well as the analysis procedures. The key results are summarized and conclusions are made regarding suitability and future development of this capture concept.

4.3.2 Brief Description

The goalpost flier capture concept, shown in Figure 1, consists of a “goalpost” on the tether (a set of light booms that guide the cable toward a cable grab) and a small tethered passive flier on the payload. The tether flier is launched on a simple trajectory and places the cable over the goalpost and into the cable grab. The flier will maintain tension in the cable until the cable grab pulls taut (occurs when the relative velocity b/n the tether and payload goes to zero). The tethered flier is then cut free and travels harmlessly into the confines of deep space. See Figure 4.3.2-1 below.

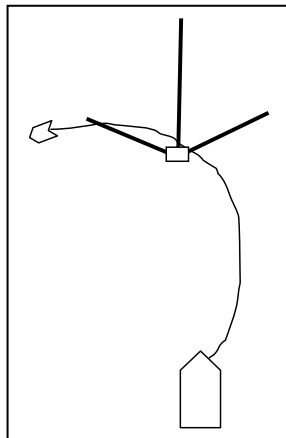


Figure 4.3.2-1: Goal-Post Filter Schematic

4.3.3 Summary of Design Points

The goalpost on the tether consists of composite booms that terminate in the base of the cable grab as shown in figure 2. The base of the tether is encased in a shield to protect it from impact with the tethered flier. The tethered flier is passively launched and can fly a fixed trajectory or a variable trajectory (if given a small thruster). The flier-cable consists of 20 mm HMPE wire rope. The

grasping mechanism is a cable grab, a cam device that allows the cable to travel in one direction only. An additional tether shearing mechanism is added to release the tethered flier after grasp.

4.3.4 Summary of Analysis Performed

Several key analyses were performed to characterize system behavior and analyze results. These were:

- 1) Dynamic simulation of the interaction between the flying cable and the light boom “goal posts”. This simulation assumed a small tension in the flying cable (approx. 1 N) and was performed in ADAMS using thin beams and line elements. The simulation demonstrated the desired performance, the flying wire would be guided toward and into the cable grab with minimal tension. Samples from the dynamic simulation are shown at the end of this report.
- 2) Size of the flying wire are determined. These are given as HMPE 20 mm dia. wire rope, total strength of 117.5 kN, weight of .188 kg/m.
- 3) Mass estimate of the system was performed. The flier is estimated at 30 kg, the flying tether at 30 kg, the goalpost booms and cable grabs at 190 kg. Total mass estimate is 250 kg.

4.3.5 Summary of Key Conclusions

In light of the resulting analyses, several conclusions are drawn.

- 1) From a dynamic standpoint, a small amount of tether tension will guide the tether along the goal post and into the cable grab. Other dynamic effects of impact do not seem to be limiting.
- 2) An appropriate trajectory needs to be determined. Currently, simple rules in defining this trajectory can be constructed. A curvilinear trajectory (an accelerating trajectory) is most likely necessary. Therefore, a completely passive flier may not be possible.
- 3) The tether itself will always exist in the field of one or more potential trajectories. It is proposed to shield the end of the tether and allow the possibility of collision b/n the tether and tethered flier. More modeling will be performed to demonstrate that this is not a problem.
- 4) The mass of the system is low, the probability of the system working seem reasonable. The complexity of the system is low to moderate.
- 5) Plans for release of the payload and release of the tethered flier are still needed.
- 6) Due to the low mass and low to moderate complexity, this design should be pursued further.

Figures 4.3.5-1 through 4.3.5-4 show a simulation of the tethered flier (performed in ADAMS) making contact with the goal post and moving toward the cable grab.



Figure 4.3.5-1: Simulation Results of Contact between Tethered Flier and Goal Posts, $t=0.0$

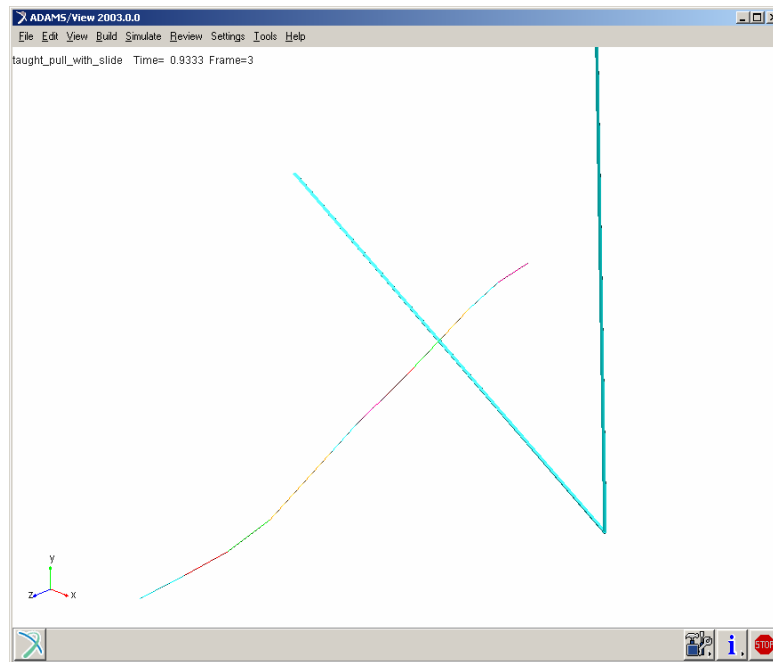


Figure 4.3.5-2: Simulation Results of Contact between Tethered Flier and Goal Posts, $t=0.93$

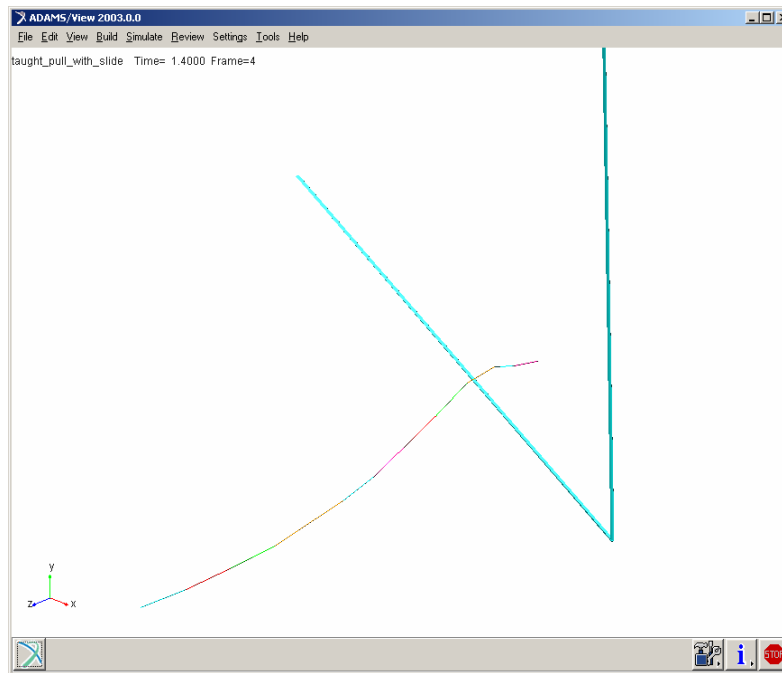


Figure 4.3.5-3: Simulation Results of Contact between Tethered Flier and Goal Posts, $t=1.4$

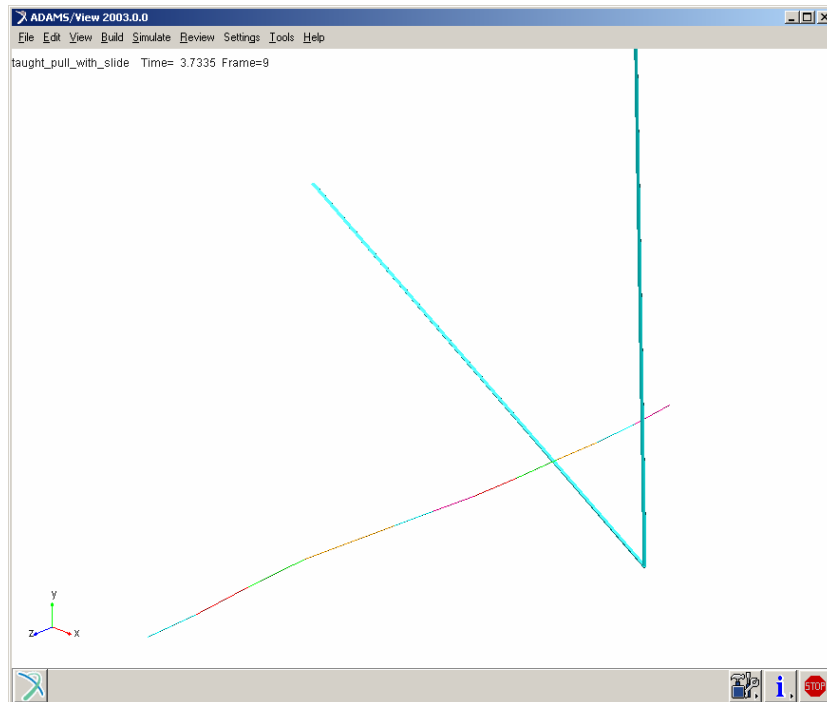


Figure 4.3.5-4: Simulation Results of Contact between Tethered Flier and Goal Posts, $t=3.7$

4.4 Modified V-Gripper: First-round Design Analysis

4.4.1 Overview

This document will summarize the results of a first-round of design and analysis of the modified V-Gripper capture concept. The primary elements of the design are described, as well as the analysis procedures. The key results are summarized and conclusions are made regarding suitability and future development of this capture concept.

4.4.2 Brief Description

The modified V-Gripper, shown in Figure 4.4.2-1 below, consists of a planar, guiding mechanism on the tether and an extended trap wire on the payload. The guiding and gripping mechanism on the tether spans an area approximately 20m x 100m, and is actuated by a cable in the center of the mechanism. As the payload and tether approach rendezvous, the V-gripper retracts to guide the trap wire toward the center of the V-gripper, and to complete the grip when the payload and tether have zero-relative velocity. The V-gripper has zero-degrees of freedom. Rather it relies on elastic deformation to form the guiding surface and to retract as the trap wire approaches the tether.

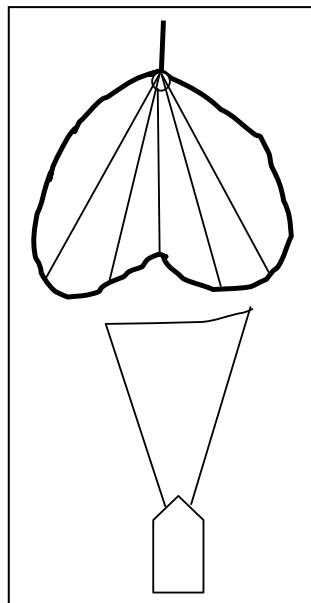


Figure 4.4.2-1: V-Gripper Schematic

4.4.3 Summary of Design Points

The modified V-gripper consists of a composite rod with annular cross-section shown in figure 2. The trap wire supported on the payload consists of 20 mm HMPE wire rope and two light-weight booms. The cable grasping mechanism is a single dof, two jaw grasping device, made of composite material. The V-gripper is driven by a 20 mm HMPE wire rope, approximately 150m in length with actuated cable drum.

4.4.4 Summary of Analysis Performed

Several key analyses were performed to characterize system behavior and analyze results. These were:

1. Dynamic simulation of trap wire impacting and sliding along the V-gripper. Simulation was performed in ADAMS using thin-beam sections to form the model. The simulation demonstrated the desired performance of the trap wire guided toward the center of the gripper

with very minimal contact force (sub 1 N force). Screen grabs of the dynamic simulation are shown at the end of this report.

2. Strain analysis was performed on the V-Gripper during a full deflection. Max strains in the device were very small (sub 1%). Some of the results of this analysis are shown at the end of this report.
3. Deflection analysis was performed on V-Gripper during normal operation. Normal operation places the device in an approximately 2g loading condition. Due to the light-weight nature of the beam, the 2g load causes large deflection of the device. Off-loading cables will be necessary to allow V-gripper to function.
4. Size of the trap-wire and actuating wire are determined. These are given as HMPE 20 mm dia. Wire rope, total strength of 117.5 kN, weight of .188 kg/m.
5. Mass estimate of the system was performed. The primary contributors to the mass were: 1) the V-gripper boom (approx. 250 m in length) 2) HMPE cable. The total mass of this device in an ideal case appears to exceed 500 kg and perhaps 1000 kg.

4.4.5 Summary of Key Conclusions

In light of the resulting analyses, four conclusions are drawn.

1. From a dynamic and operational standpoint, the modified V-Gripper device is demonstrated to work as expected. Impact b/n trap wire and V-gripper Boom does not create instabilities, dynamic response shows a clear guiding of the trap wire toward the center.
2. The strain in the boom is minimal to deflect to the desired shape.
3. Due to the accelerating state of the end of the tether, approx. 2g, the V-gripper boom is under significant quasi-static load. This can be accounted for with off-loading wires (analysis is performed to demonstrate this can work). However, the trade-off is added mass and complexity.
4. The mass of the system is exceedingly high. The long boom, off-loading wires, and long trap wire contribute to this high mass budget.
5. Due to the high mass estimate and additional complexities of off-loading, this concept will not be further pursued for the current time.

4.4.6 Finite Element Analysis of Concept Name: V-GRIPPER

A simple model of the V-Gripper is considered in a commercial finite element analysis software (ANSYS). The booms are 4 in diameter and made of graphite. Material specifications are: $E=10$ Gpa and $\rho=1800$ kg/m³ with dimensions shown in Figure 4.4.6-1. Following this, a series of figures depict typical responses of the system for various loads or displacements (Figures 4.4.6-2 through 4.4.6-13 below).

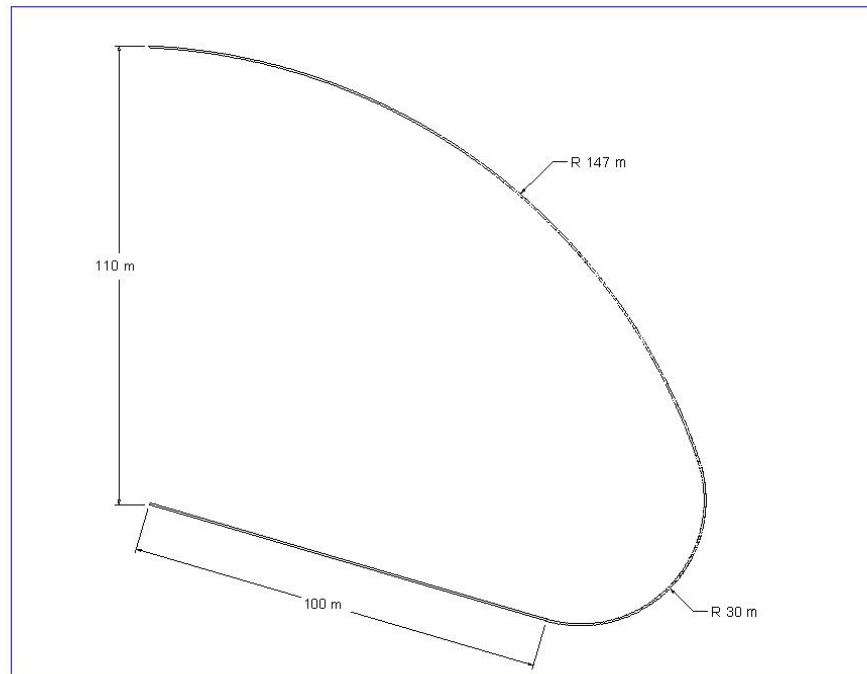


Figure 4.4.6-1: Sketch of ½ of the Ugly Stick V-Gripper

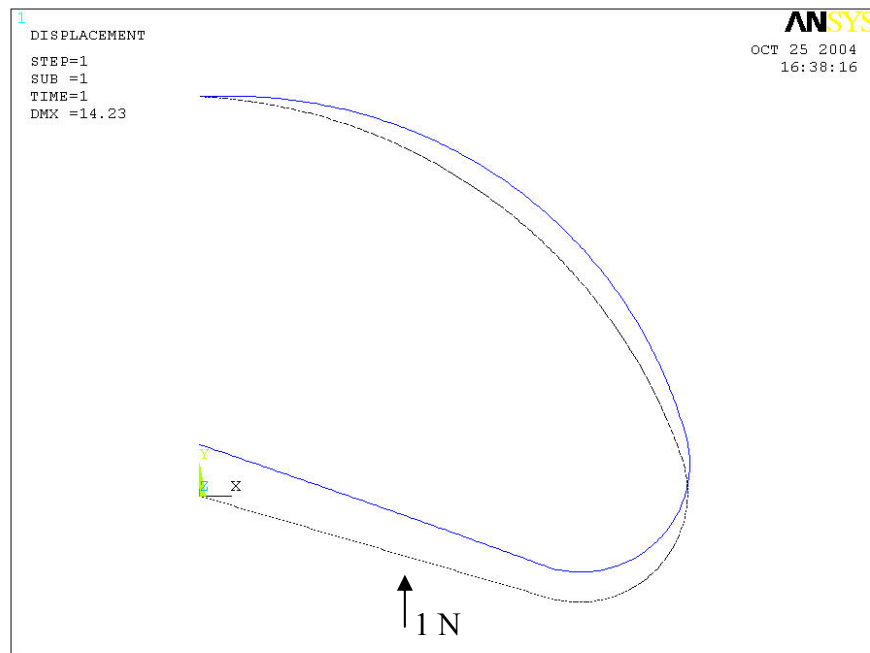


Figure 4.4.6-2: Displacement of Half of V-Gripper
 (With 1 N load applied as shown)

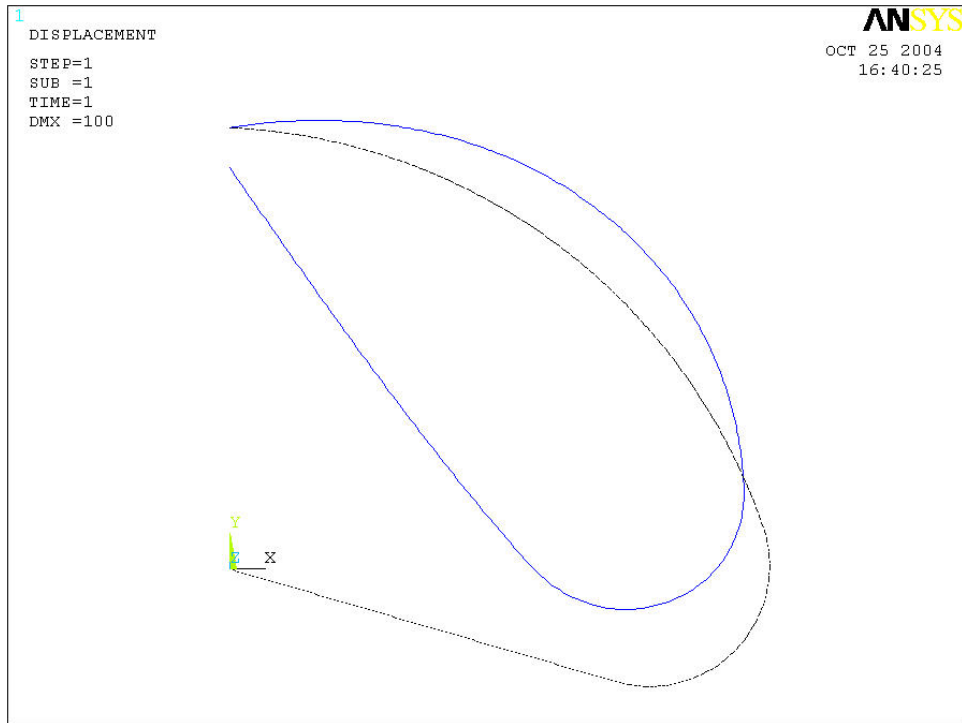


Figure 4.4.6-3: Displacement Profile
(With an input displacement of 100 m at the center)

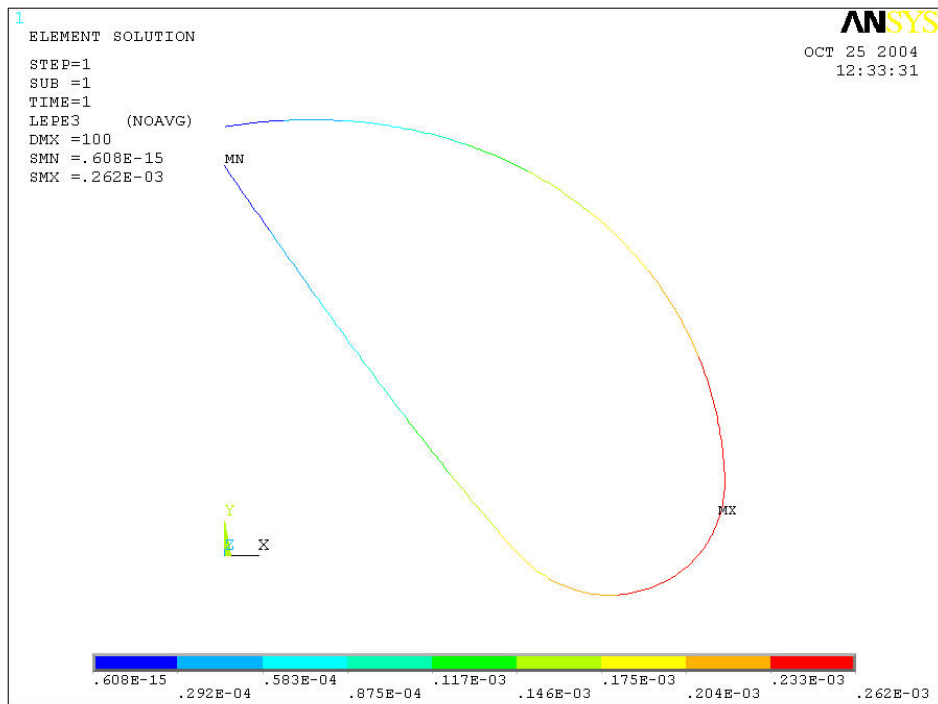


Figure 4.4.6-4: Strain Distribution for Half of V-Gripper
(With 100 m input displacement)

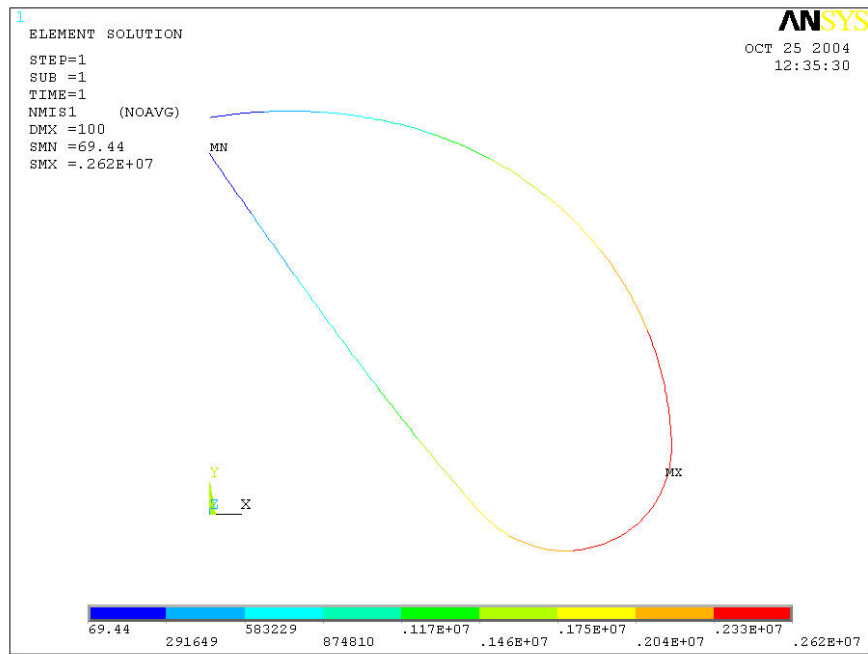


Figure 4.4.6-5: Stress Distribution for Half of V-Gripper
(With 100 m input displacement)

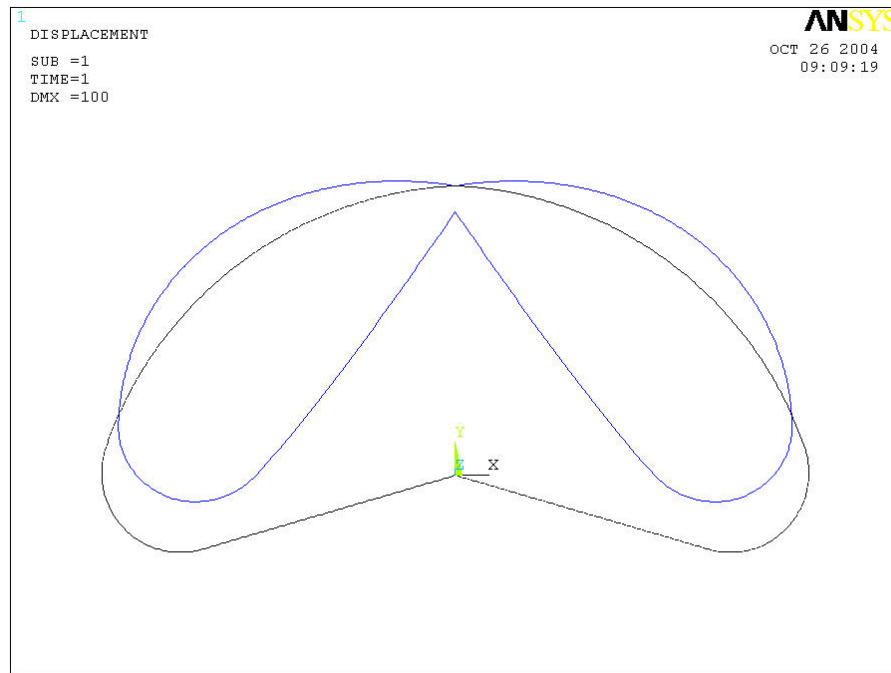


Figure 4.4.6-6: Displacement Plot
(Less than 100 m input for full case)

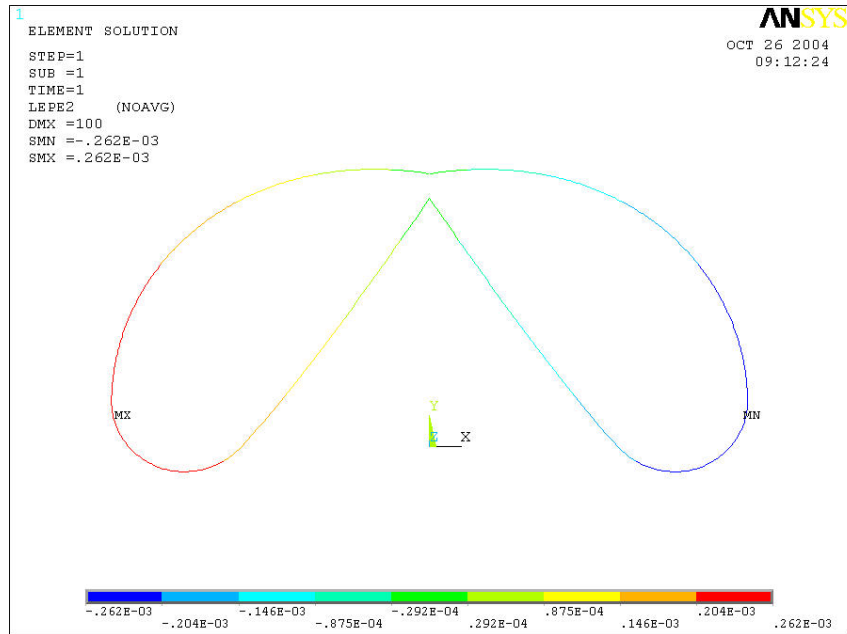


Figure 4.4.6-7: Strain Distribution
(For 100 m displacement at center)

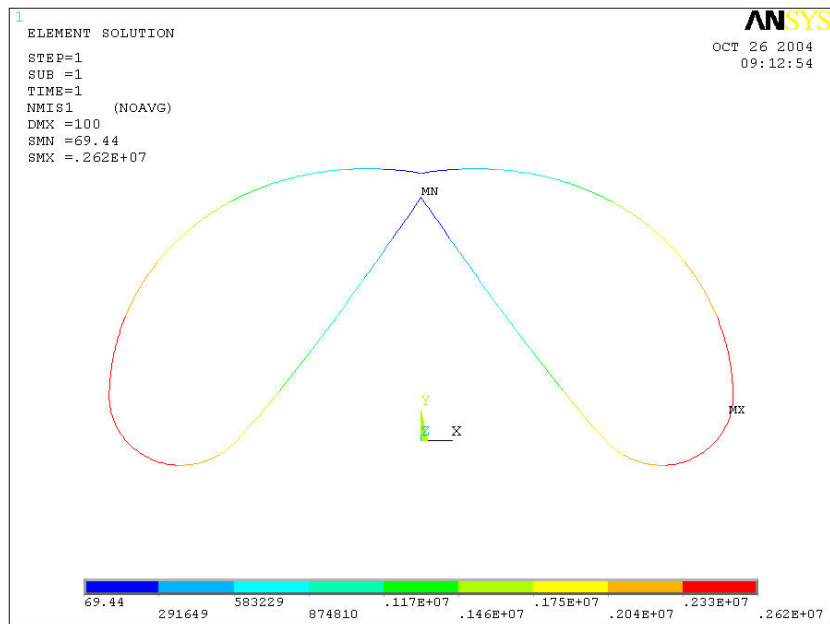


Figure 4.4.6-8: Stress Distribution
(For 100 m displacement at center)

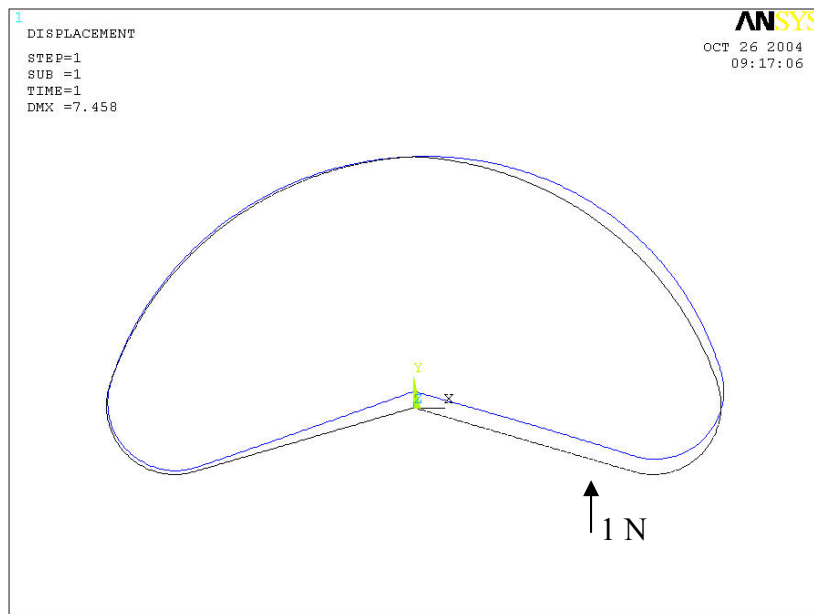


Figure 4.4.6-9: Displacement with 1 N load
(Applied off center as shown)

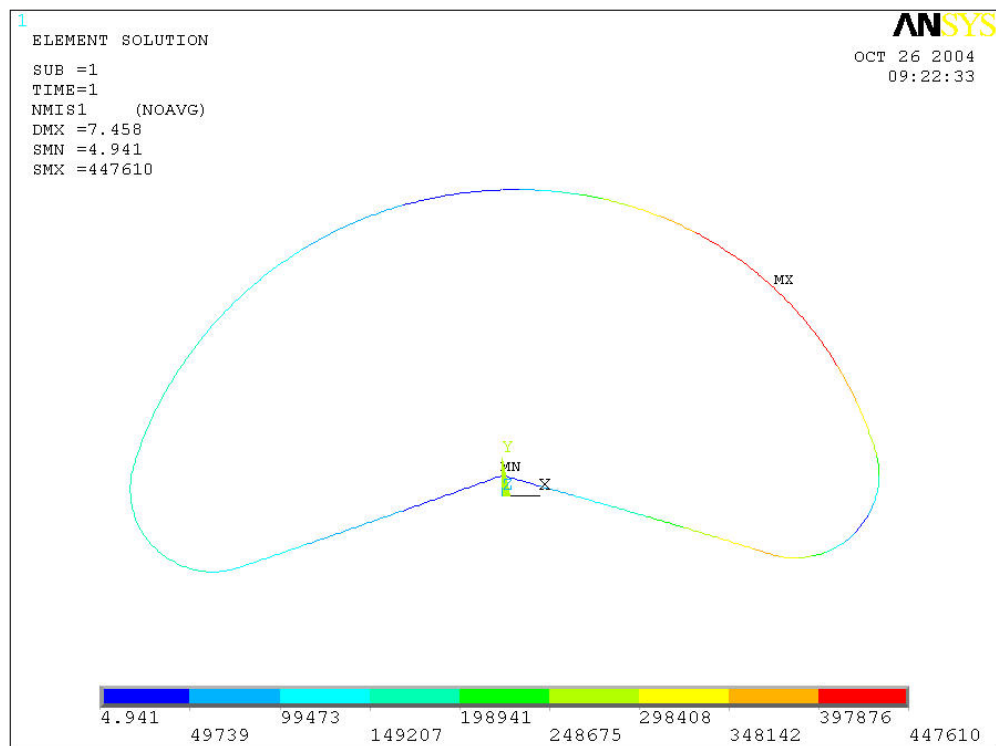


Figure 4.4.6-10: Stress Distribution
(For Figure 4.4.6-9)

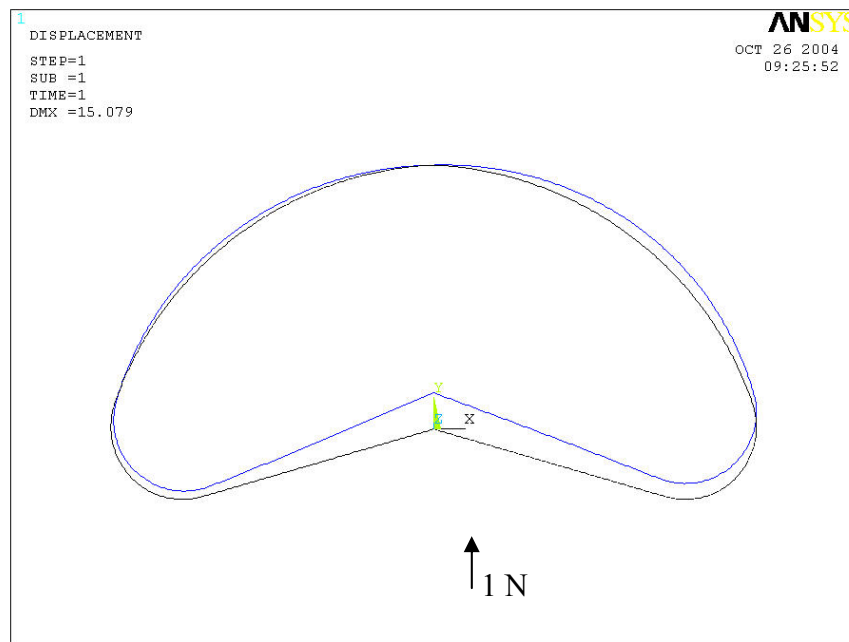


Figure 4.4.6-11: Deflection with 1 N Load
(Applied as shown)

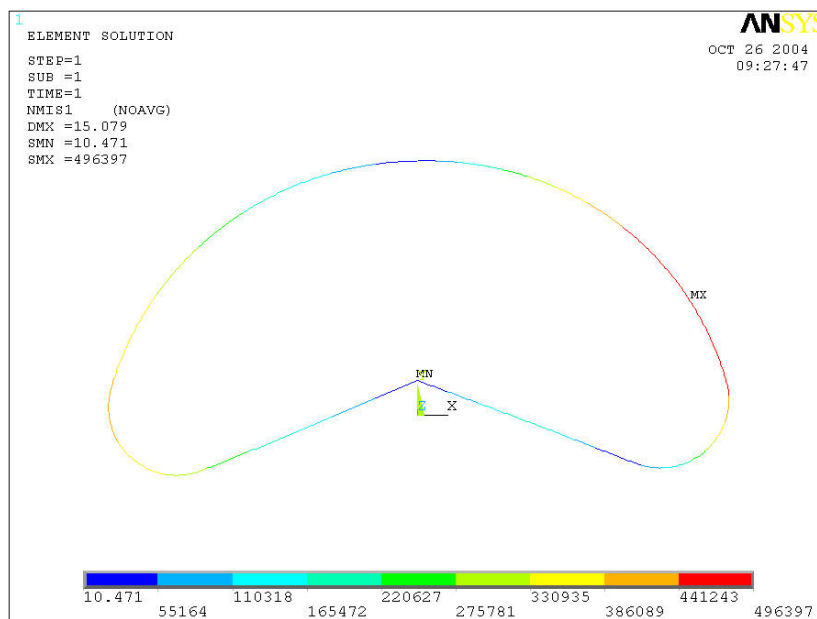


Figure 4.4.6-12: Stress Distribution
(For Figure 4.4.6-11)

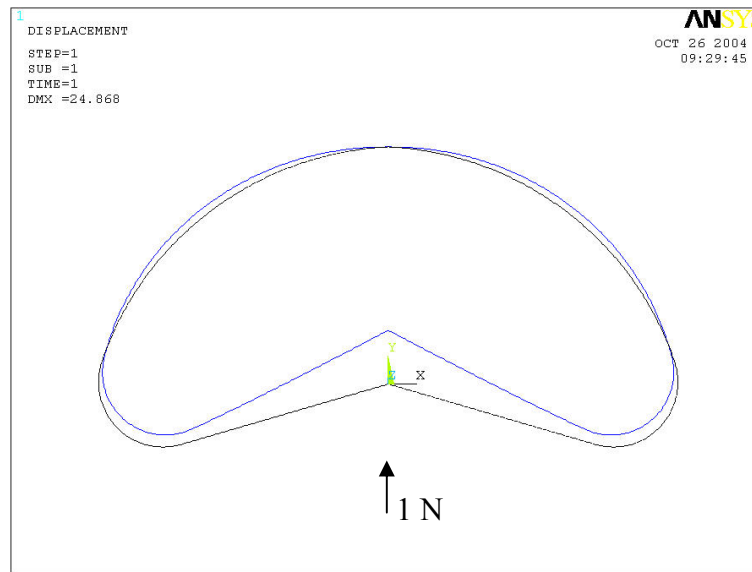


Figure 4.4.6-13: Deflection for Case of 1 N Load in Center

4.5 Trade Study on Second Round Selected Designs

After a brief study of tradeoffs on the top four choices, the Modified Iris was selected as being the simplest, most capable idea under the conditions and stipulations placed on the design process. One of the most attractive features being the passive gravity-assist closing of the device. It was noted that under the force of its own weight, the mechanism could close within an appropriate time frame. This was a colossal advantage over the active mechanisms or mechanisms requiring more complex methods or aid in closing. Upon a firm agreement and support of team members and approval from the project manager the modified Iris (Quad Trap) was designated the candidate which would be subjected to physical testing.

4.6 Develop Advanced Models of Selected Mechanism (Quad Trap)

Upon choosing an appropriate candidate for further investigation, a second order engineering analysis was performed upon the more crucial elements of the system. The exact geometry was defined and an ANSYS model was created to observe stresses and deflection due to loading. Over several weeks, this model was shaped and manipulated to meet weight/strength criteria with several tests performed permutations on shape and material. The final material choice was an intuitive guess, a titanium alloy, and the final shape can be seen in Figure 4.6-1.

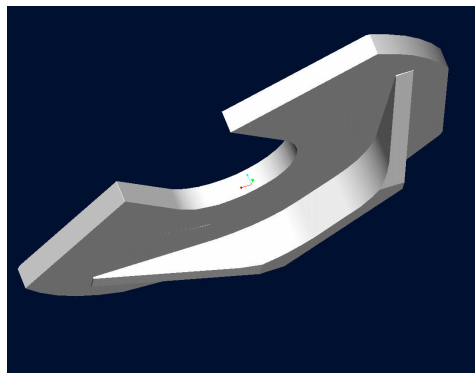


Figure 4.6-1: View of Catch Plate

The evolution of the plate was drawn from the criteria set up declaring function and weight requirements. The original concept was a method for moving weight from off axis of the tether onto a collinear position. The plate concept was the initial choice, followed closely by a set of hooks, see Figure 4.6-2 below.

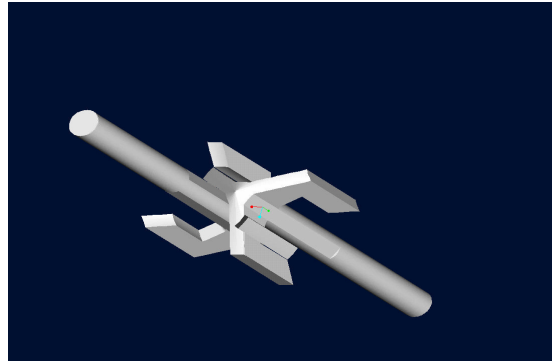


Figure 4.6-2: Capture Hooks to Replace Plate

The hooks were cast aside from the uncooperative nature of the geometry. The initial plate is shown in Figure 4.6-3 which handled stresses appropriately but held an expensive weight penalty.

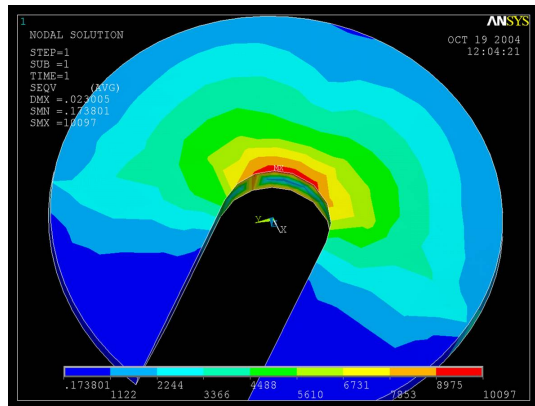
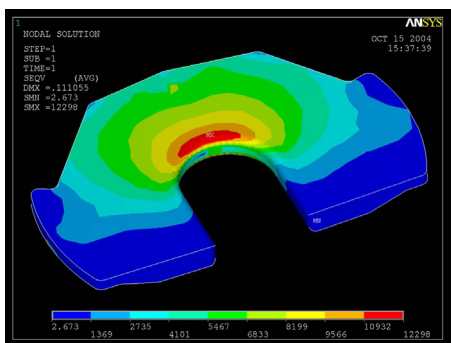
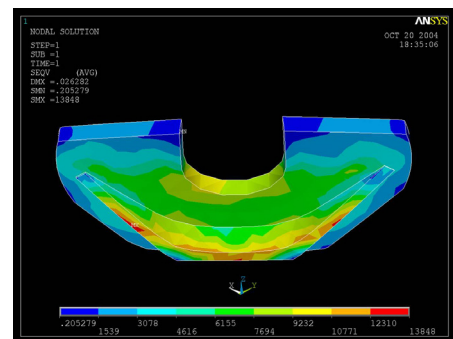


Figure 4.6-3: Initial Plate Response to Typical Loads

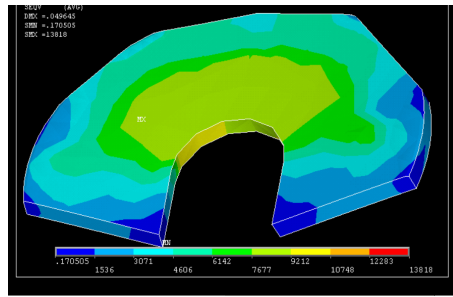
The initial plate handled the an assumed load of ten thousand pounds with resulting stresses at 10ksi, well under the limit of yield stress of titanium, 25ksi. The redesign of the plate brought its weight to 100lbs with a max stress of 12ksi which, while a significant drop in weight from the original 200lbs, was still a non-trivial weight penalty and high stresses as well. The intermediate designs are shown in Figure 4.6-4 below.



(a)



(b)



(c)

Figure 4.6-4: Intermediate Designs of Capture Plate

The final design of the plate brought its typical stresses down to under 10ksi with maximum stresses at 13ksi, but with the weight peaking at 60lbs. This was well within the design criteria and a suitable recommended design. The next design of the Modified Iris (quad trap) was to attach the plates to sliding railings. The railings were designed as I-beams for their strong moment resistance while maintaining very low weight. A picture of the final design can be seen in Figure 4.6-5.

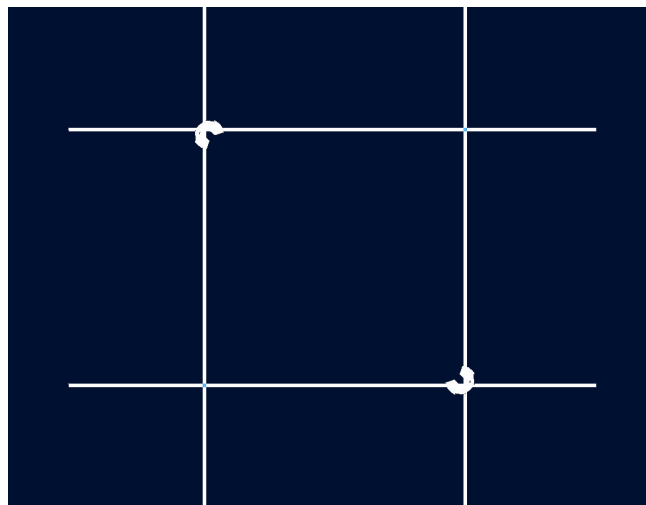


Figure 4.6-5: Final Second-Order Design of the Modified Iris

One of the other mechanisms which was addressed was the payload side of the iris. It was suggested that the payload side of the capture mechanism be simplified from the extendable boom to a single cable which would have nodes on it to be grasped by the capture plate on the modified Iris. A casting/reeling mechanism was designed to launch the lanyard to be captured by the quad trap. One of the desired features of the launcher was that it must have no limit to the number of launches, deeming all forms of propellant out of the design race. The launcher could also be packaged in a format to which satellite manufacturers could simply attach it to their satellite pre-launch with no hassles. See Figure 4.6-6 below.

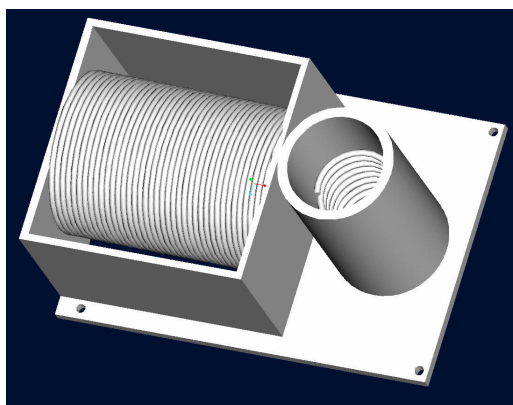


Figure 4.6-6: Schematic of Lanyard Launch Mechanism

Several models were drawn up in ADAMS dynamic modeling software during the process as well. A simplified version of the quad trap was created to aid in the design of the beams. The beam was initially modeled after an Able boom, a technology which had been discussed a great deal and generally accepted. From this model the maximum deflection of the central guidance beam was determined. The model consisted of two blocks (both steel 2' x 2' x 2") and a circular 10m long beam (8' diameter) modeled after one of the Able Booms. See Figure 4.6-7 below.

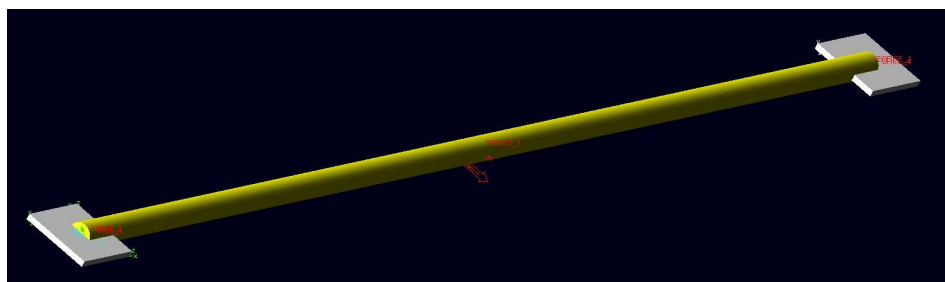


Figure 4.6-7: Simplified Version of Deployable Boom

The two blocks were simulated free to move along the pole but constrained from moving off the pole. A force of 5600N, a force assumed to occur under 2G loading, was placed on the center of mass of each of the blocks forcing them closed as well as another 5600N pushing the entire system 5m horizontally due to the symmetry of the system. This horizontal motion caused the beam to deflect and the maximum deflection with respect to time was calculated parametrically with variable beam stiffness and mass, and three different cases simulated for each. The forces required to close the mechanism in one second was also calculated for each of the masses. Figure 4.6-8 summarizes the ADAMS model of the Quadtrap system.

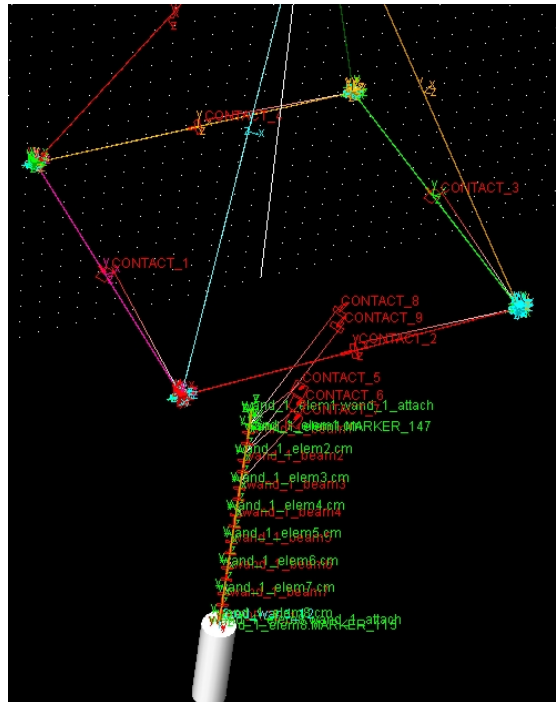


Figure 4.6-8: Schematic of ADAMS Model of Quad Trap

A summary of the results are shown in Tables 6-9. These tables demonstrate the system response in terms of displacement, velocity, system energy and acceleration respectively.

Table 6: Displacement of Quad Trap during Capture

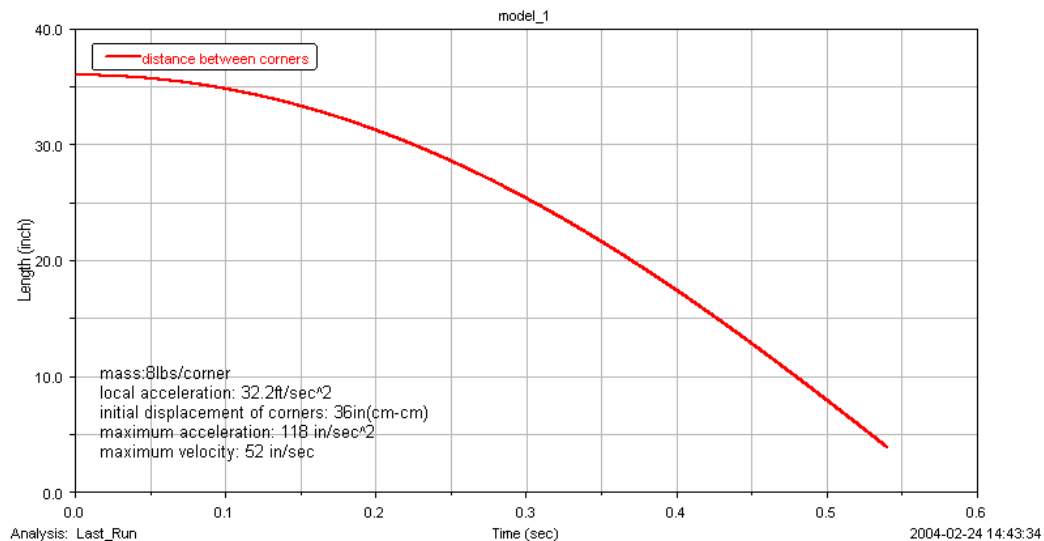


Table 7: Velocity of Quad Trap During Capture

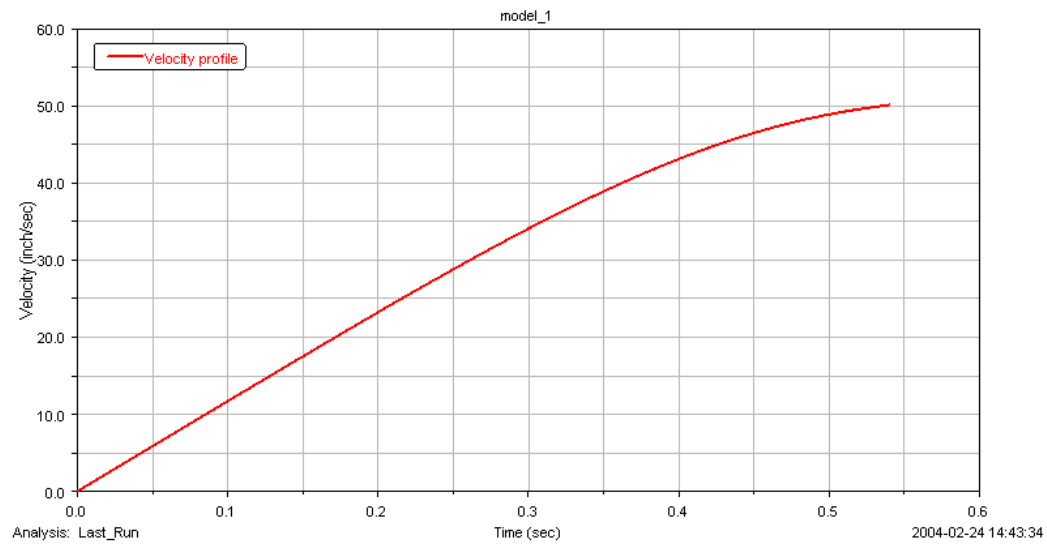


Table 8: Sum of System Energy in Quad trap

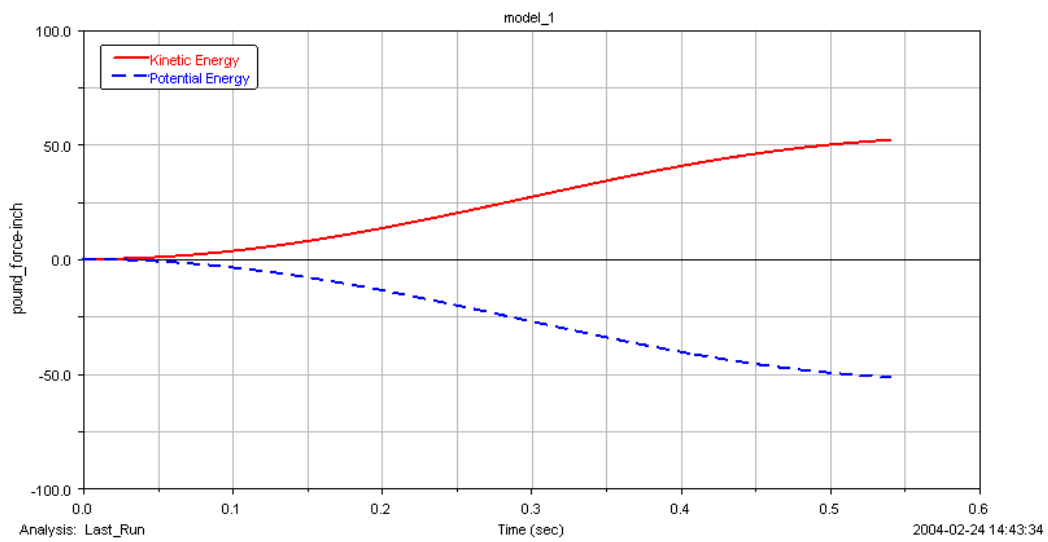
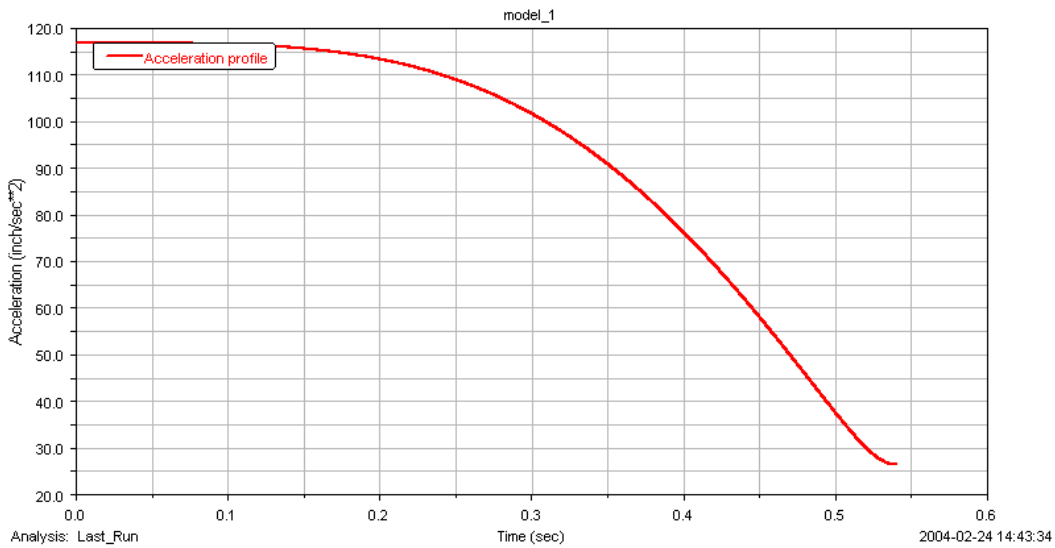


Table 9: Acceleration of Quad Trap During Capture



After these intermediate models were created, the scaled quad trap prototype was modeled. The developed prototype is discussed in the section A 5.

4.7 Evaluation of 3 DOF Spatial Joint Mechanism

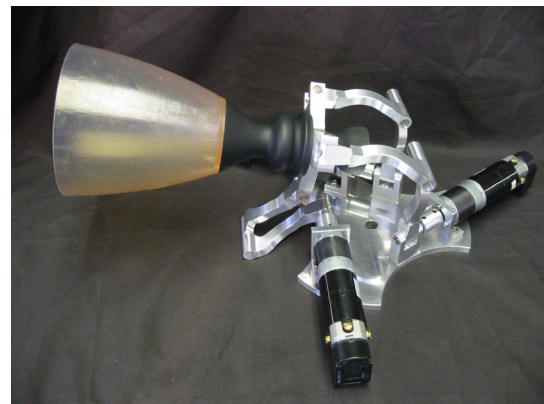
(For MXER and other in-space propulsion concepts)

4.7.1 Summary of the 3D Solar-Array Tracking Joint Design for Solar-Array Tracking

A three degree-of-freedom, spatial, parallel-architecture manipulator (referred to as a spatial joint) is investigated here as an improved gimbal mechanism for in-space applications. This spatial joint has many advantages, including large, greater-than hemispherical, singularity-free workspace, ground-relative actuation, and a high strength-to-weight ratio. For this effort, two prototype spatial joints were designed, fabricated and delivered. These prototypes demonstrated real-time closed-loop control by tracking an operator input via a joystick and are shown in Figure 4.7.1-1 (a) and (b) below.



(a)



(b)

Figure 4.7.1-1: Prototype of 3 DOF Mechanism in Two Positions

As an example of implementation, the design of this spatial joint for implementation as the primary gimbal support for a sun-tracking solar array on the CEV. The requirements for this joint are to 820 ft-lb torque load while providing tracking capability to the solar arrays (wrist pitched to 90 degrees while rotating fully). Figures 4.7.1-2 and 4.7.1-3 provide an overview of the design as a CAD model.

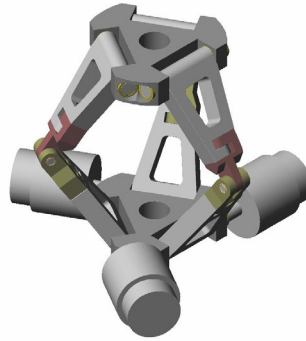


Figure 4.7.1-2: CAD Rendering of Solar Array Tracking Joint

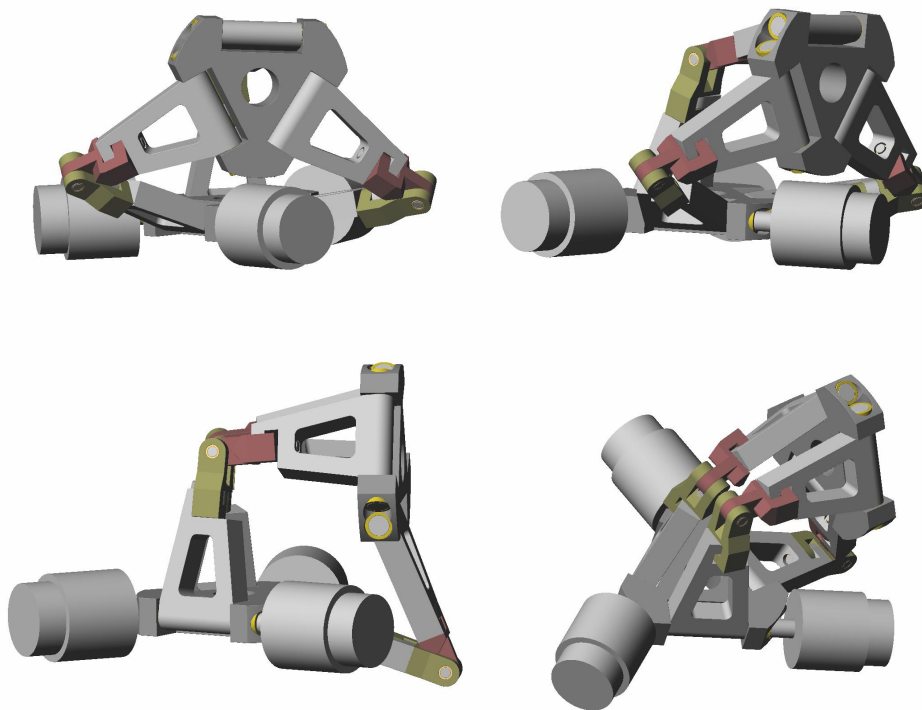
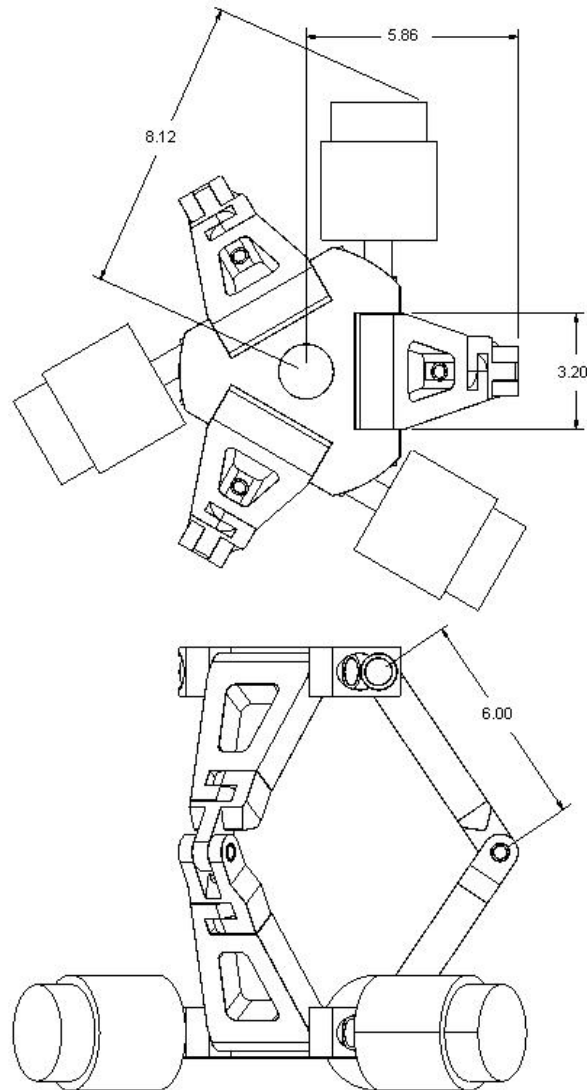


Figure 4.7.1-3: Solar Array Tracking Joint

(At 90 Degree pitch at location in full rotation)

In Figures 4.7.1-2 and 4.7.1-3 above, the Solar-Array is removed for clarity. The location in Figure 4.7.1-3 above shows the joint in the highest-load configuration. The actuation system is currently demonstrated as a combination Maxon EC-90 Flat motor and HDC-1M harmonic drive gear head. Numerous configurations for actuation are available; this one is shown for representation only.

Figure 4.7.1-4 demonstrates the overall kinematic parameters for the current joint design to achieve a greater-than hemispherical workspace. With a firmer set of requirements and more detailed design, this workspace can be scaled to a reasonable degree.



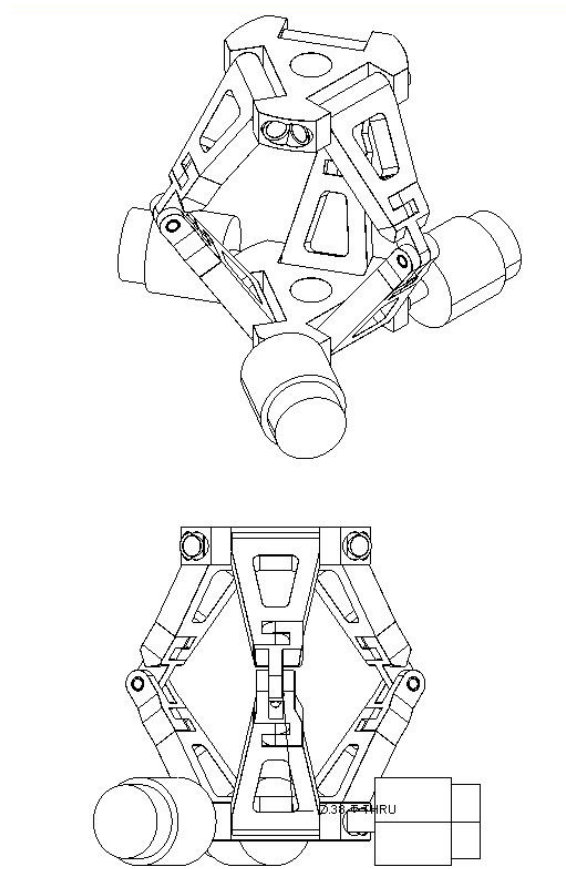


Figure 4.7.1-4: Wire Frame Solar Array Tracking Joint
(With overall dimensions)

Key metrics for the initial design of the 3D solar-array tracking mechanism are listed in the following table:

Table 10: Summary of 3D Solar-Array Tracking Mechanism

Component	Description	Mass/ Workspace
Motor Drive:	Maxon EC90 Flat Motor	1.5 lb
Drive reduction	Harmonic Drive HDC 1M	2.6 lb
Bearings	Bronze bushings, $\frac{3}{4}$, $\frac{3}{8}$ ID	
Shaft	440c SS	
Link components	7075 Al	
Mechanism weight *	(without actuation)	14.75 lb
3D Mechanism weight	(with actuation, includes a 20% factor)	32.5 lb
Working Volume*	5.5 inch radius cylinder Height is selectable	5.5 inch cylinder
Stowed Volume*	3 high x 7 radius cylinder (inches)	7x3i inch cylinder

* without actuators

Analysis and design of the structural and actuation components of the 3D solar-array tracking mechanism are based initially on a forward dynamic load analysis tool that incorporates the inverse kinematics, load specifications and kinetostatic analysis to give all loads within the mechanism as a

function of position within its workspace. Figure 4.7.1-5 represents some of the bearing loads and motor torques required in the worst-case loading scenario. The maximum of these loads was selected as requirements for actuator and bearing design.

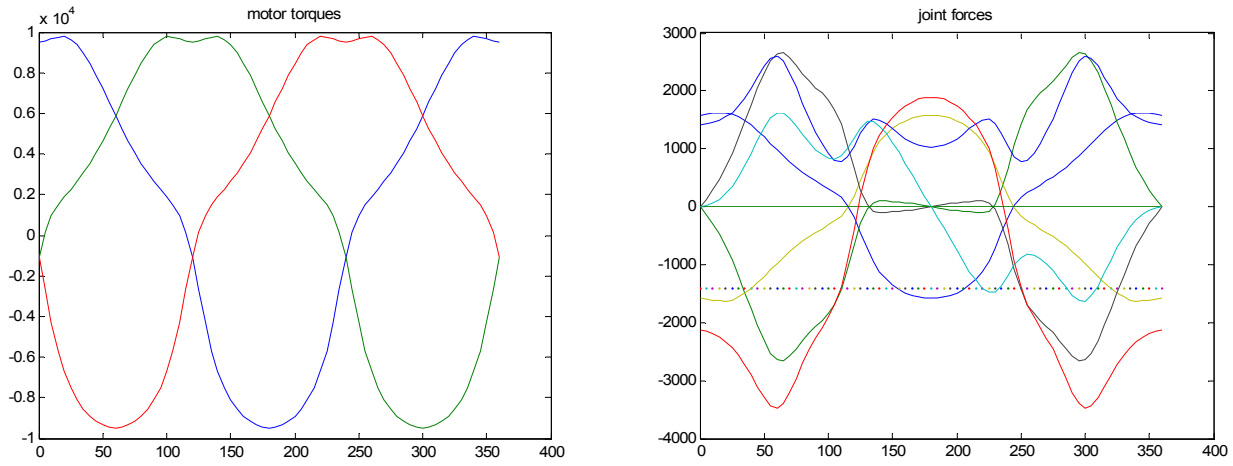


Figure 4.7.1-5: Motor and Bearing Loads

(For worst case loading condition)

4.7.2 Summary of 3-5R Spatial Parallel Architecture and Kinematics

(Pitch-Yaw-Plunge Mechanism)

A brief discussion of the parallel architecture wrist is provided followed by two a description of two potential applications.

Kinematically, the mechanism consists of 3 5-R (revolute) chains resulting in three degrees of freedom at the output (distal) plate. These dof allow pitch and yaw of the distal plate and translation along the distal plate normal axis. The 3 dof mechanism requires three inputs. This device is an in-parallel mechanism; there are multiple load-bearing paths connecting the output plate to the base plate (in-parallel). Due to this parallel mechanism topology, the device has many advantages. The advantages associated with this 3 dof joint include:

- High payload-to-weight ratio
- Good dynamic performance
- Ground-relative actuation (all input actuators located on the base plate)
- All revolute-joint design

However, historically, parallel mechanisms have found a lesser degree of implementation due to a few limiting factors: range of motion, lack of closed-form kinematic solutions and lack of topologies and designs that match the application. In the proposed mechanism and its pointing applications, these limitations have been overcome as follows:

- Closed-form forward and inverse kinematics exist
- Large range of orientation motion (pointing)

Finally, in addition to the positive improvements in areas of performance, there are a few key improvements of this approach over conventional (serial) pointing mechanisms;

- Greater-than-hemispherical singularity-free workspace

- Control algorithms are not constrained by singular regions
- Improved dexterity based on common measures of robotic dexterity.

Figure 4.7.2-1 below shows one prototype version of the wrist that demonstrates real-time inverse-kinematic control.



Figure 4.7.2-1: Prototype 3 DOF Mechanism

Our group has developed this device for many applications, including robotic wrists on industrial and EOD manipulators, high-precision manipulation devices, miniature precision control of mirrors, compliant, monolithic designs, and as motion simulation platforms. See Figure 4.7.2-2 below.

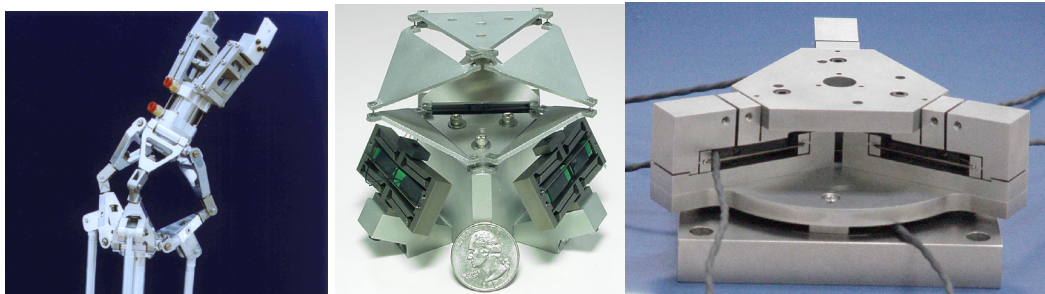


Figure 4.7.2-2: Robotic End-Effector

(Compliant design for pointing mirrors, sub 10nm precision manipulator)

Two current applications are included below and in the attached document. One briefly described the design of the joint as a solar-array tracking device as part of the CEV, the second a gimbal mount for a rocket thruster (below).

A collaborative effort between the ISPT group at MSFC, Orion Propulsion and Tennessee Tech is demonstrating the design of a gimbale thruster that integrates the pointing mechanism with the rocket. The mount is based on the 3 dof parallel-architecture joint described above and provides the large range of singularity-free motion as indicated. The primary design efforts are integrating the thruster body as part of the distal plate and incorporating the flow-passages into the parallel-branches of the mechanism. Figure 4.7.2-3 shows a current design.

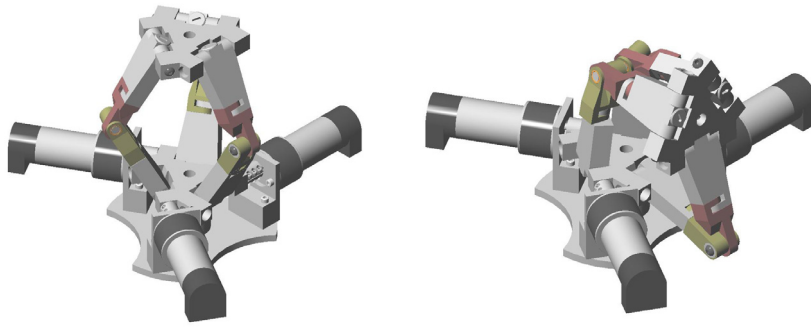


Figure 4.7.2-3: 3 DOF mechanism design for gimballing a rocket thruster

Figure 4.7.2-4 below shows one fuel-passage incorporated into the leg. This project is also investigating the ability of providing real-time thrust measurements through the force-control mapping that is provided in the manipulator control algorithm.

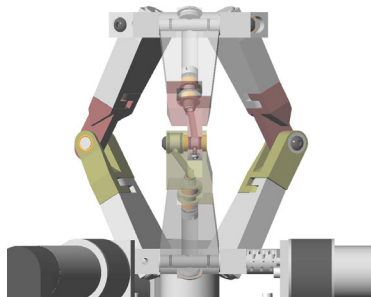


Figure 4.7.2-4: 3 DOF Mechanism with Fuel Passage Integrated into Legs

Figure 4.7.2-5 below represents the CAD models, prototype and assembly view of the Gimbal Joint Thruster Mechanism:

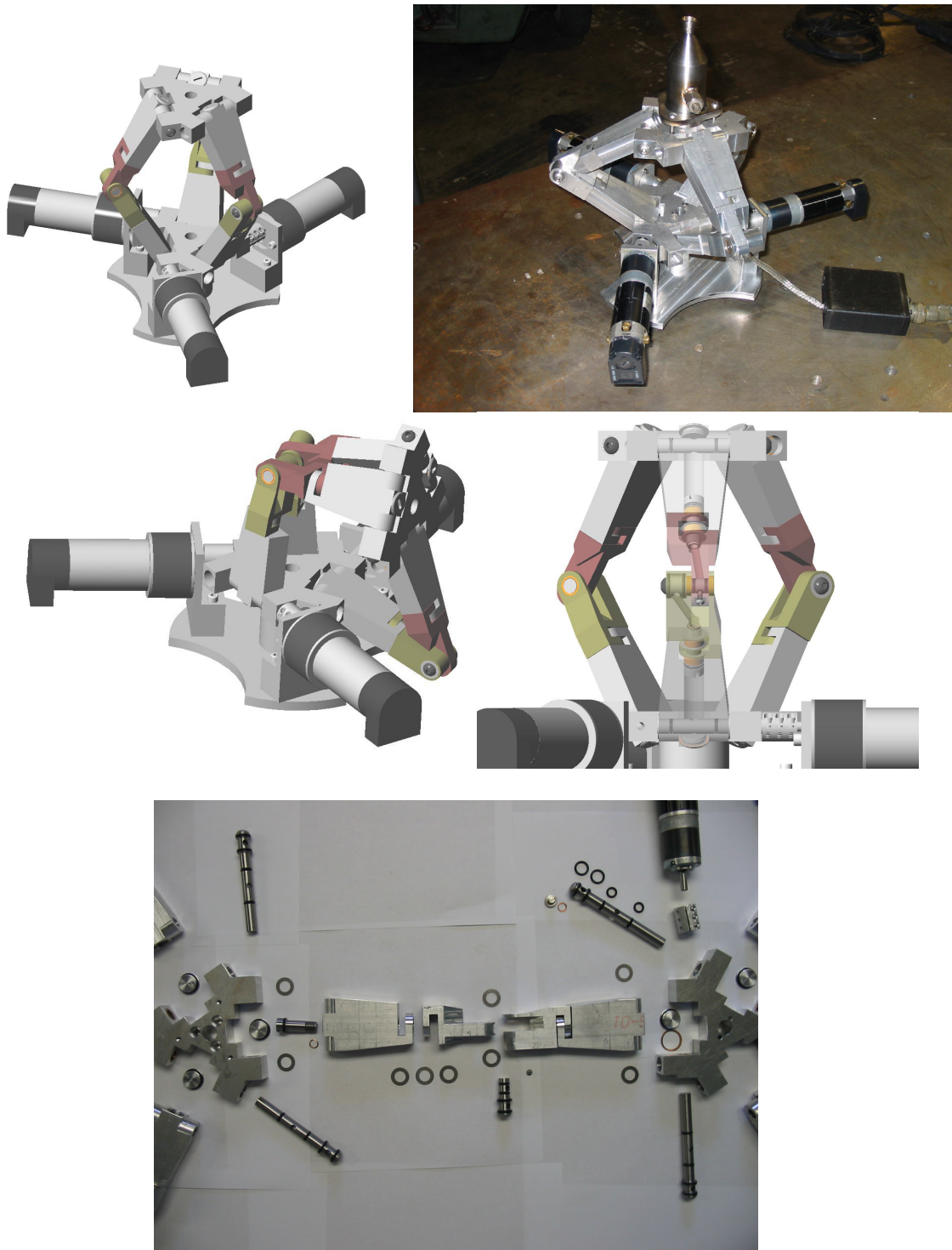


Figure 4.7.2-5: 3 DOF Mechanism as CAD Models, Assembly
(in hardware and prototype system)

5.0 DEVELOP TEST FACILITIES

(Necessary To Replicate MXER Tether Capture Dynamics)

This section summarizes the development of a physical capture test and the construction of a facility suitable for such a test. The test is used to examine the capture characteristics of a variety of mechanisms through the use of scale modeling. In order to simulate the dynamics of the capture sequence a scale model payload is propelled upward toward a scale model of the capture mechanism where the two will dock in a gravitationally accelerated environment.

5.1 General Dynamics of Test and Simulated Motion of Tether

The dynamics of the test simulate the dynamics expected of a MXER system. Due to the rotating motion of the tether system the tether tip traces a cycloidal motion profile thru space. In following this motion profile the tether tip experiences a nearly constant acceleration. When the rotational rate and orbital speed of the MXER system is set to dock with a payload the tether tip will briefly hold zero velocity relative to the payload. The extreme length of the MXER system means that only the portion of the cycloid which plunges in, stops, and then plunges out in the opposite direction is in the vicinity of the payload during capture. This means that, from the perspective of the payload, the tether tip and the capture mechanism that is mounted on the tether tip approach the payload in a nearly straight line, stop, and retreat in the direction from which they came all at a constant acceleration rate. The tests performed took advantage gravity to replicate the constant acceleration rate and singular direction of the tether motion. Taking the tether tip as the inertial reference frame the test propels a simulated payload upwards toward a stationary tether tip and allows the constant acceleration of gravity to pull the simulated payload back down. In this way the test system has a constant acceleration and the in-stop-out motion profile of the MXER system in a more convenient experimentation environment.

5.2 Description of Test Facilities

The test facility used for the capture experiments was found to be adequate and was modified to meet the needs of the experiment. A former racquetball court in the west side of the TTU stadium was chosen as the most appropriate available space for the capture test due to the size of the room. This space is a concrete room approximately 8m high and 6m wide. Initially the room was not equipped with any hardware mounting points on the walls or ceiling. In order to run the test capture mechanisms would need to be suspended from the ceiling so a scaffold was constructed and a 453 kg winch was mounted to the ceiling. Cable management hardware was also mounted to the ceiling to facilitate the test. Graduation lines were also painted on the walls of the room to provide some sense of scale in the video footage. Finally additional lighting was brought in to aid the video resolution and the scaffold was temporarily fixed to the wall to provide an additional measure of safety as well as to steady the video footage. Figure 5.2-1 below shows the resulting test facility.



Figure 5.2-1: Overview of Capture Mechanism Test Facility

5.3 Fall-Arrest Pad and Safety Measures

Safety was a primary concern during testing and a number of measures were taken to ensure that all those entering the test facility would leave safely. Each active component of the firing system was equipped with a safety off. The launcher trigger was equipped with a large red kill switch that prevented the system from energizing accidentally. A safety off came standard with the air compressor used. Every night the air compressor was decompressed to prevent an accidental discharge of the mechanism. A safety zone was established around the launch area and was not to be occupied during a test. In the event of a failed capture a “fall arrest pad” was placed under the mechanism. This pad was constructed of three 16cm thick foam pads which would absorb the impact of a failed capture preventing injury and preserving the life of the payloads. Finally a barrier ramp was constructed around the landing area. This barrier ramp was constructed using 1x1 boards and plastic netting. The intent of this barrier or “chicken coop” was to direct the payloads back onto the splashdown pad in the event that one payload took an erratic bounce. However one payload that did escape the fall arrest pad demolished the chicken coop and a more robust system is advised in any future testing.

5.4 Payload Launcher Building and Development

In order to produce the desired motion for the simulated payload a launcher device was constructed. At the time the launcher was constructed a target weight for a simulated payload had been identified how-ever a test site had not. A design goal was established which required the launcher mechanism to propel a weight of 4.5 kg a distance of 9 meters into the air. Because of the speed and length of travel needed to accomplish this goal compressed air was chosen as a power source. The necessary air pressure and flow rates were calculated and two 76cm long, 5cm diameter air cylinders were chosen to provide power to the launcher. A frame was then constructed to support two 213 cm long slide rails. The slide rails would mount parallel to one another so that a small platform can be bridged between them. Steel ropes were attached to both sides of this platform and then connected to the air cylinders via a block and tackle arrangement. In this way a simulated payload can be placed on the platform and when the system is energized with compressed air so that the air cylinders retract the platform and payload they are thrust upward at a high rate of speed. The entire system is actuated remotely using two solenoid actuated air valves. Later in the testing cycle the entire test would be fully automated using a LABVIEW virtual instrument program. However details on this program are left for later in this report. The resulting payload launch mechanism is shown from several angles in Figure 5.4-1 below.

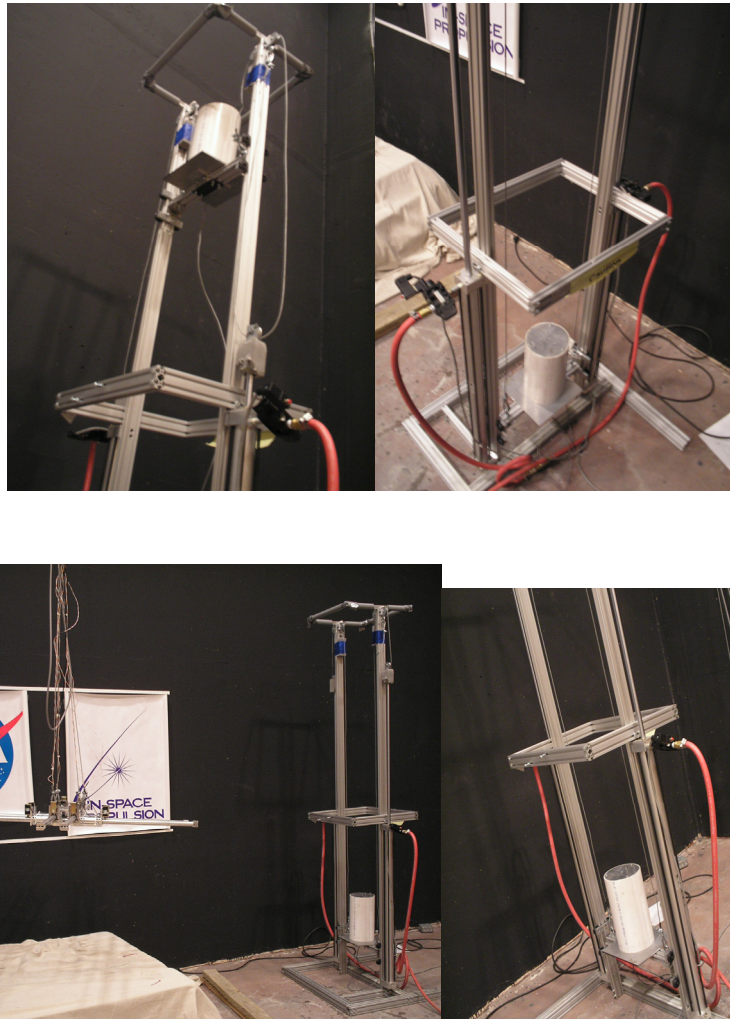


Figure 5.4-1: Payload Launching Mechanism as Built

5.5 Payload Fabrication and Development

Once the launcher was constructed an array of devices were constructed to serve as simulated payloads for the test. Two different payload design requirements were developed. The first set of payload design requirements would call for a low cost, low construction time but durable payload which would be used for the bulk of the testing. The second payload design requirement calls for a gyroscopically stabilized payload which was equally durable but would be used less frequently. It was initially hypothesized that any design would need a considerable number of “practice shots” before the launcher and capture mechanism were dialed in to their preferred test settings. Therefore a cheap, quickly made payload that could be used for a number of “practice shots” before being discarded was attractive. However, at this time the test site had not yet been decided upon. The possibility that the payload would need to be launched as much as 9 meters into the air was still quite real. During initial testing of the launcher mechanism it was noted that test payloads were considerably off-pitch from their initial orientation on the launcher. Such a variation in the payload pitch at the apex of the payloads path could cause test results to be a poor representation of the real system. Therefore a gyroscopically stabilized payload was thought to be an attractive but expensive option. In the end an approach of several cheap payloads and one gyroscopically stabilized one was thought to be the best option available.

The low cost payload design was constructed as follows. Design requirements were established to be a nominal mass of 4.5 kg, cylindrical in shape, ~15 cm in diameter and ~31 cm tall. The simulated payload was also to be fitted with a mounting plate on the top surface which could be quickly adapted to a variety of booms, cameras and sensor equipment. A design was developed which made use of the appropriate size of schedule 40 pvc pipe, two 15cm by 4.7mm thick aluminum disks, three sections of 8-32 threaded rod and a large cylindrical piece of brass left over from a previous project. (see Figure 5.5-1) Sections of the PVC pipe were cut to the 15cm length and then turned on a lathe so that both sides of the pipe had an internal “shelf” on the inside. The aluminum disks were then drilled for 3 holes 120 degrees apart near the edge of the disk. Threaded rod would be run thru these holes so that the two aluminum disks would be clamped against the shelf in the pipe. In this way the pipe and two disks made a barrel shape. Inside this barrel the brass cylinder was affixed so that it would not move inside the payload during testing. The final payload design was of an appropriate weight, very durable and adaptable to many different hardware systems. Most importantly it could be replicated quickly, easily and cheaply since multiple collisions with the ground eventually destroyed even the most durable payloads.

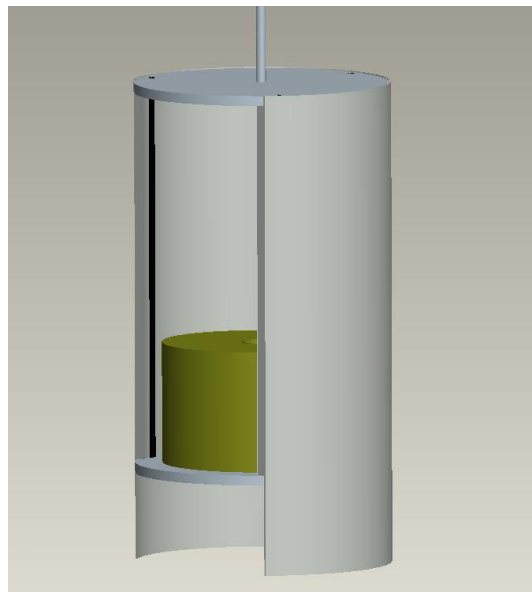


Figure 5.5-1: Base Payload

Gyroscopically stabilized payloads were constructed using the following slightly more complicated procedure. First a section of schedule 40 PVC pipe was cut to length. This pipe was not turned to create a shelf but instead holes were drilled in the sides to allow switches and power recharge ports to be mounted. Two end caps were then turned from a 9.5mm thick aluminum plate. These end caps were cut so that the outer diameter matched the outer diameter of the PVC pipe but a concentric emboss snugly fitted into the open portion of the pipe (see Figure 5.5-2). In this way when the end caps are placed onto either end of the pipe the edges of the pipe are protected by the aluminum end cap. This design proved to be much more durable as the edge of pipe proved to be an area which was vulnerable to collision. The top end cap was then drilled and tapped with three 8-32 holes spread 120 degrees from one another. The bottom end cap was drilled with three corresponding thru holes as well as three material relieves on the bottom side of the end cap. In this way when the nuts are fitted to the bottom end cap they will sink in to the material relief so that the simulated payload will sit on the flat surface of the end cap rather than resting on the nuts. The bottom end cap was also drilled so that it accepted a small bearing in the center of the end cap. A circular center plate was then constructed

from 9.5mm aluminum plate so that it slid snugly into the pipe. This center plate would also be drilled to accept a small bearing in the center and the three corresponding thru holes at 120 degrees from one another. A shaft and small commercial flywheel would be fitted to the bearings between the center plate and bottom end cap so that the flywheel can freely rotate between the two. The center plate would then be modified to accept a small 12V, 1000 rpm DC motor which engages the shaft and in turn spins the flywheel. It is this flywheel which will provide the gyroscopic stabilization. Since the flywheel is a commercially sold product it is balanced for high speeds and wobbled very little in operation. An 18V cordless drill battery was then fitted to the top plate to provide a compact, powerful and durable power supply. Finally the entire payload was assembled using three 8-32 threaded rods. The rods were installed so that they first screwed into the top plate. PVC pipe was then fitted over the rods and top plate. The center plate was then slid over the three rods and held in place by three nuts. These nuts were specially placed on the rods so that when the bottom plate was fitted over the rods the shaft holding the flywheel would be snugly fitted between the top and bottom plates so that the shaft was free to spin but could not jump free of the bearings. Once wired and tested this payload proved to be a very durable and stable test platform.

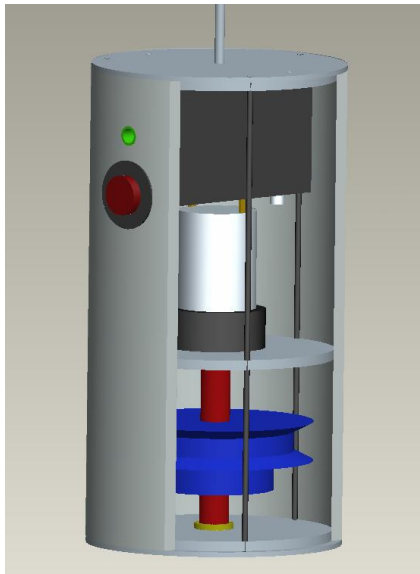


Figure 5.5-2: Payload with Gyroscope Flywheel

5.6 Data Acquisition Methods

Test data for the capture experiment was recorded using a number of video cameras and accelerometers. Video cameras were mounted on the floor of the test area as well as at the top of the scaffolding to provide two separate high resolution viewpoints of the capture. A third and smaller camera was fitted to the tether cable at the point where the four guy wires come together. This “tether cam” was pointed downward at the square formed by the modified iris to provide a bird’s eye view of the capture. A fourth camera was mounted to the payload itself. This camera was mounted to the top plate of the payload and pointed upward towards the boom. In this configuration the “payload cam” provided an up-close view of the capture itself from the perspective of the payload. Accelerometers were fitted to two corner blocks. The two corner blocks were aligned caddy-corner to one another and each block was fitted with two one-dimensional accelerometers. Accelerometers were fitted to the flat faces of the aluminum angle so that they faced 90 degrees to one another in the plane of the square. In this way the sensors could discern the full motion of the collision between iris and payload. One accelerometer was also fitted inside the payload. This accelerometer was aligned vertically to measure the amount of shock that occurred in the payload due to capture.

5.7 Design and Fabrication of the Prototype Capture Mechanism

This section describes the design and fabrication of the scale model capture concept developed by the TTU MXER team. The model is referred to as the modified iris and consists of a large open square shape which is suspended by four guy wires. When the mechanism is triggered gravity is used to draw the mechanism in to progressively smaller squares around a boom extended from a mock payload. As the squares become smaller special plates on the mechanism engage the payload boom and trap it thus affecting a capture. This mechanism was designed and fabricated on the TTU campus by the TTU MXER team.

5.7.1 General Description of the Quad-Trap Operation

The Quad-trap prototype is a working scale model of the modified iris capture concept. This capture concept uses four special booms to create a large open square at the end of the tether. During capture an appendage from the payload moves into the open space created by this square. The modified iris is then triggered and the centripetal acceleration of the tether causes the four booms to swing toward one another causing the square opening to become progressively smaller. As the booms draw closer to one another the payload appendage contacts one of the booms and is directed into one of the corner plates. These corner plates are mounted to special bearing blocks at the corners of the square. The bearing blocks slide along the booms and hold the booms together in their square configuration. As the payload appendage comes into contact with the corner plates it is directed into a special groove in the plate. The corner plates are shaped so that as the modified iris closes on a payload appendage the appendage will settle into this groove. When the modified iris is fully closed the corner plates interlock and the payload appendage is trapped inside the groove formed by the corner plates.

The modified iris prototype works in a similar manner to the full scale modified iris described above. This scale model uses 4, 1m long and 2.5cm diameter aluminum tubes called spreader bars to create an open square. These spreader bars are connected to one another via special corner blocks. Each corner block is equipped with two larger tubes which are arranged 90 degrees from one another and askew using a short section of aluminum angle. The tubes were fitted with roller bearings so that the spreader bars may slide inside each tube. In this way the modified iris can form smaller and smaller squares by sliding the spreader bars in and out thru the corner blocks. A CAD model of the Quad trap is shown in Figure 5.7.1-1 below.

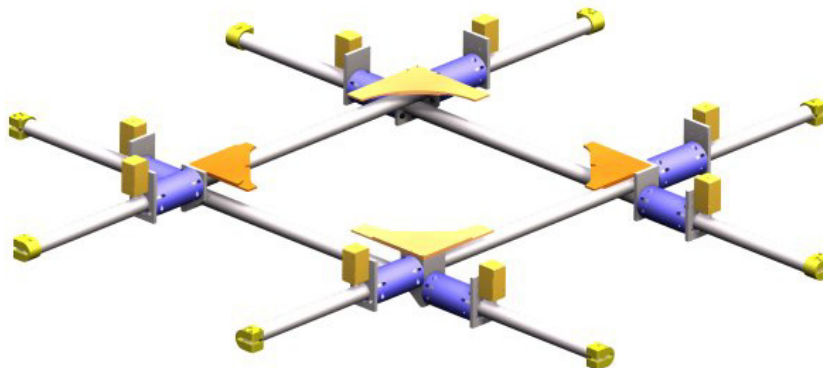


Figure 5.7.1-1: CAD Model of the Quad Trap Mechanism

Each spreader bar was equipped with a special fitting on each end. This fitting was clamped to the end of the spreader bar and has a small detent on the top side. The detent is shaped so that the plunger of a

solenoid, which is bolted to back side of the corner block, fits into the detent and holds the modified iris in the fully open configuration. The details of the actuation system is shown in Figure 5.7.1-2 below.

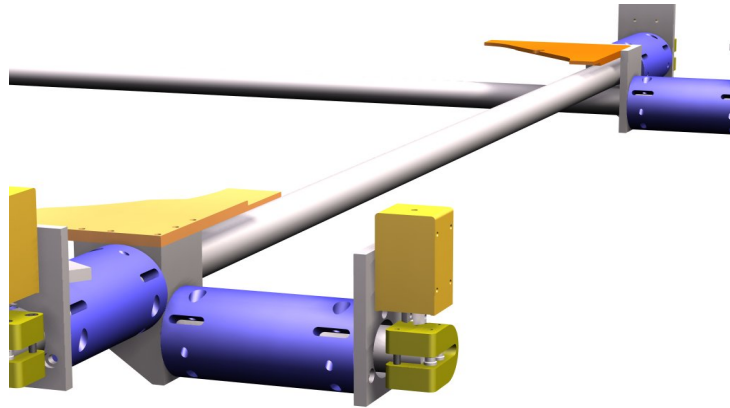


Figure 5.7.1-2: Quad Trap Actuation System

In the fully open configuration the modified iris creates an open square which is 1m wide. The modified iris was then suspended from the ceiling via four cables which were connected to the corner blocks. Because these cables were connected to one another above the center of the square the modified iris mechanism has a natural tendency to swing closed (see model in Figure 5.7.1-3 below).

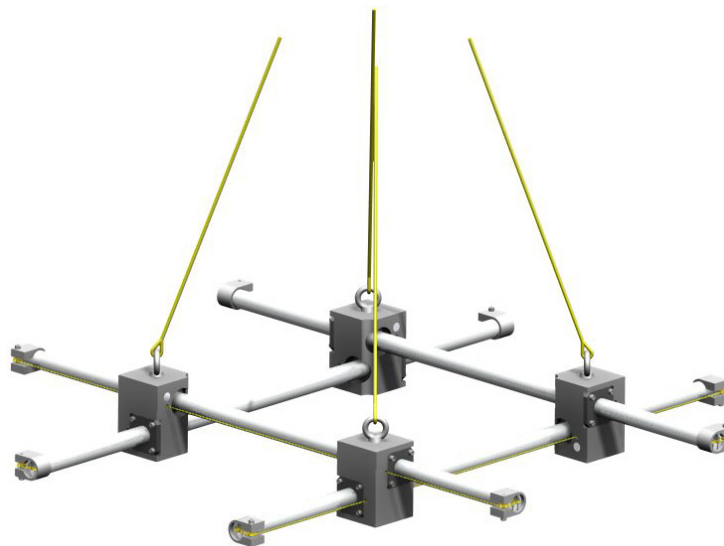


Figure 5.7.1-3: CAD Model of the Quad Trap Mechanism Prototype Attached to the Tether Tip

In fact when the solenoids are activated so that the corner blocks are released from the fitting in the spreader bar the modified iris swings closed. However this swing was not fast enough to represent the behavior expected of the actual system. Therefore springs were hidden inside the spreader bars and cables were routed from the springs to each corner block so that the mechanism will snap shut faster than if it were driven only by gravity. Figures 5.7.1-4 and 5 below show some of the details of this system.

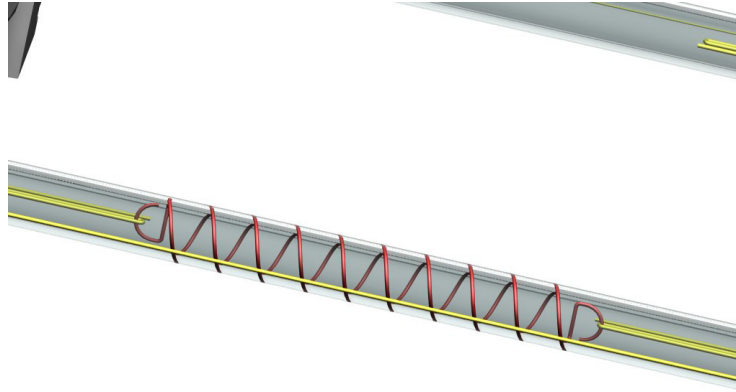


Figure 5.7.1-4: Internal Springs to Assist Closing in Quad Trap Prototype

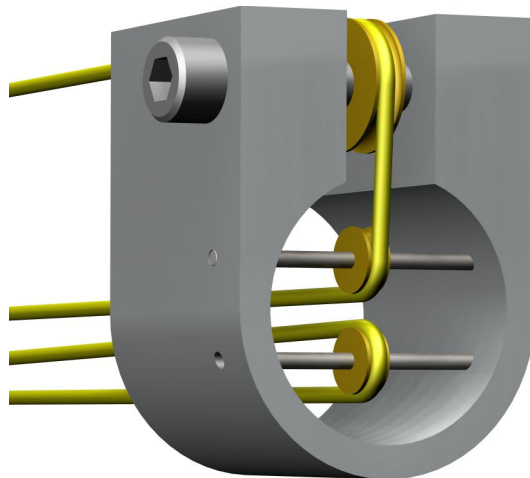


Figure 5.7.1-5: Cable Management System in Quad Trap Prototype

Finally each corner block was fitted with a specially shaped plate. This plate will serve to direct an appendage from the simulated payload away from the spreader bars and into a specially created notch in the center of the plate. The notch serves to trap the payload appendage so that it cannot escape and a capture occurs. These plates are shown in the CAD models of Figures 5.7.1-1, and 2 above.

5.7.2 Detail Drawings of Scale Model

The detailed drawings of the scale model modified iris constructed by the TTU MXER team are provided in Appendix C.

5.7.3 Autonomous Capture Functions: The Automated Capture Control System

The automated capture control system (ACCS) consists of three primary components: a central control unit, a proximity sensory device, and the capture mechanism. The central control unit is comprised of a microcontroller unit (MCU), the MCU power supply, the capture mechanism power supply, and the hardware interface. The prototype configuration utilizes a Motorola HC12 for the MCU, power provided from a single source (Topward 6302D) and an interface for the arming/disarming of the device. The proximity sensor is a Sharp GP2Y0A02YK Infrared Ranger (IR) with a range of 20cm (8in) to 150cm (60in).

The IR sensor is mounted on the PLS launch pad and positioned such that it measures the distance between the aft end of the payload and the launch pad. In this case the location of the payload is measured relative to the launch pad, but since the test setup allows for the launcher to be in a known location relative to the capture mechanism, this is equivalent to measuring the range of the payload from the capture mechanism. After the ACCS is armed, the MCU continuously monitors the range information returned by the IR sensor. This is the only external sensory device on the controller as it has no knowledge of the firing of the PLS aside from the range information returned by the IR sensor. As the payload reaches a preset distance away from the PLS launch pad, the MCU triggers the solenoids on the capture mechanism to release allowing the mechanism to close. After the successful capture has occurred, the ACCS is manually reset to await the next launch. Figure 5.7.3-1 below shows this system in schematic form.

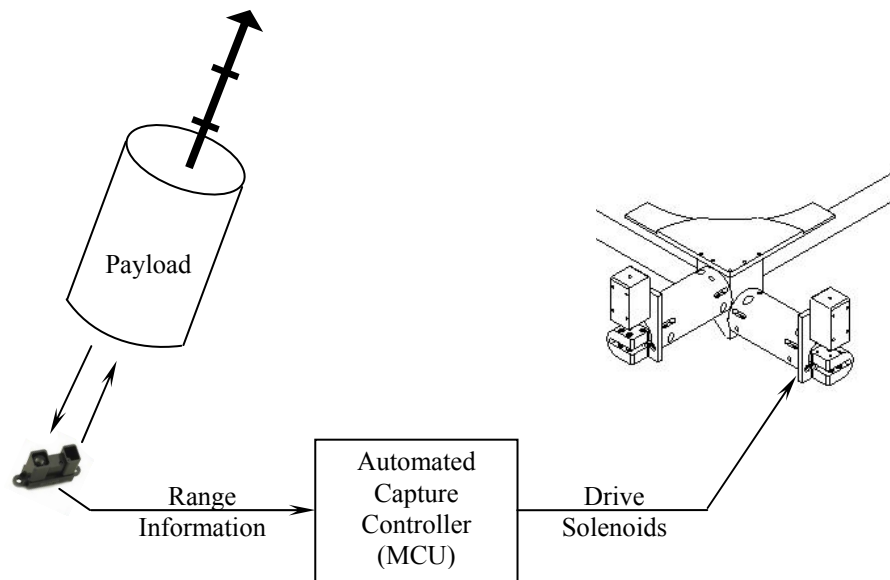


Figure 5.7.3-1: Schematic Representation of the Automated Capture Control System

Procedure for operating the ACCS:

1. Reset capture mechanism to open position, and payload launch mechanism to base launch position
2. Place payload on the launch pad covering the IR ranger
3. Turn on the power to the MCU for the automated capture circuit
4. Perform a reset of the MCU by pressing the reset button
5. Arm the solenoids by flipping the master switch to the upward position
6. Fire the launch mechanism
7. After capture, disable the automated capture electronics by returning both the solenoid arming switch and controller power switch to their off positions

5.8 Perform Testing and Demonstration

(On Proof-of-Concept Prototypes of Capture System Concepts Developed in Task 2.4)

This section describes the physical testing done on the modified iris (TTU), dart (LM) and pat-trap (LM) mechanisms. Each mechanism was tested physically in the TTU capture lab in order to prove out each mechanism and ensure that no aspects of the design had been neglected. The procedure for conducting the tests is summarized and a brief description of the tests done is provided. An account of the test results is also added into this section.

5.8.1 Testing Procedure

The procedure for running capture tests for the modified iris is as follows. Using the ceiling mounted winch the capture mechanism is lowered to a workable height. Two or more people then reload the capture mechanism by retracting the spreader bars to the fully open position and positioning the solenoid plungers into their detent slots locking the mechanism open. The payload is then recovered from the mechanism and reset on the launcher platform. Video recordings and sensors are then reset to their ready positions before the winch is used to lift the capture mechanism to its test height. Safety mechanisms are then deactivated before the video cameras are set to record and the launch program is started. The launch program uses a data acquisition board and a LABVIEW program to fire the launcher, delay for a set period of time and then trigger the capture mechanism. Delay time is varied for each test to represent the positioning tolerance inherent in the MXER capture process. During the entire launch and capture process the LABVIEW program is recording data from all five accelerometers for a total of 15000 samples per test at a sample rate of 500 Hz. Captures are recorded as successful or unsuccessful and the data recorded is stored for later analysis. Safety catches are then restored and the test process is repeated.

The test procedure for the dart mechanism is as follows. A single 1/4-20 bolt is threaded into the provided hole in the rear of the dart mechanism to connect it to the simulated payload. The simulated payload is used with the dart mechanism because the narrow base of the device makes it somewhat unstable during launch. The wider base of the simulated payload helps to stabilize the device in both launch and flight. Use of the simulated payload also reflects a more realistic test scenario. The cables of the net device are checked to ensure that they are all equally tight and no individual strand has worked its way loose. This net device is then suspended from the winch cable and raised to test height. A safety procedure check is conducted before the air compressor is charged and the launcher is aimed for the center of the net. Air pressure is set to its highest level for this test to ensure that the dart will collide with the net with adequate velocity for penetration. The launcher is then fired and the procedure is repeated.

The pat trap mechanism is tested as follows. Four eye bolts are used to suspend the mechanism from the winch cable. Drivers and motors are then connected using the diagram provided with the mechanism. A computer terminal is then connected to the control port of the driver board and power is applied to the driver as per the driver manual. Great care is taken to ensure that the current thru the driver is properly limited. The executable file sent with the mechanism is then opened. That executable file is used to slowly open the trap and hold it in the open position. Using careful hand to eye timing the launcher is manually triggered and the trap closed separately using the executable file provided with the mechanism. Safety catches are then reset and the procedure starts over again.

5.8.2 Brief Summary of Testing Activity

Tests were performed according to a test plan developed based on pragmatic and statistical design of experiment techniques. Outputs for the test were recorded as a capture/fail to capture criterion and a maximum acceleration shock criterion. The test plan and resulting testing processes are summarized on Table 11 below. Details of these tests are contained in the following subsections.

Table 11: Summary of Capture Mechanism Testing Activity

Test Series	Description	Dates	Summary of testing
PLM 1	Payload Launch mechanism testing	7/04-10/04	Used to perfect PLM for use on capture mechanism testing: Approximately 100+ tests performed at varying payloads
QT1	Initial tests of the Quad-trap mechanism	2/05-4/05	Tests demonstrated robust operation of the Quad-trap. Approximately 50 tests performed with > 75% capture rate
QT2	Extended tests of the Quad-trap mechanism, dynamic measurement	5/05-7/05	Tests to collect key acceleration data during capture event on the Quad-trap. Data included 8+ channels of acceleration + 2 channels of video. 10+ tests performed with data captured
Net1	Basic testing of the net mechanism	6/05-9/05	Four test performed before failure of capture mechanism. Capture was successful, significant dynamic transients occurred and resulted in mechanism failure.*
BT1	Basic testing of the Pat-trap mechanism	6/05-9/05	Pat-Trap mechanism tested for static operation (basic trap closure). Trap closure achieved 1 time before failure of drive electronics.*
QT3	Extended dynamic testing of the Quad-Trap mechanism	10/05 – 2/06	Second phased of tests to collect key acceleration data during capture event on the Quad-trap. 15+ tests performed with data captured. Quad-trap mechanism required repair of pulley units prior to these tests
QT4	Autonomous operation of Quad-trap mechanism	2/06-4/06	Implementation of real-time ranging and autonomous operation of the Quad-trap

* Tests on Net1 and BT1 did not receive equivalent implementation period to Quad-trap mechanism by TTU team, and the results should be correspondingly evaluated.

5.8.3 Test Results for the Quad Trap

This section will briefly describe the test cases that were considered for experimental testing and dynamic simulation along with the data collected. First, a brief description of how the quadtrap prototype (and correspondingly the ADAMS model) were instrumented for testing is provided. Instrumentation consists of six accelerometers in three-axis triplets attached to the quadtrap prototype (see Figure 5.8.3-1) and four cameras; two cameras inertially fixed with vertical and horizontal view points, one camera attached to the payload and one camera attached to the quadtrap. The accelerometers are located at the center of mass of opposing corner nodes (see Figure 5.8.3-1) and are aligned such that the z axis corresponds to the vertical while the x and y axes lie in the plane of the trap and are aligned with the spreader bars.

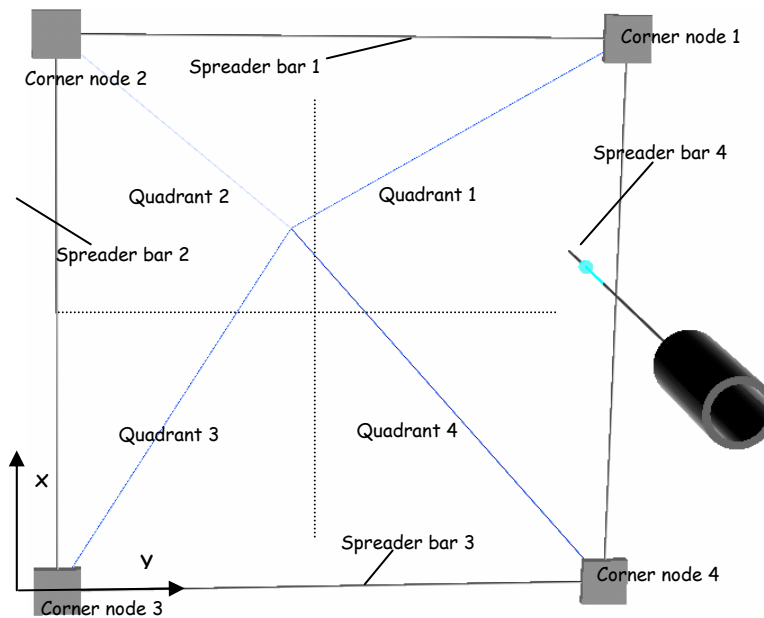


Figure 6: Schematic of quadtrap instrumentation

Figure 5.8.3-1: Schematic of the Quad Trap for Instrumentation

Two tests will be considered to demonstrate the capture process;

Case 1: capture occurs in quadrant 1 (Figure 5.8.3-1)

Case 2: capture occurs in quadrant 3 (Figure 5.8.3-1).

Results from these tests are shown in the following section.

5.8.3.1 Results from Case 1

Case 1 consists of a capture of the payload in quadrant 3. One of the inertially fixed cameras records the position of the payload as it enters the plane of the trap as shown in Figure 5.8.3.1-1. Figures 5.8.3.1-2 and 5.8.3.1-3 show the accelerometer data for nodes 1 and 3 respectively over a duration of time spanning the capture event. Figures 5.8.3.1-4 & 5 show the individual components of accelerations (x , y) for nodes 1 and 3 respectively. Each figure shows both the experimentally collected data along with that predicted by the ADAMS model for this capture case.



Figure 5.8.3.1-1: Image Record of the Case One Test

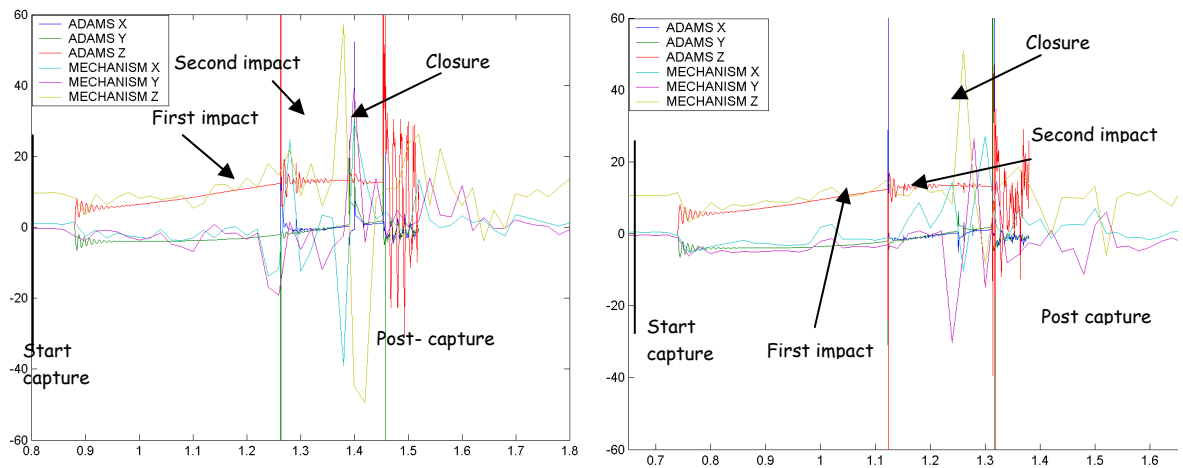


Figure 5.8.3.1-2: (left): X,Y,Z Accelerations for Node 3

Figure 5.8.3.1-3: (right) X,Y,Z Accelerations for Node 1

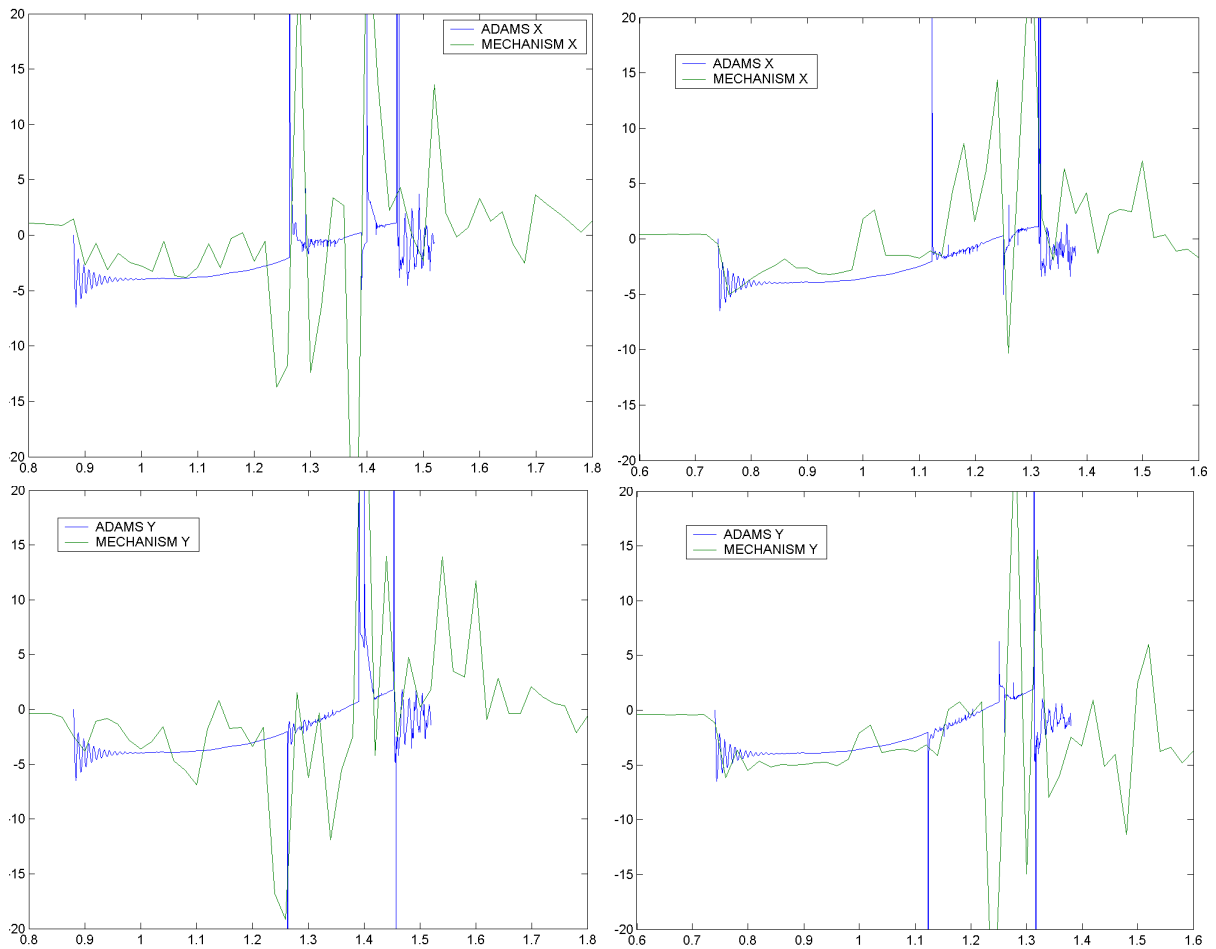


Figure 5.8.3.1-4 (left): X (above), Y (below) Accelerations for Node 3

Figure 5.8.3.1-5 (right) X (above), Y (below) Accelerations for Node 1

5.8.3.2 Results from Case 2

The second case consists of a payload capture in quadrant 4. The position of the payload as it enters the plane of the trap is shown in Figure 5.8.3.2-1. Figures 5.8.3.2-2, 3 show the accelerometer data for nodes 3 and 1 respectively over a duration of time spanning the capture event. Figures 5.8.3.2-4, 5 show the individual components of accelerations for nodes 3 and 1 respectively. Each figure shows both the experimentally collected data along with that predicted by the ADAMS model for this capture case.

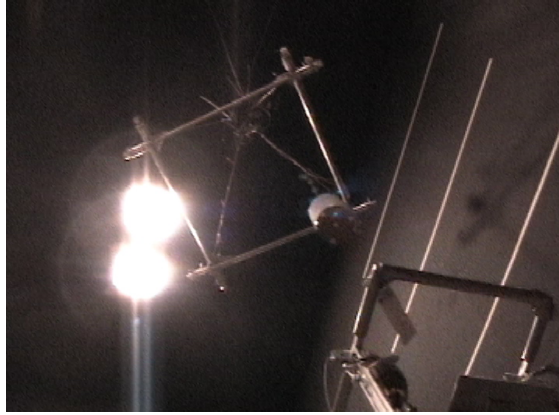


Figure 5.8.3.2-1: Image Record of the Error in the Case 2 Test

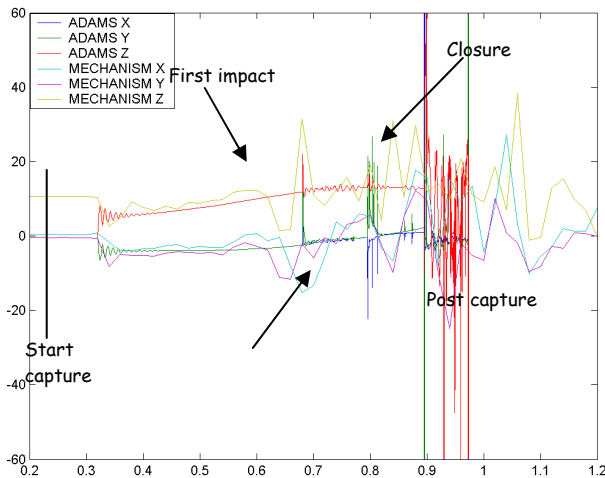


Figure 5.8.3.2-2 (left): X,Y,Z Accelerations for Node 3

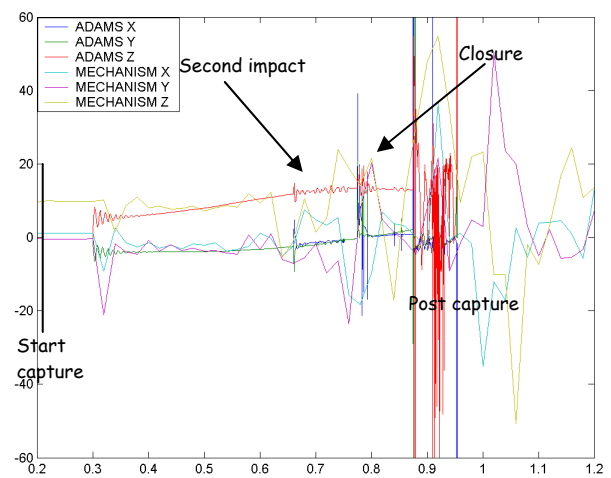


Figure 5.8.3.2-3 (right): X,Y,Z Accelerations for Node 1

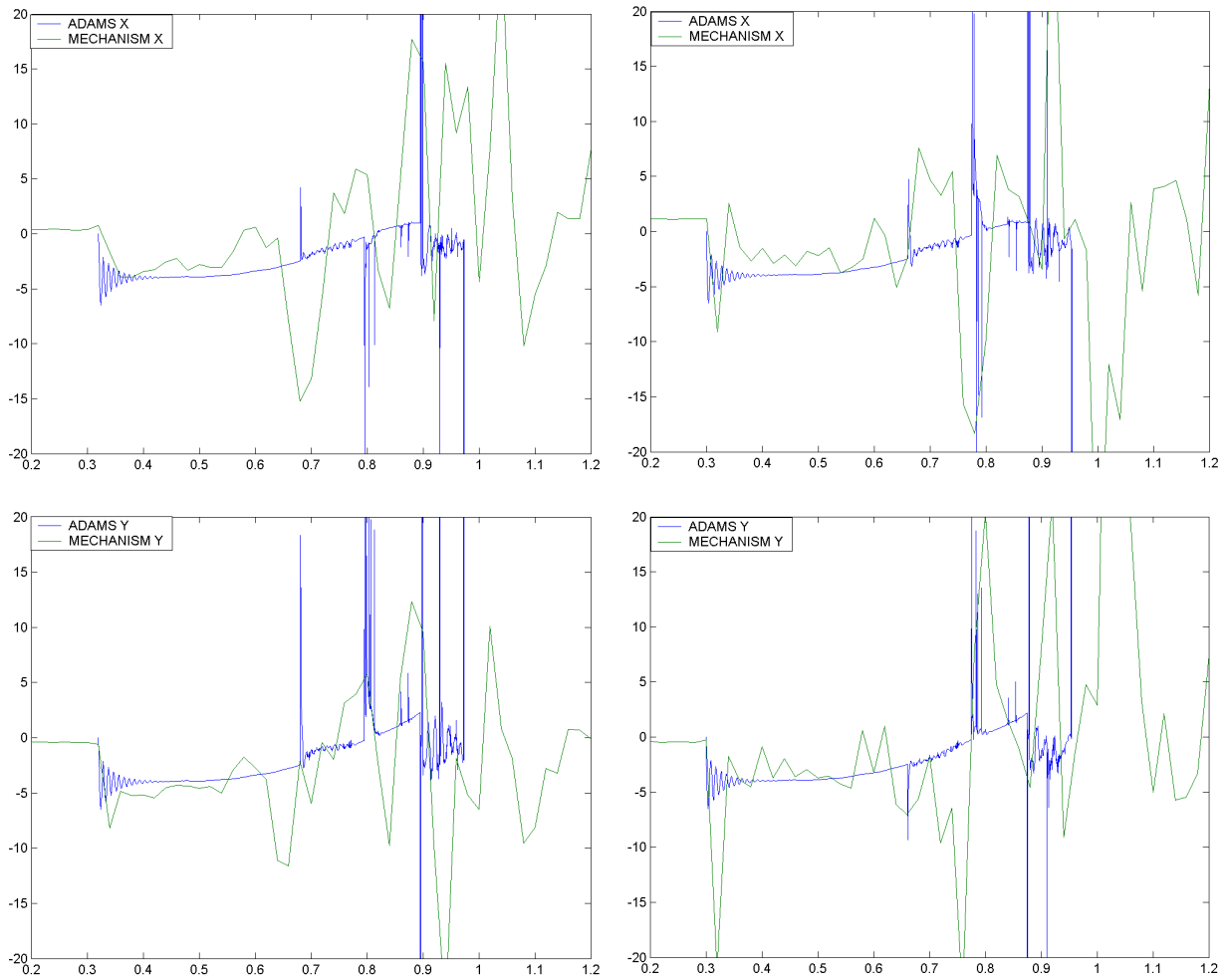


Figure 5.8.3.2-4 (left): X (above), Y (below) Accelerations for Node 3

Figure 5.8.3.2-5 (right): X (above), Y (below) Accelerations for Node 1

5.8.3.3 Discussion of these Results

The dynamic measurements observed in the experimental tests and those provided by model simulation are evaluated both quantitatively and qualitatively for the purposes of demonstrating proof of concept, validating the dynamic model, and providing better understanding of the capture process.

5.8.3.3.1 Observations of the Capture Event

The capture process that was experimentally simulated in the lab and modeled in software can be divided into five stages. The events that divide these stages are labeled on Figures 5.8.3.1-2, 3. The first stage covers the period of time prior to initiation of the capture event. In this stage, the capture mechanism observes a uniform z -component of acceleration due to motion along an accelerating path (simulated in the lab by gravity). The second stage of the capture process starts when the capture event is triggered and the capture mechanism begins to close. The capture mechanism now momentarily moves along a non-accelerating path and the z -component of acceleration goes to zero as the trap begins its motion along a pendular closing path. As the rate of closure increases, the z acceleration increases due to centripetal acceleration about the attachment point to the tether. The x and y axes also observe a sinusoidal component of this acceleration ($\omega^2 r \sin(\theta)$). The third stage begins with the initial impact occurring between the payload-boom and one side of the quadtrap. From the

acceleration response in Figures 5.8.3.1-2 - Figures 5.8.3.1-5 and the photograph in Figures 5.8.3.1-1, it is observed that this first impact occurs between the payload boom and quadtrap spreaderbar #3 (Figures 5.8.3-1). The fourth stage starts with subsequent impact events that may occur during capture; impact between the boom and a second side of the quadtrap, and final closing of the quadtrap. From the acceleration response in Figures 5.8.3.1-2 - Figures 5.8.3.1-5, it is observed that the second impact occurs between the payload boom and quadtrap spreaderbar #2 (Figures 5.8.3-1). Final closing of the trap is not as distinct in Fig. 8. The final stage covers the period of time after capture. During this time, transient vibrations die out and the capture mechanism and captured payload observe steady acceleration in the z direction.

5.8.3.3.2 Comparisons with the dynamic model

Based on this quantitative comparison of results over the series of events that define the capture process the model simulation is seen to correspond well with the experimental data collected. The order and nature of dynamic behavior over the series of capture events are in good agreement. The expected direction of dynamic response are consistent and the magnitudes conform (within approximately 10% over many portions of the capture process). Some discontinuities are also observed between the experimental and simulation results. First, some degree of variation in the timing of events is observed, such as time of the first and second impact events. This is due in part to the ability to estimate the error in payload position for a given experimental trial, and the inability to accurately represent all energy losses in the prototype system. The second variation observed is the degree of transient or higher-order dynamic phenomena seen in the experimental results, but not the model. Again, this is attributed to the imprecise nature of the prototype, in particular issues such as chatter, non-perfect bearings and a non-perfect inelastic collision as predicted in the ADAMS model. Damping was added to the dynamic model to mimic the friction introduced by the bearings and other such components, but an accurate measurement of the amount of damping needed has not been performed at this point. Third, some variation in the magnitude of z axis acceleration observed during the impact process. Again, this is attributed to the variable location at which the boom penetrates the x - y plane of the trap and the variation in vertical error of the experimental system. In some capture experiments, the payload is trapped while still rising relative to the trap (causing a positive z acceleration) and in other cases the payload is falling when capture, causing a negative z acceleration on the quadtrap.

5.8.3.3.3 General observations on the capture process

Some final observations are made on the conceptual design and the capture process. Based on the predicted error window and the experimental tests that were performed over this predicted range of error, the quadtrap capture mechanism proved surprisingly robust at performing the capture process. Capture with some degree of error (position or velocity) results in one or more impact events between the payload boom and the sides of the quadtrap. However, these events take place between components of relatively low mass (the quadtrap and payload boom) and therefore limit negative overall effects on the system. The acceleration forces observed on the quadtrap at times were quite high, at levels up to 6-7 g, but these impacts are experienced to a much lesser degree on the payload. Similarly, the impact forces between the payload boom and quadtrap spreader bars in some cases were significant, but were well within the design criteria specified for the capture mechanism. The payload boom in general must be the lightest possible device that could deploy in a reduced gravity environment, and could be damaged in the capture process. However, the payload boom has a one-time use and thus plastic deformation is not necessarily a critical factor. Some degree of plastic deformation was observed in the payload boom. It was observed over a significant number of tests that the system is robust to both positional error as well as timing of the release of the capture

mechanism. However, proper timing of the capture mechanism can reduce the dynamic impact of the capture process making the capture mechanism more effective.

5.8.4 Test Results for the Harpoon and Net (LM)

A total of four tests were conducted using this mechanism and three of those tests were successful captures. Tests were set up so that there was a great deal of differential velocity between the dart and net. In the single failed test the dart mechanism failed to penetrate the net and therefore had no opportunity to snag. Two of the tests snagged the net with three fingers where a third snagged the net with only two. The number of tests was limited to four because the fourth test broke the cable suspending the net and testing was discontinued in lieu of repairs.

5.8.5 Test Results for the PatTrap (LM)

Testing of the PatTrap mechanism consisting of static, ground-level testing of open/closing operation for the device. Approximately one open/close cycle was performed before a failure occurred in the drive electronics. The drive electronics were repaired (purchase of a new driver) for continued static testing. The second failure occurred almost immediately with a combination failure of the new driver and the mechanical mounts for one drive-train mechanism.

SECTION B—DYNAMIC MODELS FOR MXER TETHER SYSTEMS

Table of Contents

1.0 DEVELOPMENT OF THE MXER TETHER SYSTEM	80
1.1 OVERVIEW	80
1.2 EQUATIONS OF MOTION FOR ELASTIC BODY TETHER	80
1.2.1 Strain Formulation	80
1.2.2 Reference Coordinate System	81
1.2.3 Tether Geometry	82
1.2.4 Equations of Motion from Newton's Second Law	84
1.2.5 Forms of Equations of Motion	85
1.2.6 Application to Variable Length Tether	90
1.3 COMPARE WITH BEAD & SPRING MODELS	92
1.4 ALTERNATIVE REFERENCE COORDINATE SYSTEM	92
1.5 TETHER DAMPING, STRAIN-RATE-PROPORTIONAL DAMPING (MATERIAL)	95
2.0 VALIDATION OF TETHER SYSTEM MODELS	96
2.1 PROCEDURE	97
2.2 RESULTS OF TYPE A COMPARISONS	99
2.2.1 Case 1	99
2.2.2 Case 2	103
2.2.3 Case 3	105
2.2.4 Case 4	106
2.3 VALIDATION RESULTS FOR TYPE-B CASES	108
2.4 DISCUSSION OF RESULTS	113
3.0 BASIC IMPLEMENTATION AND DEMONSTRATION	115
3.1 TETHER DYNAMIC MODELS	115
4.0 BASIC APPLICATION OF THE DYNAMIC MODEL	120
5.0 DEVELOP INITIAL AND BOUNDARY CONDITION MODELS	121
6.0 RESULTS AND CONCLUSIONS:	123

List of Figures

Figure 1.2.1-1: Tether in Displaced and Deformed Condition	80
Figure 1.2.1-2: Displacement of Tether Element.....	80
Figure 1.2.1-3: Tether Element Geometry	81
Figure 1.2.2-1: Tether System.....	82
Figure 1.2.3-1: Tether Frame (u,v,w) and Base Frame (x,y,z).....	83
Figure 1.2.3-2: Tether System with Frames.....	84
Figure 1.2.4-1: FBD of Tether Element	84
Figure 1.2.5.1.3-1: FBD of End-Body on Tether System	87
Figure 1.2.5.1.3-2: FBD of End-Body on Tether System with Tether Reeling	87
Figure 2.2.1-1: Comparision of String Solution of Wave Equation and FD Code	100
Figure 2.2.1-2: Difference in Displacement of String Solution of Wave Equation and FD Code.....	100
Figure 2.2.1-3: Comparision of String Solution of Wave Equation and FD Code	101
Figure 2.2.1-4: Difference in Displacement of String Solution of Wave Equation and FD Code.....	101
Figure 2.2.1-5: Comparision of String Solution of Wave Equation and FD Code	102
Figure 2.2.1-6: Difference in Displacement of String Solution of Wave Equation and FD Code.....	102
Figure 2.2.2-1: Nodal Convergence for 3 Point FD Formulation	103
Figure 2.2.2-1a: Nodal Convergence for 3 Point FD Formulation	104
Figure 2.2.2-2: Difference in Nodal Convergence for 3 Point FD Formulation.....	104
Figure 2.2.2-2a: Difference in Nodal Convergence for 3 Point FD Formulation	105
Figure 2.2.3-1: Comparison of 4 th Order RK and ABM FD Code.....	106
Figure 2.2.3-2: Difference in Displacement of 4th Order RK and ABM FD Code	106
Figure 2.2.4-1: Comparison of 3 and 5 Point FD Code	107
Figure 2.2.4-2: Difference in Displacement of 3 and 5 Point FD Code.....	107
Figure 2.3-1: Average Tether Length over Case 5a.....	109
Figure 2.3-2: Mid and Quarter Node Vibration, Case 5a.....	110
Figure 2.3-3: Average Tether Length over Case 5b.....	110
Figure 2.3-4: Mid and Quarter Node Vibration, Case 5b	111
Figure 2.3-5: Average Tether Length over Case 5c.....	111
Figure 2.3-6: Mid and Quarter Node Vibration, Case 5c.....	112
Figure 2.3-7: Orbit of Tether Center of Mass, Case 6.....	112
Figure 2.3-8: Average Length of Tether, Case 6.....	113
Figure 2.3-9: Mid and Quarter Node Vibration, Case 6	113
Figure 3.1-1: Flow Chart, General Tether Dynamics Integration.....	116
Figure 3.1-2: Flow Chart, Overview of Runge Kutta Routine.....	117
Figure 3.1-3: Flow Chart, Details of 4th Order Runge Kutta	117
Figure 3.1-4: Flow Chart, Overview of 3-Point Spatial Difference Routine	118
Figure 3.1-5: Flow Chart, Obtaining Tether Force Components	119
Figure 3.1-6: Flow Chart, Adams-Bashfort Mouton Integration	119
Figure 3.1-7: Flow Chart, Obtain Initial Conditions.....	120
Figure 5.0-2: Free Body Diagram of Tether Element	121
Figure 5.0-3: Tether Strain Over Length for Steady State Initial Condition	123

List of Tables

Table 1: State versus Time	97
Table 2: Validation Cases versus Model Formulation	98
Table 3: Parameters for Representative MXER Application	99

1.0 DEVELOPMENT OF THE MXER TETHER SYSTEM

(For Dynamic Model and Algorithms)

1.1 Overview

The following provides discussion of an approach to tether dynamic modeling process and numerical analysis that derives the governing equations of a continuous elastic system representing the tether. Every attempt will be made to describe the scope as well as assumptions and limitations of each step of this algorithm.

1.2 Equations of Motion for Elastic Body Tether

A derivation of the equations of motion followed by a discussion of various solution procedures will be presented here for a continuous elastic space tether.

1.2.1 Strain Formulation

Consider an elastic space tether as shown in Figure 1.2.1-1. In this model, the tether is represented as a one-dimensional object moving in Euclidean space. Consider the tether in both an undisplaced and displaced condition as shown in Figure 1.2.1-1.

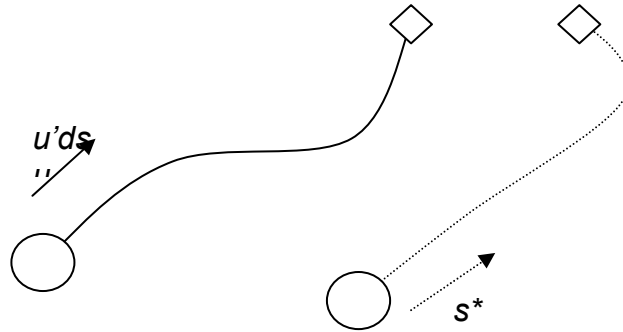


Figure 1.2.1-1: Tether in Displaced and Deformed Condition

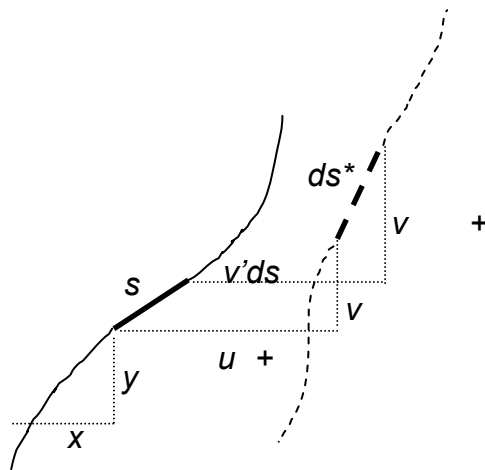


Figure 1.2.1-2: Displacement of Tether Element

In this figure, two metrics for parameterization are shown, s , a material coordinate and s^* , a geometric coordinate. The coordinate s is invariant with respect to space and time while the geometric

coordinate s^* is uniform with respect to geometric or deformed length. Due to static and dynamic forces on the tether, the tether undergoes a combination of rigid body and elastic displacements. The displacement of a small element from ds to ds^* is shown in Figure 1.2.1-2, where u , v and w represent displacements in the x , y and z (not shown) directions respectively and a trailing prime indicates partial derivatives with respect to space (geometrical space coordinate). The geometry of the displaced element can be defined as shown in Figure 1.2.1-3.

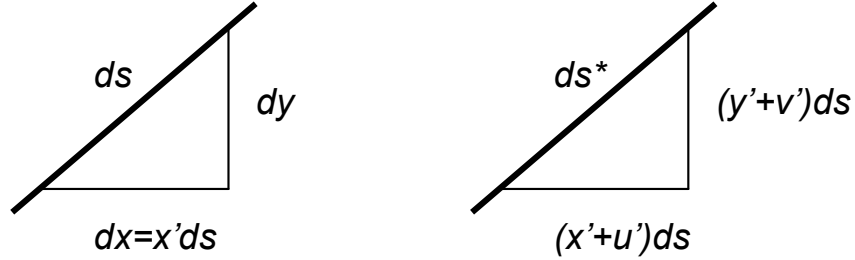


Figure 1.2.1-3: Tether Element Geometry

The length of this tether element can be defined as,

$$ds^* = \sqrt{(x'+u')^2 + (y'+v')^2 + (z'+w')^2} ds \quad 1$$

where again s is the coordinate based on the tether material, while s^* is the coordinate based on current tether length. From these equations, the total length of the tether can be determined at any time as,

$$l^* = \int_{s=0}^{s=l} \sqrt{(x'+u')^2 + (y'+v')^2 + (z'+w')^2} ds. \quad 2$$

The strain can be defined at any point along the tether as a function of tether element displacement. An engineering strain definition will first be implemented for the tether as,

$$\varepsilon(s,t) = \frac{ds^* - ds}{ds} = \frac{ds^*}{ds} - 1. \quad 3$$

with ε the strain given as a function of space and time. The ratio of stretched to original element length, $\frac{ds^*}{ds}$, will be defined as η with $\eta = \sqrt{(x'+u')^2 + (y'+v')^2 + (z'+w')^2}$. η gives a relation between the element differentials, $ds^* = \eta \cdot ds$.

1.2.2 Reference Coordinate System

First consider an reference system based on the coordinate, $\mathbf{r}(s,t)$ which will represent the tether position with respect to an inertial reference frame (selected as an earth-centered, non rotating frame, (Figure 1.2.2-1), defined as;

$$\begin{aligned} \mathbf{r}(s,t) &= \{ (x+u)\hat{i}, (y+v)\hat{j}, (z+w)\hat{k} \} \\ \mathbf{r}'(s,t) &= \{ (x'+u')\hat{i}, (y'+v')\hat{j}, (z'+w')\hat{k} \} \end{aligned} \quad \text{Eq. 4a}$$

or

$$r_x' = (x'+u'), r_y' = (y'+v'), r_z' = (z'+w') \quad 4b$$

With $\mathbf{r} = \mathbf{r}(s,t)$ the primary parameter describing the tether with respect to space and time, the strain equation can be written as:

$$\varepsilon(s,t) = \eta - 1$$

with

$$\eta = \sqrt{(r'_x)^2 + (r'_y)^2 + (r'_z)^2}$$

4c

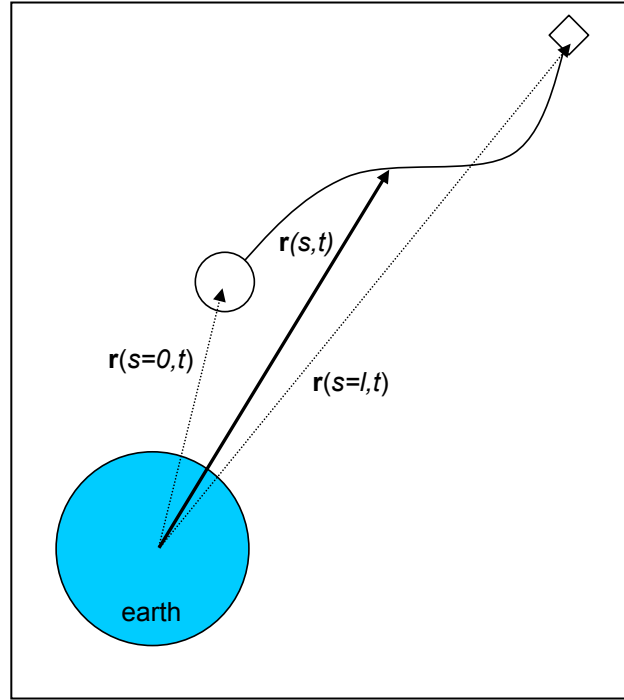


Figure 1.2.2-1: Tether System

1.2.3 Tether Geometry

This section will describe the process of making transformations between the tether frame and the base (fixed) frame or coordinate system¹. Consider an inertial base frame, $\{\mathbf{B}\}$ (x,y,z), and a tether-fixed frame, $\{\mathbf{T}\}$ (u,v,w) such that $u(s,t)$ is the tether tangential direction at s , $v(s,t)$ is the tether radius of curvature direction at s and $w(s,t)$ defined to complete the right hand frame (fig. 5). The tether tangential is given in \mathbf{r}' (called χ) while the tether radius of curvature is given as $(\mathbf{r}'' = \chi')$. The magnitudes of χ and χ' are defined as η and κ respectively

($\eta = \sqrt{\chi_x'^2 + \chi_y'^2 + \chi_z'^2}$, $\kappa = \sqrt{\chi_x'^2 + \chi_y'^2 + \chi_z'^2}$). Then, for the general case of tether orientation in space, the tether frame orientation with respect to the base frame is defined by the rotation $\mathbf{R}_{\mathbf{B}}^{\mathbf{T}}$ (see Figure 1.2.3-1 below) This rotation matrix (defined to be a member of valid homogenous rotation matrices) is given as,

¹ Certain parameters will be easier to describe first in the tether frame, such as internal tether forces/moments and tether mass moment of inertia, and then converted to the base frame (all motion must be described with respect to an inertial or Newtonian frame for later developments).

$$\mathbf{R}_B^T = \begin{bmatrix} r'_x/\eta & \chi'_x/\kappa & \sqrt{1 - \left(\left(r'_x/\eta \right)^2 + \left(\chi'_x/\kappa \right)^2 \right)} \\ r'_y/\eta & \chi'_y/\kappa & \sqrt{1 - \left(\left(r'_y/\eta \right)^2 + \left(\chi'_y/\kappa \right)^2 \right)} \\ r'_z/\eta & \chi'_z/\kappa & \sqrt{1 - \left(\left(r'_z/\eta \right)^2 + \left(\chi'_z/\kappa \right)^2 \right)} \end{bmatrix}. \quad 5a$$

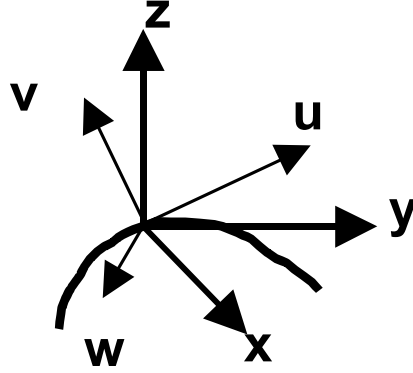


Figure 1.2.3-1: Tether Frame (u,v,w) and Base Frame (x,y,z)

The rotation from fixed to tether frame can equally be defined as the Euler $(\theta, -\phi, \gamma; w, v, u)$ rotation set,

$$\mathbf{R}_B^T = \begin{bmatrix} c\theta c\phi & -s\theta c\gamma - c\theta s\phi s\gamma & s\theta s\gamma - c\theta s\phi c\gamma \\ s\theta s\phi & c\theta c\gamma - s\theta s\phi s\gamma & -c\theta s\gamma - s\theta s\phi c\gamma \\ s\phi & c\phi s\gamma & c\phi c\gamma \end{bmatrix}. \quad 5b$$

The derivation is readily seen based on the fact that projections of the tether tangent onto the fixed frame are (r'_x, r'_y, r'_z) and the projections of the tether curvature direction onto the fixed frame are $(\chi'_x, \chi'_y, \chi'_z)$.

For this geometry, a number of special cases may exist. For example, the case of planar motion, or motion in which the tether tangent and curvature vectors lie in the orbital plane (with x, y defining the orbital plane) is considered. In this case, angles ϕ and γ in equation 5b are both zero, allowing the rotation matrix to become,

$$\mathbf{R}_B^T = \begin{bmatrix} r'_x/\eta & -r'_y/\eta & 0 \\ r'_y/\eta & r'_x/\eta & 0 \\ 0 & 0 & 1 \end{bmatrix} \quad 6$$

An example of use of this homogenous transformation is provided. Consider the reaction forces, \mathbf{P} at a point along the tether consisting of an axial (tangential) force, N in the \mathbf{u} direction, an in-plane shear

force acting in the direction of curvature (\mathbf{v}) as Q , and an out of plane force O acting in the \mathbf{w} direction. This reaction set can be resolved into the base coordinate system as,

$$\mathbf{P}_B = \mathbf{R}_B^T \mathbf{P}_T = \begin{bmatrix} \frac{r'_x}{\eta} & -\frac{r'_y}{\eta} & 0 \\ \frac{r'_y}{\eta} & \frac{r'_x}{\eta} & 0 \\ 0 & 0 & 1 \end{bmatrix} \begin{Bmatrix} N \\ Q \\ O \end{Bmatrix} = \begin{Bmatrix} N \frac{r'_x}{\eta} - Q \frac{r'_y}{\eta} \\ N \frac{r'_y}{\eta} + Q \frac{r'_x}{\eta} \\ O \end{Bmatrix} \quad 7$$

Figure 1.2.3-2 shows the tether with base and tether frames attached. For purposes of this work, the inertial frame $\{\mathbf{B}\}$ can be given as any convenient “near inertial” frame, such as an ecliptical coordinate system or equatorial coordinate system.

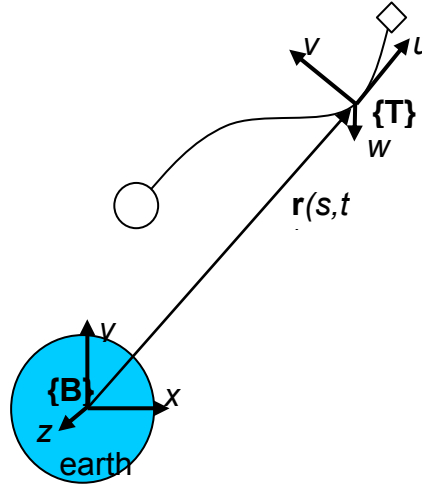


Figure 1.2.3-2: Tether System with Frames

1.2.4 Equations of Motion from Newton's Second Law

A free-body diagram (fbd) of an element of stretched length, ηds of the tether is shown in Figure 1.2.4-1. This element undergoes a combination of distributed and concentrated forces.

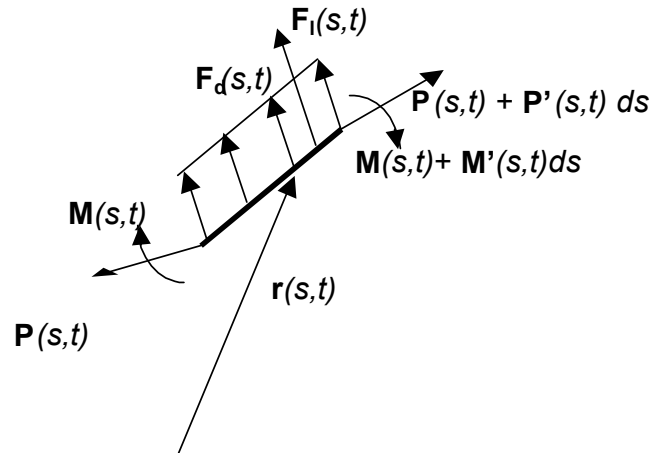


Figure 1.2.4-1: FBD of Tether Element

The forces acting on the element are summed and set equal to the time derivative of linear momentum,

$$\frac{d}{dt}(\rho A ds \partial \mathbf{r} / \partial t) = \mathbf{P} + \frac{\partial \mathbf{P}}{\partial s} ds - \mathbf{P} + \mathbf{F}_d \eta ds + \mathbf{F}_l \quad 8a$$

or

$$\rho A \ddot{\mathbf{r}} = \mathbf{P}' + \mathbf{F} \eta \quad 8b$$

which assumes that ρ and A are functions of space but not functions of time, \mathbf{r} , \mathbf{P} , \mathbf{F}_d , \mathbf{F}_l , and \mathbf{F} are functions of space and time and an over dot represents derivatives with respect to time and a trailing prime representing derivatives with respect to space (the material space coordinate). Note that \mathbf{F} represents the resultant of the external forces given on a per length basis ($\mathbf{F} = \mathbf{F}_d + \mathbf{F}_l / (\eta ds)$). These forces will consist of a combination of gravity, electrodynamic drag, aerodynamic drag and the like. In a similar manner, the sum of moments acting about one end of the tether are evaluated,

$$\frac{1}{2} \frac{\partial \mathbf{r}}{\partial s} ds \times (\rho A ds \partial^2 \mathbf{r} / \partial t^2) + d\mathbf{I} \boldsymbol{\alpha} + \boldsymbol{\omega} \times d\mathbf{I} \boldsymbol{\omega} = (\mathbf{M} + \frac{\partial \mathbf{M}}{\partial s} ds) - \mathbf{M} + \frac{\partial \mathbf{r}}{\partial s} ds \times (\mathbf{P} + \frac{\partial \mathbf{P}}{\partial s} ds) + \frac{1}{2} \frac{\partial \mathbf{r}}{\partial s} ds \times \mathbf{F} ds \quad 9a$$

or

$$\frac{1}{2} \mathbf{r}' \times (\rho A \ddot{\mathbf{r}}) ds^2 + d\mathbf{I} \boldsymbol{\alpha} + \boldsymbol{\omega} \times d\mathbf{I} \boldsymbol{\omega} = \mathbf{M}' ds + \mathbf{r}' ds \times (\mathbf{P} + \mathbf{P}' ds) + \frac{1}{2} \mathbf{r}' \times \mathbf{F}(s, t) ds^2 \quad 9b$$

where parameters \mathbf{r} , \mathbf{P} , \mathbf{F} , \mathbf{M} , \mathbf{I} , $\boldsymbol{\alpha}$, and $\boldsymbol{\omega}$ remain functions of space and time and ρ and A are functions of space only. Note that in Eq. 9 that the resultant force is assumed to act at the center of the element. Equations 8 and 9 represent general equations of motion for the tether element.

1.2.5 Forms of Equations of Motion

The following sections will provide several reduced forms of these equations. The following cases will be presented. Case 1) will consider tangential loading only within the tether (tether carries no bending or shear) and will assume the tether mass to be lumped at the element center. Case 2) will extend case 1) and will consider tangential as well as shear and bending loads, all occurring within an orbital plane (each end of the element considered to have three dof). Case 3) will add the potential for torsion to case 2 as well as consider mass moments of inertia of the element. Case 4) will consider a case of spatial force and bending (six dof at each end of the element).

1.2.5.1 Case 1) Tether with Tangential Loads Only

The equations 8 and 9 are first reduced first by dropping all higher order space derivative terms, and assuming the element such that $d\mathbf{I}$ is negligible. This yields,

$$\rho A \ddot{\mathbf{r}} = \mathbf{P}' + \mathbf{F} \eta \quad 10a$$

$$\mathbf{0} = \mathbf{M}' + \mathbf{r}' \times \mathbf{P} \quad 10b$$

In case 1, the tether is assumed to carry axial loads only (behaves as a string). In such a case, the element reaction end load \mathbf{P} is given as,

$$\mathbf{P} = N \mathbf{u}$$

where N is the magnitude of the tensile force and \mathbf{u} represents the tether tangential direction (the direction of \mathbf{r}'). Equation 10b then vanishes, while Eq. 8b can be written in scalar form for the base coordinate system, x, y, z using the rotation operator of Eq. 5a as,

$$\rho A \ddot{r}_k = \left(N \frac{r'_k}{\eta} \right)' + F_k \eta, \quad k = x, y, z. \quad 11$$

where N , the tensile force is defined from the tether material constitutive relation as,

$$N = EA \varepsilon = EA(\eta - 1) \quad 12$$

where E and A are functions of space, and ε and η are functions of space and time. Thus Eq. 11 becomes:

$$\rho A \ddot{r}_k = \left(\frac{EA(\eta-1)r_k'}{\eta} \right)' + F_k \eta, \quad k = x, y, z. \quad 13$$

with the function η given in Eq. 4c as,

$$\eta = \sqrt{r_x'^2 + r_y'^2 + r_z'^2} \quad 14$$

Equation 13 represents three, second-order partial differential equations (pde) in space and time that can be solved in terms of the unknowns, $r_x(s, t)$, $r_y(s, t)$ and $r_z(s, t)$. The solution to this boundary value problem requires initial conditions of the state and two boundary conditions to be specified. A discussion of general solution approaches for this pde is discussed in a later section.

1.2.5.1.1 Expand Partial Differential Equations of Motion

The partial differential equations developed in Eq. 13 are expanded to yield the following set of relations,

$$\rho A \ddot{r}_k = EA[\eta' r_k' + \eta(\eta-1)r_k'']\eta^{-2} + F_k \eta, \quad k = x, y, z \quad 15$$

with,

$$\eta' = [r_x' r_x'' + r_y' r_y'' + r_z' r_z'']\eta^{-1} \quad 15a$$

In this expansion, ρ and A remain functions of s , but A' is assumed to be 0. Equation 15 clearly shows the order (second order in space and time) as well as the nonlinearities of this problem.

1.2.5.1.2 State-Space Partitioning

A state-space representation of these partial differential equations of motion is constructed to result in a $3n$ first order equations of motion (where n is the number of second order equations of motion). The third set of equations is based on the time derivative of χ . This state-space vector is defined as,

$$\mathbf{X} = \begin{Bmatrix} \mathbf{r} \\ \mathbf{v} \\ \chi \end{Bmatrix} = \begin{Bmatrix} \mathbf{r} \\ \partial \mathbf{r} / \partial t \\ \partial \mathbf{r} / \partial s \end{Bmatrix} \quad 16$$

The equations of motion can then be written as;

$$\dot{\mathbf{X}} = \begin{Bmatrix} \dot{\mathbf{r}} \\ \dot{\mathbf{v}} \\ \dot{\chi} \end{Bmatrix} = \begin{Bmatrix} \mathbf{v} \\ \frac{1}{\rho A} \left[(EA(\eta-1)\mathbf{r}' / \eta)' + \mathbf{F} \eta \right] \\ \mathbf{v}' \end{Bmatrix} \quad 17$$

where the third set of relations is derived from the assumption that tether motion is separable in space and time, or $\frac{\partial^2 \mathbf{r}}{\partial s \partial t} = \frac{\partial^2 \mathbf{r}}{\partial t \partial s}$. The expanded relations in Eq. 15 can be written as,

$$\rho A \dot{v}_k = EA[\eta' \chi_k + \eta_k(\eta-1)\chi']\eta^{-2} + F_k \eta, \quad k = x, y, z \quad 18$$

with,

$$\eta' = [\chi_x \chi_x' + \chi_y \chi_y' + \chi_z \chi_z']\eta^{-1} \quad 18a$$

$$\eta = \sqrt{\chi_x^2 + \chi_y^2 + \chi_z^2} \quad 18b$$

1.2.5.1.3 Boundary Conditions

Two boundary conditions are required for the second-order pde tether model. In the MXER tether model, the tether boundaries consist of end-bodies whose dynamics are coupled with those of the

tether. Therefore, the boundary conditions are defined from the equations of motion of the end-bodies. Consider first the case in which the end-bodies are attached to the end of a fixed-length tether. A free-body diagram of a general end-body is shown in the following Figure 1.2.5.1.3-1.

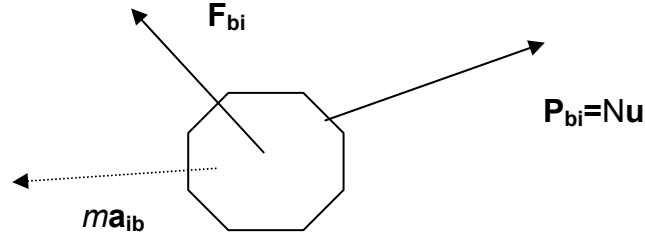


Figure 1.2.5.1.3-1: FBD of End-Body on Tether System

$$ma_{bi} = F_{bi} + P_{bi} \quad \text{BC. 1a}$$

Thus, the tether end-load is given as $-P_{bi}$ at $s=0, l$ or,

$$m_{b1}a_{b1} = F_{b1} + N(0,t)u(0,t) \quad \text{BC. 1b}$$

$$m_{b2}a_{b2} = F_{b2} - N(l,t)u(l,t) \quad \text{BC. 1c}$$

Next, consider the case in which the tether length is varied by reeling tether either in or out of the end bodies. In this case, the boundary conditions must account for this state of mass flow of tether, as given in the following equations, (see Figure 1.2.5.1.3-2,)

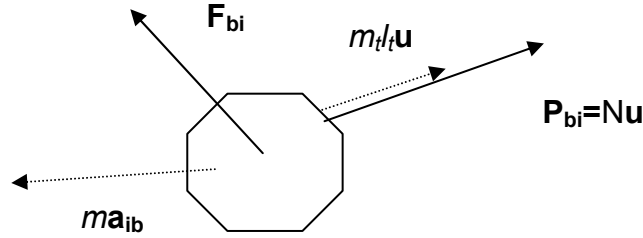


Figure 1.2.5.1.3-2: FBD of End-Body on Tether System with Tether Reeling

$$m_{b1}a_{b1} = -\dot{m}(0,t)l(0,t)u(0,t) + F_{b1} + N(0,t)u(0,t) \quad \text{BC. 2a}$$

or

$$m_{b1}a_{b1} = -\frac{\rho A l^2 \chi}{\eta} \Big|_{(0,t)} + F_{b1} + \frac{EA(\eta-1)\chi}{\eta} \Big|_{(0,t)} \quad \text{BC. 2b}$$

$$m_{b2}a_{b2} = -\frac{\rho A l^2 \chi}{\eta} \Big|_{(l,t)} + F_{b2} + \frac{EA(\eta-1)\chi}{\eta} \Big|_{(l,t)} \quad \text{BC. 2c}$$

1.2.5.2 Case 2) Tether with Bending in the Orbital Plane

Case 2 considers the tether with both axial and bending stiffness, all acting in the orbital plane. In such an example the element end reaction \mathbf{P} becomes,

$$\mathbf{P} = N\mathbf{u} + Q\mathbf{v}$$

while the end moment \mathbf{M}' becomes

$$\mathbf{M}' = M'\mathbf{w}.$$

Now, starting with Eqs. 10 (EOM with higher order differential terms dropped),

$$\rho A \ddot{\mathbf{r}} = (\mathbf{N}\mathbf{u} + Q\mathbf{v})' + \mathbf{F}\eta \quad \text{Eq. 19a}$$

$$0 = M'\mathbf{w} + \eta\mathbf{u} \times (\mathbf{N}\mathbf{u} + Q\mathbf{v}) \quad \text{Eq. 19b}$$

describe the modified EOMs where certain elements are described in the tether frame for convenience. Eq. 19b is expanded to yield,

$$0 = (M' + \eta Q)\mathbf{w} \quad \text{Eq. 20a}$$

$$Q = -M'/\eta \quad \text{Eq. 20b}$$

Assuming a simple beam theory for the small tether element, the bending moment is proportional to curvature and bending stiffness as,

$$M(s, t) = EI(s) \|\mathbf{r}''(s, t)\|. \quad \text{Eq. 21}$$

So Eq. 20b becomes,

$$Q = -\frac{EI|\chi'|}{\eta}. \quad 22$$

Eq. 22 is substituted into Eq. 19a and transformed to the base coordinate system to yield the system of equations,

$$\rho A \dot{v}_x = \left(EA(\eta - 1) \frac{\chi_x}{\eta} \right)' + \left(EI \frac{\kappa'}{\eta} \frac{\chi_y}{\eta} \right)' + F_x \eta \quad 23a$$

$$\rho A \dot{v}_y = \left(EA(\eta - 1) \frac{\chi_y}{\eta} \right)' - \left(EI \frac{\kappa'}{\eta} \frac{\chi_x}{\eta} \right)' + F_y \eta \quad 23b$$

or

$$\rho A \dot{v}_j = EA[\eta' \chi_j + (\eta - 1) \eta \chi_j'] \eta^{-2} + EI[\eta(\kappa'' \chi_k + \kappa' \chi_k') - 2\eta' \kappa' \chi_k] \eta^{-3} + F_j \eta, \quad 24$$

(j, k) = (x, y), (y, x),

with

$$\kappa = \sqrt{\chi_x'^2 + \chi_y'^2 + \chi_z'^2} \quad 25a$$

$$\kappa' = [\chi_x' \chi_x'' + \chi_y' \chi_y'' + \chi_z' \chi_z''] \kappa^{-1} \quad 25b$$

$$\kappa'' = [-[\chi_x' \chi_x'' + \chi_y' \chi_y'' + \chi_z' \chi_z''] \kappa' + [\chi_x' \chi_x''' + \chi_x'' \chi_x'' + \dots] \kappa] \kappa^{-2}. \quad 25c$$

Thus it can be seen that the new system equations (24) are second order in time and fourth order in space. For this system, four boundary conditions are required. The boundary conditions will be defined as the end force and moments that satisfy the equations of motion for the end bodies.

1.2.5.2.1 Boundary Conditions

The boundary conditions for case 2 consider both tangential forces and moments that satisfy the equations of motion for the end bodies. In this case, assume that the tether is attached to the end-body through a pinned connection (frictionless). In this case, the additional two boundary criteria require that no moment can be passed through the end of the tether. Hence, the boundary conditions become,

$$m_{b1} \mathbf{a}_{b1} = -\frac{\rho A l^2 \chi}{\eta} \Big|_{(0,t)} + \mathbf{F}_{b1} + \frac{EA(\eta - 1) \chi}{\eta} \Big|_{(0,t)} \quad \text{BC. 2b}$$

$$m_{b2} \mathbf{a}_{b2} = -\frac{\rho A l^2 \chi}{\eta} \Big|_{(l,t)} + \mathbf{F}_{b2} + \frac{EA(\eta - 1) \chi}{\eta} \Big|_{(l,t)} \quad \text{BC. 2c}$$

$$\chi'|_{(0,t)} = 0 \quad \text{BC. 3a}$$

$$\chi'|_{(l,t)} = 0 \quad \text{BC 3b}$$

1.2.5.3 Case 3) Tether Element with Mass Moment of Inertia

In all prior cases, the assumption that the tether element can be treated as a particle has been made, leading to an elimination of dl terms from Eqs. 8 and 9. Case 3) will modify Case 2) by including the mass moment of inertia terms. The justification for the removal of rotational inertia terms in previous cases was made on the assumption that a given tether element would remain small. However, in solution, it may be desirable to reduce the overall number of tether elements. Therefore, the ability to account for moment of inertia effects may be desirable. Rotation of the element is defined almost completely from the end node motions through kinematics, an extra degree-of-freedom (dof) is included to account for rotation about the tether element centerline. The kinematic relations that define the angular rate are given in the following equations (derived from the concepts of instantaneous screw axis). The result is a functional relation between angular rate, ω and nodal positions and velocities, \mathbf{r} and \mathbf{v} .

$$\hat{\omega} = \frac{\mathbf{v}_i \times \mathbf{v}_{i+1}}{|\mathbf{v}_i \times \mathbf{v}_{i+1}|} \quad 30$$

$$\begin{aligned} \omega |\mathbf{r}_i - \mathbf{r}_o| &= \mathbf{v}_i \\ \omega |\mathbf{r}_{i+1} - \mathbf{r}_o| &= \mathbf{v}_{i+1} \\ \omega |\mathbf{r}_{i+1/2} - \mathbf{r}_o| &= \mathbf{v}_{i+1/2} \end{aligned} \quad 31$$

Equation 30 is used to determine the direction of the angular rate vector, while Eq. 31 is used to determine the location and magnitude of this vector (magnitude given by ω , location given by \mathbf{r}_o). The angular acceleration term, α , can be determined from a difference approximation of $\alpha = d\omega/dt$. The mass moment of inertia of the element is

$$\mathbf{I} = \int \mathbf{r}^2 dm = \int \mathbf{r}^2 \rho A ds. \quad 32$$

With this information, Eq. 9b is reevaluated. In evaluating the moment of inertia related terms in Eq. 9b, the body fixed frame will be used to perform the initial vector manipulation, and then as a last step converted to base frame coordinates. Also, it is noted that as a matter of convenience the body fixed frame will be assumed to represent the principle frame for the tether element allowing terms in Euler's equation to reduce as follows,

$$\mathbf{R}_B^T \left[\begin{Bmatrix} I_{uu} \dot{\omega}_u \\ I_{vv} \dot{\omega}_v \\ I_{zz} \dot{\omega}_z \end{Bmatrix} + \begin{Bmatrix} (I_{ww} - I_{yy}) \omega_v \omega_w \\ (I_{uu} - I_{ww}) \omega_u \omega_w \\ (I_{vv} - I_{uu}) \omega_u \omega_v \end{Bmatrix} \right]. \quad 33$$

When these equations are substituted back into Eq. 9b (with higher order differential terms dropped), the equations become,

$$\begin{Bmatrix} I_{uu} \dot{\omega}_u \\ I_{vv} \dot{\omega}_v \\ I_{zz} \dot{\omega}_z \end{Bmatrix} + \begin{Bmatrix} (I_{ww} - I_{yy}) \omega_v \omega_w \\ (I_{uu} - I_{ww}) \omega_u \omega_w \\ (I_{vv} - I_{uu}) \omega_u \omega_v \end{Bmatrix} = \begin{bmatrix} JG\theta_u \\ -|\chi|O \\ EI|\chi|' + |\chi|Q \end{bmatrix} \quad 34$$

From Eq. 34, shear terms O and Q can be solved and substituted into the translational dynamic equation. The additional degree of freedom, rotation about the tether axis, defined by q_u will be included in the state space representation of the tether. Euler's rotational equations will be employed to give a first order differential relation between θ_u and ω (using the Euler rotation operations

discussed in section 2.1). Thus, the state space system becomes a system of $(3(3)+1)*n$ equations that can be solved forward in time.

1.2.6 Application to Variable Length Tether

The equations of motion resulting from the case in section 2.5.1 were given in Eq. 17 as,

$$\dot{\mathbf{X}}(s,t) = \begin{Bmatrix} \dot{\mathbf{r}} \\ \dot{\mathbf{v}} \\ \dot{\chi} \end{Bmatrix} = \begin{Bmatrix} \mathbf{v} \\ \frac{1}{\rho A} \left[(EA(\eta-1)\mathbf{r}'/\eta)' + \mathbf{F}\eta \right] \\ \mathbf{v}' \end{Bmatrix}. \quad 1$$

For a fixed-length tether, the spatial domain for these equations is,

$$0 \leq s \leq l \quad 2$$

where the length of the tether is initially defined and fixed in time. This case allows direct spatial discretization to be applied (for example through a finite difference or finite element approach) with fixed boundaries on the domains. Alternatively, a variable length tether model may be desired, for example if tether reeling is to be permitted at either boundary. In this case, the spatial domain of the tether becomes dependent on time as,

$$0 \leq s \leq l(t) \quad 3$$

where,

$$l(t) = l_0 + \int_{t=0}^{t=t} (\dot{l}_1 + \dot{l}_2) dt \quad 4$$

with l_0 the initial tether length and \dot{l}_1, \dot{l}_2 the rate of tether reel-out at each end of the tether. In order to maintain constant domains for future spatial discretization procedures, a new spatial variable ξ is introduced (following the procedure and notation introduced in Kohler, [zz]) to replace s . ξ will be defined as,

$$\xi = \frac{s}{l} \quad 5$$

which has the fixed domain of $0 \rightarrow 1$. Based on this new spatial parameter, we can define the tether coordinates with the function,

$$\tilde{\mathbf{r}}(\xi, t) = \mathbf{r}(s, t). \quad 6$$

which is dependent on variables ξ and t and is represented with an over tilde. Based on this new parameterization, the derivatives of the tether coordinates become,

$$\chi_k = r_k' = \xi' \frac{\partial \tilde{r}_k}{\partial \xi} \quad 7$$

$$\mathbf{v}_k = \dot{\mathbf{r}}_k = \frac{\partial \tilde{\mathbf{r}}_k}{\partial t} + \dot{\xi} \frac{\partial \tilde{\mathbf{r}}_k}{\partial \xi} \quad 8$$

$$\dot{\mathbf{v}}_k = \ddot{\mathbf{r}}_k = \frac{\partial^2 \tilde{\mathbf{r}}_k}{\partial t^2} + \dot{\xi} \frac{\partial^2 \tilde{\mathbf{r}}_k}{\partial \xi \partial t} + \ddot{\xi} \frac{\partial \tilde{\mathbf{r}}_k}{\partial \xi} + \dot{\xi} \frac{\partial^2 \tilde{\mathbf{r}}_k}{\partial t \partial \xi} + \dot{\xi}^2 \frac{\partial^2 \tilde{\mathbf{r}}_k}{\partial \xi^2} \quad 9$$

with derivatives of the new spatial coordinate given as,

$$\xi' = \frac{1}{l} \quad 10$$

$$\dot{\xi} = -\frac{s}{l^2} \dot{l} = -\frac{s}{l^2} (\dot{l}_1 + \dot{l}_2) \quad 11$$

$$\ddot{\xi} = -\frac{s}{l^2} \ddot{l} + \frac{s}{l^3} \dot{l}^2. \quad 12$$

and the stretch ratio defined as,

$$\eta = \xi' \sqrt{\left(\frac{\partial \tilde{r}_x}{\partial \xi}\right)^2 + \left(\frac{\partial \tilde{r}_y}{\partial \xi}\right)^2 + \left(\frac{\partial \tilde{r}_z}{\partial \xi}\right)^2}. \quad 13$$

The remaining state variables (and stretch ratio) are defined as functions of the new spatial parameter as indicated by an over-tilde as,

$$\tilde{\chi}_k = \frac{\partial \tilde{r}_k}{\partial \xi} \quad 14a$$

$$\tilde{v}_k = \frac{\partial \tilde{r}_k}{\partial t} \quad 14b$$

$$\tilde{\eta} = \sqrt{\tilde{\chi}_x^2 + \tilde{\chi}_y^2 + \tilde{\chi}_z^2} \quad 14c$$

Allowing the variables from Eq. 1 to be written in terms of the new state variables,

$$\chi_k = \xi' \tilde{\chi}_k \quad 15a$$

$$\chi'_k = \xi'^2 \frac{\partial \tilde{\chi}_k}{\partial \xi} \quad 15b$$

$$v_k = \tilde{v}_k + \xi' \tilde{\chi}_k \quad 15c$$

$$\dot{v}_k = \frac{\partial \tilde{v}_k}{\partial t} + 2\xi' \frac{\partial \tilde{v}_k}{\partial \xi} + \xi'' \tilde{\chi}_k + \xi'^2 \frac{\partial \tilde{\chi}_k}{\partial \xi} \quad 15d$$

$$\eta = \xi' \tilde{\eta} \quad 15e$$

$$\eta' = \xi'^2 \left[\tilde{\chi}_x \frac{\partial \tilde{\chi}_x}{\partial \xi} + \tilde{\chi}_y \frac{\partial \tilde{\chi}_y}{\partial \xi} + \tilde{\chi}_z \frac{\partial \tilde{\chi}_z}{\partial \xi} \right] \tilde{\eta}^{-1}. \quad 15f$$

The equations of motion in terms of the new parameterization become;

$$\frac{\partial \tilde{r}_k}{\partial t} = \tilde{v}_k \quad 16$$

$$\frac{\partial \tilde{v}_k}{\partial t} = \frac{EA}{\rho A} \left[\xi'^2 \left[\tilde{\chi}_x \frac{\partial \tilde{\chi}_x}{\partial \xi} + \tilde{\chi}_y \frac{\partial \tilde{\chi}_y}{\partial \xi} + \tilde{\chi}_z \frac{\partial \tilde{\chi}_z}{\partial \xi} \right] \tilde{\eta}^{-1} (\xi' \tilde{\chi}_k) + \xi' \tilde{\eta} (\xi' \tilde{\eta} - 1) \xi'^2 \frac{\partial \tilde{\chi}_k}{\partial \xi} \right] \eta^{-2} + F_k \xi' \tilde{\eta}, \quad 17$$

$$\frac{\partial \tilde{\chi}_k}{\partial t} = \frac{\partial \tilde{v}_k}{\partial \xi} \quad 18$$

for

$$k = x, y, z$$

with the new state vector,

$$\tilde{\mathbf{X}}(\xi, t) = \begin{Bmatrix} \tilde{\mathbf{r}}(\xi, t) \\ \tilde{\mathbf{v}}(\xi, t) \\ \tilde{\chi}(\xi, t) \end{Bmatrix} \quad 19$$

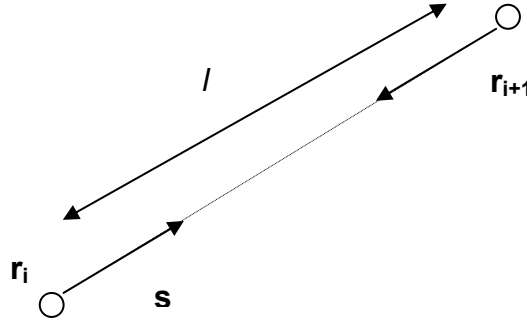
a function of the new spatial variable ξ and time with domains,

$$0 \leq t \leq \infty$$

$$0 \leq \xi \leq 1$$

1.3 Compare with Bead & Spring models

Consider the bead and spring model for an elastic tether in two-dimensions with axial stiffness only. Figure 10 shows one section of tether between two beads.



The tensile force s between the beads is given as a function of tether stiffness and bead positions as,

$$s = k \left[\sqrt{(r_{i+1,x} - r_{i,x})^2 + (r_{i+1,y} - r_{i,y})^2} - l \right] \quad 3-1$$

Expanding,

$$s = k \left[\sqrt{\left(r_x + l \frac{\partial r_x}{\partial s} + \dots - r_{i,x} \right)^2 + \left(r_y + l \frac{\partial r_y}{\partial s} + \dots - r_{i,y} \right)^2} - l \right] \quad 3-2$$

or

$$s = k \left[l \sqrt{\left(\frac{\partial r_x}{\partial s} \right)^2 + \left(\frac{\partial r_y}{\partial s} \right)^2 + \dots} - l \right] \quad 3-3$$

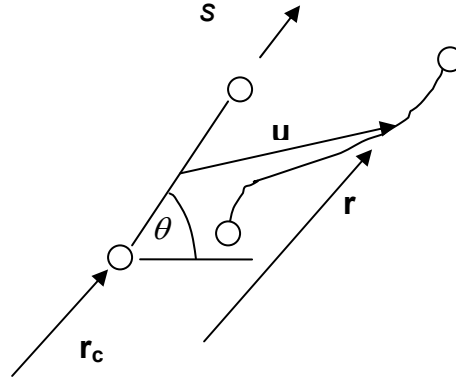
with higher order terms neglected, s becomes,

$$s = EA \left[\sqrt{\left(\frac{\partial r_x}{\partial s} \right)^2 + \left(\frac{\partial r_y}{\partial s} \right)^2} - 1 \right] \quad 3-4$$

with $k = EA/l$. Thus, the bead and spring model is consistent with Hooke's law relating Eulerian stress to engineering strain.

1.4 Alternative Reference Coordinate System

An alternative reference coordinate system for describing tether motion is considered. Numerical solutions of the equations of motion, for example Eq. 18, are used to predict tether behavior. An alternative reference system for the tether is suggested as one approach to improve or validate the numerical solutions. The initial system tracks each point the tether relative to a fixed position (for example earth center), resulting in large numerical values for position coordinates relative to the other parameters. The first alternative considered here will describe the tether motion relative to another orbiting body. In this case, the orbiting body will be an "equivalent" rigid tether model, equivalent in terms of end mass and tether mass. The tether state will now be composed of the position and orientation of the rigid tether (6 dof) plus the three position coordinates of each point along the tether relative to a point on the rigid tether. The total number of coordinates is given as $3*n + 6$.



A point on the tether is referenced with vector \mathbf{r} as,

$$\mathbf{r} = \mathbf{r}_c + \mathbf{s} + \mathbf{u} \quad 4-1$$

and in-plane coordinates,

$$\begin{aligned} r_x &= r_{cx} + s \cos(\theta) + u_x \\ r_y &= r_{cy} + s \sin(\theta) + u_y \end{aligned} \quad 4-2$$

The strain follows from the partial derivatives of these coordinates with respect to the material coordinate,

$$\begin{aligned} \frac{\partial r_x}{\partial s} &= \cos(\theta) + \frac{\partial u_x}{\partial s} \\ \frac{\partial r_y}{\partial s} &= \sin(\theta) + \frac{\partial u_y}{\partial s} \end{aligned} \quad 4-3$$

$$\varepsilon(s, t) = \frac{ds^* - ds}{ds} = \frac{ds^*}{ds} - 1 = \eta - 1 \quad 4-4$$

with

$$\eta = \sqrt{\left(\frac{\partial r_x}{\partial s}\right)^2 + \left(\frac{\partial r_y}{\partial s}\right)^2} = 1 + 2(\cos(\theta)u'_x + \sin(\theta)u'_y) + u'^2_x + u'^2_y. \quad 4-5$$

Here, the deflections u_x and u_y are specified in the base coordinate frame and are functions of space and time. These deflections describe the location of any point along the tether with respect to the rigid-body tether. Note that these deflections account for all departure from rigid body tether motion (elastic deflections, dynamics, etc). For convenience, these deflections will be written in the rigid body frame, u and v as;

$$\begin{Bmatrix} u_x \\ u_y \\ u_z \end{Bmatrix} = \begin{bmatrix} c\theta & -s\theta & 0 \\ s\theta & c\theta & 0 \\ 0 & 0 & 1 \end{bmatrix} \begin{Bmatrix} u \\ v \\ w \end{Bmatrix} \quad 4-6$$

or

$$\mathbf{u}^B = \mathbf{R}\mathbf{u}^T \quad 4-7$$

with \mathbf{B} , \mathbf{T} referring to the base and tether frames respectively and $c\theta$, $s\theta$ as $\cos(\theta)$, $\sin(\theta)$. Similarly, the partial derivatives of these deflections are given as,

$$\mathbf{u}^{B'} = \mathbf{R}\mathbf{u}^{T'} \quad 4-8$$

allowing the strain to be rewritten in tether coordinates as;

$$\varepsilon = \eta - 1 \quad 4-9$$

with

$$\eta = \sqrt{(1 + u')^2 + v'^2} \quad 4-10$$

Similarly, the position can be rewritten in terms of deflections in the tether frame as,

$$\begin{aligned} r_x &= r_{cx} + s \csc \theta + u \csc \theta - v s \theta \\ r_y &= r_{cy} + s s \theta + u s \theta + v \csc \theta \end{aligned} \quad 4-11$$

Expressions for the tether acceleration then become,

$$\begin{aligned} \ddot{r}_x &= \ddot{r}_{cx} - (s+u)\ddot{\theta} s \theta - (s+u)\dot{\theta}^2 \csc \theta + \ddot{u} \csc \theta - 2\dot{u}\dot{\theta} s \theta - \ddot{v} s \theta - 2\dot{v}\dot{\theta} \csc \theta - v\ddot{\theta} \csc \theta + v\dot{\theta}^2 s \theta \\ \ddot{r}_y &= \ddot{r}_{cy} + (s+u)\ddot{\theta} \csc \theta - (s+u)\dot{\theta}^2 s \theta + \ddot{u} s \theta + 2\dot{u}\dot{\theta} \csc \theta + \ddot{v} \csc \theta - 2\dot{v}\dot{\theta} s \theta - v\ddot{\theta} s \theta - v\dot{\theta}^2 \csc \theta \end{aligned} \quad 4-12$$

These expressions are then placed into the equations of motion for a tether with negligible bending stiffness (Eq. 13),

$$\rho A \ddot{r}_k = \left(\frac{EA(\eta-1)r_k'}{\eta} \right)' + F_k \eta, \quad k = x, y, z. \quad 13$$

or

$$\begin{aligned} \rho A \{ \ddot{r}_{cx} - (s+u)\ddot{\theta} s \theta - (s+u)\dot{\theta}^2 \csc \theta + \ddot{u} \csc \theta - 2\dot{u}\dot{\theta} s \theta - \ddot{v} s \theta - 2\dot{v}\dot{\theta} \csc \theta - v\ddot{\theta} \csc \theta + v\dot{\theta}^2 s \theta \} = \\ \left(\frac{EA(\eta-1)((1+u')\csc \theta - v' s \theta)}{\eta} \right)' + F_x \eta \end{aligned} \quad 4-13a$$

and

$$\begin{aligned} \rho A \{ \ddot{r}_{cy} + (s+u)\ddot{\theta} \csc \theta - (s+u)\dot{\theta}^2 s \theta + \ddot{u} s \theta + 2\dot{u}\dot{\theta} \csc \theta + \ddot{v} \csc \theta - 2\dot{v}\dot{\theta} s \theta - v\ddot{\theta} s \theta - v\dot{\theta}^2 \csc \theta \} = \\ \left(\frac{EA(\eta-1)((1+u')s \theta + v' \csc \theta)}{\eta} \right)' + F_y \eta \end{aligned} \quad 4-13b$$

for the in-plane coordinates. These equations described in the tether frame coordinates,

$$\rho A \{ \ddot{r}_{cx} \csc \theta + \ddot{r}_{cy} s \theta - (s+u)\dot{\theta}^2 + \ddot{u} - v\ddot{\theta} - 2\dot{v}\dot{\theta} \} = \left(\frac{EA(\eta-1)(1+u')}{\eta} \right)' + F_x \eta \csc \theta + F_y \eta s \theta \quad 4-14a$$

$$\rho A \{ -\ddot{r}_{cx} s \theta + \ddot{r}_{cy} \csc \theta - (s+u)\ddot{\theta} - 2\dot{u}\dot{\theta} + v\dot{\theta}^2 - \ddot{v} \} = \left(\frac{EA(\eta-1)v'}{\eta} \right)' - F_x \eta s \theta + F_y \eta \csc \theta \quad 4-14b$$

or

$$\begin{aligned} \ddot{u} &= \frac{1}{\rho A} \{ EA(\eta'(1+u')\eta^{-2} + (\eta-1)u''\eta^{-1}) + (F_x \csc \theta + F_y s \theta)\eta \} - \{ \ddot{r}_{cx} \csc \theta + \ddot{r}_{cy} s \theta - (s+u)\dot{\theta}^2 + -v\ddot{\theta} - 2\dot{v}\dot{\theta} \} \\ \ddot{v} &= \frac{1}{\rho A} \{ EA(\eta'v'\eta^{-2} + (\eta-1)v''\eta^{-1}) - (F_x s \theta + F_y \csc \theta)\eta \} - \{ -\ddot{r}_{cx} s \theta + \ddot{r}_{cy} \csc \theta - (s+u)\ddot{\theta} - 2\dot{u}\dot{\theta} + v\dot{\theta}^2 \} \end{aligned} \quad 4-15$$

These equations are coupled with the rigid body equations of motion,

$$\mathbf{A} \begin{Bmatrix} r_c \\ \gamma \\ \theta \end{Bmatrix} = \mathbf{B} \quad 4-16$$

with

$$\mathbf{A} = \begin{bmatrix} (m_1 + m_2 + m_3) & 0 & -\left(m_2 + \frac{m_3}{2}\right)l s(\gamma - \theta) \\ 0 & (m_1 + m_2 + m_3)r_c^2 & \left(m_2 + \frac{m_3}{2}\right)r_c l c(\gamma - \theta) \\ -\left(m_2 + \frac{m_3}{2}\right)l & \left(m_2 + \frac{m_3}{2}\right)r_c l c(\gamma - \theta) & \left(m_2 + \frac{m_3}{4} + \frac{I}{l^2}\right) \end{bmatrix}, \quad 4-17a$$

$$\mathbf{B} = \left\{ \begin{bmatrix} -(m_1 + m_2 + m_3)r_c \dot{\gamma}^2 + (m_2 + m_3/2)(l\dot{\theta}(2\dot{\gamma} - \dot{\theta})c(\gamma - \theta)) \\ -\frac{\mu m_1}{r_c^2} - \mu m_2(r_c^2 + l c(\gamma - \theta))a^{-3/2} - \mu m_3(r_c^2 + \frac{l}{2}c(\gamma - \theta))b^{-3/2} \end{bmatrix} \right. \\ \left. \begin{bmatrix} (m_1 + m_2 + m_3)2r_c \dot{\gamma} \dot{\gamma} + (m_2 + m_3/2)r_c l \dot{\theta}^2 s(\gamma - \theta) \\ + \mu m_2 r_c l s(\gamma - \theta)a^{-3/2} + \mu m_3 r_c \frac{l}{2} s(\gamma - \theta)b^{-3/2} \end{bmatrix} \right. \\ \left. \begin{bmatrix} (m_2 + m_3/2)(r_c \dot{\gamma} l(\dot{\gamma} - 2\dot{\theta})s(\gamma - \theta) + 2\dot{r}_c l \dot{\theta} c(\gamma - \theta)) \\ - \mu m_2 r_c l s(\gamma - \theta)a^{-3/2} - \mu m_3 r_c \frac{l}{2} s(\gamma - \theta)b^{-3/2} \end{bmatrix} \right\} \quad 4-17b$$

with r_c, γ locating the reference position on the rigid tether and θ the rigid tether absolute orientation in the orbital plane, m_1, m_3 the end body masses, m_2 the tether mass (tether mass assumed to be uniform), I the tether mass moment of inertia, l the rigid body tether length, and

$$a = \left[(r_c c \lambda + l c \theta)^2 + (r_c s \lambda + l s \theta)^2 \right] \\ b = \left[\left(r_c c \lambda + \frac{l}{2} c \theta \right)^2 + \left(r_c s \lambda + \frac{l}{2} s \theta \right)^2 \right]. \quad 4-17c,d$$

This set of equations of motion, 4-15 and 4-16, are equivalent to those given in Eq. 13 and can be used to evaluate the numerical solutions imposed. An example state vector for the equations of motion from section 4 based on a finite difference solution approach with n nodes might look like,

$$\mathbf{x} = \begin{Bmatrix} r_c \\ \gamma \\ \theta \\ u_1 \\ v_1 \\ u_2 \\ v_2 \\ \vdots \\ u_n \\ v_n \end{Bmatrix}. \quad 4-18$$

1.5 Tether Damping, Strain-Rate-Proportional Damping (Material)

A model that includes strain-rate proportional damping is provided here. This damping is included in the constitutive relation (Eq. 11) as,

$$N = (EA\varepsilon - c\dot{\varepsilon}) \quad 5-1$$

where c is the strain-rate damping coefficient and the strain rate defined as,

$$\dot{\varepsilon} = \frac{\partial}{\partial t}(\eta - 1) = \dot{\eta} = [\chi_x \dot{\chi}_x + \chi_y \dot{\chi}_y + \chi_z \dot{\chi}_z] \eta^{-1}. \quad 5-2$$

The equations of motion that include this strain-rate proportional damping become,

$$\rho A \dot{\mathbf{v}} = \left[\frac{EA(\eta-1) + c\dot{\eta}}{\eta} \boldsymbol{\chi} \right]' + \mathbf{F}. \quad 5-3$$

Upon expansion, this system of equations in scalar form becomes,

$$\rho A \dot{v}_k = [EA(\eta' \chi_k + \eta_k(\eta-1)\chi') + c(\dot{\eta}' \eta \chi_k + \dot{\eta} \eta \chi'_k - \dot{\eta} \eta' \chi_k)] \eta^{-2} + F_k, \quad k = x, y, z \quad 5-4$$

with

$$\eta = \sqrt{\chi_x^2 + \chi_y^2 + \chi_z^2} \quad 5-5a$$

$$\eta' = [\chi_x \chi'_x + \chi_y \chi'_y + \chi_z \chi'_z] \eta^{-1} \quad 5-5b$$

$$\dot{\eta} = [\chi_x \dot{\chi}_x + \chi_y \dot{\chi}_y + \chi_z \dot{\chi}_z] \eta^{-1} \quad 5-5c$$

$$\dot{\eta}' = [(\chi'_x \dot{\chi}_x + \chi_x \dot{\chi}'_x + \chi'_y \dot{\chi}_y + \chi_y \dot{\chi}'_y + \chi'_z \dot{\chi}_z + \chi_z \dot{\chi}'_z) \eta - (\chi_x \dot{\chi}_x + \chi_y \dot{\chi}_y + \chi_z \dot{\chi}_z) \eta'] \eta^{-2} \quad 5-5d$$

2.0 VALIDATION OF TETHER SYSTEM MODELS

In developing any engineering model and subsequent computational solution schemes, validation forms a critical process. Many traditional techniques for solution validation exist including convergence tests, comparison with closed-form solutions, and tests with physical experiments. There are many situations however when some of these techniques cannot be directly applied, for example in comparing a solution with direct physical evidence. Such situations often arise in the aerospace and space technology arenas and demand therefore a greater emphasis on validation of engineering models. This chapter will demonstrate a specific model validation procedure that will be applied to multiple formulations to the tether dynamic simulation code.

MXER Tether simulation benchmarks and validation/evaluation of specific tether model algorithms is perceived to be a critical element in the MXER system design and development process. This section will discuss activities toward model validation through a multi-stage process that includes, 1) model validation against simple lab tests, 2) model validation against limiting cases permitting approximate closed-form solutions, 3) model validation against previous tether missions, 4) verification across multiple alternate formulations and 5) verification across multiple, separate parties involved in model formulation. The initial goal of this work would provide a benchmark solution set, future work will evaluate the efficiency of specific model formulations in achieving a desired precision.

The equations that govern tether behavior are invariant to method of model derivation with respect to the underlying physics. However, the interpretive procedures used to describe these physics are often approximate or not fully understood. Further, these equations result in differential functions of space and time which in the most general sense do not permit exact solutions. As such, approximating techniques are applied to these governing equations to arrive at the desired result, prediction and analysis of the dynamic tether behavior. In general, these approximating techniques can be divided into spatial approximations and temporal approximations. The spatial approximating techniques are generally applied to reduce the partial derivative equations (pde's) into ordinary differential equations (ode's) or into a form that allows a specific, known solution. The temporal approximations provide numerical integration procedures to solve the time dependent derivative functions. Taken together, space and time approximating techniques create a process to solve the governing tether equations. The techniques for space and time in general can be treated independent of each other and allow a variety of combinations. Further, these techniques provide some level of variation and should find applications in which they are more ideally suited. Therefore, a process of examining a variety of these techniques will both provide a process they may indicate convergence toward a benchmark

solution to the inverse dynamics problem as well as indicate formulations that are most ideally suited to this problem. Table I provides an overview of spatial and temporal techniques that are being implemented by TTU:

Table 1: State versus Time

(Approximate techniques that could be considered)

Space / Time Approximation	4 th Order RK, 6 th ORK	Adaptive time-step routines (RK78)	Adams-Bashforth Moulton	Explicit/Implicit Adams – Moulton	Implicit Gear method
Finite difference solution (over multiple coordinate systems)	x	x	x		x
Assumed modes based on Ritz formulation	x				
Finite element formulation					
Discrete finite element formulation	x				

2.1 Procedure

The validation process will proceed through a sequence of test cases prepared for comparison either with some known or predicted result, or for comparison among multiple solution techniques. As such, the cases will be classified as either type A (known or predicted results and over alternate numerical strategies) or type B (comparison with independently developed models). Table II presents an overview of a series of cases that will be involved in the validation process and provides an overview of the current state of the validation process. Discussion of the results from Table II follow.

Table 2: Validation Cases versus Model Formulation

Validation Cases → Model formulation 	Mods.	Case 1) (type A) Compare with the Wave Equation	Case 2) (type A) Spatial/temporal convergence models	Case 3) (type A) Compare RMA over time integration routines	Case 4) (type A) Compare RMA over spatial approximations	Case 5) (type B) Symmetric, Non-symmetric tether rotating in free-space	Case 6) (type B) RMA
Finite difference solution (inertial-coordinates)	RK4	Sect. 2.2.1	Sect. 2.2.2	Sect. 2.2.3			Sect. 2.3
	RK6						Sect. 2.3
	ABM			Sect. 2.2.3			Sect. 2.3
	3-Pt. FD				Sect 2.2.4		Sect. 2.3
	5-Pt. FD				Sect 2.2.4		Sect. 2.3
	RK78					Sect. 2.3	Sect. 2.3
Finite difference solution (rigid-body-relative coordinates)						Sect. 2.3	Sect. 2.3
Finite element formulation (inertial coordinates)							
Finite difference formulations from TSIM						Sect. 2.3	Sect. 2.3
Assumed modes based on Ritz formulation							

CFS – closed-form solution

RMA – representative MXER application

2.2 Results of Type A comparisons

This section contains a description of the results of specific tests performed as indicated in Table II. Table III below contains the specific data used to initiate the representative MXER application containing two design nodes. The performance over a single orbit is presented in the subsequent graphs (approximately 1100 seconds).

Table 3: Parameters for Representative MXER Application

Constants		Tether Facility Orbit	
μ	3.986E+14	Perigee (m)	6,785,136.00
Number of Design nodes	2	Apogee (m)	14,823,136.00
Design node 1 mass (ballast mass)	10000 kg	Time for one orbit (s)	11,176.25
Design node 2 mass (capture mass)	500 kg	SMA	10,804,136.00
Tether Length (m)	90000	e	0.371987172
Cross Sect Area (m ²)	1.9635E-05	Perigee Velocity (m/s)	8977.690593
ρ (kg/m ³)	970	Apogee Velocity (m/s)	4109.444293
		ω of tether fac. (rad/s)	-0.013881192

2.2.1 Case 1

Case 1 consists of validation of the finite difference code model (4th order Runge-Kutta integration and 3 point finite difference routines) against an exact solution for the vibration of a simple string. The string is massless, I s fixed at both ends, has parameters chosen to provide for the first natural frequency, and is given an initial starting condition that matches its first mode shape.

Results:

The model was compared using three scenarios. The first case uses 20 nodes and a time step of 0.1 seconds. The second case uses 20 nodes and a time step of 0.05 seconds. The last case uses 100 nodes and a time step of 0.05 seconds. These results are shown the following 6 Figures. Figures 2.2.1-1 and 2.2.1-2 are representative of $n=20$ and $\Delta t=0.1$ for one single node (middle node) along the tether. Figure 2.2.1-2 shows the error over time between the exact solution and the model for the same node. Similarly, Figures 2.2.1-3 and 2.2.1-4 are derived using $n=20$ and $\Delta t=0.05$ again for a single node in the middle of the tether. Notice no improvement on the error between the two results. Lastly, Figures 2.2.1-5 and 2.2.1-6 are shown using $n=100$ and $\Delta t=0.05$ for the middle node of the tether. Notice a remarkable improvement in the reduction of error between the exact string solution and the tether finite difference code.

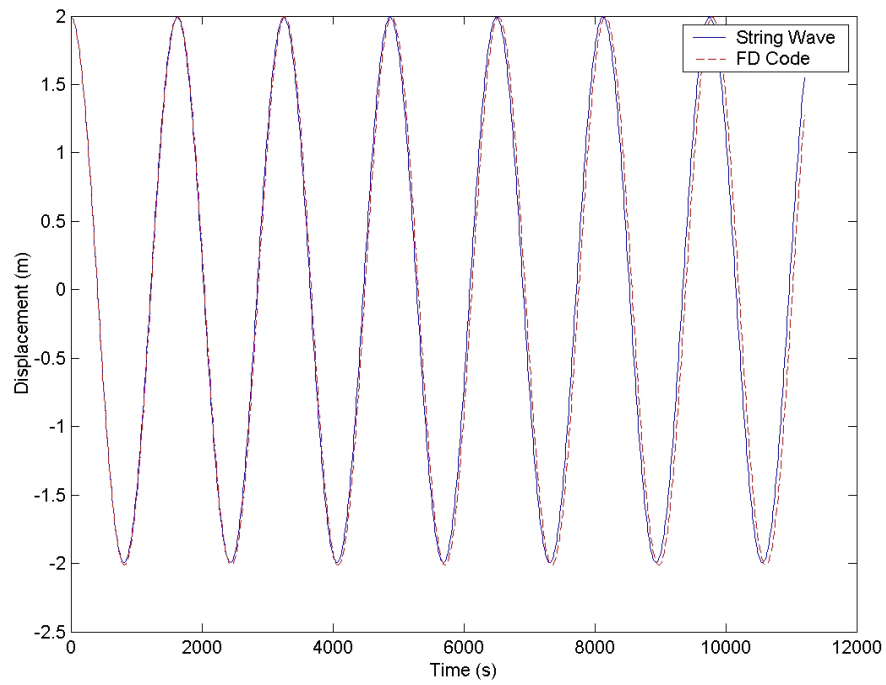


Figure 2.2.1-1: Comparison of String Solution of Wave Equation and FD Code
(20 nodes, 0.1 sec time step)

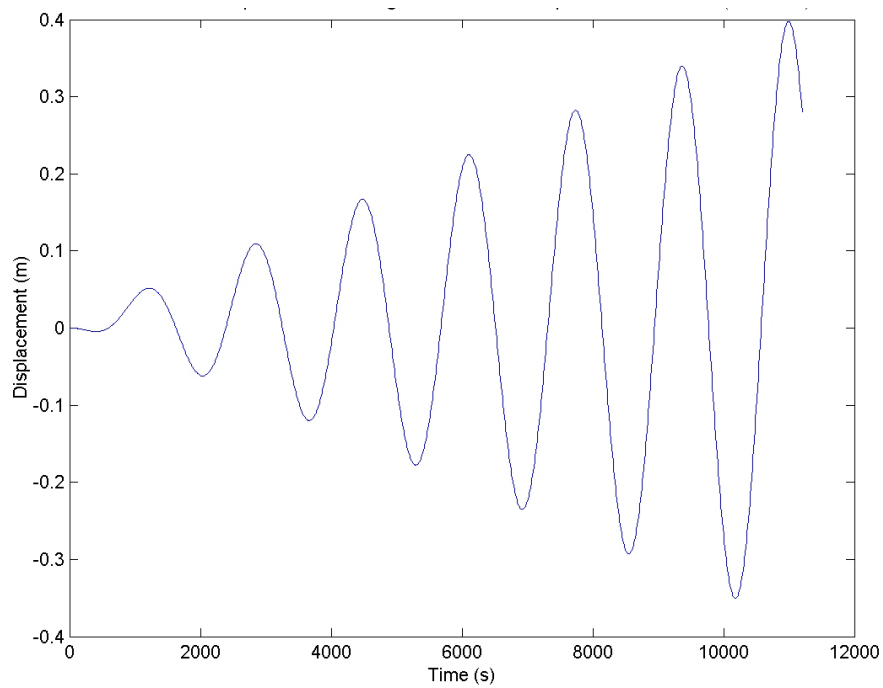


Figure 2.2.1-2: Difference in Displacement of String Solution of Wave Equation and FD Code
(1 node)

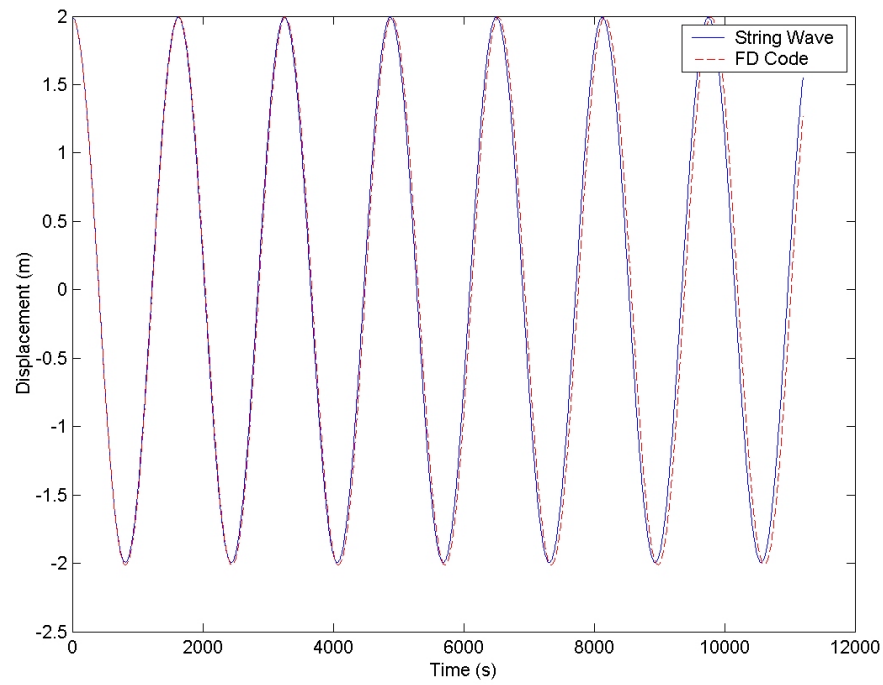


Figure 2.2.1-3: Comparison of String Solution of Wave Equation and FD Code
(20 nodes, .05 sec time step)

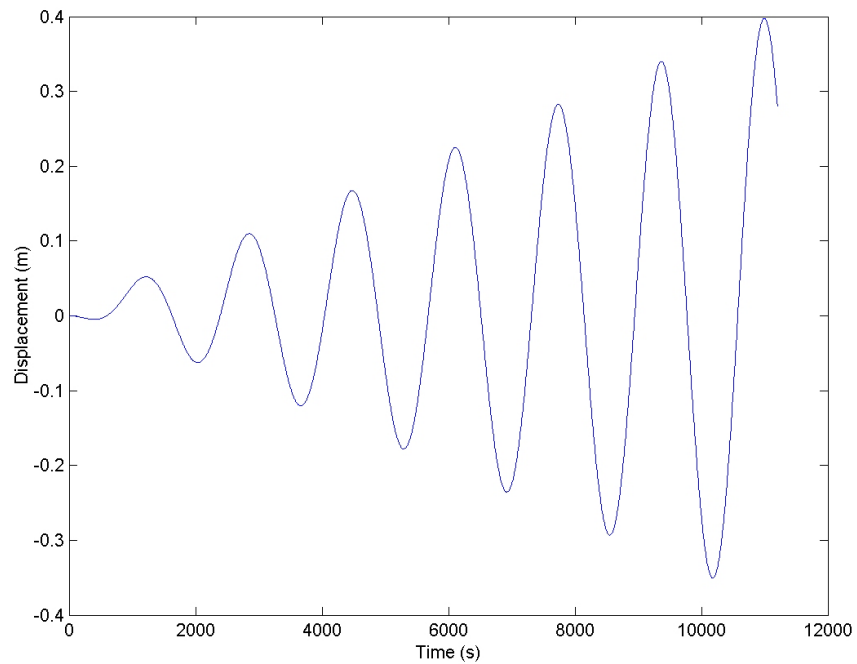


Figure 2.2.1-4: Difference in Displacement of String Solution of Wave Equation and FD Code
(1 node)

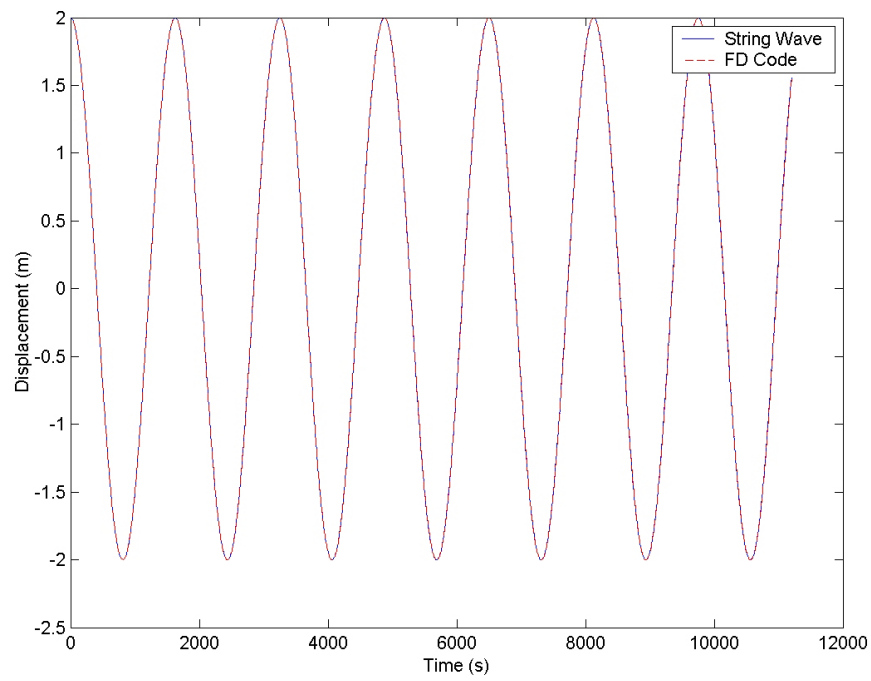


Figure 2.2.1-5: Comparison of String Solution of Wave Equation and FD Code
(100 nodes, .05 sec time step)

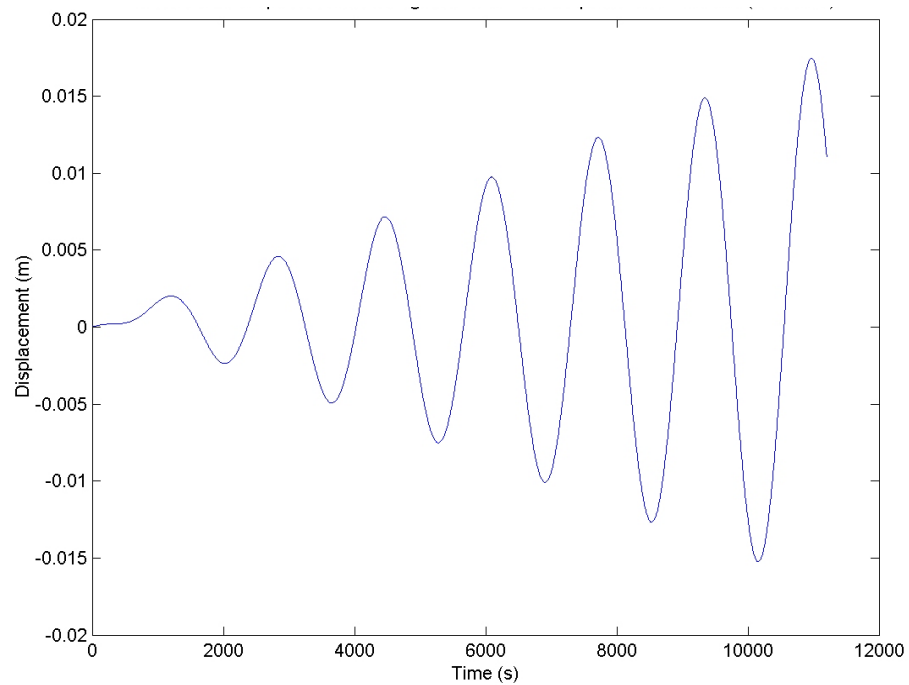


Figure 2.2.1-6: Difference in Displacement of String Solution of Wave Equation and FD Code
(1 node)

2.2.2 Case 2

Case 2 consists of a series of convergence tests performed on a single algorithm to verify the stability of a given result. The convergence tests will also be used to indicate the step size in space and time that can be used for a given result.

Results

First, convergence on spatial step size was considered. Multiple simulations were performed with decreasing step size (increasing number of nodes) using the 3-point finite difference formulation and a fourth-order Runge Kutta integration routine. Overall tether length was considered as a metric for comparison, determined as the sum of the strained tether segments. Three cases are compared, $n = 50$, 100 and 150 with the criteria, $c=\Delta t/\Delta x \geq 1$ ensured for each case. These results are shown in the following 2 Figures. Figures 2.2.2-1 and 2.2.2-1a shows plots all three cases over one orbit and at the end of the orbit. Notice that converged results are observed in the 100 node case. Figures 2.2.1-2 and 2.2.1-2a plot the difference in the 50 and 100 node from the 150 node case demonstrating sub .15 m tolerance in convergence for the 100 node case.

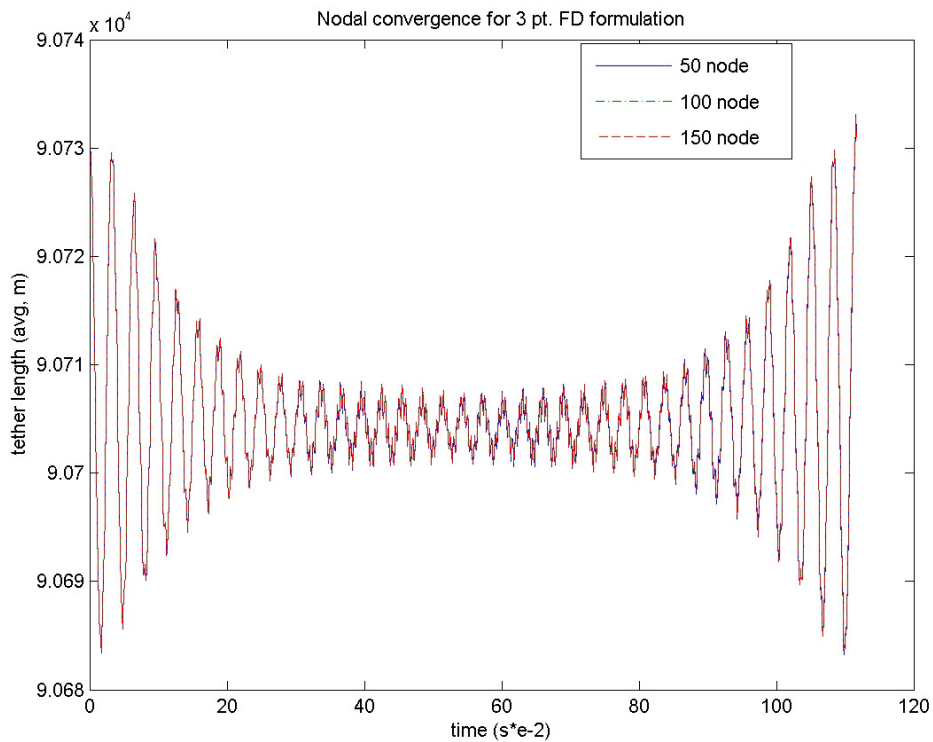


Figure 2.2.2-1: Nodal Convergence for 3 Point FD Formulation

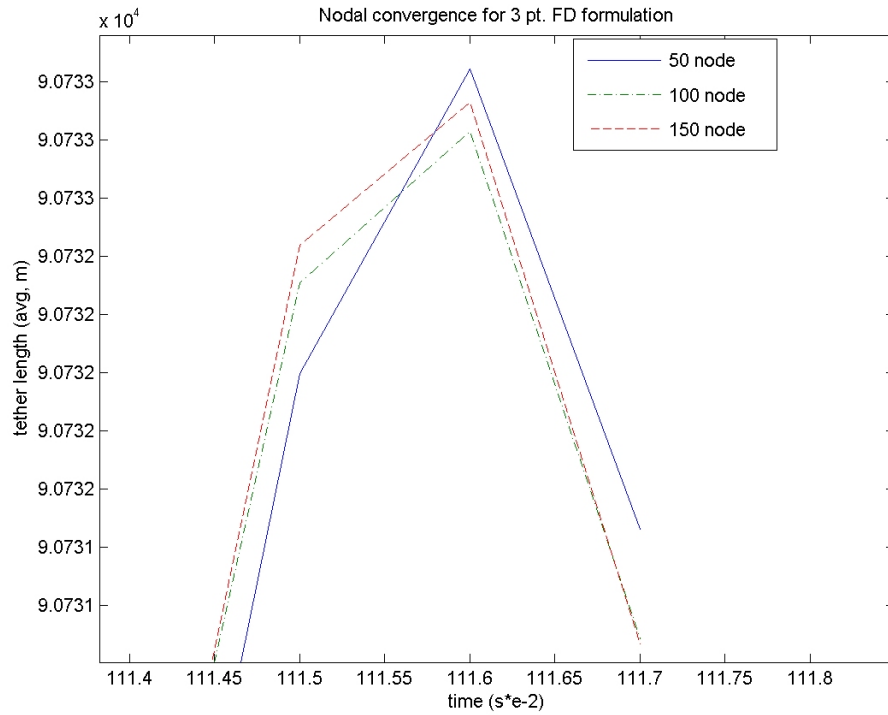


Figure 2.2.2-1a: Nodal Convergence for 3 Point FD Formulation

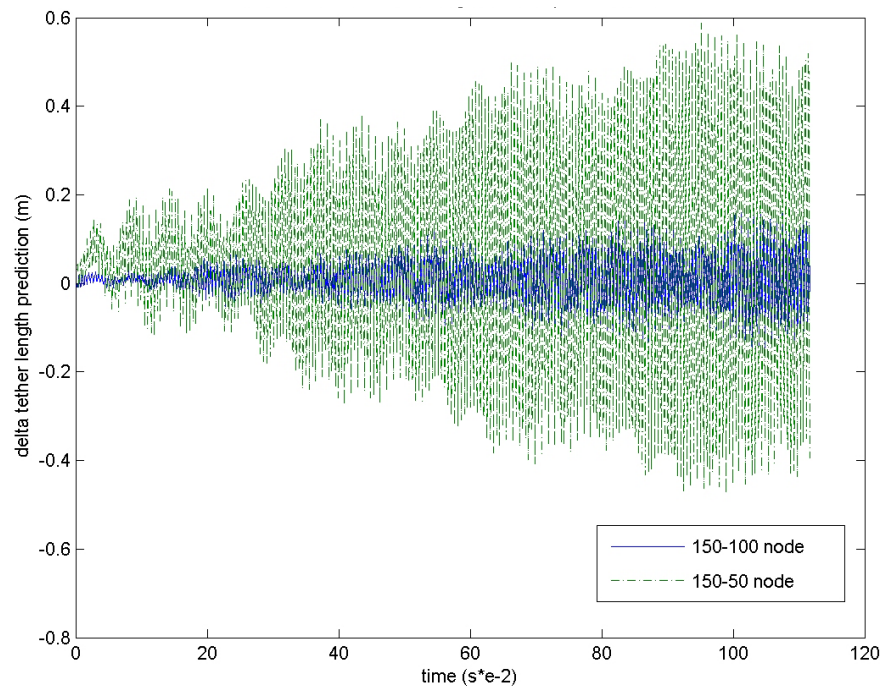


Figure 2.2.2-2: Difference in Nodal Convergence for 3 Point FD Formulation

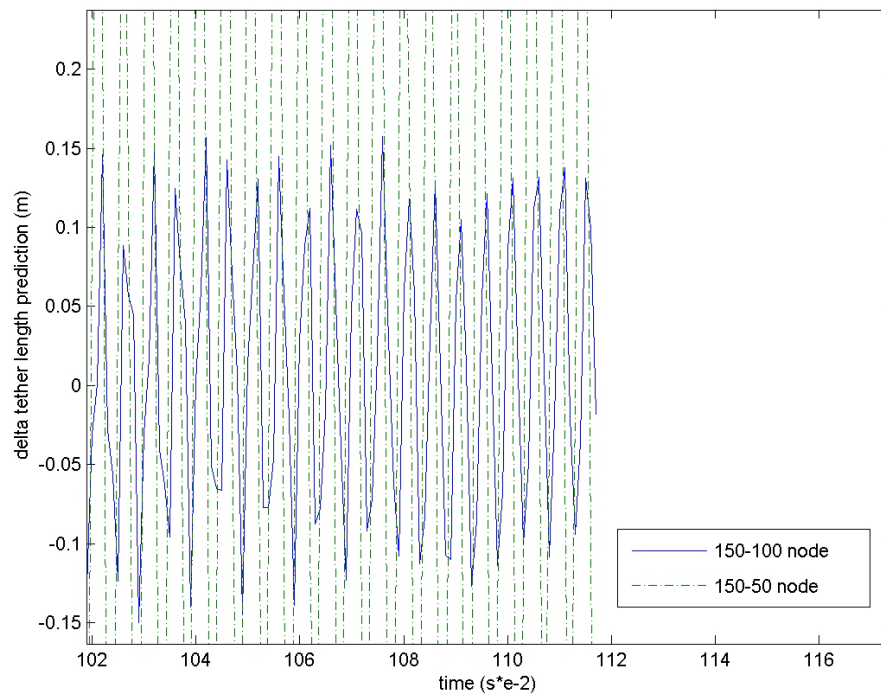


Figure 2.2.2-2a: Difference in Nodal Convergence for 3 Point FD Formulation

Summary

Convergence of both the spatial step size and time step size has been successfully performed. The results demonstrate that for a 90 km tether, 100 nodes and .1 second time step provides desirable and accurate performance for this formulation.

2.2.3 Case 3

Case 3 consists of validation between two different integration routines in the tether finite difference model. The case to be validated against is the standard tether model consisting of 3 point finite difference and 4th order Runge-Kutta integration routines. The case validated is one using the same 3 point finite difference routine but an Adams-Bashforth-Moulton 4th order integration routine is employed.

Results

Both models were compared using $n=20$ and $\Delta t=0.1$ and recorded for a complete orbit. Figures 2.2.3-1 and 2.2.3-2 show the results of the comparison between the two models when observed for a single node (middle node). Figures 2.2.3-2 is the error difference between the two models for the middle node over the entire orbital period.

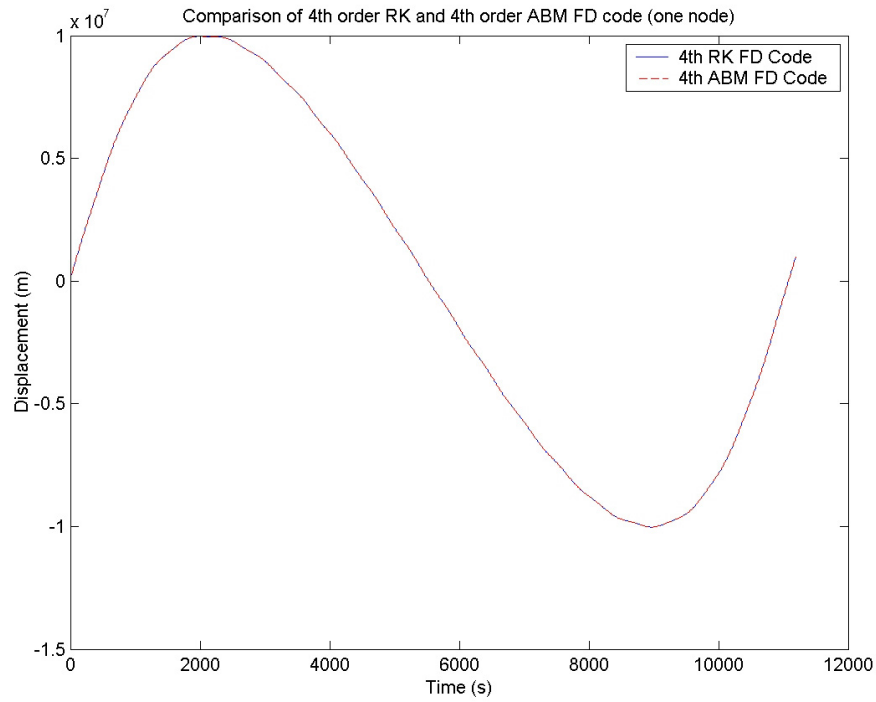


**Figure 2.2.3-1: Comparison of 4th Order RK and ABM FD Code
(1 node)**

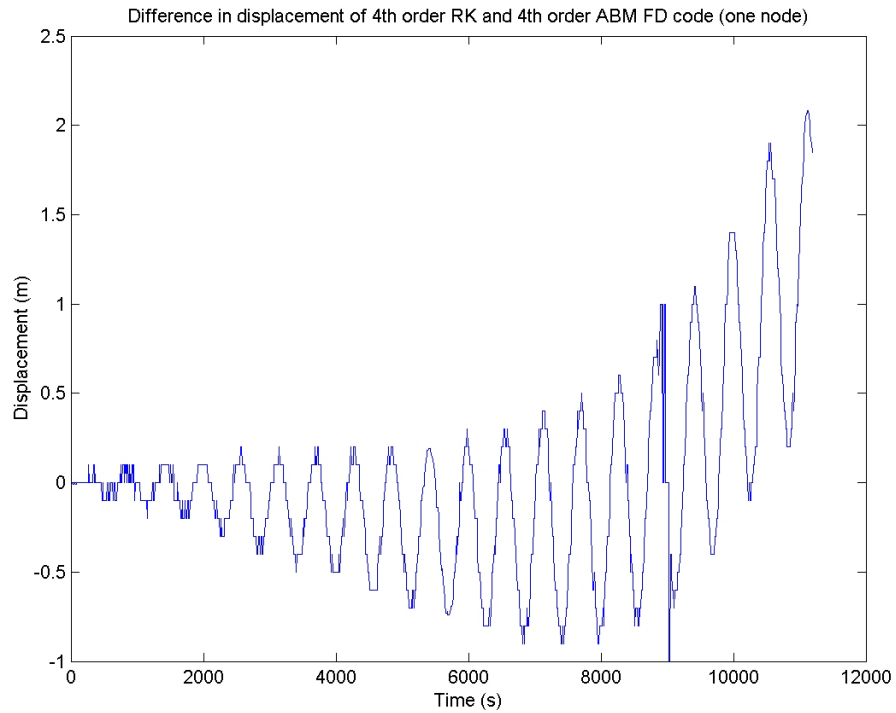


**Figure 2.2.3-2: Difference in Displacement of 4th Order RK and ABM FD Code
(1 node)**

2.2.4 Case 4

Case 4 consists of comparison between two different spatial differentiation routines in the tether finite difference model. The case to be validated against is the standard tether model consisting of 3 point

finite difference and 4th order Runge-Kutta integration routines. The comparison case employs a 5 point finite difference routine but a 4th order Runge-Kutta integration routine.

Results

Both models were compared using $n=20$ and $\Delta t=0.1$ and recorded for a complete orbit. Figures 2.2.4-1 and 2.2.4-2 show the results of the comparison between the two models when observed for a single node (middle node). Figures 2.2.4-2 is the error difference between the two models for the middle node over the entire orbital period.

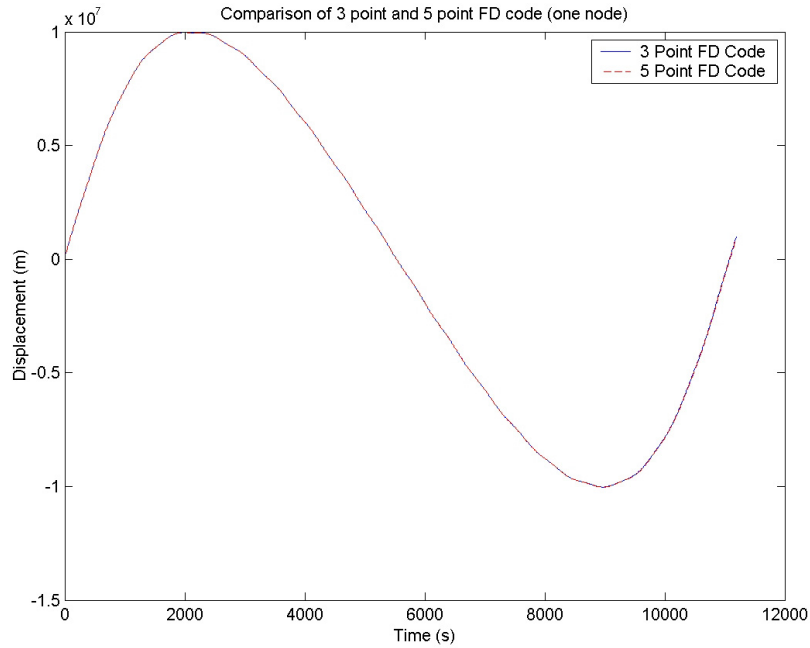


Figure 2.2.4-1: Comparison of 3 and 5 Point FD Code

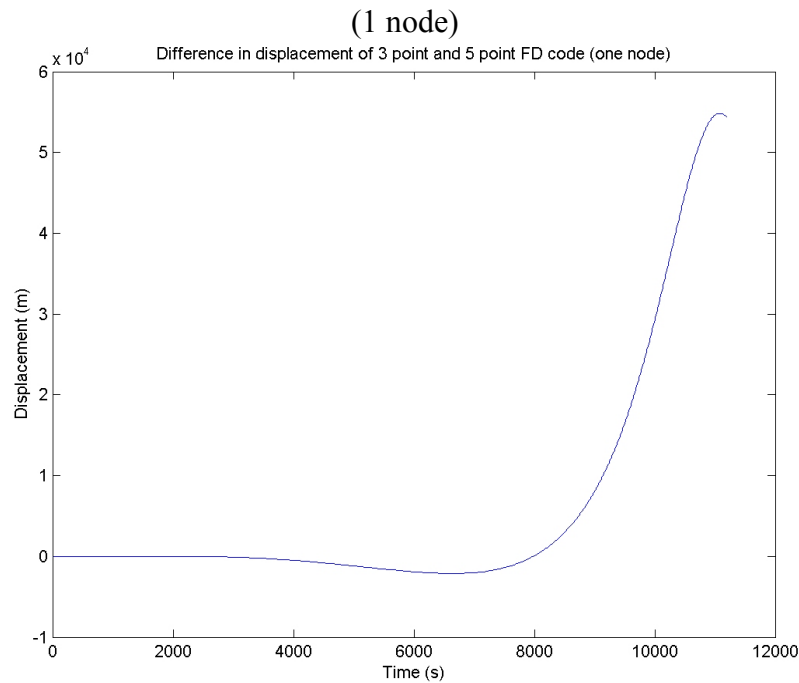


Figure 2.2.4-2: Difference in Displacement of 3 and 5 Point FD Code

(1 node)

2.3 Validation Results for Type-B Cases

The type-B validation cases compare results across multiple code platforms and looks for commonalities and differences. While not a definitive means of validation, corroboration of important dynamic phenomena by several codes is desired from the standpoint of code validation. Note that this cross-comparison may be used in the future to validate more efficient coding procedures, such as those using an assumed-modes method for example. A summary of this work has been prepared in formal paper format and is included at the end of this section.

The following three primary cases are first considered. These cases are chosen to isolate potential dynamic effects. Each of the following cases consider a uniform tether without bending, tether mass of .0048 kg/m.

Data for comparison:

- 1) total tether length
- 2) transverse vibration at nodes 6 and 12 (quarter and mid node)

Case 5a)

Brief description: massless, symmetric tether rotating in free space

Purpose: Observe effects of rotation on a symmetric tether (no end masses)

Parameters: $m_1 = 0\text{kg}$, $m_2 = 0\text{kg}$, $l = 10,000\text{ m}$,

Initial uniform stretch of .0002, rotation rate = .01 rad/s

Number of nodes =23

No damping, bending, aerodynamic, gravity or other effects considered

Run time: up to 5000 s

Response for this case is shown in average tether length (Figure 2.3-1) and transverse vibration at mid and quarter nodes (Figure 2.3-2)

Case 5b)

Brief description: Massive, symmetric tether rotating in free space

Purpose: Observe effects of rotation on a symmetric tether

Parameters: $m_1 = 1000\text{kg}$, $m_2 = 1000\text{kg}$, $l = 10,000\text{ m}$,

Initial uniform stretch of .0002, rotation rate = .01 rad/s

Number of nodes =23

No damping, bending, aerodynamic, gravity or other effects considered

Run time: up to 5000 s

Response for this case is shown in average tether length (Figure 2.3-3) and transverse vibration at mid and quarter nodes (Figure 2.3-4)

Case 5c)

Brief description: Non-symmetric tether rotating in free space

Purpose: Observe effects of rotation on a non-symmetric tether

Parameters: $m_1 = 1000\text{kg}$, $m_2 = 500\text{kg}$, $l = 10,000\text{ m}$,

Initial uniform stretch of .0004, rotation rate = .01 rad/s

Number of nodes =23

No damping, bending, aerodynamic, gravity or other effects considered
Run time: up to 5000 s

Response for this case is shown in average tether length (Figure 2.3-5) and transverse vibration at mid and quarter nodes (Figure 2.3-6)

Case 6)

Brief description: Non-symmetric, fully-rotating tether in earth orbit

Purpose: Observe tether behavior with gravitational effects

Parameters: $m_1=1000\text{kg}$, $m_2 = 500\text{kg}$, $l = 10,000 \text{ m}$,

Initial uniform stretch, stretch_ratio = .0004, rotation rate = .01 rad/s

Number of nodes =23

No damping, bending, aerodynamic or other effects considered

Earth orbit: $r_p = 6723 \text{ km}$, $r_a = 16373\text{km}$, $e = .4178$, spherical-earth gravity model

Run time: up to 1 orbit (12.6 ks)

Response for this case is shown in the motion of the center of mass (Figure 2.3-5), average tether length (Figure 2.3-6) and transverse vibration at mid and quarter nodes (Figure 2.3-7)

TTU simulation results from case 5a:

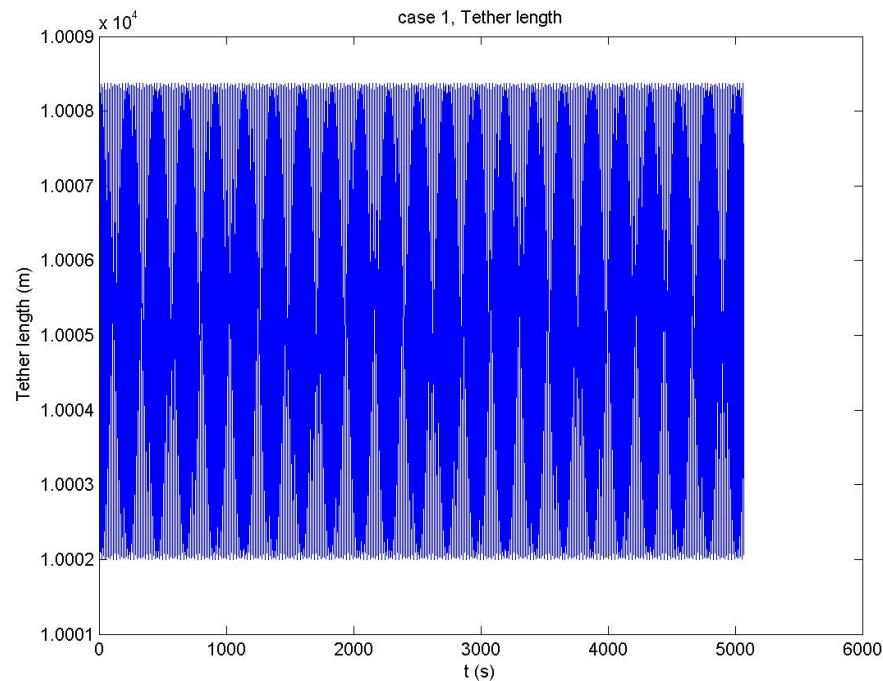


Figure 2.3-1: Average Tether Length over Case 5a

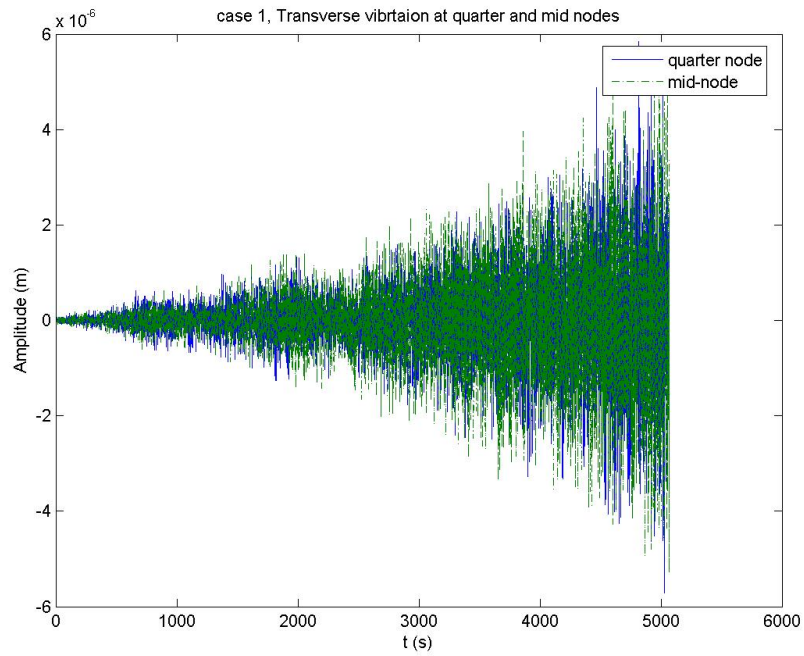


Figure 2.3-2: Mid and Quarter Node Vibration, Case 5a

TTU simulation results from case 5b:

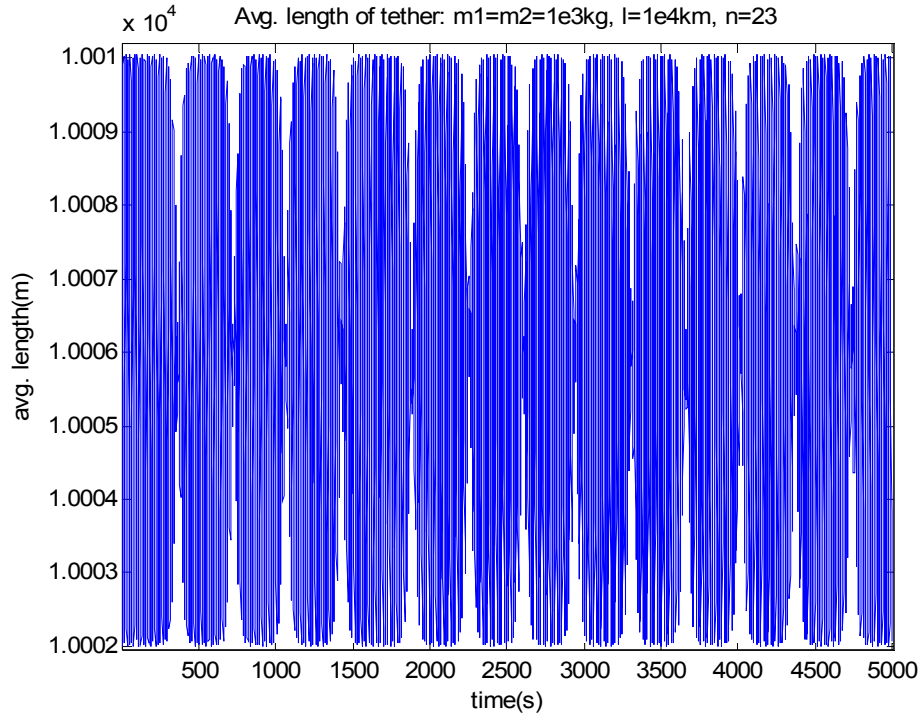


Figure 2.3-3: Average Tether Length over Case 5b

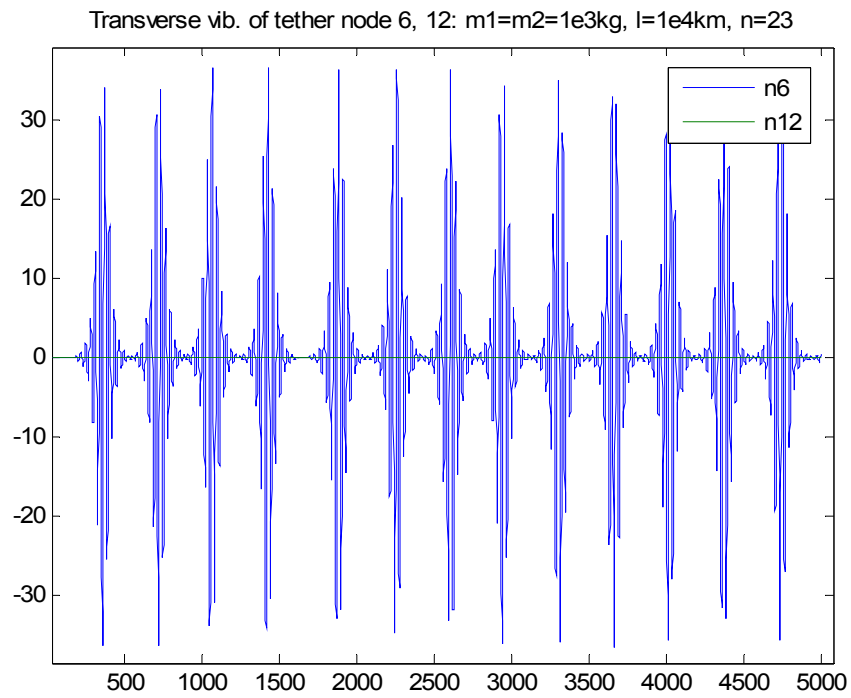


Figure 2.3-4: Mid and Quarter Node Vibration, Case 5b

TTU simulation results from case 5c:

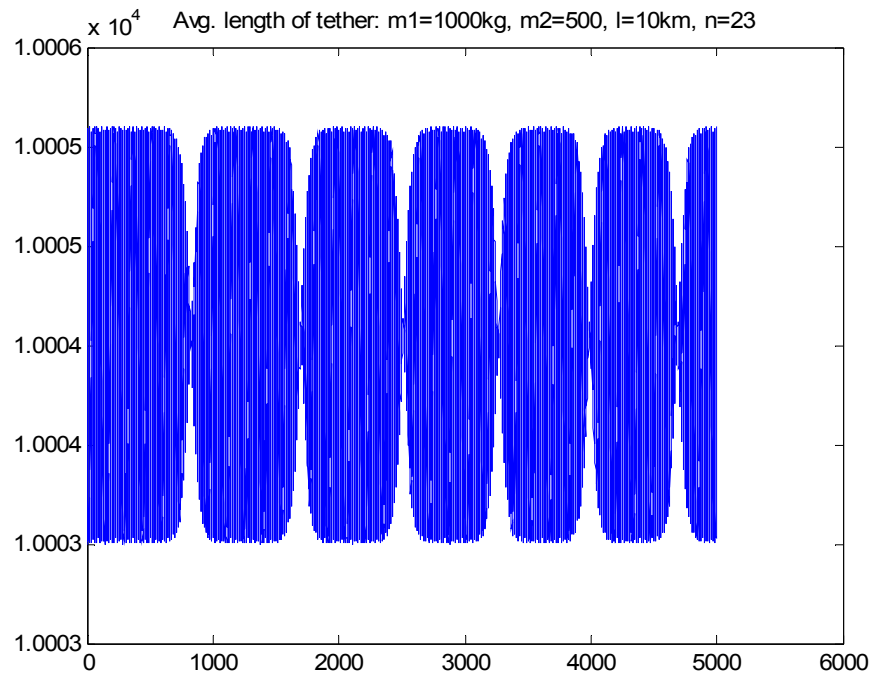


Figure 2.3-5: Average Tether Length over Case 5c

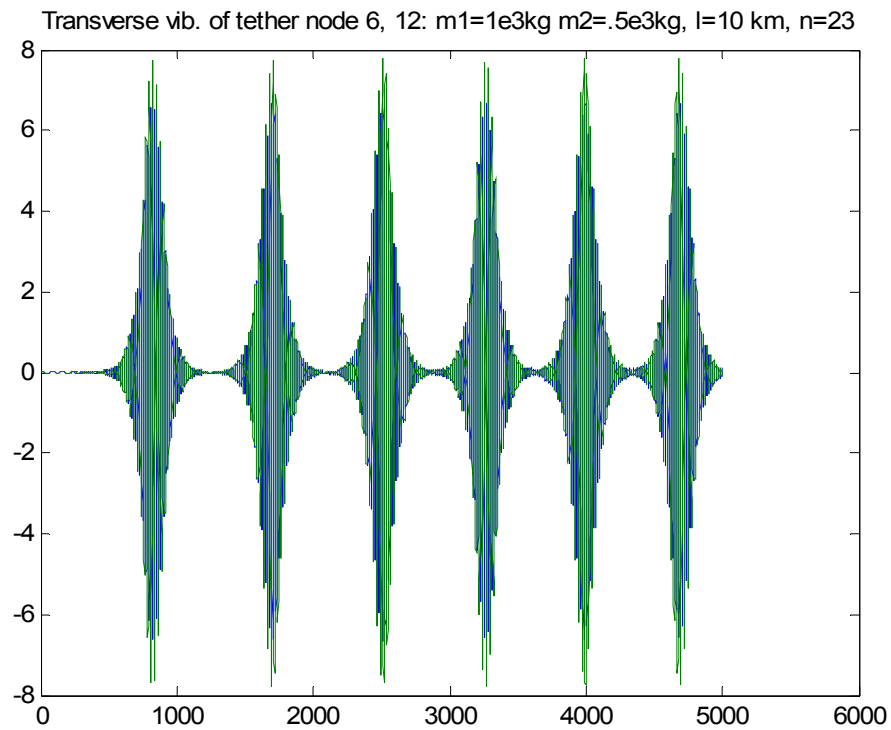


Figure 2.3-6: Mid and Quarter Node Vibration, Case 5c

TTU simulation results from case 6:

non-symmetric tether, $m_1= 1000\text{kg}$, $m_2= 500\text{kg}$, $l=10\text{km}$, initial stretch=.0004

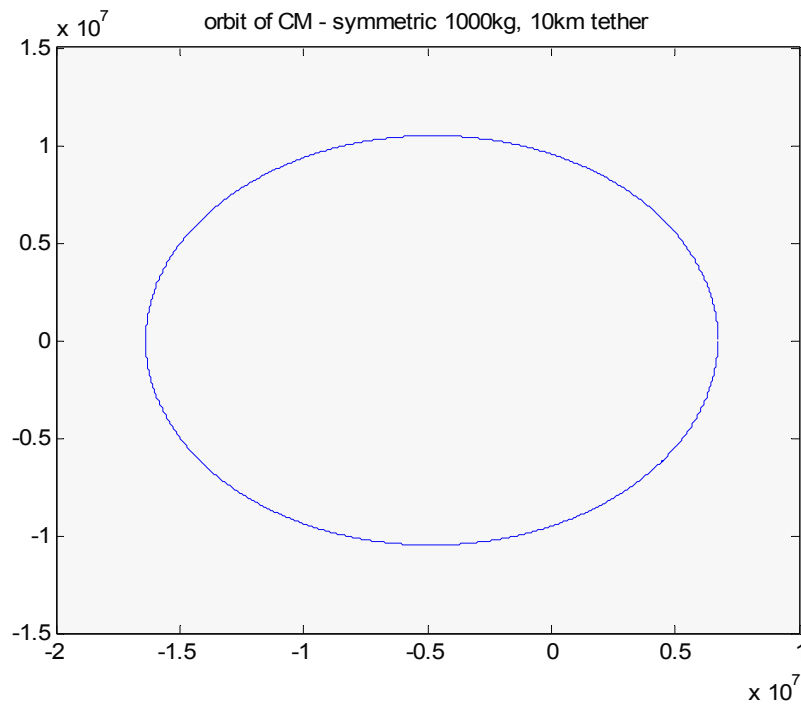


Figure 2.3-7: Orbit of Tether Center of Mass, Case 6

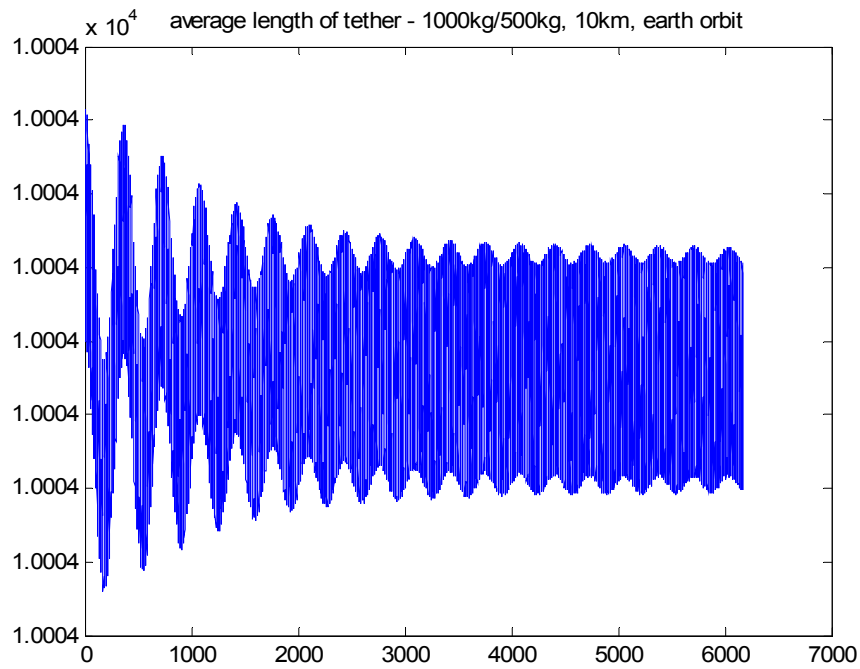


Figure 2.3-8: Average Length of Tether, Case 6

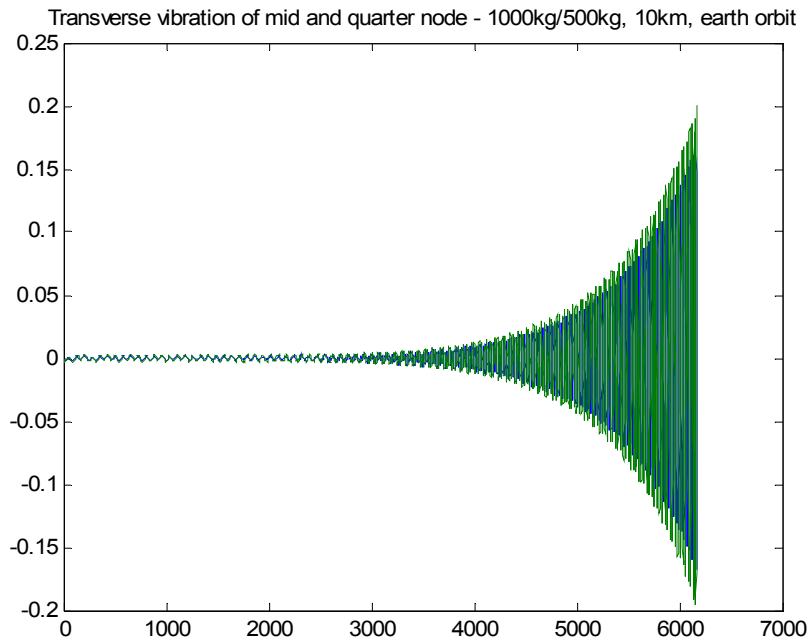


Figure 2.3-9: Mid and Quarter Node Vibration, Case 6

2.4 Discussion of Results

Sections 2.2 through 2.3 provide a variety of comparison of simulated tether response with known response functions as well as side-by-side comparison of tether response as predicted by independently developed models. These models are based on an identical set of equations of motion, but vary matters such as base coordinates and propagation approaches. Reasonable measures were taken to help minimize numerical error, such as the use of adaptive time step integration routines and monitoring the system energy (no damping is considered in these models). The examples are arranged in such a way that some cases consider tether motion absent of external excitation effects, while others consider the tether in a gravitational field (spherical gravity model). In general, these comparisons taken together

provide a good level of verification for the developed model, leading to a validated model for use in simulating the MXER tether system. Some observations are made on some of the specific cases considered here. In particular comparisons between a finite-difference based model (described in section 1) and an assumed-modes model (developed at the University of Delaware) will be discussed.

Case 5a considers a massless tether with symmetric endmasses, rotating in a deep-space environment (no external effects). Figures 2.3-1 and 2 show the predicted response for this case. Since the tether is massless, it is expected to behave as a linear spring vibrating in an extensive fashion according to the initial conditions. The models correspond readily and predict primary longitudinal period of approximately 13 seconds.

Case 5b extends case 5a by allowing dynamic effects of the tether mass (massive tether considered). Figures 2.3-3 and 4 show the predicted response for this case and again the models in general show positive agreement. Again, amplitude and period of longitudinal vibrations correspond (8 meters peak to peak with 15 second period). However, a departure in the predicted results is also observed, the finite-difference model developed in section 1 predicts a beating phenomena to occur that suggests a coupling between the longitudinal and transverse modes of vibration. Such a coupling is not seen in the assumed-modes-based model.

Case 5c considers a massive tether with non-symmetric end-masses, again rotating in a deep space environment, with results shown in Figures 2.3-5 and 6. As in case 5b, the models correspond in some aspects, such as amplitude of longitudinal vibration and period, but depart again in the suggested beating phenomena. The finite difference approach seems to predict a coupling in energy between the transverse and longitudinal vibration modes.

Finally, case 6 adds external forces to the model of case 5c, by placing this massive, non-symmetric end-mass tether in a circular earth orbit. The primary effects of longitudinal and transverse vibration are shown in Figures 2.3-7 and 8 for the two models. These primary effects are consistent in terms of amplitude and frequency data. Coupling between these modes is not evident in either approach.

In general, the comparison between the two alternative spatial integration approaches demonstrate reasonable agreement in most expected, linear-type behavior. The agreement in response is near complete in cases 5a and 6 considered. In the two central cases (cases 5b, c), considering a massive tether without external excitation, a phenomena (herein termed beating) is observed in the finite-difference-based approach, but not in the assumed-modes method. This dynamic behavior seems to be described as a coupling between the transverse and longitudinal modes, such that vibrational energy is passed from one to the other. This takes place with no net change in energy over time, as expected in these cases that do not consider any type of damping. The explanation, source or even verification that this is a dynamic phenomena and not numerical is currently unavailable. On one hand, it is possible that this is a nonlinear effect that is seen in the finite difference approximating technique, but not spanned by the modes used in this analysis. Alternatively, the approximations incurred by the finite difference method could generate unexpected numerical behavior. Due to correspondence in case 5a, the former is currently expected and an effort to identify the contributing nonlinear dynamic effect is underway. It should be noted that this coupling behavior is not observed in case four for an earth-orbiting tether. It is proposed that the external effects of gravity shift the frequencies in such a way that the beating phenomena is not seen in the time span considered, or may be eliminated completely. It should also be noted that in case 6, agreement is demonstrated in the tether modal behavior. However, it is noted that observing the motion of the center of mass would predict two different phenomena. In the finite difference approach, the center of mass is seen to migrate above and below

the keplerian orbit, as expected due to the gravity gradient effects on the rotating massive tether. However, due to the polynomial modes selected, the assumed-modes method does not permit motion of the tether center of mass off the local reference coordinate system, imposing an arbitrary constraint on its overall motion.

3.0 BASIC IMPLEMENTATION AND DEMONSTRATION

(In Selected Software Platform)

3.1 Tether Dynamic Models

(Formulation-Specific Algorithms)

The dynamic models and specific formulations appropriate for the MXER tether system have been demonstrated in Section B 1.0. The results of that section demonstrated a number of formulations, all of which require computational treatment (most through numerical solution techniques). This section (Section B, 3.0) will demonstrate specific algorithmic routines in diagram form through the use of flow charts. The algorithm flowcharts will first be presented in the most general form, showing the primary functions that need to be implemented and their relation to program flow control. Subsequent flowcharts will demonstrate the specific processes performed in the each function, and will present the variety of functional approaches dictated by the various formulations. A few notes are made for the following algorithm flow charts. The algorithms as suggested here will be implemented with strong dependence on the use of functions. Information passed to and from these functions will be presented within the flowchart. Further, unless additionally specified, the scope of any defined variables will be limited to its own functional block. Functional blocks will be demonstrated in the following flowcharts with the use of dashed border lines. An additional note regarding variables is provided. To add detail to the function-specific flowcharts, some variable names will be introduced and used in a general fashion. These variable names are introduced as a guideline rather than a necessity for developing subsequent code. Of more importance is the variable structure suggested in these flowcharts, with the tether state contained as a one dimensional array, \mathbf{S} containing specific state vectors in the order of \mathbf{r} , \mathbf{v} , $\boldsymbol{\chi}$. As a final note, this section is designed to detail the computational implementation and ease code design. To do this, the flow charts will be grouped together at the end of the descriptive text, with each flow chart occupying one page allowing the flowchart to be printed or copied and tagged as a description to each computational function.

1. The general program formulation for evaluation tether dynamics over a period time is first presented as shown in Figure 3.1-1.

Functions to define initial conditions as well as techniques for post-processing are general to most problem formulations and will be presented later in this document.

2. The first specific instance of the general formulation of the dynamics main code is presented next. This first formulation implements a fourth-order Runge Kutta time integration routine and a three-point finite difference spatial approximation routine as shown in Figure 3.1-2. Function-specific details then follow in flowcharts Figure 3.1-3 for the time integrator and Figure 3.1-4 for the EOM/finite difference routine.

Note that the evaluation of forces on the tether still exists as a function block. Evaluation of the tether force merits significant discussion and detail which will follow later. Note that full consideration of tether forces will most likely include a number of dynamic, gravitation and aerodynamic models which

will be called upon as independent functions made available from a variety of sources (indicated in a general format in Figure 3.1-5). Current implementation however considers only a simple gravity model that is embedded completely within the EOM function.

3. A second implementation of the general tether dynamic simulation routine considered will implement an alternative integration routine based on the Adams-Bashforth-Moulton technique (Hoffman, 2000). This implementation will be based on the same Dynamics-Main function demonstrated in Figure 3.1-2 with the new (ABM) integration technique inserted. The detailed implementation of the ABM integration routine is demonstrated in Figure 3.1-6

The general algorithm determining initial conditions is given in Figure 3.1-7. This code takes in tether design and orbit parameters and returns the tether initial state as well as the properties structure.

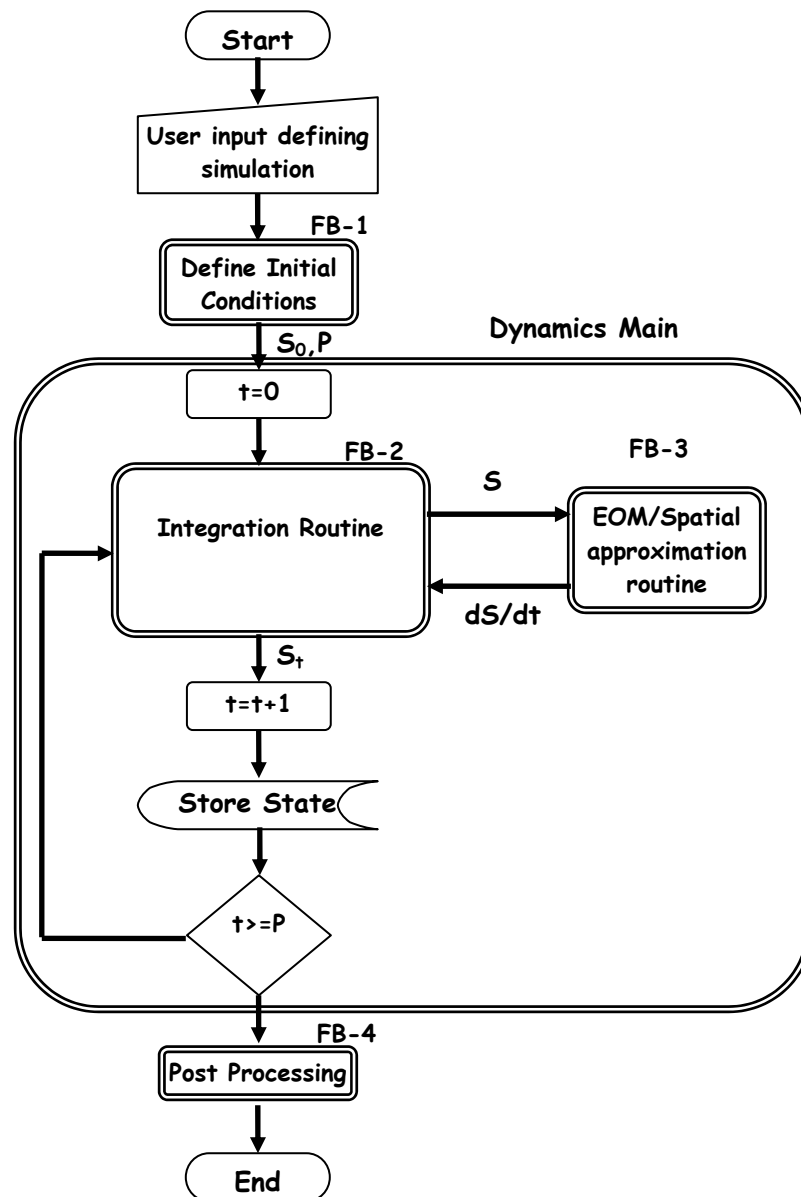


Figure 3.1-1: Flow Chart, General Tether Dynamics Integration

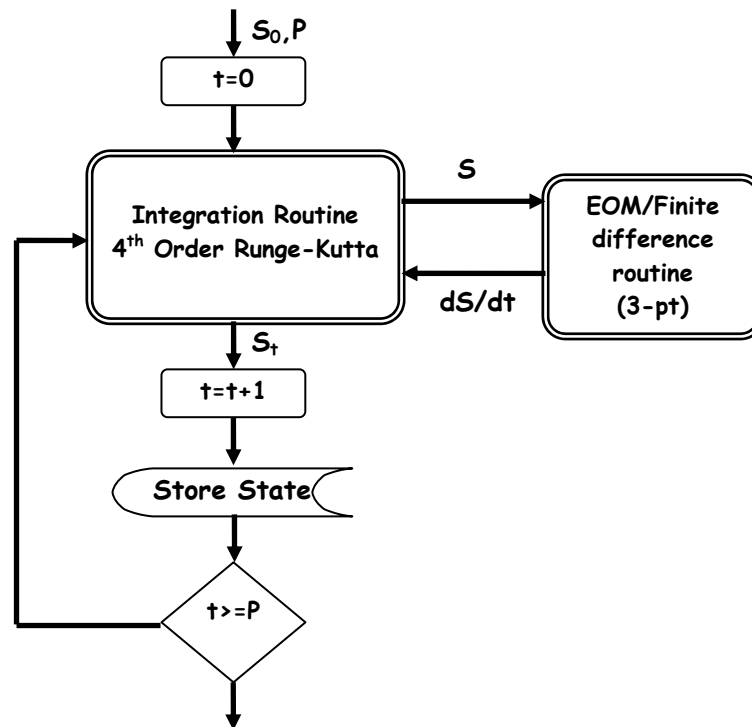


Figure 3.1-2: Flow Chart, Overview of Runge Kutta Routine

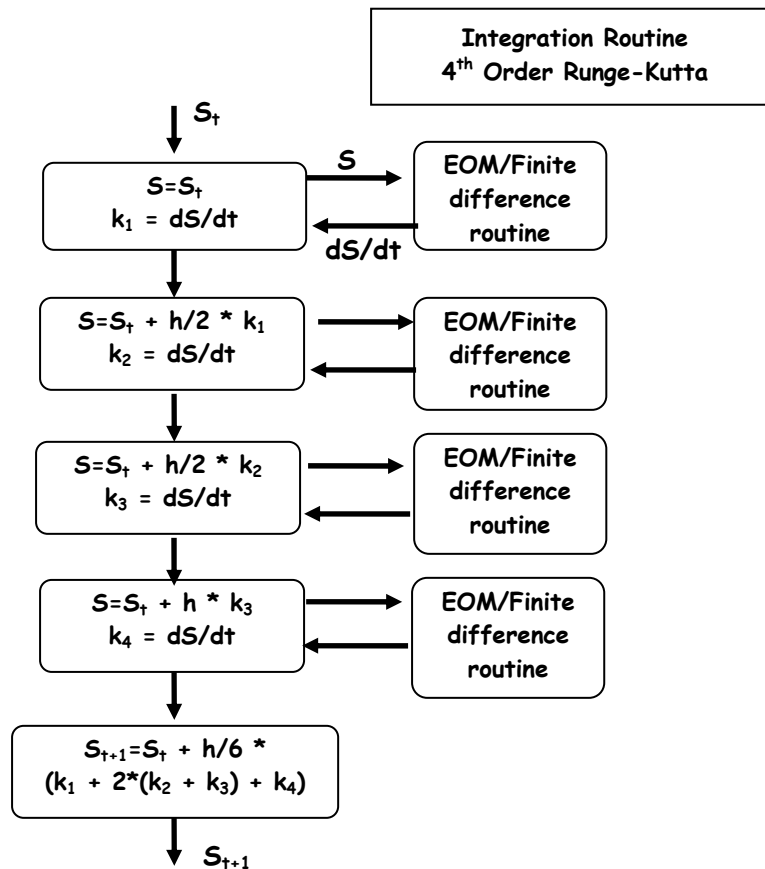


Figure 3.1-3: Flow Chart, Details of 4th Order Runge Kutta

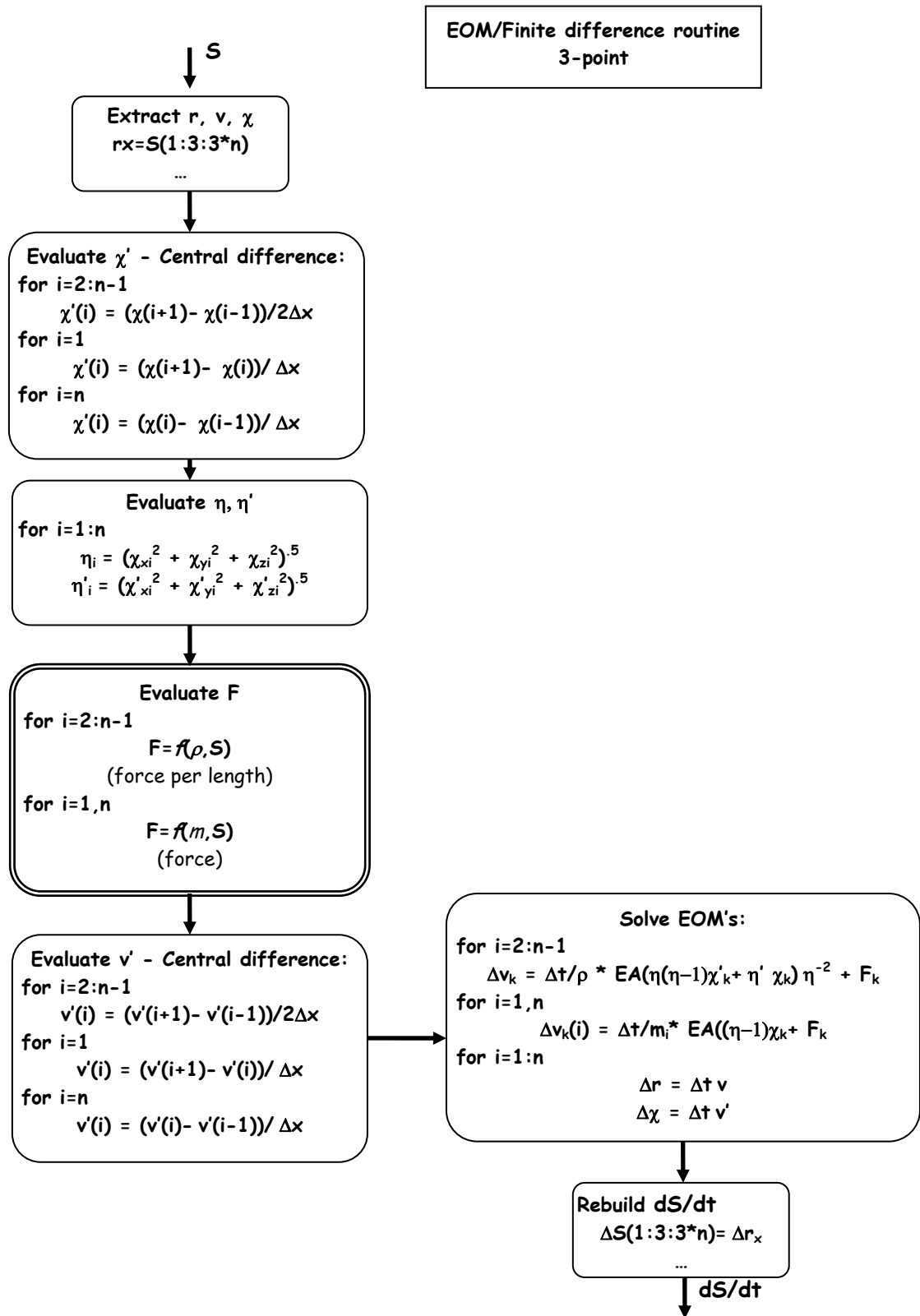


Figure 3.1-4: Flow Chart, Overview of 3-Point Spatial Difference Routine

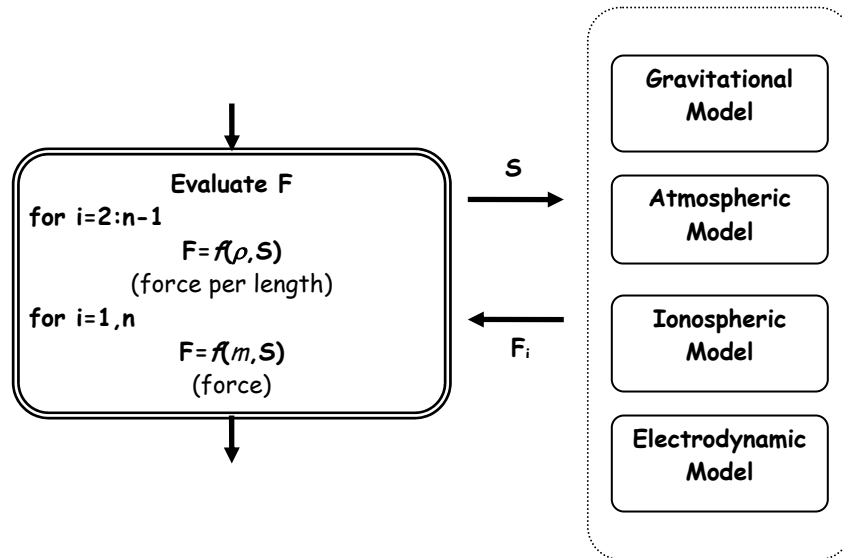


Figure 3.1-5: Flow Chart, Obtaining Tether Force Components

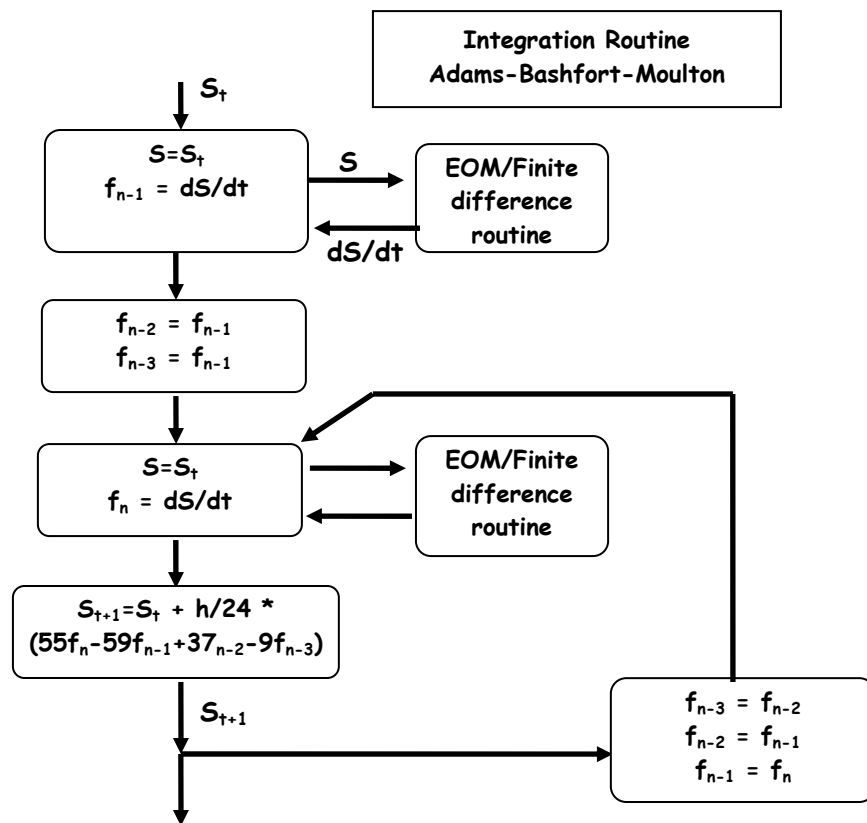


Figure 3.1-6: Flow Chart, Adams-Bashfort Mouton Integration

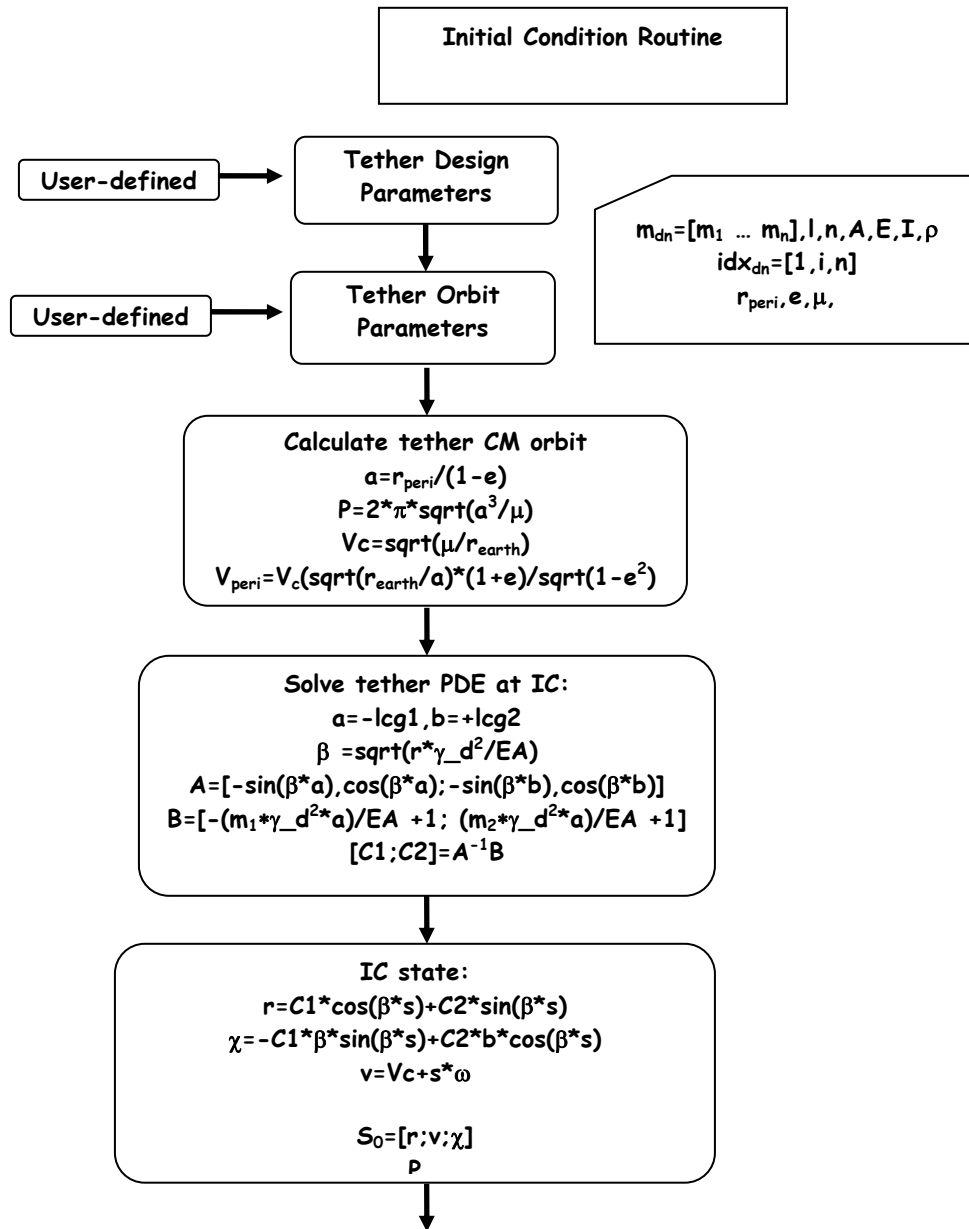


Figure 3.1-7: Flow Chart, Obtain Initial Conditions

4.0 BASIC APPLICATION OF THE DYNAMIC MODEL

(As A Simulation, Analysis and Design Tool)

Based on the models (section 1) and algorithmic implementation (section 3), general software is developed for implementation. This implementation has been conducted on three primary platforms, Matlab, C++ and Adams. Code listings for the developed software are included in Appendix B.4. This code has been demonstrated as an analysis and design tool in section A.1 of this report for example, where the dynamic modeling code is used as a basis for stochastic sampling of the tether propagation process.

5.0 DEVELOP INITIAL AND BOUNDARY CONDITION MODELS

Initial conditions for the tether are derived from a tether model that is reduced to the level of analytical solution. The assumptions that give this reduction include a uniform tether, constant rotation rate and absence of gravity gradients. The initial conditions are derived here with a reference location selected as the instant center of the tether at the initial state as shown in Figure 5.0-1.

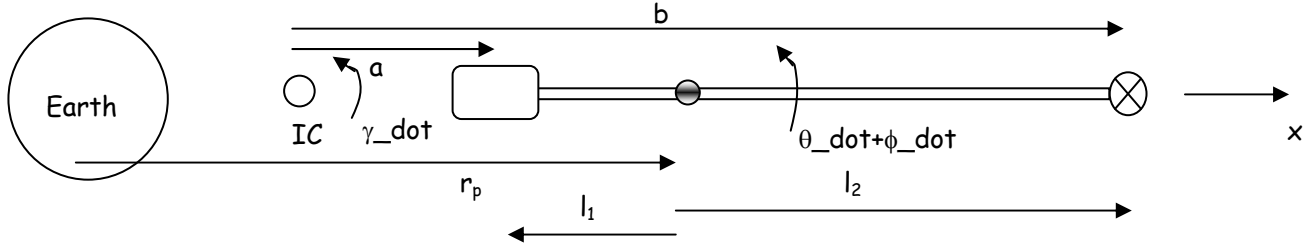


Figure 5.0-1: Schematic of Tether Configuration to Provide Steady State Initial Conditions

Consider nominal tether motion with instant center of rotation as shown in Figure 5.0-1. The initial parameters given are; end masses, tether nominal length, uniform tether, end mass and center of mass velocities. Additional parameters in Figure 5.0-1 are determined as;

$$\dot{\gamma} = \dot{\theta} + \dot{\phi} \quad 6-1$$

$$a = \frac{l}{1 - v_1/v_2} - l, b = \frac{l}{1 - v_1/v_2}, l = l_1 + l_2 \quad 6-2a-c$$

and

$$a_o = \frac{v_1^2}{(r_p - l_1)} - \dot{\gamma}^2 a \quad 6-3$$

is the acceleration of the instant center in a direction aligned with the tether. The tether's initial state referenced from the instant center is shown in Figure 5.0-2.

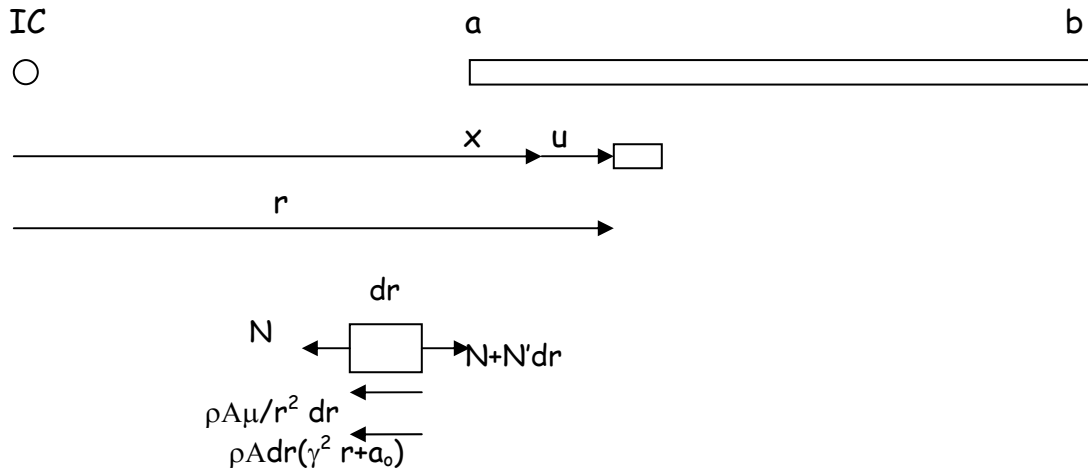


Figure 5.0-2: Free Body Diagram of Tether Element

Equations of motion for an element in the initial tether is;

$$N' - \rho A \frac{\mu}{r_p^2} = -\rho A (\dot{\gamma}^2 r + a_o) \quad 6-4$$

with

$$\begin{aligned} N &= EA\varepsilon = EA(r' - 1) \\ N' &= EA r'' \end{aligned} \quad 6-5a,b$$

Equation 6-4 becomes

$$r'' + \frac{\rho \dot{\gamma}^2}{E} r = \frac{\rho}{E} \left(\frac{\mu}{r_p^2} - a_o \right) \quad 6-6$$

with the solution,

$$r = C_1 \cos(\beta x) + C_2 \sin(\beta x) + \left(\frac{\mu}{r_p^2} - a_o \right) \quad 6-7$$

$$\beta = \frac{\rho \dot{\gamma}^2}{E}. \quad 6-8$$

The two constants in Eq. 6-7 are determined from the following two boundary conditions.

At $x=a$,

$$r'(a) = \frac{m_1}{EA} \left(\frac{\mu}{r_p^2} - (\dot{\gamma}^2 a + a_o) \right) + 1 = -C_1 \beta \sin(\beta a) + C_2 \beta \cos(\beta a) \quad 6-9$$

At $x=b$,

$$r'(b) = \frac{m_2}{EA} \left((\dot{\gamma}^2 b + a_o) - \frac{\mu}{r_p^2} \right) + 1 = -C_1 \beta \sin(\beta b) + C_2 \beta \cos(\beta b) \quad 6-10$$

Yielding the coefficient solution,

$$\begin{Bmatrix} C_1 \\ C_2 \end{Bmatrix} = \begin{bmatrix} -\sin(\beta a) & \cos(\beta a) \\ -\sin(\beta b) & \cos(\beta b) \end{bmatrix}^{-1} \begin{Bmatrix} \frac{m_1}{EA} \left(\frac{\mu}{r_p^2} - (\dot{\gamma}^2 a + a_o) \right) + 1 \\ \frac{m_2}{EA} \left((\dot{\gamma}^2 b + a_o) - \frac{\mu}{r_p^2} \right) + 1 \end{Bmatrix}. \quad 6-11$$

With coefficients C_1 and C_2 known, the initial state is given in Eq. 6-7 for the position coordinates and

$$r' = -C_1 \beta \sin(\beta x) + C_2 \beta \cos(\beta x). \quad 6-12$$

Figure 5.0-3 below plots a sample resulting initial value (η) for a tether case.

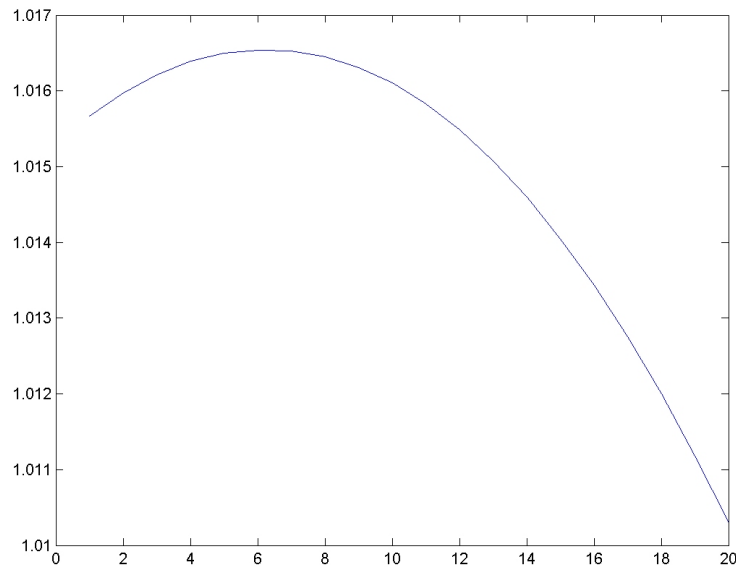


Figure 5.0-3: Tether Strain Over Length for Steady State Initial Condition

6.0 RESULTS AND CONCLUSIONS:

This report has described the significant activities that were performed by the TTU organization during 2004-2005 on the MXER tether system. Significant results of these activities include the following;

1. A capture mechanism was developed, designed, fabricated and tested. This mechanism demonstrated robust and reliable capture within the design parameters of the tests. Further, within the assumptions of tether motion prediction capabilities, it is believed that this mechanism will provide allow the MXER system to achieve its necessary rendezvous and capture process. While the final stage of capture, release, was not specifically addressed, it is considered to be a tractable issue within the design capabilities of the proposed mechanism.
2. A series of other mechanisms were proposed and are considered realistic alternatives to achieving MXER tether system capture. The advantage of multiple options is believed to be significant. Further development, design and testing would be necessary to achieve the same confidence in these mechanisms as in the primary proposed mechanism (Quad-Trap).
3. A facility was developed that provides a dynamically realistic environment for testing scaled MXER tether capture mechanisms.
4. Dynamic models suitable for the elastic, rotating MXER tether have been developed, along with associated algorithms. Multiple formulations of these models are demonstrated.
5. A rigorous validation of the dynamic modeling capabilities for the MXER tether system was conducted. This process consisted of several components, including comparison with closed form solutions, limiting cases and comparisons over multiple codes developed by different groups. The result includes validation of specific dynamic models as well as the development of a series of test cases.

6. Significant nonlinear effects are recognized in the tether behavior that have not been reported in the literature. The ability to accurately characterize such nonlinear behavior represents the level of fidelity that may be desired in such code.
7. The models and algorithms developed in this work are recognized to be limited in terms of processor demands relative to other algorithms that have been developed. However, the primary, significant contribution of this effort is to serve as a tool that will allow the development and verification of time-efficient codes.

SECTION C—ERROR SPACE PREDICTION

This section presents a formal paper prepared for submission to AIAA journal transactions

Error Space Prediction and Dynamic Response of Passive Capture Mechanisms in Tether Momentum Exchange

Momentum-exchange/electrodynamic reboost (MXER) tether systems may enable high-energy missions to the Moon, Mars and beyond by serving as an "upper stage in space". Existing rockets that use a MXER tether station could double their capability to launch communications satellites and help improve US competitiveness. A MXER tether station would boost spacecraft from low Earth orbit to a high-energy orbit quickly, like a high-thrust rocket. Then, using the same principles that make an electric motor work, it would slowly rebuild its orbital momentum by pushing against the Earth's magnetic field-without using any propellant. One of the significant challenges in developing a momentum-exchange/electrodynamic reboost tether system is in the analysis and design of the capture mechanism and its effects on the overall dynamics of the system (Sorensen, 2001)¹. This paper will provide qualitative and quantitative information about the nature of the capture window due to parametric uncertainties in the MXER tether and will consider the dynamic effects of capture at various locations within this error window.

Nomenclature

ρ	=	tether material density
A, I	=	tether cross sectional area, area moment of inertia
E	=	tether modulus
m_1	=	facility mass
m_2	=	capture-end mass
v	=	velocity
r	=	position
ε, η	=	strain
F	=	force
χ	=	spatial derivative of position
κ	=	absolute value of χ
X	=	state vector
a	=	acceleration
R	=	orbital radius
μ	=	gravitational constant
C_1, C_2, β	=	constants of integration
x_c, y_c	=	centroid
I_{xx}, I_{yy}, I_{xy}	=	mass moment of inertia
a, b	=	error ellipse major and minor axes
σ	=	standard deviation

Introduction

A critical component in the development of a MXER tether system is an appropriate capture device, which will accommodate kinematic and dynamic variation between the tether and payload during the rendezvous and capture process. Further, it is desirable to do this as efficiently as possible through the design of a passive capture mechanism. Therefore, a necessary step in the design of this capture mechanism is to define the kinematic and dynamic requirements for this device. This paper will attempt to address this need through developing qualitative and quantitative information about the nature of the capture window due to uncertainty in input parameters in the MXER tether model. This data will form a capture window and will be used to guide the design of an appropriate capture mechanism devices to ensure reliable rendezvous between the MXER tether system and its target payload. This information will consist of an estimation of the geometric nature of the capture window, both in shape, size and orientation relative to the tether as seen by the payload. The capture window will be based on a heuristic assumption for its geometric form. Confirmation and quantitative evaluation of the properties of this error geometry will be determined stochastically through the use of a Monte Carlo simulation based on

uncertainty in tether parameters within an elastic numerical tether model. Transformations are introduced to express the stochastic error data in terms of geometric parameters relative to the tether motion. Information from these analyses can be used in both capture mechanism design and will indicate bounds for the capture process based on stability of tether motion.

Past research in the field of space tether modeling has seen a significant amount of work in modeling the dynamic characteristics of these systems (see for example [1-3] (Misra, A.K. and Modi, Beletsky and Levin, Quadrelli, B.M., and Lorenzini, E.C)). The proposed space tether application as a momentum exchange vehicle requires information about the location of the tether tip at time of capture and the sensitivity of the tether tip location to parametric variance. However, studies of sensitivity of tether model dynamics due to parametric variance are much more limited in the field of space tethers. The few examples that are available are briefly mentioned. Tragessar et al., consider stochastic error effects on tether-based aerocapture [4]. Pelaez and Lorenzini consider sensitivity of unmotorized deployers such as the SEDS (Small Expendable Deployment System) on tether-based satellite injection [5]. Finally, Leamy et al. develop sensitivity coefficients for electrodynamic response of bare-wire tether systems [6]. While these papers develop considerations based on tether sensitivities, a sensitivity model that will allow extension to the rendezvous capture process associated with the MXER tether system is needed and is the focus of this paper.

The remainder of the paper will proceed in the following manner. First, a summary of the numerical tether model used for simulation is provided. Then, the Monte Carlos simulations are performed to result in predictions of the capture error box. Appropriate transformations are defined to express the error values into a geometric form for the capture window and are evaluated for the various simulations performed. Analysis of the dynamic behavior over these capture windows is conducted and presented through a series of phase portraits. Finally, the results of these efforts and their implications on capture mechanism design are presented.

Overview of the Tether Momentum Exchange Model

The equations of motion for an elastic space tether within its orbital plane are derived using Newton mechanics, in a manner similar to that presented by Kohler et al, (1978)². The resulting equations, which consider both axial and flexural stiffness of the tether, are given as,

$$\rho A \dot{v}_j = EA[\eta' \chi_j + (\eta - 1)\eta \chi_j'] \eta^{-2} + EI[\eta(\kappa'' \chi_k + \kappa' \chi_k') - 2\eta' \kappa' \chi_k] \eta^{-3} + F_j, \quad (1)$$

$$(j,k) = (x,y), (y,x),$$

with tether parameters ρ , E , A , and I representing tether density, modulus, area and area moment of inertia respectively, F_j the external force on the tether, trailing primes represent spatial derivatives (with respect to the geometric coordinate), overdots represent time derivatives and parameters η, χ and κ , are defined as,

$$\eta = \varepsilon + 1 = \frac{ds^*}{ds}, \quad (2)$$

$$\chi = \frac{\partial r}{\partial s} \quad (3)$$

and

$$\kappa = \sqrt{\chi_x'^2 + \chi_y'^2 + \chi_z'^2} \quad (4)$$

$$\kappa' = [\chi_x' \chi_x'' + \chi_y' \chi_y'' + \chi_z' \chi_z''] \kappa^{-1} \quad (5)$$

$$\kappa'' = [-[\chi_x' \chi_x'' + \chi_y' \chi_y'' + \chi_z' \chi_z''] \kappa' + [\chi_x' \chi_x''' + \chi_x'' \chi_x'' + \dots] \kappa] \kappa^{-2} \quad (6)$$

with ε the tether strain and s and s^* the tether parameteric coordinate based on stretched and unstretched length respectively. The equations defined in terms of the time and spatial derivatives of \mathbf{r} defined in the state vector, \mathbf{X} as,

$$\mathbf{X} = \begin{Bmatrix} \mathbf{r} \\ \mathbf{v} \\ \chi \end{Bmatrix} = \begin{Bmatrix} \mathbf{r} \\ \partial \mathbf{r} / \partial t \\ \partial \mathbf{r} / \partial s \end{Bmatrix} \quad (7)$$

The equations of motion (1) are second order in time and fourth order in space. For this system, four boundary conditions and the initial state are required. The boundary conditions will be defined as the end force and moments that satisfy the equations of motion for the end bodies, given in the following equations as,

$$m_{b1} \mathbf{a}_{b1} = -\frac{\rho A \dot{\chi}^2 \chi}{\eta} \bigg|_{(0,t)} + \mathbf{F}_{b1} + \frac{EA(\eta-1)\chi}{\eta} \bigg|_{(0,t)} \quad (8)$$

$$m_{b2} \mathbf{a}_{b2} = -\frac{\rho A \dot{\chi}^2 \chi}{\eta} \bigg|_{(l,t)} + \mathbf{F}_{b2} + \frac{EA(\eta-1)\chi}{\eta} \bigg|_{(l,t)} \quad (9)$$

$$\chi' \big|_{(0,t)} = 0 \quad (10)$$

$$\chi' \big|_{(l,t)} = 0 \quad (11)$$

with m_{b1} , m_{b2} , \mathbf{F}_{b1} , and \mathbf{F}_{b2} the mass and force at the tether boundaries. Initial conditions for the tether are derived by considering the tether in an instantaneous sense, with the tether lying along the axis of true anomaly and its motion described as pure rotation about an accelerating instant center. In this initial case, gravity gradient effects are also ignored. This allows the tether to be described with a partial differential equation that can be solved in closed form;

$$EA r'' + \rho \dot{\gamma}^2 r = \rho \left(\frac{\mu}{R^2} - a_0 \right) \quad (12)$$

with r describing the initial position of points along the tether relative to the instant center, $\dot{\gamma}^2$ the rotation rate of the tether about its instant center, μ the gravitational constant, R the distance of the tether center of mass (from earth center) and a_0 the acceleration of the center of mass. From Eq. (12), the initial state can be solved as,

$$r = C_1 \cos(\beta x) + C_2 \sin(\beta x) + \left(\frac{\mu}{R^2} - a_0 \right) / \dot{\gamma}^2 \quad (13)$$

with x the undeformed positions of the tether a coefficients C_1 and C_2 determined from the equations of motion for the tether end-bodies.

The tether equations of motion given in Eq. (1) along with the tether along with boundary conditions initial conditions are solved in time to give a simulation of the tether. The numerical algorithm employed in this work uses a finite difference approach to transform the governing equations for the tether into a system of ordinary differential equations that are integrated in time using a This model used a Runge-Kutta-Fehlberg formula [7]. The solution is validated through comparison with solutions presented by Fried [8] and Henghold and Russell [9] for an earth-based dynamic cable system, and through comparison with exact derivations of a space tether modeled as a two-mass orbital system connected by an extensible mass-less rod.

Monte Carlo Simulation Approach

A prediction of the capture window as seen by an observer on the payload is constructed based on uncertainties in the tether parameters. The capture window will be defined as the spatial region of computed tether tip positions relative to the payload at the point of capture. For this effort, the capture window will be initially described geometrically as an ellipsoid, with an assumed normal distribution (i.e., the relative position or error between tether tip and payload is distributed normally). This window will be called an error ellipsoid. The spatial region of tether tip error will be generated using the Monte Carlo technique and will consider stochastic uncertainties in the tether input parameters. In particular, the Monte Carlo method employed here is that which Morgenthaler [10] has termed model sampling with the primary variability in the system assumed to come from uncertainty in tether parameters.

The Monte Carlo simulation will be conducted as follows. Numerical simulation of the MXER tether model is conducted using the model given in part II, starting from a steady state condition of the tether on orbit and ending when the tether reaches the point of capture. This numerical simulation is conducted repetitively with stochastic variation in tether parameters in place to yield variability between the payload and tether tip at the defined point of capture. The collection of this output positional variability then results in the data for the desired capture window. With an eye toward the eventual purpose of the error window analysis, the capture window will be assumed to take the geometric form of an ellipse (ellipsoid) which can be described in terms of center and major and minor axes. The span of the capture window can now be defined based on the major and minor axes of the error ellipse. The distribution of this data within the ellipse will also be assumed to be normally distributed. A comparison of the Monte Carlo simulation results with this assumed form will be conducted to ensure the reasonable nature of these assumptions.

The Monte Carlo method is selected for use in this paper based on its generality and adaptability in implementation. As indicated by Kushner et al., [11] the Monte Carlo method is advantageous in highly nonlinear problems, is insensitive to system dimensionality and is demonstrated to provide a robust result for sensitivity estimates. Further, the programming algorithm based on the Monte Carlo approach provides a means to avoid numerical integration or derivation and provides reasonable convergence as demonstrated by Thompson and Cluett [12], [13].

Implementation

The primary details for implementing the Monte Carlo simulation involve definition of parameter variability and proposed models for defining the point of capture. Stochastic variability in the tether parameters is assumed to be purely random or white noise with no correlation between parameters or successive parameter values [13] centered about the parameter nominal value with a normal distribution. Table 1 lists the specific tether parameters that will be varied along with their nominal (mean) value and standard deviation. The mean parameter value is assigned as the baseline nominal parameter value while the standard deviation is assigned and 1/3 the maximum variation expected of a given parameter. Table 2 provides the remaining parameters used in defining the tether and payload system model.

Table 1: Specific Tether Parameters

Parameter	% Variation
Capture Mechanism Mass	0.01
Ballast Mass	0.01
Total Tether Length	0.01
Cross Sectional Area	1
Elastic Modulus	2
Mass Moment of Inertia	0.01
Mass Per Unit Length	0.01

Table 2: Tether and Payload Parameters

Constants		1.1.1.1.1.1.1 Tether Facility Orbit	
μ	3.986E+14	Perigee (m)	6,785,136.00
Payload Mass (kg)	1000, 2500	Apogee (m)	14,823,136.00
Capture Mass (kg)	250	Time for one orbit (s)	11,176.25
Ballast Mass (kg)	11000	SMA	10,804,136.00
Tether Length (m)	90000	e	0.371987172
Cross Sect Area (m ²)	1.9635E-05	Perigee Velocity (m/s)	8977.690593
ρ (kg/m ³)	970	Apogee Velocity (m/s)	4109.444293
Payload orbit		ω of tether fac. (rad/s)	-0.013881192
Orbit Radius (m)	6694275.739		
Vp (m/s)	7716.44186		
Time for one orbit (s)	5450.876936		

The overall process consists of repetitive evaluations of individual tether simulation. At the beginning of each tether simulation, values for in the input parameters with variance are selected in a random fashion. Each tether simulation will begin with the tether in a state of uniform strain (0.4% strain) one orbit prior to capture. The initial state will assume to be a known condition and therefore will not be considered as a parameter of uncertainty in this analysis. The tether simulation will continue to the point of capture, which is defined below. Upon reaching the point of capture, the error in capture (position of tether relative to payload) is determined and stored and the individual tether simulation is complete. The procedure will then continue with random variation in input parameters defined. The stopping criterion is given as a pre-defined number of iterations.

Defining point of capture:

The resultant error in capture that occurs in each tether simulation is recorded as the vector from the payload to the tether tip at the point of capture. Since the goal of this work is to develop a capture window as the starting point for the design of a passive capture mechanism, point of capture will be considered the ideal capture position that occurs (i.e., point of minimum distance between tether tip and payload). Note that the ideal capture position is a function of the orbits of the tether and payload. However, the scope of this paper considers variability in the tether model only and therefore will consider the payload orbit in an ideal sense. It still remains that the capture process is a function of space and time and could be specified in varying ways. This paper will consider the capture event over three possible definitions for point of capture; the first temporal, the second spatial, and the third a combination of space and time.

Capture method 1: In the first method, the point of capture is defined to occur at a fixed, specific point in time. Capture error is measured as the position vector from the payload to the tether tip at the point of capture. The location of the payload is fixed in space and defined such that zero capture error results when the nominal tether parameters are used. Since the simulation will nominally consider one full orbit of the MXER tether, the end of period of the tether will be chosen as the time for capture, and this method will be referred to as End Of Period (EOP).

Capture method 2: In the second method, the point of capture is defined to occur when the tether tip reaches its minimum distance to the payload where the payload position is fixed and defined uniquely as the location of the tether tip at a specific point in time such that zero capture error results when the nominal tether parameters are used.. Since this method looks for the closest approach of the tether to a fixed payload point, it will be referred to as Closest Approach (CAP).

Capture method 3: In the third method, the point of capture is defined to occur when the tether tip reaches its minimum distance to the payload where the payload is now defined as a point mass traveling on a keplerian orbit such that zero capture error results when the nominal tether parameters are used. Since this method considers an orbiting payload, it will be referred to as ORBit (ORB).

Capture Window Results

The resulting data from the Monte Carlo simulations over the three methods of capture are shown in the following graphs. This data is plotted in a tether-tip frame with the x axis the line connecting the two ends of the tether, the y axis normal to x and lying in the orbital plane and the zero error position defining the origin of these axes. The resulting error data is shown in Fig. 1-3 for tether capture method 1-3 respectively. The data in each case represents 250 data points.

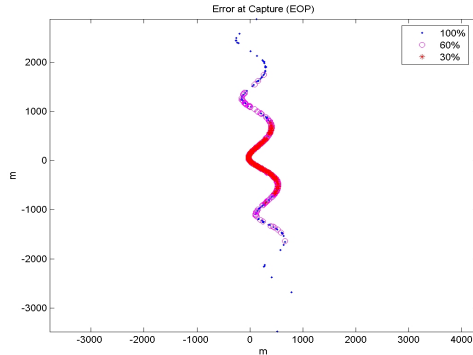


Figure 1, case 1

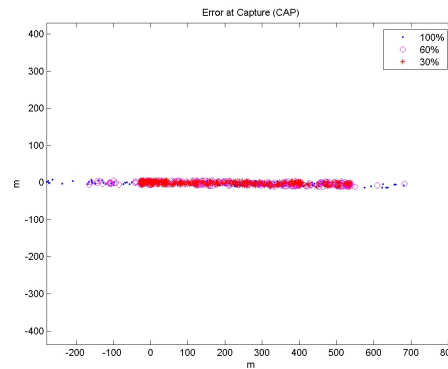


Figure 2, case 2

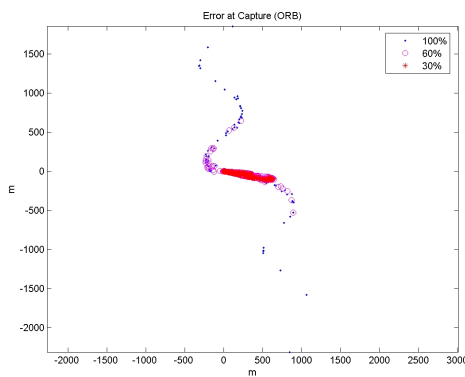


Figure 3, case 3

Figure 1-3: Tether tip uncertainty plots for case 1, 2 and 3

It is desired to mathematically describe these capture windows parametrically such that they can be defined in terms of a frame corresponding to axial and transverse displacements of the tether tip. A transformation is defined by considering error plots as a collection of error particles each with equivalent weighting. The density of error points resulting from the Monte Carlo simulation gives the form and density of this error body. This body can be described in terms of its centroid and equivalent moment of inertia, both given in base-frame coordinates, with centroid defined as;

$$x_c = \frac{\sum_{i=1}^n x_i dm_i}{\sum_{i=1}^n dm_i} \quad y_c = \frac{\sum_{i=1}^n y_i dm_i}{\sum_{i=1}^n dm_i} \quad (14)$$

and body inertia tensor;

$$\mathbf{I} = \begin{bmatrix} \sum_{i=1}^n y_i^2 dm_i & -\sum_{i=1}^n x_i y_i dm_i \\ -\sum_{i=1}^n x_i y_i dm_i & \sum_{i=1}^n x_i^2 dm_i \end{bmatrix} \quad (15)$$

with dm_i representing a single error particle with position x_i , y_i . and having unit mass.

With the equivalent inertia tensor defined, the principle inertia and principle directions can be determined. The principle direction will define the orientation of the capture window relative to the tether while the principle inertias will be used to define the direction of major influence of the capture window.

The capture window will now be described in the form of an ellipse (called error ellipse). Assuming a uniform density (albeit unknown) of the ellipse, the principle inertias defined in terms of the major and minor axes (a , b) are equated to the numerically derived values, resulting in closed form solutions for the ellipse axes as follows;

$$a^8 = \frac{16I_{\max}^3}{\pi^2 I_{\min}}; b^8 = \frac{16I_{\min}^3}{\pi^2 I_{\max}}; \quad (17)$$

or as preferred, defined as ellipse eccentricity and radius at perigee.

The error ellipse can now be described in terms of its eccentricity, axes, a and b and its orientation relative to the tether, θ . This ellipse that contains 99.7% of the error points will be called the 3σ error ellipsoid, such that standard deviation for the major and minor axes is defined as;

$$\sigma_a = \frac{a}{3}; \sigma_b = \frac{b}{3}; \quad (18)$$

The results for the three cases considered above are shown in Table 3 and in Fig. 2. The table reports the results for the equivalent principle inertia's, orientation, and error ellipse major and minor axes for the three cases considered in tether parameter error. The figure demonstrates an error ellipsoid plotted over the error estimate points for case 1.

Table 3: Error Ellipsoid Parameters for cases 1, 2 and 3

	Centroid (m)	I_{\max} (m ⁴)	I_{\min} (m ⁴)	θ (deg.)	a (m)	b (m)	σ_a (m)	σ_b (m)
CASE 1	(10.8,-.11)	1.3007e6	1.0941e3	8.6e-3	86.9	2.52	28.7	0.83
Case 2	(37.1,0)	5.2739e7	1.4194e6	-2.1e-3	142.2	23.3	46.9	7.69

Analysis of Tether Behavior through Rendezvous with Payload

The resulting error windows observed for capture definitions of cases 1-3 are now considered. It is observed that the results from case 2 and 3 seem well suited to the error ellipse definition, each with major axis generally aligned with the tether. However, the error ellipse generated for case one does not seem to provide as good a descriptor of the error data, rather the error data seems to be aligned along an approximate sinusoidal curve. Further, in this case the major axis of this ellipse is generally orthogonal to the tether axis. To better explain the motion resulting from case 1, the end of period evaluation, a survey of tether tip motion is conducted for a variety of inputs, as shown in figure 4. This data for the error window for case 1 could be reconstructed from this tether tip data by finding the minimum length vector from the payload position (0,0) and the tether tip path.

The second item that is considered from this motion is the general distribution of the data that constructed the error windows. It is believed that as the variance of the input parameters is increased, the size of the error ellipses will also increase, while retaining their same general form. This premise is evaluated through numerical analysis of the data, now considering three cases, the original case called the 100% variance case, and two additional (one with 200 % variance and the third with 333% of the original variance). The results of these analyses are shown in the blue markers in Figs. 1-3.

It can be seen that in each case, the error window is increased, and in general retains its original form. The one exception is that in case three, it is observed that as the input variance increases past a certain level, the error in the tether normal direction increases significantly. It is proposed that this is due to the fact that a significant change in the tether arrival time occurs, and the initially dominant effect, tether axial vibration, is over-ridden by a second effect, tether rotation.

Summary and Conclusions

This paper has performed an analysis of the capture error window for a MXER tether system based on uncertainty in tether parameters within a numerical tether model. Due to the nature of tether behavior, a system consisting of axial and transverse vibrations, it is postulated that the error bounds resulting from uncertainty in tether behavior could be best described geometrically through an error ellipse or an error ellipsoid. Plots of the error distribution based on uncertainty in tether parameters are created using a Monte Carlo simulation of the tether numerical model for several scenarios of error prediction. The plots of these error distributions (Fig. 1 a-c) indeed depict an error profile that is spatially distributed along two primary axes much like the major and minor axis of the ellipse. In case 1 and 2 (closest approach to a fixed point in space), the distribution is generally normally distributed about the zero error position, with the density dropping off at the boundary of the errors. In case 3 (closest approach to an orbiting payload) the error distribution again falls within an ellipse type pattern, with the error points distributed largely along the boundary of the ellipse. The error of case 3 may be better described as a cycloid with the primary error resulting from timing issues between the payload and tether (these are not accounted for in this model).

A transformation is defined to convert error data into an equivalent error ellipse as shown in Eqs. 14-18. The results for all three cases are shown in Table III. The cases are averaged to result in a current estimate for the error ellipse, with properties given in the last row of Table III. The major axis of this error ellipse is approximately 10 times greater than the minor axis, and is aligned with the axis of the tether. Thus, the major axis represents axial displacements of the tether while the minor axis represents transverse vibrations.

Tether response due to the capture process is observed through phase portraits of average tether axial strain and tether rotation. The tether response prior to capture and after capture is shown in Figs. 4-6. It can be noted that the capture process maintains the periodic nature of the tether response, but greatly increases the amplitudes of response in both longitudinal vibrations and in rotational rate. The response demonstrated in Figs. 4-6 is apparently equivalent, but represents capture at three distinct points within the error ellipse (minimum, median and maximum error). This result demonstrates that, over the error represented in this error ellipse, that the jerk forces introduced in capture greatly outweigh the potential impact forces in the region of error considered.

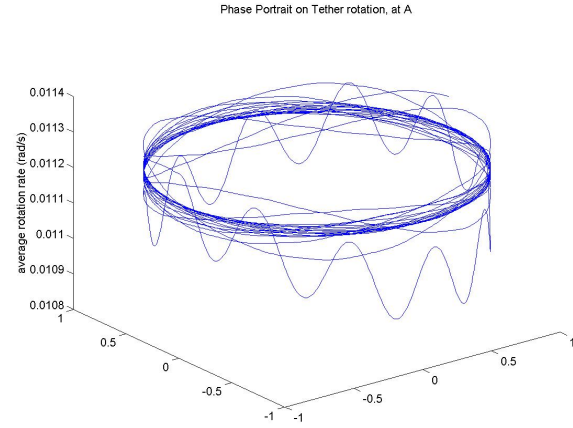
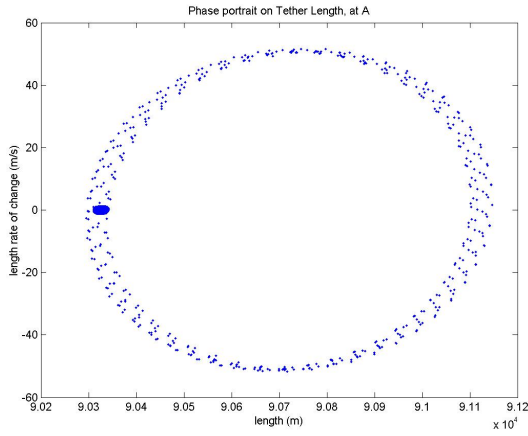


Figure 4: Phase portraits at point A

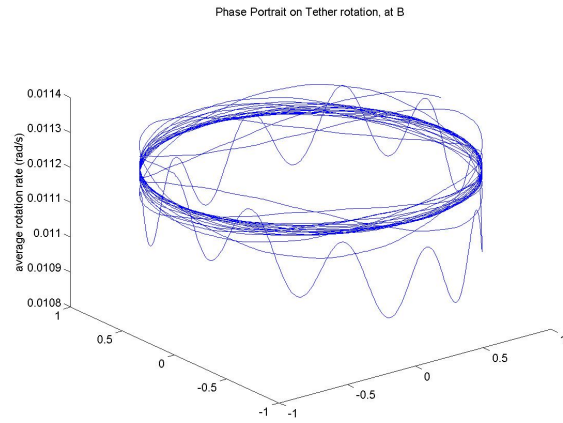
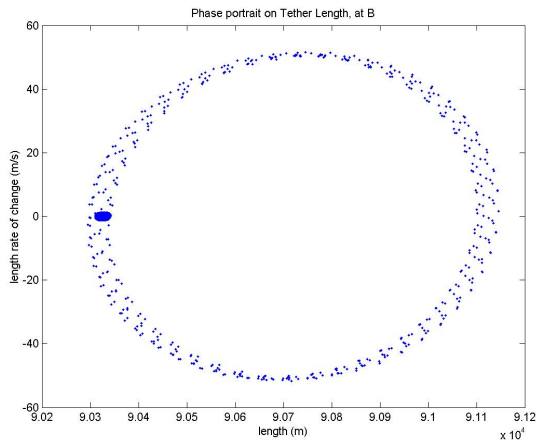


Figure 5: Phase portraits at point B

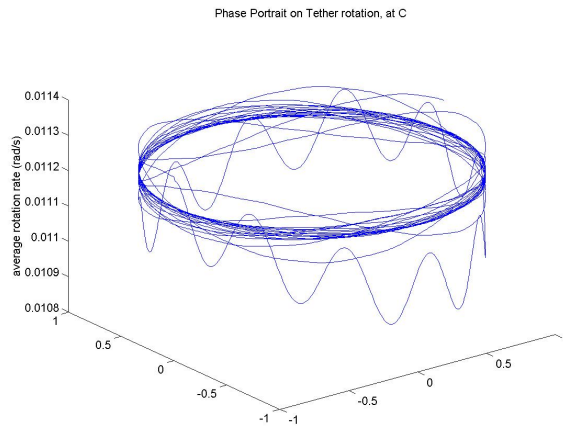
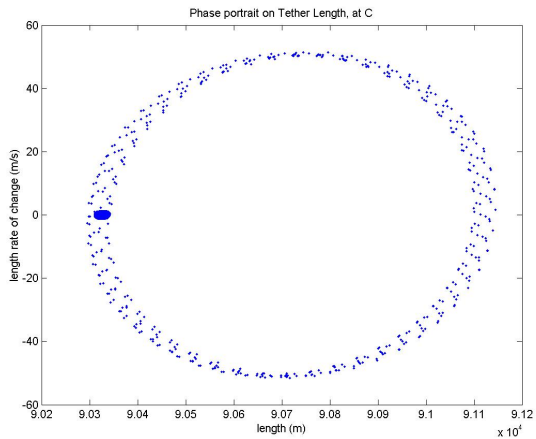


Figure 6: Phase portraits at point C

The results of this work will be used in the design of appropriate capture mechanisms for the MXER tether system. These results imply that an ideal capture mechanism would be able to account for error that is distributed about spatial axes with the error along the most significant axis (tether axis)

approximately ten times greater than errors in the other axes (transverse axes). By design the capture mechanism to the expected error can result in optimal configurations in terms of weight savings, reliability, and maximizing the capture window. Several areas of additional work are suggested in reaching improved estimates of the error window for capture. While this work only considers error due to uncertainties in tether parameters, many other sources of error may exist, for example in initial conditions or on-orbit properties. In addition, in the transformation process defined, it should be noted that the error distribution is generally normal while the inertias calculated for the ellipse are based on a uniform distribution. This could be corrected through an ellipse moment of inertia definition based on both ellipse geometry and mass distribution.

References

- [1] Misra, A.K. and Modi, V.J., "A Survey on the Dynamics and Control of Tethered Satellite Systems," AAS 86-246, Tethers in Space, Advances in the Astronautical Sciences, Vol. 62, San Diego, CA, 1987, pp. 667-719.
- [2] Beletsky, V. V and Levin, E. M, 1993, *Dynamics of Space Tether Systems, Vol. 83, Advances in the Astronautical Sciences*, Univelt Incorporated, San Diego CA.
- [3] Quadrelli, B.M., and Lorenzini, E.C., "Three-Dimensional Dynamics of a Spinning Tethered System in LEO," AAS 89-456, Microfiche Series Vol. 59, pp. 518-547.
- [4] Tragesser, Steven G. (Perdue Univ); Longuski, James M; 1998, *Analysis and Design of Aerocapture Tether with Accounting for Stochastic Errors*, Journal of Spacecraft and Rockets, Vol. 35, No. 5, Sept-Oct. pp. 683-689
- [5] Pelaez, J. (Universidad Politecnica de Madrid); Lorenzini, E.C.; 1996, *Sensitivity Analysis of Tether-Mediated Orbital Injection*, Journal of the Astronautical Sciences, Vol. 44, No. 4, Oct-Dec, pp. 491-514
- [6] Leamy, M.J.; Noor, A.K.; Wasfy, T.M.; 2001, *Sensitivity Analysis of Bare-wire Space Tether Systems*, Computer Methods in Applied Mechanics and Engineering, Vol. 190, No. 42, Aug 3, pp. 5495-5503
- [7] e. fehlberg, nasa technical report TR-287, 1968
- [8] Fried, I, 1982, "Large Deformation Static and Dynamic Finite Element Analysis of Extensible Cables," *Computers and Structures*, Vol. 15, No. 3, pp. 315-319.
- [9] Henghold W. M. and J. J. Russell, 1976, "Equilibrium and natural frequencies of cable structures (a nonlinear finite element approach)," *Computers and Structures*, Vol.6, No. 4, pp. 267-271.
- [10] Rubinstein, Reuven Y., 1981, *Simulation and The Monte Carlo Method*, John Wiley and Sons, New York, NY]
- [11] Kushner, Harold J., Yang, Jichuan, March 1992 "A Monte Carlo Method for Sensitivity Analysis and Parametric Optimization of Nonlinear Stochastic Systems: The Ergodic Case." *Siam Journal of Control and Optimization*, Vol. 30, No.2, pp. 440-464.]
- [12] Thompson, Adrian M., Cluett, William R. ,2005 "Stochastic Iterative Dynamic Programming: A Monte Carlo Approach to Dual Control," *Automatica*, Vol. 41, pp. 767-778
- [13] P.M. Bouton and F. Ma, "On Monte Carlo simulations of dynamic systems"

SECTION D—QUAD TRAP CAPTURE MECHANISM PROTOTYPE MODEL

CAD

This appendix presents the CAD model used to construct the prototype Quad trap capture mechanism. First, isometric views of the Quad Trap prototype cad model are provided demonstrating the mechanism in an open and closed position (Figures Appendix D-1, 2). Following that individual component drawings are provided for all components that are designed and manufactured specifically for the Quad trap prototype mechanism (Figures App.C-3 through Appendix D-10). The remaining materials used to construct the prototype are commercially available materials. Finally, a photograph of the fabricated Quad trap prototype is provided in Figure Appendix D-11.

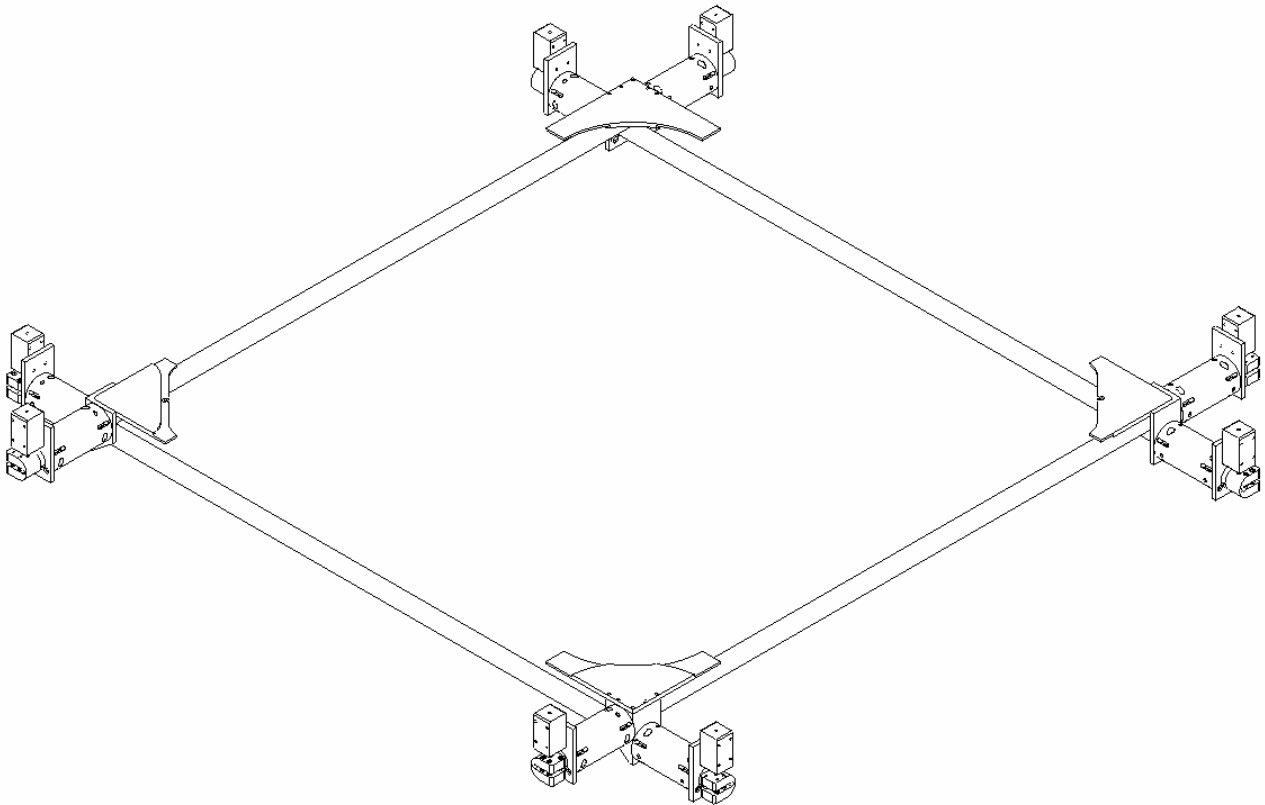


Figure 1: Isometric View of the Quad trap prototype in an open configuration

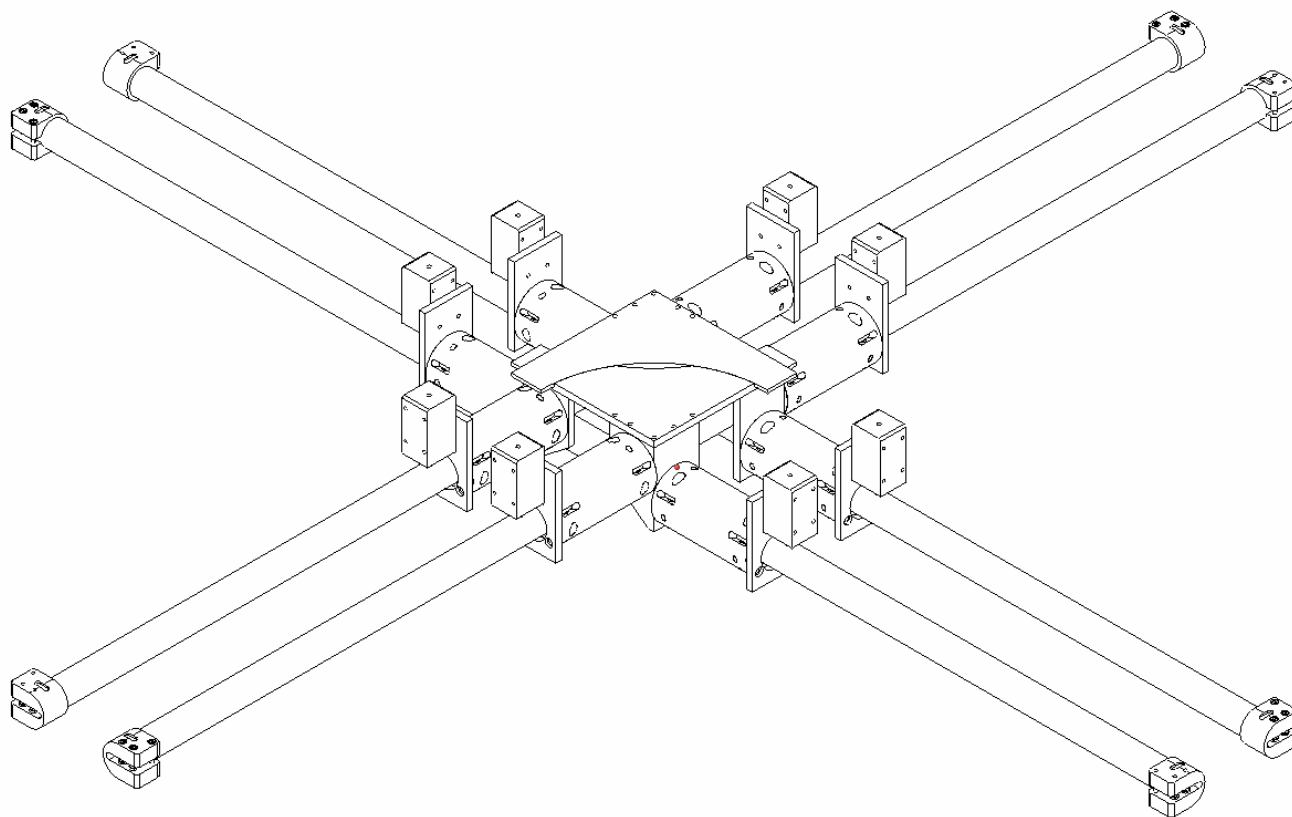


Figure 2: Isometric View of the Quad trap prototype in a closed configuration

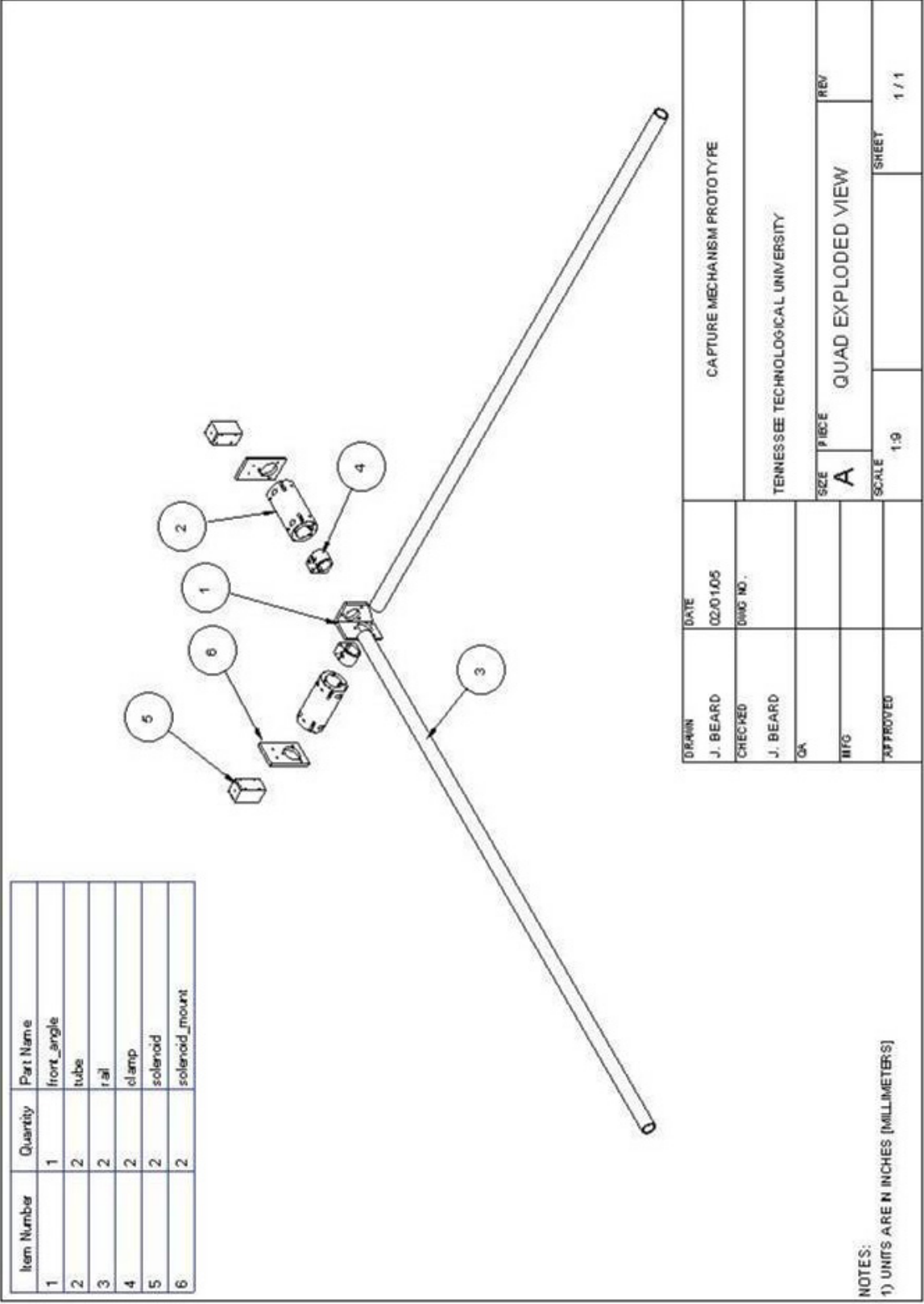


Figure 3: Quad Trap Exploded view, One Corner

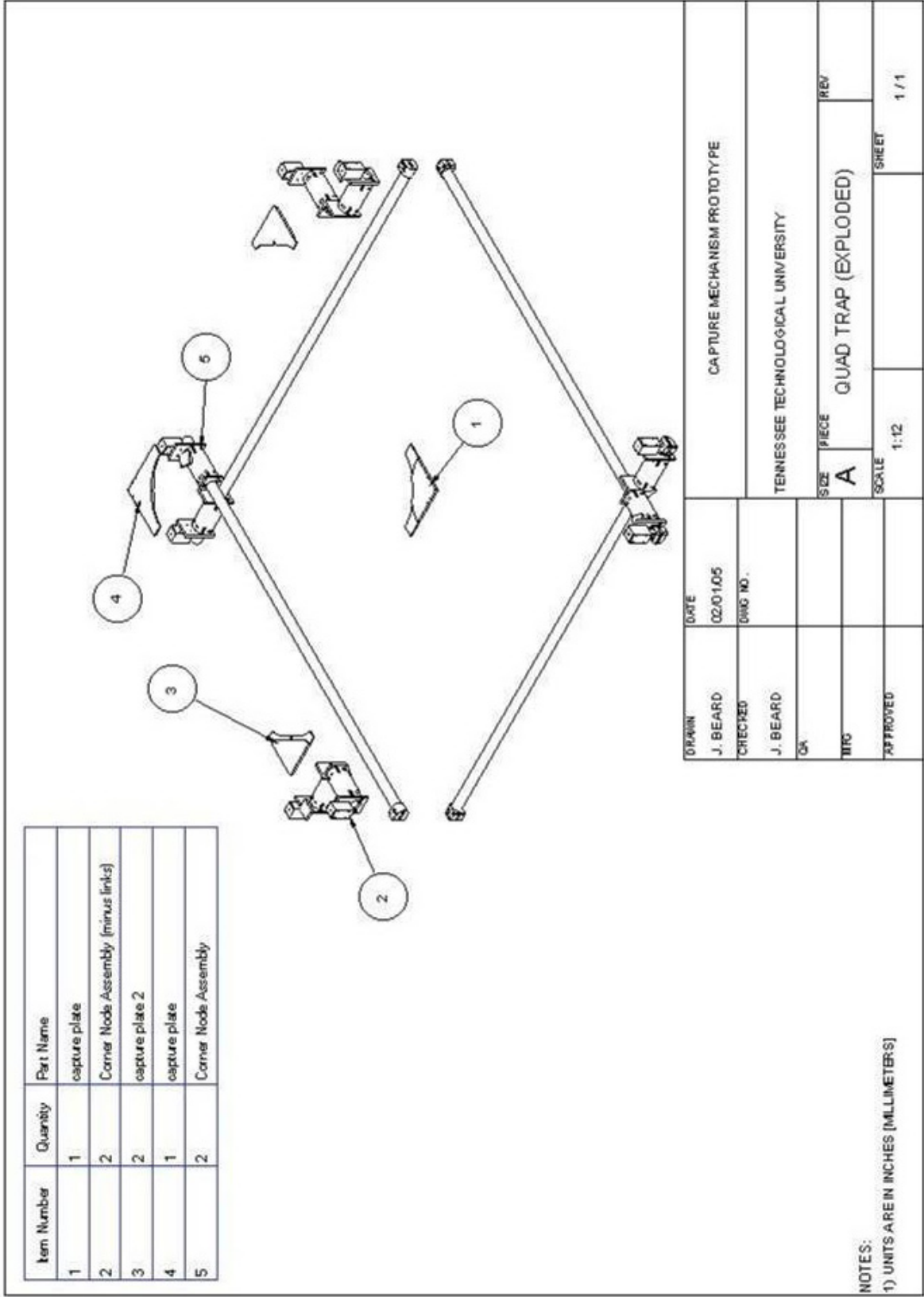


Figure 4: Quad Trap Exploded View

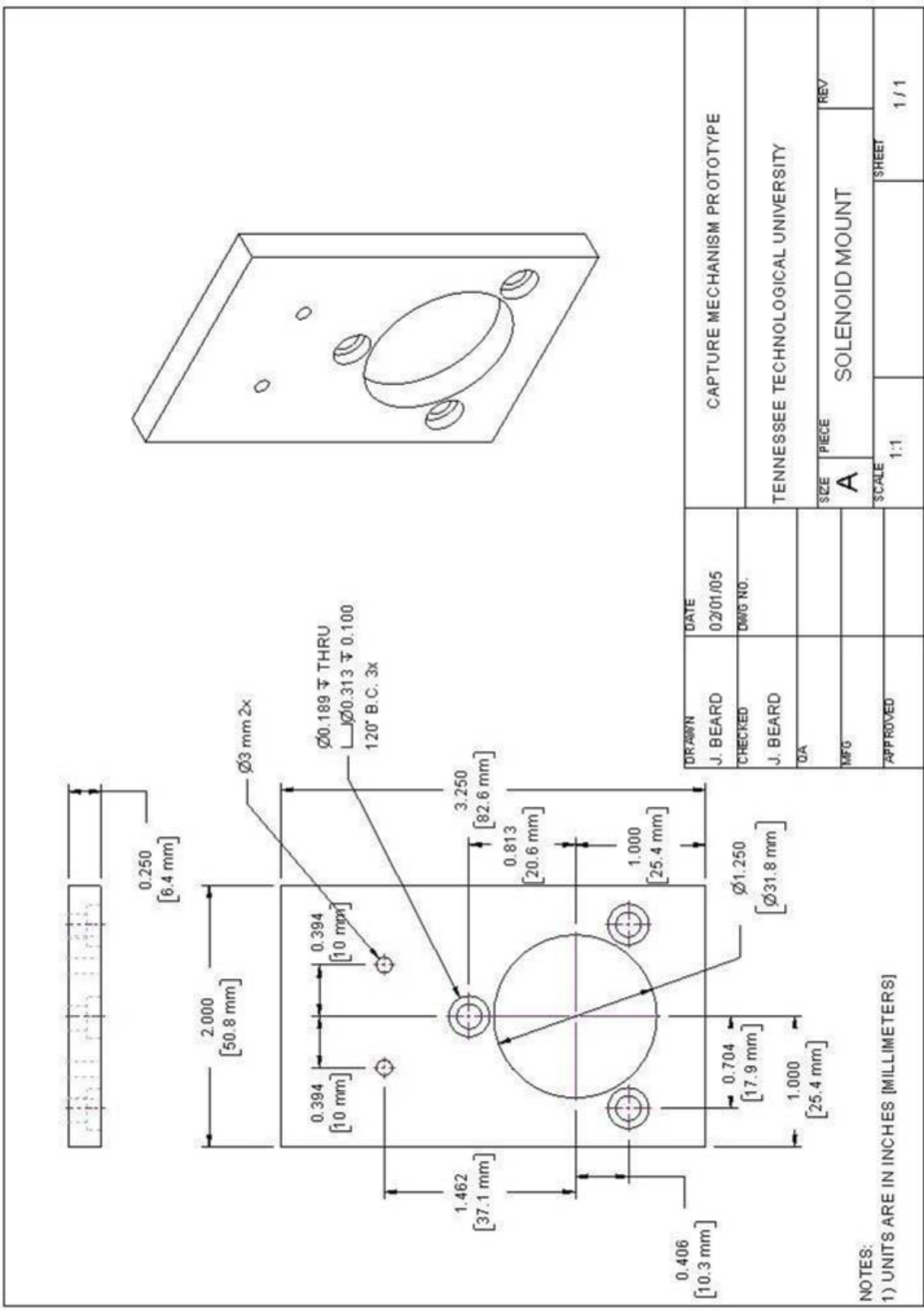


Figure 5: Component drawing: Solenoid Mount

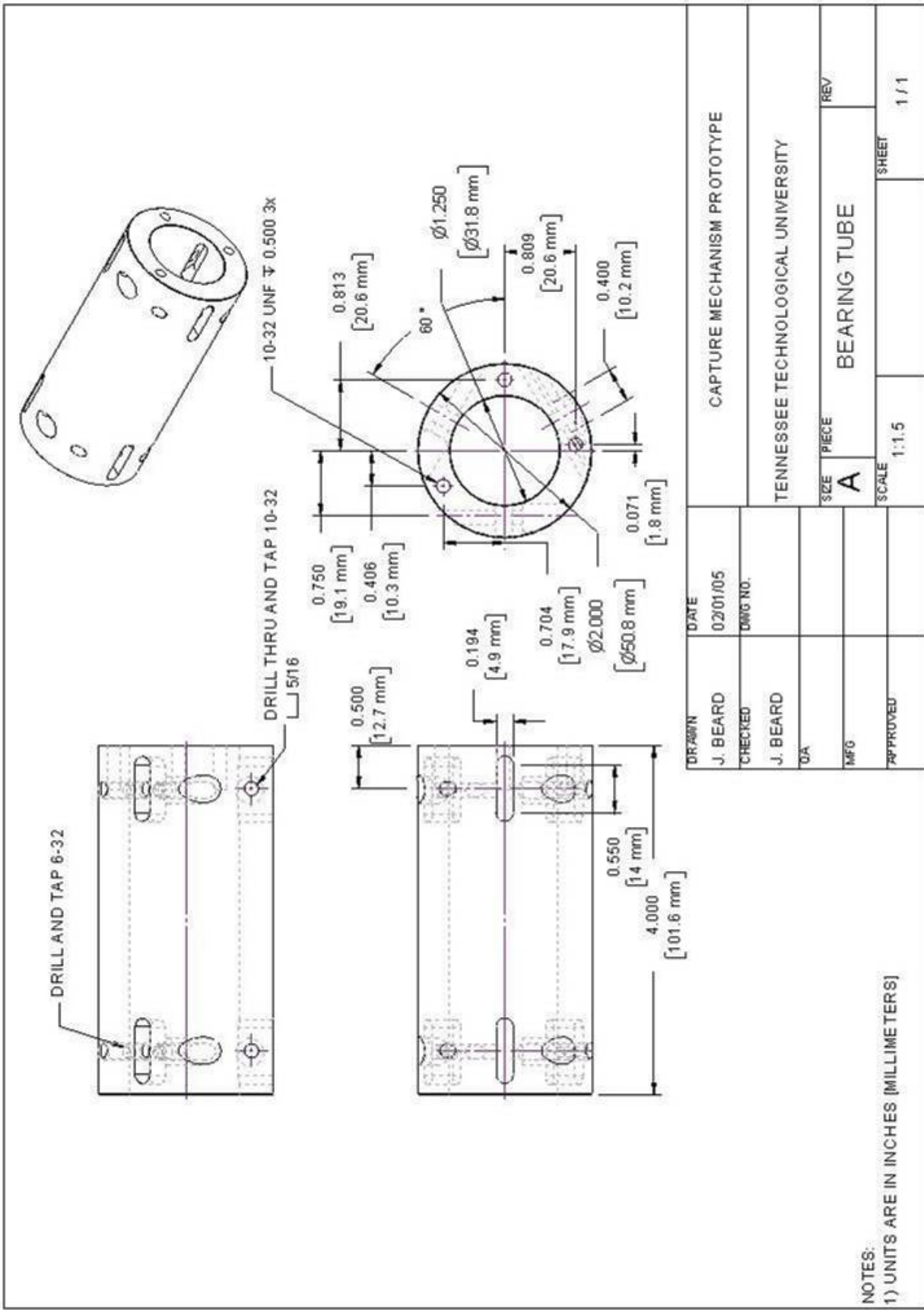
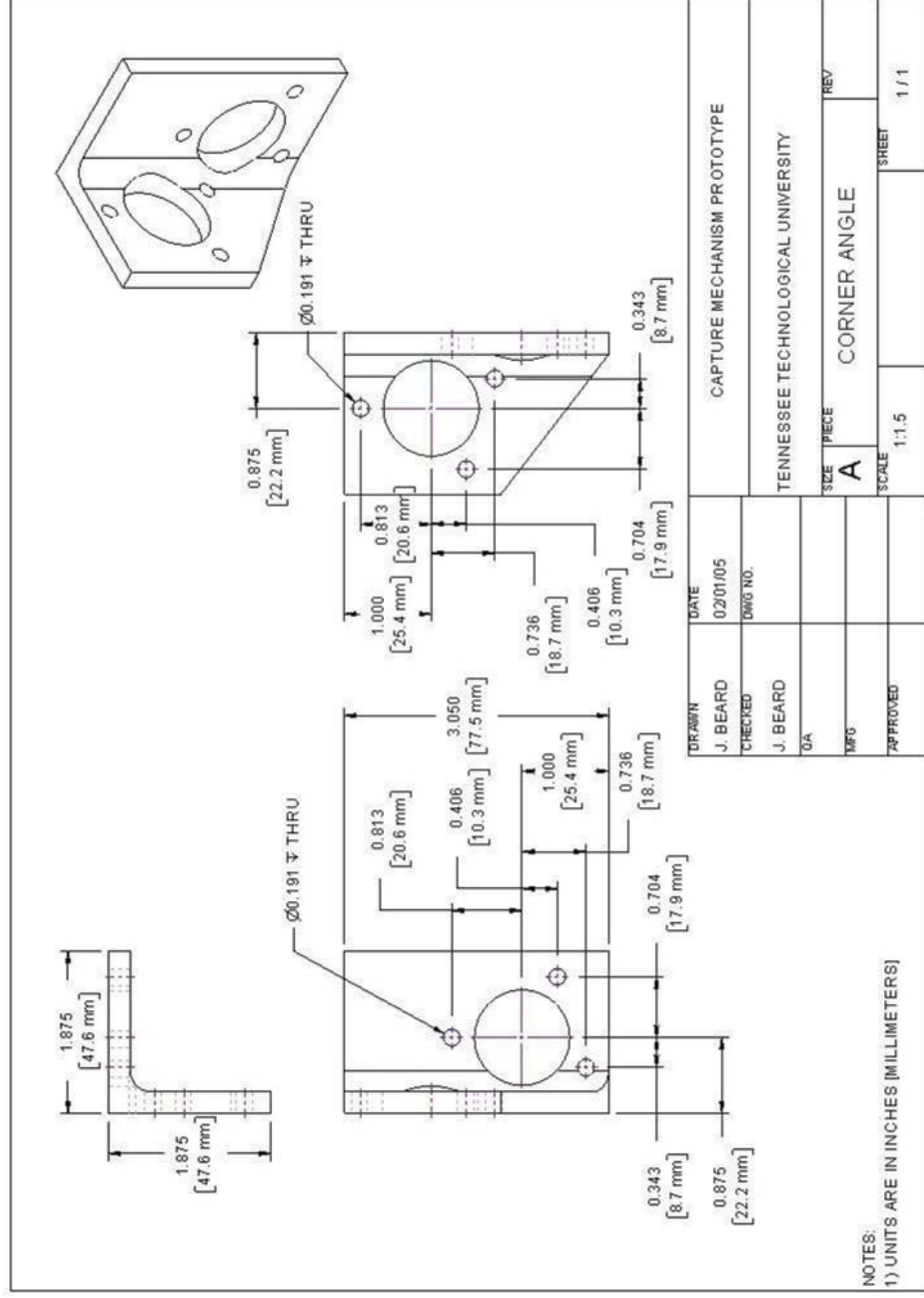


Figure 6: Component drawing: Bearing Tube



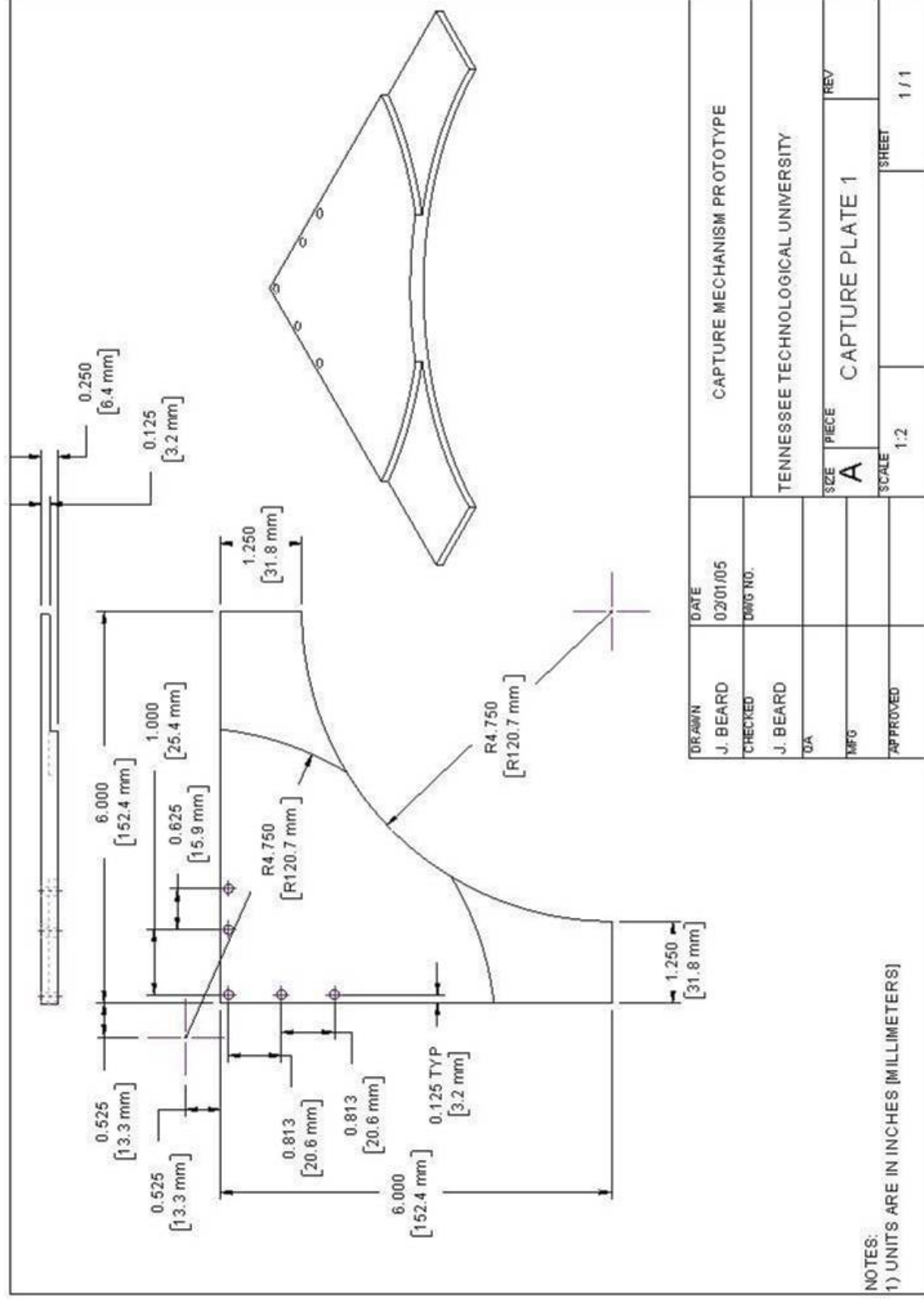


Figure 8: Component drawing: Capture Plate 1

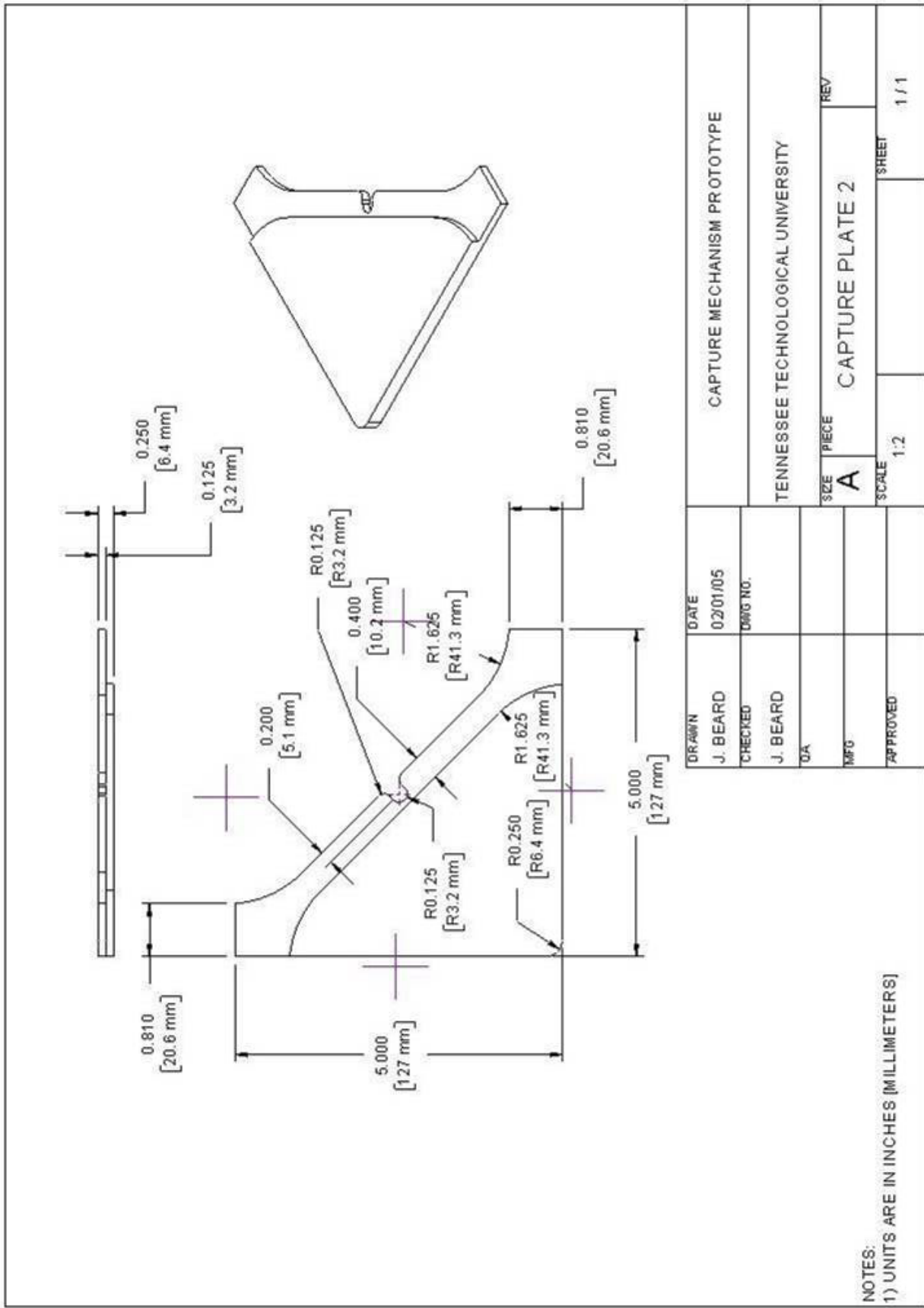
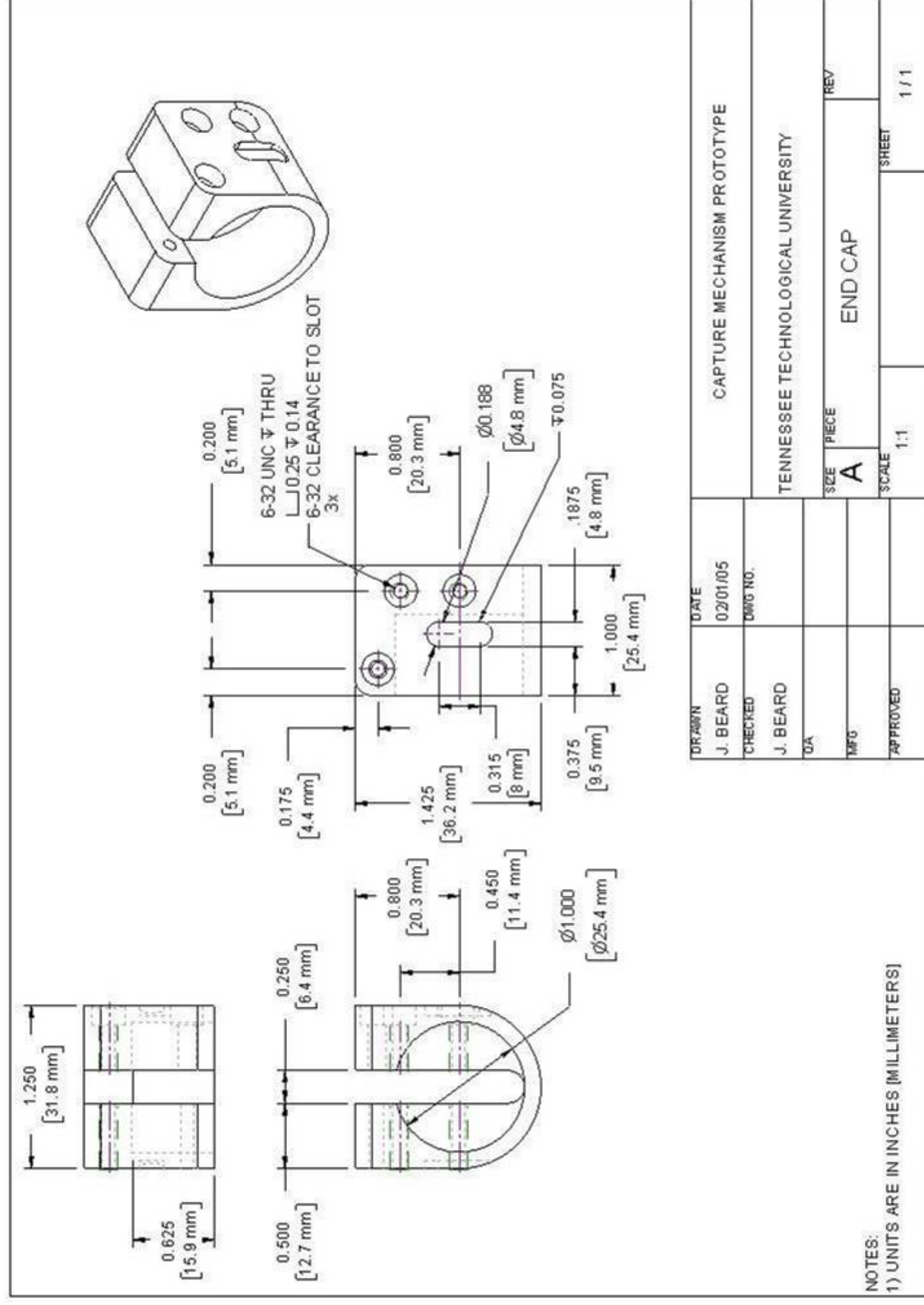


Figure 9: Component drawing: Capture Plate 2



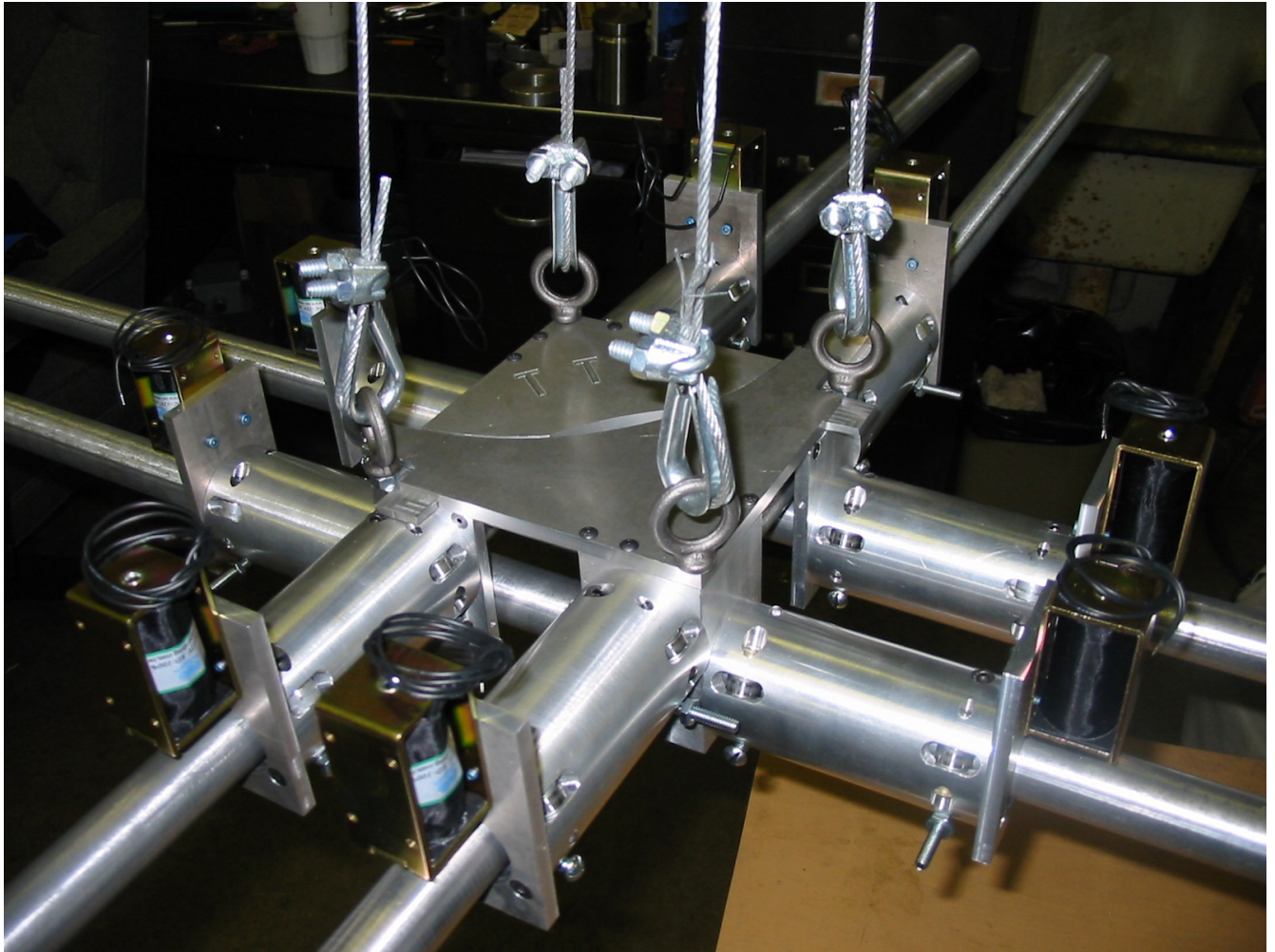


Figure 11: Quad Trap Prototype as Fabricated

REPORT DOCUMENTATION PAGE			Form Approved OMB No. 0704-0188	
Public reporting burden for this collection of information is estimated to average 1 hour per response, including the time for reviewing instructions, searching existing data sources, gathering and maintaining the data needed, and completing and reviewing the collection of information. Send comments regarding this burden estimate or any other aspect of this collection of information, including suggestions for reducing this burden, to Washington Headquarters Services, Directorate for Information Operation and Reports, 1215 Jefferson Davis Highway, Suite 1204, Arlington, VA 22202-4302, and to the Office of Management and Budget, Paperwork Reduction Project (0704-0188), Washington, DC 20503				
1. AGENCY USE ONLY (Leave Blank)	2. REPORT DATE September 2007	3. REPORT TYPE AND DATES COVERED Contractor Report		
4. TITLE AND SUBTITLE Developing Capture Mechanisms and High-Fidelity Dynamic Models for the MXER Tether System		5. FUNDING NUMBERS NNM04AB13C		
6. AUTHORS S. L. Canfield				
7. PERFORMING ORGANIZATION NAME(S) AND ADDRESS(ES) Tennessee Technological University Cookeville, TN 38505		8. PERFORMING ORGANIZATION REPORT NUMBER M-1202		
9. SPONSORING/MONITORING AGENCY NAME(S) AND ADDRESS(ES) National Aeronautics and Space Administration Washington, DC 20546-0001		10. SPONSORING/MONITORING AGENCY REPORT NUMBER NASA/CR—2007-215076		
11. SUPPLEMENTARY NOTES Prepared for the Science & Mission Systems Directorate, Science Research & Technology Projects Office Technical Monitor: J. Bonometti				
12a. DISTRIBUTION/AVAILABILITY STATEMENT Unclassified-Unlimited Subject Category 18 Availability: NASA CASI 301-621-0390			12b. DISTRIBUTION CODE	
13. ABSTRACT (Maximum 200 words) A team consisting of collaborators from Tennessee Technological University (TTU), Marshall Space Flight Center, BD Systems, and the University of Delaware (herein called the TTU team) conducted specific research and development activities in MXER tether systems during the base period of May 15, 2004 through September 30, 2006 under contract number NNM04AB13C. The team addressed two primary topics related to the MXER tether system: 1) Development of validated high-fidelity dynamic models of an elastic rotating tether and 2) development of feasible mechanisms to enable reliable rendezvous and capture. This contractor report will describe in detail the activities that were performed during the base period of this cycle-2 MXER tether activity and will summarize the results of this funded activity. The primary deliverables of this project were the quad trap, a robust capture mechanism proposed, developed, tested, and demonstrated with a high degree of feasibility and the detailed development of a validated high-fidelity elastic tether dynamic model provided through multiple formulations.				
14. SUBJECT TERMS in-space tethers, dynamics, capture mechanisms, autonomous rendezvous			15. NUMBER OF PAGES 154	
			16. PRICE CODE	
17. SECURITY CLASSIFICATION OF REPORT Unclassified	18. SECURITY CLASSIFICATION OF THIS PAGE Unclassified	19. SECURITY CLASSIFICATION OF ABSTRACT Unclassified	20. LIMITATION OF ABSTRACT Unlimited	

National Aeronautics and
Space Administration
IS20

George C. Marshall Space Flight Center

Marshall Space Flight Center, Alabama
35812